The Tectono-metamorphic Evolution of the Rhodope Massif, Bulgaria

David Andrew Thomas Collings

Submitted in accordance with the requirements for the degree of doctor of philosophy

The University of Leeds
Institute of Geophysics and Tectonics
School of Earth and Environment

June 2014

Acknowledgments

This work would not have been possible without the help and support of many people. First, I would like to thank my Supervisors Ivan Savov and Bruce Yardley for their support and encouragement over the course of my PhD. Ivan, thank you for being such an enthusiastic supervisor, always making time for me and my ideas, and for introducing me to the Rhodope Massif, a truly stunning part of the world. Bruce, thank you for your advice over the course of this project, ensuring that I have stayed on track, and for squeezing in time to provide me invaluable feedback on chapters.

I am deeply indebted to Jason Harvey and Bob Cliff for all of their help and guidance in the lab, particualry to Jason for introducing me to Ethan and facilitating the garnet geochronology performed in this study. I am very grateful for all the help I received from Richard Walshaw and Eric Condliffe on the probe/SEM, particularly Eric who endured numerous calls from me thinking I had found a microdiamond – thankfully my persistence paid off!

Thank you to Ethan Baxter and his group at Boston for allowing me to use their amazing facilities, and for being such welcoming hosts. A massive thankyou to Katie Eccles and Denise Honn; without their help I don't see how I would have finised the garnet geochronology study. I am very grateful

The fieldwork in Bulgaria would not have been possible without Laki Dimitrov, Nikki Bonev, and the geologists at Dundee Precious Metals in Krumovgrad. I am very appreciative of alll of their help and advice during my field seasons, and especially to Laki, for driving me around the Rhodopes, showing me the best localiies in the vicinity of Chepelare and providing me with two specimens of kyanite garnet schist from the Natural History Museum of Sofia collections. The various Leeds University undergraduate students that have mapped the area around Chepelare have provided me with a number of fantastic specimens, taken me to great outcrops, challenged my views on the area and made my field seasons all the more enjoyable for which I am very grateful. Special thanks go to Darryl, John, Katie, Luke, Ben, Elliot, Joe and Mat.

I have had an amazing time at Leeds over the last four years, largely thanks to the great group of people I have met and worked with. Special thanks must go to officemates Andy, Dave, Fran, Grace, Haggis, Hannah, Julia, Katie, Lucy and Will and fellow postagrads/postdocs Becky, Curls, Laura, Jen and Jo. Thank you for putting up with my geochemical rambling, my messy desk and my endless chatter. Over the past four years you have learnt when to let me work and when (despite my protests) to drag me to the pub. I could not have done it without you all, you have kept me sane.

I was very lucky to start my PhD with a fantastic group of people who have become great friends. Andy, thank you for making the last 4 years so entertaining. Dan, your competitiveness (even if it does drive me mad at times) has driven me to achieve more. Lynz, your copious amount of gin and coffee have been very much appreciated (alongside your crash course in sedimentology and paleontology in Cyprus), and Sandra, you have been a constant source of gossip, support and German Beer for which I am very grateful.

Great thanks go to my family for all of their support and encouragement throughout my time at University. And finally, Jo, my soon to be wife. None of this would have been possible without your help, support (both emotional and financial) and endless encouragement over the course of the PhD. I cannot wait to move to Peru to start our new life together.

This research was funded by a NERC studentsip, and supplemented by research grants from the Geological Society of London, Mineralogical Society of Great Britain and Northen Ireland, Geochemistry Group of the Mineralogical Society and the Insititute of Geophysics and Tectonics, University of Leeds.

Abstract

In recent years the Rhodope Massif has risen in prominence due to the discovery of microdiamond in garnet from metapelites in the Greek Rhodope Mts., establishing the region as a rare UHP province. This study is the first to establish that the UHP conditions continue through to Bulgaria, owing to the discovery of a microdiamond inclusion in garnet from metapelite in the vicinity of the town of Chepelare in the Bulgarian Central Rhodope Mts. This UHP metapelite outcrops within the Chepelare Shear zone (CSZ), a 'melange' of meta-igneous and meta-sedimentary rocks located on the edge of the Variscan Arda dome, one of three metamorphic core complexes that dominate the regional geology. Through a combination of petrographical and geochemical analysis, the metamorphic conditions experienced by these UHP samples have been reconstructed.

Two populations of metabasic units in the Central Rhodope Mts. were identified in this study; one within the melange units of the CSZ, and one as boudins in orthogneiss overlying the CSZ. The boudins are shown to be retrogressed eclogites with a supra-subduction zone origin unrelated to the metabasic units within the CSZ. Correlations are observed with Neoproterozoic/Ordovician metabasic samples previously reported from the Eastern Rhodope Mts., which represent remnants of the Variscan Orogeny in this region. Metabasic melange samples within the CSZ instead have an N-MORB affinity, and display no evidence of a shared P-T history with the UHP metapelites.

Sm-Nd garnet dating of the metapelites from the CSZ performed in this study indicates a Late Cretaceous age for the UHP metamorphic event. This is significantly younger than previously reported ages, and suggests a formation history associated with the northwards subduction of the Vardar Ocean beneath the Moesian Platform during the Late Mesozoic. The present day structure of the massif is the result of complex Cenozoic tectonics following post orogenic extension and formation of the metamorphic core complexes that are observed across the Rhodope Massif.

Common Abbreviations used in text

Ab: Albite
Alm: Almandine
An: Anorthite
CSZ: Chepelare Shear Zone
E-MORB: Enriched - Mid Ocean Ridge Basalt
EDS: Energy Dispersive Spectroscopy
EPMA; Electon Probe Micro Analyser
Grs: Grossular
HFSE: High Field Strength Element
HREE: Heavy Rare Earth Element
IAB: Island Arc Basalt
ICP-AES: Inductively Couple Plasma – Atomic Emission Spectrometry
ICP-MS: Inductivelty Coupled Plasma – Mass Spectrometry
LILE: Large Ion Lithophile Element
LREE: Light Rare Earth Element
MORB: Mid Ocean Ridge Basalt
N-MORB: Normal- Mid Ocean Ridge Basalt
NSZ: Nestos Shear Zone
Pyp: Pyrope
REE: Rare Earth Element
RM: Rhodope Massif
SEM: Scanning Electorn Microscope
Sps: Spessartine
TIMS: Thermal Ionisation Mass Spectrometry
UHP: Ultra high pressure
VF: Variegated Formation
WDS: Wavelength Dispersive Spectroscopy

Table of contents

List of Tables

List of Figures

Chapter 1 : Introduction

1.1 Introduction to Ultra High Pressure metamorphism

In 1984, the understanding of subduction zone metamorphism fundamentally changed. Coesite, the high pressure polymorph of quartz, was found as inclusions in clinopyroxene from eclogite within the Caledonides of Norway (Smith, 1984) and as inclusions in pyrope garnet from a high grade blusechist within the Doria Maira Massif, Western Alps (Chopin, 1984). These discoveries established that subducted continental crust can be exhumed from depths greater than 100km. Following this discovery, diamond inclusions were found in garnet from the Kokchetav Massif (Sobolev and Shatsky, 1990) suggesting metamorphism at even greater pressures (>40 kbar) and establishing the link between continental collision events and exhumation of deep crustal material. These discoveries led to the development of a new field of metamorphic petrology, ultrahigh pressure (UHP) metamorphism; the study of metamorphic processes occurring at pressures > 28 kbar (the minimum pressure required for coesite formation at 700 °C (Coleman and Wang, 1995)). Other indicators of UHP conditions, including quartz exsolution lamellae in clinopyroxene (Liou et al., 2009), α-PbO_2-structured TiO_2 (Yang et al., 2007) and supersilicic titanite (Ogasawara et al., 2002) have since been recognised, and as a result more than 20 UHP localities worldwide have been recognised (Figure 1-1).

Recently, evidence has even arisen for the occurrence of decompressed stishovite in crustal rocks, suggesting that exhumation of crustal material from depths > 350 km is possible (Liu et al., 2007). Despite the large global effort to identify new UHP localities, a lot remains unknown about their formation, exhumation and preservation. Many of the UHP localities are in remote places where little geological work has been performed, and as such it is difficult to link numerical models for UHP formation and exhumation with field evidence. Only through increased understanding of the evolution of these UHP localities will the uncertainties surrounding their formation and preservation be understood.

1.2 Formation of UHP terranes

Globally, UHP terranes are dominated by quartzofeldspathic rocks, with only a small proportion of mafic/ultramafic rocks containing UHP indicators (Hacker and Gerya, 2013).

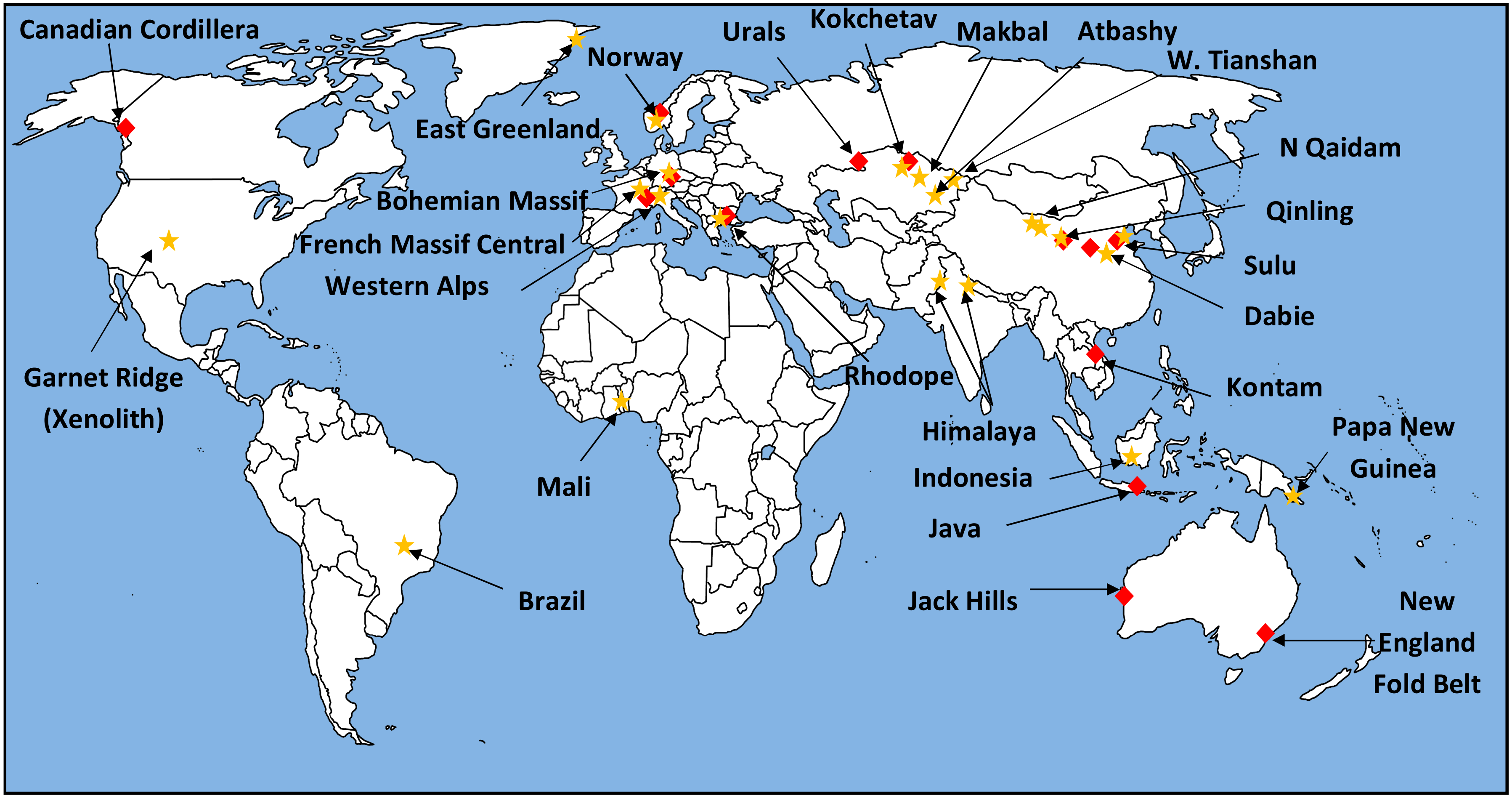

Figure 1-1: Map of all known UHP microdiamond and coesite localities after (Dobrzhinetskaya, 2012), ★= coesite loaclity, ♦= microdimoand locality

As a result, any scenario for formation of these UHP terranes requires the subduction of ordinarily buoyant continental crust to great depths. Six distinct mechanisms that would theoretically allow the subduction of buoyant material to great depths in the mantle have been proposed: 1) continental margin subduction, 2) micro-continent subduction, 3) sediment subduction, 4) intra-continental subduction, 5) subduction erosion and 6) foundering of a crustal root (Hacker and Gerya, 2013). A number of these mechanisms are valid irrespective of whether the upper plate is oceanic or continental. Each mechanism has been proposed for a number of locations worldwide. All are summarised graphically in Figure 1-2 and examples of each are presented in Table 1-1.

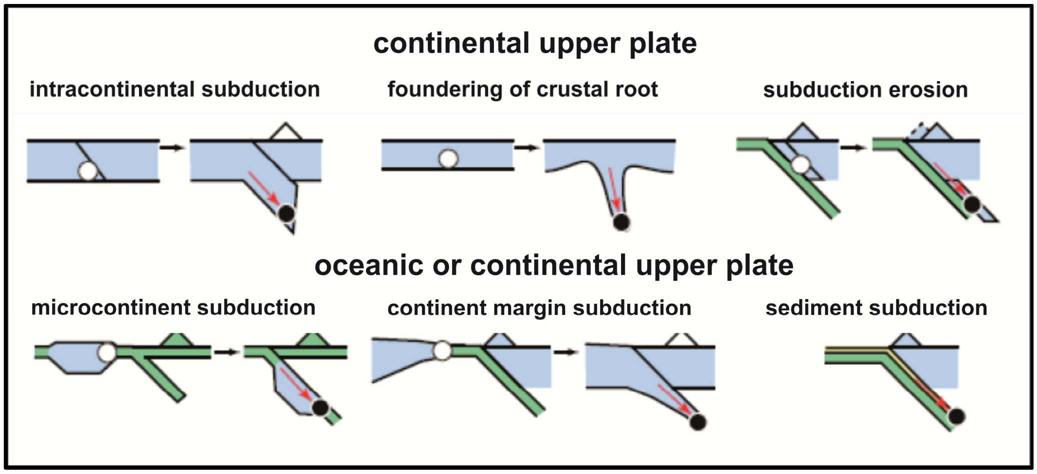

Figure 1-2 : Graphical representation of the six proposed formation mechanisms for UHP rocks, redrawn from Hacker and Gerya (2013). Green plate is oceanic crust, blue plate is continental crust. White dot is sample protolith, black dot is sample experiencing UHP conditions.

Recent work has also identified that UHP terranes can loosely be divided into two distinct groups termed ‘large, old, thick and slow’ and ‘small, young, thin and fast’ (Kylander-Clark et al., 2012). These have been linked with different continental orogenic stages, the result of variation in buoyancy, traction forces, subduction rate and proportion of crust to mantle. The small, young terranes are believed to form during the initial stages of a subduction, owing to the larger amount of dense oceanic crust in the subduction system leading to rapid subduction and steep exhumation. Proposed examples are the Alps, and Himalaya. The large, older terranes are instead believed to be related to more evolved subduction zones, with greater amounts of continental crust in the subduction channel. The increased amount of buoyant material slows convergence and decreases the subduction angle, resulting in a longer lasting exhumation event. Proposed examples are the Western Gneiss Region of Norway and the Dabie-Sulu mountain range in China.

Mechanism	Present day example	Ancient example
Continental margin Subduction	Banda Arc, Australia (Harris, 2003)	Dabie Shan, China (Schmid et al., 2003)
Micro continent subduction	Yakutat Terrane, Alaska (Eberhart-Phillips et al., 2006)	Kokchetav Massif, Kazakhstan (Dobretsov et al., 1995)
Sediment subduction	Island arcs worldwide (Scholl and von Huene, 2007)	unknown
Intra-continental subduction	Pamir (Sippl et al., 2013)	Greenland (Gilotti and McClelland, 2007)
Subduction erosion	Island arcs worldwide (Scholl and von Huene, 2007)	Pamir (Hacker et al., 2005)
foundering of a crustal root	The Pamir (Burtman and Molnar, 1993)	unknown

Table 1-1: Table to show both ancient and present day examples of each of the UHP formation mechanisms

It is conceivable that established UHP terranes could/should contain UHP phases formed as a result of both orogenic stages, but currently there is no documented evidence of either small younger UHP terranes within ancient larger UHP terranes, or vice versa. This is ascribed to preferential erosion of the small continental slivers within large terranes and the long timescales required for the exhumation of the large terranes. It is plausible that in younger UHP belts, large UHP terranes are trapped in the continental lower crust and are yet to manifest at the surface, as proposed by Walsh and Hacker (2004). This hypothesis of splitting UHP localities into two distinct groups is a recent development, and unfortunately there has been insufficient work at most UHP localities to test it.

The significance of tectonic overpressure in the formation of UHP units is another factor that remains unclear. Whilst it is plausible, and has both been predicted by numerical models (Li et al., 2010) and used to explain largely conflicting P-T histories (~ 1.5 GPa difference) for rocks of the same age in the same area of the Western Gneiss Region of Norway (Vrijmoed et al., 2009), it remains unclear whether the subducting lithosphere is strong enough to withstand such substantial overpressures (Warren, 2013).

1.3 Preservation of UHP phases

UHP samples are typically highly retrogressed, which traditionally has rendered thermobarometers unsuitable for constraining the peak P-T conditions experienced by a sample. As a result, identification of UHP phases (microdiamond and/or coesite) was the only established method to confirm UHP conditions. These phases are only preserved as inclusions in refractory minerals such as garnet and zircon, which protect the UHP phases from the effects of post peak metamorphism or retrogression. Recent advances in P-T estimation using thermobarometric calculations, combined with microstructural features such as spinel inclusions in garnet or exsolution of clinoenstatite have led to the proposal of several new UHP localities where no UHP phases are preserved (Dobrzhinetskaya and Faryad, 2011).

With coesite commonly transforming to quartz upon exhumation, microdiamond inclusions are the easiest and most definitive identifier of UHP conditions, with diamond being easily confirmed via Laser Raman Spectroscopy. A great deal of work has recently focused on establishing how microdiamonds form in UHP environments. Diamond was first synthesized from graphite in a laboratory by heating the graphite to extreme pressures and temperatures in the presence of both fluids rich in CH_4, CO_2 and H_2O at specific fO_2 conditions and a metal solvent catalyst which is required to break the C-C Sp^2 bond (Bundy et al., 1955). Following this, many experiments have been conducted to attempt to synthesize diamonds under conditions that are more realistic in nature. Two different theories have been proposed; diamond formation via crystallisation from a supercritical C-O-H fluid/melt (Stöckhert et al., 2001), or via direct transformation from metastable graphite to diamond (Korsakov et al., 2010a). The latter was used to explain carbon inclusions, with a graphite core and diamond rim in the Kokchetav Massif, but the calculated required P-T conditions are much higher than any proposed for continental orogenies (P > 12 GPa, T = 2000 °C (Dobrzhinetskaya, 2012)). Globally, microdiamonds are significantly more abundant in metasedimentary rocks than mafic or ultramafic samples, which can also be explained if as proposed by Stöckhert et al. (2001) an organic carbon rich fluid is required for diamond crystallisation. As such, this is the currently favoured formation mechanism (Dobrzhinetskaya, 2012).

1.4 Exhumation mechanisms

The mechanism for exhumation of UHP terranes is an important aspect of metamorphic petrology/plate tectonics that remains poorly understood; largely the result of overprinting during exhumation commonly destroying any structures that formed under UHP conditions. The problem can be divided into two key issues 1) What facilitates the initiation of exhumation and detachment of the subducting slab, and 2) What mechanism(s) allows the return of UHP units to the surface? A number of different theories have been proposed (Hacker and Gerya, 2013, Warren, 2013), and as such a brief summary of the current understanding is presented below.

1.4.1 Exhumation triggers

Exhumation of UHP material requires decoupling and detachment of crust from the subducting slab, and a number of processes known to occur in subduction zones have been proposed to facilitate this. It remains unclear whether there is one overriding process that drives detachments from the subducting slab, or instead a combination factors trigger the eventual exhumation of UHP terranes.

Partial melting of the subducted crust is a highly effective way to weaken rocks (Warren, 2013). Migmatisation is widely documented in a number of UHP settings, and is therefore suggested as a driver of exhumation initiation in a number of numerical models (Gerya et al., 2008). A key uncertainty in all migmatised samples is when did melting occur? Did it occur during UHP metamorphism and therefore trigger exhumation, or is it instead the result of exhumation related decompression? Although an effective trigger for rock weakening, extraction of large degrees of partial melt will also remove the natural buoyancy of quartzofeldspathic units relative to the mantle (Hacker and Gerya, 2013).

Serpentinization of the mantle due to dehydration of the subducting slab is a commonly proposed mechanism for exhumation of HP rocks, and has been used to explain blocks of HP metabasites within a sheared serpentinite matrix in places like Zermatt Saas/Monviso (Schwartz et al., 2001). Serpentinites have also been proposed to act as lubricants within the subduction channel by forming a mechanically weak zone along the roof of the subduction zone (Guillot et al., 2001). This zone lowers the viscosity of the wall of the subduction channel, ultimately assisting both subduction and subsequent exhumation.

A reduction in grain size is frequently observed in metamorphic shear zones. There is an established inverse relationship between the amount of strain a rock experienced and its grain size. Metamorphic reactions, triggered either by fluids or deformation, and dynamic recrystallization are possible candidates to account for the observed grain size reduction in HP metamorphic rocks (De Bresser et al., 2001). Both mechanisms result in significant weakening, ultimately aiding exhumation (Warren, 2013).

1.4.2 Proposed geodynamic processes for exhumation of UHP terranes

It is accepted that the natural buoyancy of quartzofeldspathic units relative to the mantle is the key driver behind exhumation of most UHP terranes (Massonne et al., 2007). This alone can explain the dominance of quartzofeldspathic UHP terranes worldwide, although surface traction, pressure gradients and local tectonic plate motions are likely to contribute towards exhumation to some degree (Chemenda et al., 1996, Hacker and Gerya, 2013, Heuret and Lallemand, 2005). As such, numerical models of exhumation that can take into account temperature and pressure related effects on variables like composition, density and rheology complement traditional analogue experiments. To date, six different geodynamic processes have been proposed to return crustal material from great depths within the mantle. These are, eduction, microplate rotation, crustal stacking, slab rollback, channel flow and trans-mantle diapirs (See Figure 1-3)

1) Eduction is simply the reversal of plate motion. If continental crust follows ocean crust into a subduction zone the downwards slab pull forces will eventually exceed the strength of the slab, resulting in necking, and the eventual break off of the oceanic slab (van Hunen and Allen, 2011). The removal of the slab pull force, combined with the positive buoyancy of the continental crust results in exhumation. It was first proposed as an exhumation mechanism for the Western Gneiss Region of Norway (Andersen et al., 1991). Weak deformation, clear observable P-T gradient, no basal thrust fault, and an exhumation cycle up to 10 Ma are proposed diagnostic features (Duretz and Gerya, 2013).

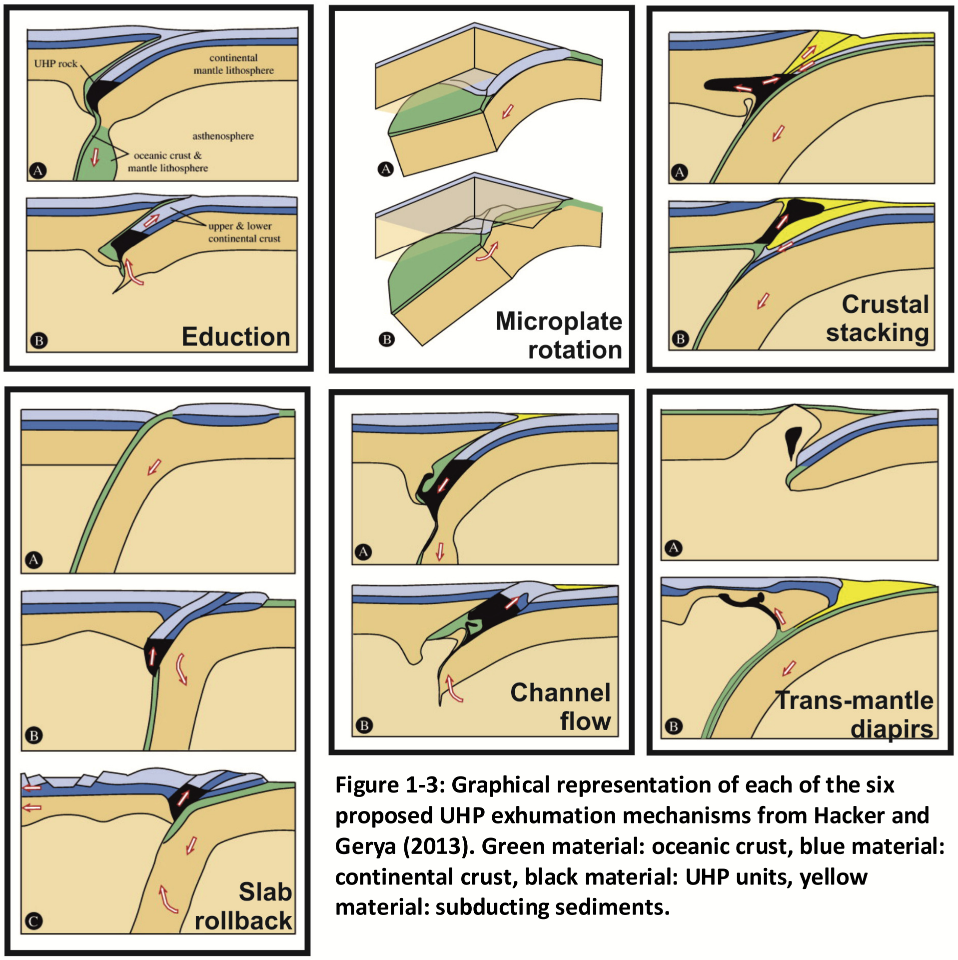

Figure 1-3: Graphical representation of each of the six proposed UHP exhumation mechanisms from Hacker and Gerya (2013). Green material: oceanic crust, blue material: continental crust, black material: UHP units, yellow material: subducting sediments.

2) Microplate rotation is the exhumation of UHP units as a result of rotation of the down going slab due to changing boundary conditions or body forces (Hacker and Gerya, 2013). A possible scenario is the subduction of continental crust into a small subduction zone, which could change both the direction and strength of slab pull forces. A coherent terrane, with a clear metamorphic gradient away from the point of rotation and associated stretching lineations are all expected. It has never been modelled computationally, but has been proposed to account for the formation of Dabie Shan, Eastern China (Hacker et al., 2000).

3) Crustal stacking involves a weak buoyant layer above a stronger negatively buoyant zone. When the subducting crust reaches a depth where buoyancy is greater than slab pull, the buoyant portion detaches, exhuming a semi coherent sheet. This was first proposed for the coesite bearing Doria Maira Massif by Chopin (1987)**,** and modelled in analogue experiments by Chemenda et al. (1995). It has since been reproduced via numerical models with a long heavy oceanic slab causing deep continental subduction (Sizova et al., 2012). Crustal stacking occurs on a large scale by brittle/plastic failure along the continental MOHO of the down going slab, resulting in the continental crust being thrust over the down going plate. It is thought to be favoured by slow subduction systems (Duretz and Gerya, 2013).

4) Slab roll back is closely associated with the subduction of microcontinents. When a microcontinent enters a subduction system, its buoyant nature slows the subduction rate. This allows gravity to exert a more dominant force, leading to steepening of the subduction angle (Warren et al., 2008). The trench will retreat away from the upper plate, causing extension and thinning of the accretionary wedge which creates space for the buoyant UHP rocks to exhume into. When the buoyant part of the subducting slab detaches, the remaining dense part will roll back to its original position, driving arc extension and aiding exhumation of the UHP crustal material. This model has been used to explain the multiple subduction exhumation cycles observed in the Aegean and the Calabria-Apennine orogens (Brun and Faccenna, 2008).

5) Channel flow involves the subduction of buoyant material in a confined channel bounded by the rigid subducting slab and overriding plate. A convection like cell forms, driven at the base by the traction of the downgoing slab, and the return by the relative buoyancy of the units, resulting in ductile return flow. Drivers of exhumation include introduction of new material into the channel (Li and Gerya, 2009), the pushing out of old material in a plunger like system (Warren et al., 2008) or buoyancy within the channel exceeding subduction related traction. This process is thought leads to the generation of nappes or a melange, with mixing of units of vastly different P-T-t histories (Warren et al., 2008, Beaumont et al., 2009, Li and Gerya, 2009). The French Massif Central is a possible examples of channel flow (Lardeaux et al., 2001),

6) Exhumation via trans mantle diapirs involves crustal material rising in plumes beneath the hinterland of the subduction zone, forming a melange like sheet. It was first proposed for some of the smaller Alpine UHP terranes (Stöckhert and Gerya, 2005), and has since been used as a possible explanation for the formation of a series of eclogite bearing gneiss dome in the D'Entrrecteaux Islands off the coast of Papa New Guinea (Little et al., 2011).

In addition to these mechanisms it is also worth noting the effect of processes such as erosion, which although does not occur at a sufficient rate to trigger exhumation, it would certainly decrease the downwards forces and assist in exhumation of the units (Warren, 2013). Ultimately, there remains a number of uncertainties surrounding the exhumation of units from mantle depths, and a combination of processes/mechanisms may be involved in the exhumation of UHP units.

1.5 Thesis Overview

In this thesis I will discuss the tectono-metamorphic evolution of UHP units from the northern part of the Rhodope Massif (RM) in Bulgaria. The RM is an established UHP terrane that spans the Greek-Bulgarian border. Currently all UHP discoveries are restricted to the Greek portion of the Massif, and as such this area has been the focus of the majority of geological studies of the RM in recent years. This thesis attempts to address this imbalance, and through detailed petrological, geochemical and geochronological investigations test whether current theories about the evolution of the RM hold true for the Bulgarian part of the Massif.

Key questions that I will address are:

- Are there UHP units in Bulgaria? If so, how extensive are they? When did they form, and do they share a common formation history across the RM?
- How did metabasic units associated with the UHP metapelites form? Are they all related to the same subduction-exhumation cycle?
- What was the exhumation mechanism for UHP units across the RM? Is it shared by all UHP localities in the RM?

The outline for this thesis is as follows:

- In **Chapter 2** I outline the current understanding of the geological evolution of the RM
- In **Chapter 3** I evaluate the petrogenesis of UHP metapelitic units from the Central Rhodope Mts, Bulgaria
- In **Chapter 4** I evaluate the petrogenesis of metabasic units from across the Central and Eastern Rhodope Mts.
- In **Chapter 5** I use high precision Sm/NdO$^+$ garnet geochronology to place constraints on the timing of the UHP event
- In **Chapter 6** I discuss my new results and their impact on the tectono-metamorphic evolution of the Rhodope Massif

Chapter 2 : Geological History

2.1 Introduction

The Rhodope Massif forms part of the Hellenides, the manifestation of the Alpine orogenic system in the Eastern Mediterranean. The Hellenides are an accretionary orogen composed of an amalgamation of terranes that were emplaced along the European margin as a result of the collision of the Apulian and European plates, and resultant closure of the Tethys and Vardar oceans (Papanikolaou, 1997, Stampfli and Borel, 2002). This region has experienced a particularly complicated geological history, owing to the opening and closure of multiple oceanic basins over the course of geological time. Since the advent of modern day plate tectonic theory, a number of different paleotectonic models have been proposed, largely involving contrasting geodynamic settings for the numerous ophiolite fragments found throughout the Hellenides, or invoking differing numbers of oceanic basins in the region (Robertson, 2004, Robertson et al., 1996).

Current consensus is that the Hellenides can be divided into a series of NW-SE trending imbricated nappes or terranes, separated by ophiolitic fragments and thrust faults (Jacobshagen et al., 1986, Papanikolaou, 1997, Papanikolaou, 2013). These terranes can be divided into two distinct groups – the External and Internal Hellenides, separated by relicts of the Pindos Ocean, an ophiolite bearing suture zone containing Mesozoic sediments (Liati et al., 2004, Robertson, 2004). The External Hellenides are predominantly made up of Mesozoic and Cenozoic supracrustal carbonates and flysch sediments, forming an orocline that connects the Dinarides to the NW with the Taurides to the SE (Mountrakis, 1986). The Internal Hellenides are characterized by Mesozoic/Paleozoic crystalline basements, and can be separated into three distinct massifs, the Pelagonian Massif, the Serbo-Macedonian Massif and the Rhodope Massif, the focus of this study (Figure 2-1).

2.2 Geology of the Internal Hellenides

2.2.1 The Pelagonian Massif

The Pelagonian Massif forms the westernmost and largest part of the Internal Hellenides. It merges to the south with the Attic-Cycladic massif (Dürr et al., 1978), and is separated from the metamorphic hinterland by the ophiolite bearing Vardar zone (Mercier et al., 1975). The basement is predominantly Permo-Carboniferous arc related granitic gneisses and late Paleozoic – Mesozoic metaclastic sediments and carbonates overlain by Tertiary cover (Anders et al., 2005). Originally believed to be a fragment of the Cimmerian continent that separated the Paleo and Neo-Tethys oceans (Mountrakis, 1986), subsequent work has shown that Pelagonia was part of the European Plate in the Variscan, and was rifted away as a result of back arc extension and the opening of the Mailac Ocean (Vavassis et al., 2000).

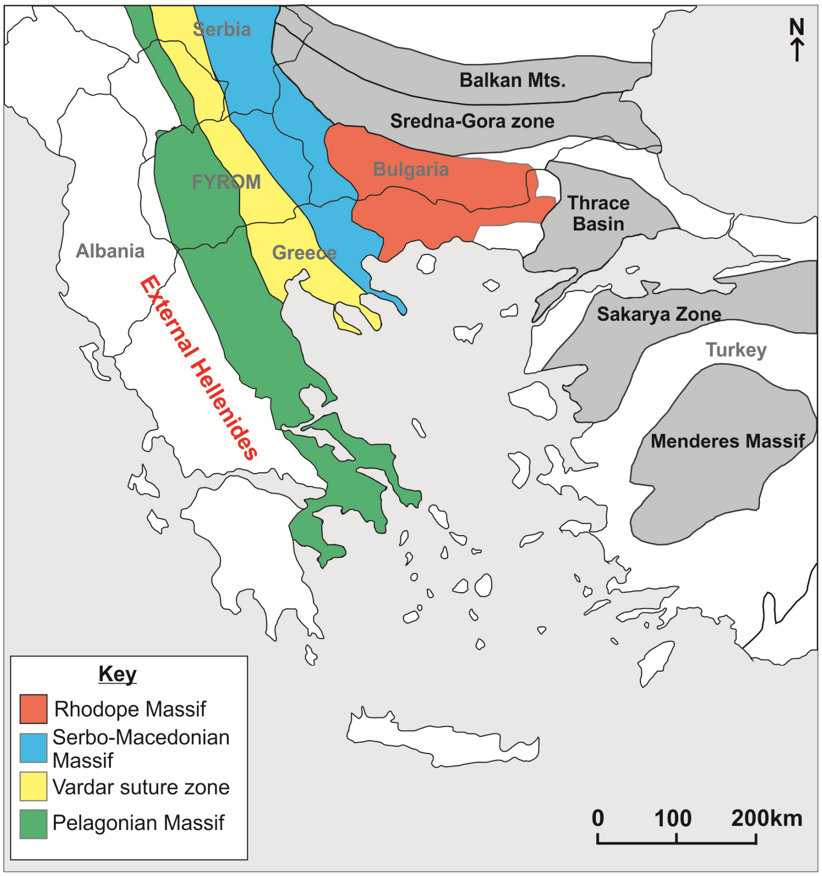

Figure 2-1: Simplified geological map of the Eastern Mediterranean, highlighting major tectonic zones/massifs in SE Europe, after Meinhold et al. (2008)

2.2.2 The Vardar Zone

The Vardar zone separates the Pelagonian Massif from the Serbo Macedonian massif. It hosts an Upper Jurassic suture (Zachariadis, 2007), with abundant ophiolitic fragments that can be divided into three distinct zones on the basis of their age, lithology and metamorphic grade. From West to East there are the Almopias, Paikon and Peonias subzones (Mercier, 1966).

The Almopias zone forms the westernmost part of the Vardar Zone, and is characterized by ophiolite fragments, metavolcanic and metasidemintary rocks. It is interpreted as an oceanic basin that was subducted eastwards under the Serbo-Macedonian Massif in the mid – late Jurassic (Zachariadis, 2007). The Paikon zone, the next zone east, has an unclear origin (Anders et al., 2005). It is predominantly neritic marbles, clastic sediments, mica schists and Late Jurassic volcanics, thought to represent either a tectonic window into the underlying basement of the Pelagonian massif (Ricou et al., 1998), or the subduction of the Almopias zone under the Serbo-Macedonian Massif (Brown and Robertson, 2004). The Peonias zone forms the easternmost part of the Vardar zone, and is predominantly unmetamoprhosed Mid-Triassic – late Jurassic sedimentary sequences and ophiolitic material. The zone is dominated by the Jurassic Guevgueli ophiolite that originated in a back arc basin to the east of the Paikon volcanic arc (Bebien, 1982, Brown and Robertson, 2003). Final suturing of the Vardar zone occurred in the Tertiary, resulting in the present day thrust structure seen in the Voras mountains, spanning the entire width of the Vardar zone (Brown and Robertson, 2004).

2.2.3 Serbo-Macedonian Massif (SMM)

The SMM is sandwiched between the Vardar suture and the Rhodope Massif (RM), situated between the Axios Basin to the West, and the Strimon Basin to the East (Dinter and Royden, 1993). The Athos-Volvi zone, also referred to as the Circum Rhodope Belt separates the SMM from the Vadra zone to the west. This zone is a series of low grade metasediments (predominantly greenschist facies) in an ophiolite bearing melange of either Jurassic (Meinhold, 2007) or Cretaceous olistostromic flysch (Ricou et al., 1998)

Originally the SMM was separated from the Rhodope Massif on the basis of contrasting metamorphic grades (Kockel and Walther, 1965). Subsequent works have suggested that the SSM and RM share a common formation history, the result of similar isotopic geochemical signatures, ages and structural features (Ricou et al., 1998). Current understanding indicates the SMM can be divided into two distinct units, the Kerdillon unit and the Vertiskos unit (Kockel et al., 1971). The Kerdillon unit is interpreted as the westwards extension of the RM, composed of banded biotite gneiss and migmatite domes (Himmerkus et al., 2006a, Himmerkus et al., 2009a, Ricou et al., 1998), with magmatic pulses of similar ages to the RM reported across the area (Himmerkus et al., 2006b).

The Vertiskos unit is the most widespread unit of the SMM, predominantly composed of Silurian continental magmatic arc orthogneiss, intruded by Triassic leucocractic granites (Himmerkus et al., 2009b). A further sub unit, the Pirgadika unit has also been delineated along the Chalkidiki Peninsula (Himmerkus et al., 2006a). Both the Vertiskos and the Pirgadikia units have been shown to be exotic crustal fragments that are unrelated to the surrounding parts of the Inner Hellenides (Himmerkus et al., 2006a, Himmerkus et al., 2009a).

2.2.4 Rhodope Massif

The Rhodope Massif (RM) forms the innermost part of the Hellenides, extending over large areas of SW Bulgaria and NE Greece. It is bounded to the North by the Sredna Gora zone – a Late Cretaceous volcanic arc chain of arc granite-monzodiorite intrusions (von Quadt et al., 2005), separated from the RM by the Maritza dextral strike slip fault (Naydenov et al., 2009). To the west it is bounded by the SMM/Vardar suture zone (Ricou et al., 1998) defined by the

Strimon low angle normal fault (Dinter and Royden, 1993). The southern extent of the massif is obscured by the Aegean Sea, and the eastern – north eastern boundary is covered by the large late Paleogene-Noegene Thrace- Maritza sedimentary basins. The eastwards lateral extension of the Rhodope Metamorphic complex towards Turkey is unclear (Bonev and Beccaletto, 2007) and obscured by greenschists units and ophiolites of the Circum Rhodope Belt (Kauffmann et al., 1976).

The geological history of the RM has proved to be complex. It was originally considered a Precambrian crustal unit sandwiched between two branches of the Alpine Himalayan Orogenic belt; the Balkan belt to the North and the Dinarides-Hellenides belt to the South (Hsu et al., 1977). Subsequent work has instead indicated a more complex evolution, with Precambrian, Varsican and Alpine metamorphic and igneous activity (Burchfiel, 1980, Ivanov et al., 1985, Carrigan et al., 2003, Haydoutov et al., 2004) followed by extensive Alpine deformation and complex extensional tectonics (Baziotis et al., 2008, Burg, 2011, Burg et al., 1996, Ricou et al., 1998, Jahn-Awe et al., 2010, Kirchenbaur et al., 2012, Nagel et al., 2011).

The overall structure of the RM is a 300 x 300 km open NW-SE trending antiform. Current understanding suggests the RM is a south directed nappe complex formed as a result of a north dipping Cretaceous subduction zone associated with the closure of the Vardar Ocean (Ricou et al., 1998). By the late Eocene-Miocene, the RM experienced post orogenic extension, which led to the emplacement of a series of large scale metamorphic domes (core complexes) that dominate the regional geology (Bonev et al., 2010b, Burg et al., 1990, Burg et al., 1996, Nagel et al., 2011).

2.3 Paleogeographic evolution of the RM

The RM has a complex tectonic history spanning the Neoproterozoic to present day, involving a number of distinct orogenic events. In this section the evolution of the RM is overviewd in the broader context of paleogeographic reconstructions of the Eastern Mediterranean.

2.3.1 Pre-Variscan History

The oldest units within the RM are Neoproteroic and Early Paleozoic metamafic units found within the Central and Eastern Rhodope Mts. As discussed in Chapter 4, this suite can be distinguished on the basis of bulk rock geochemistry, with protoliths ranging from MORB to SSZ units. Granitic bodies of similar age have been reported from the SMM (Graf et al., 1998, Himmerkus et al., 2006a, Kounov et al., 2012) and the Stranzha zone and Istanbul Terranes of Turkey (Okay et al., 2008, Yilmaz Şahin et al.). Formation of these samples is the result of subduction of the Prototethys ocean under the northern Gondwanan margin (Figure 2-2a). Metamafic samples from the RM formed in a back arc setting above the Cambrian-Early Ordivican subduction system related to the opening of the Eastern Rheic Ocean and northwards drift of peri gondwanan fragments (Figure 2-2b). These samples were emplaced into Neoproterozoic- Early Palaeozoic basement units, accounting for the large spread in both lithologies and sample age seen within these units (Bonev et al., 2013).

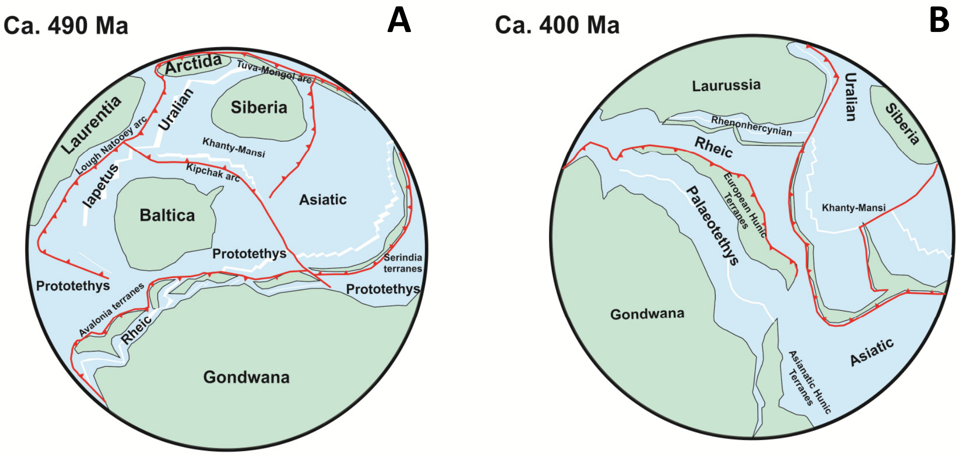

Figure 2-2: Early Paleozoic paleogeographical plate reconstructions, redrawn from Stampfli and Borel (2002). A: Cambrian opening of the Rheic Ocean alongside rifting from Northern Gondwanan margin B: Devonian closure of the Rheic Ocean

2.3.2 The Variscan Orogeny – Formation of the Lower allochthon

During the Variscan, the Paleotethys was subducted Northwards under the Southern boundary of Laurussia (Figure 2-3a), resulting in the accretion of Peri-Gondwanan terranes prior to the late Paleozoic suturing of Laurussia with Gondwana associated with the formation of Pangea (Stampfli and Kozur, 2006). U-Pb zircon dating of metamafic samples from the RM suggests subduction to eclogite facies during this orogenic event (Arkadakskiy et al., 2003, Carrigan et al., 2003), in keeping with HP relics of the Variscan Orogeny recognised across Western Europe (Friedl et al., 2011, Roger and Matte, 2005). Continental arc magmatism associated with this northwards subduction event formed the granitic protolith of the Lower high grade basement unit found across the RM (Cherneva and Georgieva, 2005).

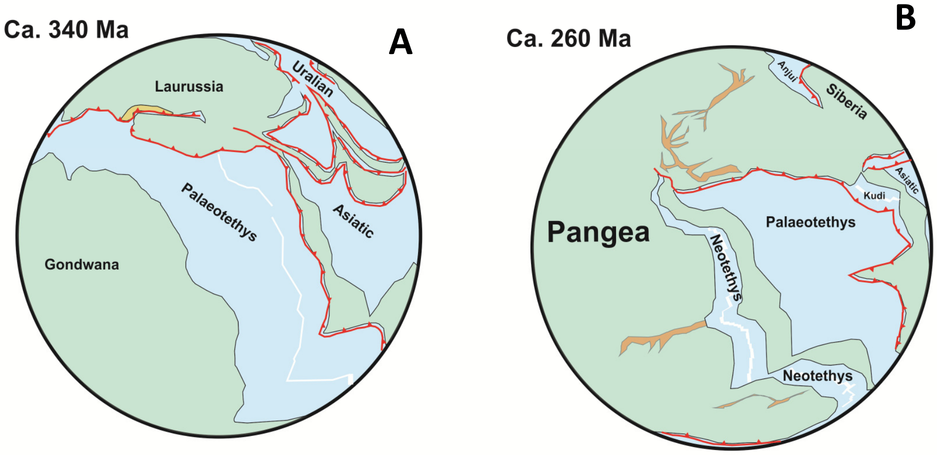

Figure 2-3: **Mid-Late Paleozoic paleogeographical plate reconstructions, redrawn from Stampfli and Borel (2002). A: Carboniferous, with Northwards subduction of the Palaeotethys ocean, B: Late Permian, with opening of the Neotethys ocean. Yellow areas: Suture zones, Orange areas: Rifting zones.**

2.3.3 Mesozoic History

The Neotethys ocean opened during the Permian-Triassic following rifting along the Northern Gondwanan margin, the result of the breakup of Pangea (Figure 2-3b). Simultaneous northwards subduction of the Paleotethys ocean under the Eurasian margin occurred, with associated back arc rifting resulting in the opening of the Meliata and Maliac Oceanic basins (Stamplfi and Kozur, 2006, Figure 2-4a). The southwards subduction of the Meliata-Meliac oceanic crust during the Late Triassic/Jurassic led to the establishment of the Eastern Rhodope-Evros arc system, with associated back arc extension leading to opening of the Vardar Ocean (Bonev et al., 2010c, Bonev and Stampfli, 2011). A change in subduction polarity occurred, and the Vardar Ocean was subducted beneath the Moesian platform during the Late Cretaceous (Bonev and Stampfli, 2011, Stampfli and Borel, 2002, Stampfli and Hochard, 2009). To the east, northwards subduction of the Neotethys under the Eurasian margin is continuous throughout this time (Stampfli and Borel, 2002, Figure 2-4b). The position of the RM during this period is poorly constrained, and will be discussed at length in section 6.1.

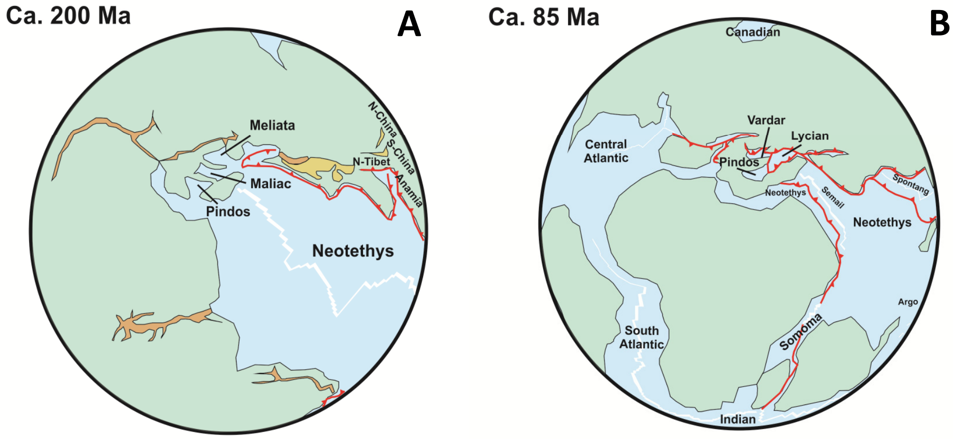

Figure 2-4: **Mesozoic paleogeographical plate reconstructions, redrawn from Stampfli and Borel (2002). A: with opening and Southern Subduction of the Meliata and Malicac Ocean basins, B: Late Cretaceous northwards subduction of the Vardar ocean under the Eurasian margin. . Yellow areas: Suture zones, Orange areas: Rifting zones.**

2.3.1 Cenozoic History

During the Cenozoic, the Northern African margin remained passive, whilst the Hellenic orogenic front migrated southwards, resulting in the accretion of distinct terranes to the Eurasian margin (Papanikolaou, 2013).

2.4 Stratigraphy of the Rhodope Massif

Over the years a large number of different names for individual litho-tectonic sub-units across the Rhodope Massif have been used, often precluding direction comparisons between areas. To combat this, two simplifications of the geology of the RM have been proposed, grouping together units that share a common formation history. The first scheme, as proposed by Bonev (2006) divides the metamorphic basement into an upper high grade basement and lower high grade basement, whereas the second divides this basement into four distinct units, the lowermost, middle,upper and uppermost allochthon (Jahn-Awe et al., 2010).

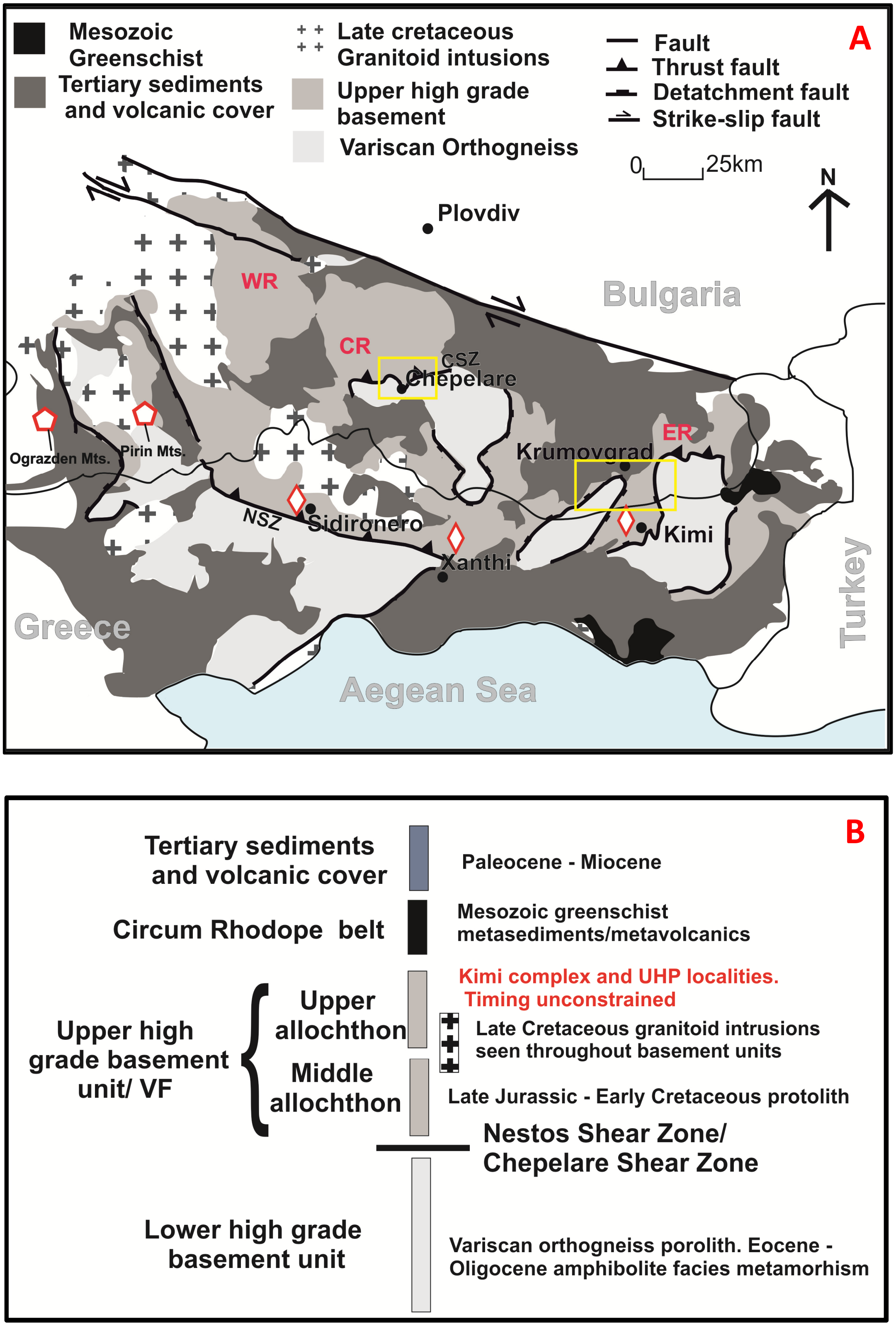

Figure 2-5A: Summary map of the geology of the Rhodope Massif (after Bonev 2006 IJES and Bonev and stampfli 2007). ER: Eastern Rhodope Mts. CR: Central Rhodope Mts. WR: Western Rhodope Mts, NSZ: Nestos Shear Zone, CSZ: Chepelare Shear Zone.◇: Microdiamond locality, ⬠: proposed coesite locality, yellow boxes: field areas studied in this thesis. B: Simplified sratigraphic column to show the startigraphic relationship of the different lithological units across the RM.

2.4.1 Lower High Grade Basement Unit

The Lower high grade basement unit and lower allochthon are the same in both classification schemes, being predominantly orthogneiss with associated clastic metasediments, metamafic and ultramafic rocks (Jahn-Awe et al., 2010). The largest exposure is seen in the Pangeon-Pirin complex, outcropping south of the Netsos Shear zone in Northern Greece/Southern Bulgaria, but this basement unit also forms the core of the three extensional gneiss domes (Arda, Byala-Reka, and Kesebir-Kardamos) that dictate the present day structure of the RM. The origin for this basement unit remains controversial. Studies of the gneiss domes have suggested a Variscan granitic protolith (Cherneva and Georgieva, 2005, Peytcheva and Von Quadt, 1995, Peytcheva et al., 2004) that has experienced amphibolite facies metamorphism during the Eocene- Oligocene, although the paleogeographic origin is unclear (Figure 2-5). With the RM forming the metamorphic hinterland of the Internal Hellenides, it has been suggested that this lower unit is a micro-continent that marks the first accretionary stage of the Hellenic Orogeny. Various suggestions for this continent have been put forward, Drama (Ricou et al., 1998), Thracia (Turpaud and Reischmann, 2010) or a fragment of the European margin (Krenn et al., 2010). The alternative view is that this unit is derived from the Apulian margin, and is exposed beneath an orgogen-scale out-of-sequence thrust fault – the Nestos Shear Zone, which cuts through the entire Jurassic-Cretaceous Nappe pile of the Hellenides (Dinter, 1998, Krohe and Mposkos, 2002, Nagel et al., 2011).

In this scenario, the three metamorphic core complexes to the North of the NSZ are envisaged as linked to the Pangeon-Pirin complex, and the Chepelare Shear Zone on Figure 2-5 is viewed as a continuation of the Nestos Shear Zone (Nagel et al., 2011). This link is the result of a commonly observed top to the southwest shear sense in mylonites from both the Arda dome and the NSZ, in-keeping with the idea of exhumation of units SW along a NE dipping subduction zone. An increased metamorphic grade has also been observed in the 3 core complexes relative to the Pangeon Pirin complex, in-keeping with a common south trending exhumation, as the Northern units must have been exhumed from greater depths in the Arda dome.

2.4.2 Upper High Grade Basement Unit

The next stratigraphic level in the RM is an extensive heterogeneous unit of meta-igneous and metasedimentary rocks of currently unresolved age and origin. This suite is the focus of this study. Ricou et al. (1998) and Bonev (2006) both grouped all lithological units at this level together into the Rhodope Terrane and Upper high grade basement unit respectively, whereas Jahn-Awe et al. (2010) subdivided it further into a middle and upper allochthon on the basis of contrasting protolith ages and tectonometamorphic histories. For the purpose of this study it will be referred to as the Variegated Formation (VF), a term used locally in the Bulgarian Central Rhodope Mts.

The middle allochthon is composed of intermingled amphibolites, marbles, eclogites, metapelites, ultramafics, ortho- and para-gneiss that have experienced upper amphibolite/eclogite facies metamorphism. Late Jurassic – Early Cretaceous protolith ages have been reported for orthogneiss in the middle allochthon from both above the NSZ (Turpaud and Reischmann, 2010) and the eastern extent of the Arda dome (Ovtcharova et al., 2004). The Upper allochthon is petrologically similar, but is proposed to represent a higher stratigraphic level in the RM, containing all recorded examples of UHP metamorphism in the Rhodope Massif (Jahn-Awe et al., 2010). The timing of metamorphism in this allochthon is poorly constrained and will be discussed in detail in Chapter 5. The exact criteria of whether a sample belongs to the middle or upper allochthon is not clear in the literature, but the melange zone found along the Nestos and Chepelare Shear Zones, and the Kimi complex of the Eastern Rhodope Mts. have all been attributed to the upper allochthon (Jahn-Awe et al., 2010, Nagel et al., 2011, Jahn-Awe et al., 2012).

2.4.3 Overlying units

Overlying the high grade metamorphic basement of the RM are a series of Mesozoic greenschist-blueschist metasediments and metavolcanics, thought to be a continuation of the Circum Rhodope belt from the Athos-Volvi zone, Greece (Boyanov and Russeva, 1989, Papanikolaou, 1997). This unit is made of greenschists and phylites overlain by arc tholeitic-boninitic mafic lavas, which are in turn overlain by meta-pyroclastic rocks and turbiditic clastic and carbonaceous deposits (Bonev et al., 2010b). The entire sequence has been interpreted as an island arc accretionary assemblage (Bonev and Stampfli, 2008). Fragments have been identified in unmetamorphosed Jurassic sediments in the region (Kockel et al., 1971), suggesting formation pre-dates the main regional HP/UHP orogenic event(s).

The entire sequence is overlain by a series of syn and post tectonic cover sequences. These supracrustal units consist of clastic, carbonanaceous and volcanic material, with ages ranging from Paleocene – Miocene (Boyanov and Goranov, 2001). Widespread post metamorphic magmatic activity has been related to post orogenic extensional collapse (Harkovska et al., 1989, Jones et al., 1992), likely a result of slab rollback due to a change in composition of the subducting crust (Jolivet and Brun, 2010)

2.5 UHP metamorphism in the Rhodope Massif

In the last few decades the RM has been the focus of extensive research due to the discovery of microdiamond inclusions in garnets from kyanite-garnet gneiss of the Kimi Complex, part of the upper high grade basement in the Greek part of the RM (Mposkos and Kostopoulos, 2001). Two additional diamond localities have since been identified along the Nestos Shear Zone in the South of the Massif (Figure 2-5) and in the Sidironero Complex (Perraki et al., 2006, Schmidt et al., 2010). These discoveries have established the region as one of the few UHP provinces in Europe. Microdiamond inclusions are restricted to almandine-rich garnets from kyanite-garnet gneiss/schist units that are part of the VF/upper allochthon (melange) that is common throughout the upper high grade basement unit of the RM (Haydoutov et al., 2004). Kyanite-garnet schist is the only lithology to preserve evidence of UHP conditions.

Pressure and temperature estimates for the Greek UHP localities range between 3.1 and 3.9 GPa and 600 – 900 °C (for the Greek Central Rhodope Mts.) and > 4 GPa and at least 1100 °C (for the Greek Eastern Rhodope Mts.) (Liati et al. 2011). Thermobarometric studies of eclogites from the westernmost segments of the RM in Bulgaria (i.e. Pirin Mts.; Janak et al, 2011) and possible coesite discoveries from the neighbouring Ograzden Mts. of the SMM (Savov et al. 2007) (see Figure 2-5) suggest that other parts of the RM may have experienced UHP conditions.

2.6 Timing of key tectono-metamorphic events in the Rhodope Massif

2.6.1 Protolith formation

The geochronological record in the RM spans from the Proterozoic to the present day (figure 3). The oldest recorded ages are U-Pb zircon ages from a metagabbro unit near Bubino in the Eastern Rhodope Mts., which record a core age of 572 ± 5 Ma (Carrigan et al., 2003). Similar ages have been reported from eclogite boudins in the Central and Western Rhodope Mts. (Arkadakskiy et al., 2003, Savov et al., 2007). All of these samples record a Variscan metamorphic overprint event ca. 350 – 260 Ma, similar to ages reported from the SMM leading to the suggestion of a common history (Himmerkus et al., 2006a). Late Permian – Early Triassic protolith ages are also reported from U-Pb SHRIMP dating of eclogites from both the Western and Eastern Rhodope Mts**.** (Liati, 2005, Liati and Fanning, 2005). These ~ 250 Ma ages are interpreted as the result of underplating associated with Permo-Triassic rifting in the Paleo-Tethys (Liati et al., 2011).

U-Pb zircon dating of orthogneiss reveals two widespread magmatic events across the RM. The oldest protolith ages are ~ 320 – 250 Ma, recorded in migmatic orthogneiss that forms the lower high grade basement unit across the RM (Peytcheva and Von Quadt, 1995, Ovtcharova et al., 2002, Peytcheva et al., 2004, Liati and Fanning, 2005, Liati and Gebauer, 1999). This event is also recorded in the core of monazite crystals from the island of Thasos, Greece (Wawrzenitz and Mposkos, 1997). A second Jurassic (ca. 150 Ma) magmatic event is recorded in orthogneiss from within the VF (Gebauer and Liati, 1997, Liati, 2005, Liati et al., 2011, Ovtcharova et al., 2004, Turpaud and Reischmann, 2010), suggested to be the magmatic product of an UHP subduction zone (Turpaud and Reischmann, 2010). Recent work to constrain the timing of the peak metamorphic event has questioned this interpretation (Liati et al., 2011), and this topic will be the subject of further discussion in chapters 5 and 6.

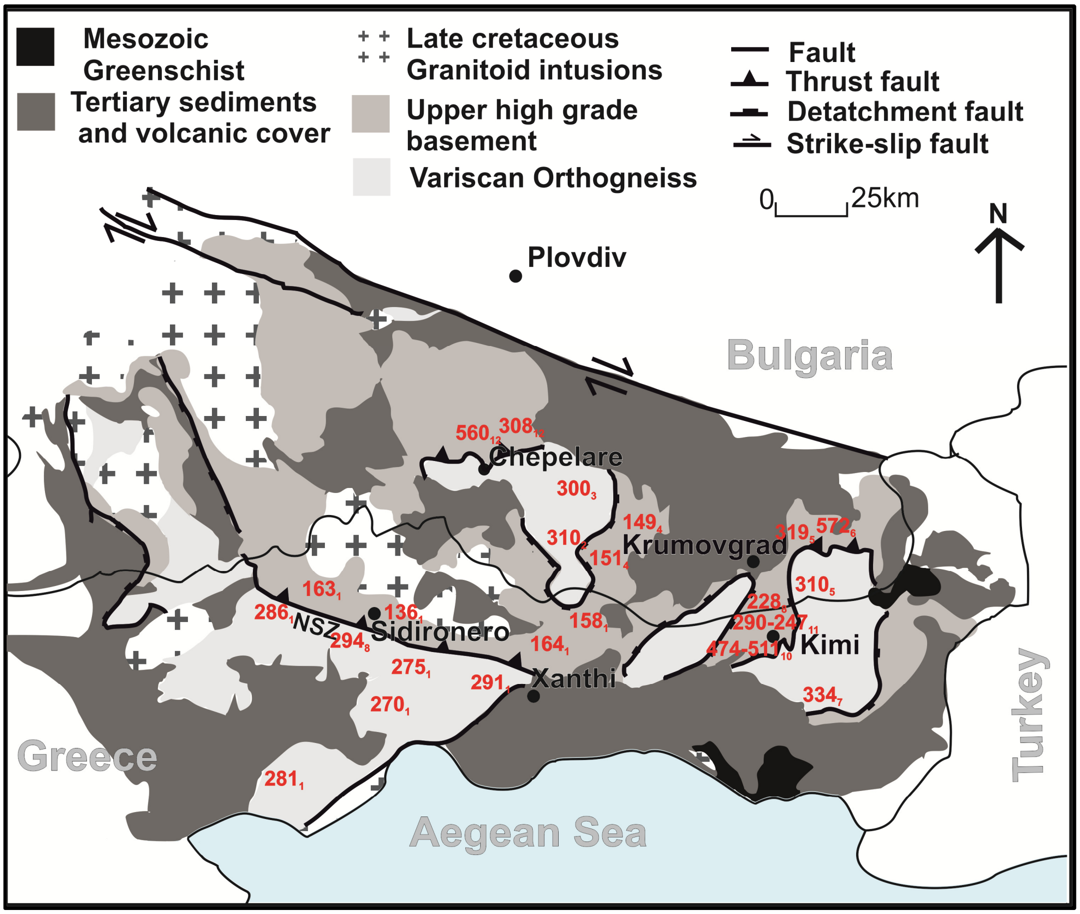

Figure 2-6: Published protolith ages from across the Rhodope Massif. 1: Turpaud and Reischmann, 2010, U-Pb zircon SHRIMP, 2: Ovtcharova et al. 2002, U-Pb zircon TIMS, 3: Peytcheva et al. 2004, U-Pb zircon TIMS, 4: Ovtcharova et al. 2004, U-Pb zircon TIMS, 5: Peytcheva and Quadt, 1995, U-Pb zircon TIMS, 6: Carrigan et al., 2003, U-Pb zircon, 7: Mposkos and Wawrzenitz, 1995, Rb-Sr, 8: Bauer et al. 2007, U-Pb zircon SHRIMP, 9: Liati and Gebauer, 1999, U-Pb zircon, 10: Bonev et al. 2010a, U-Pb zircon LA-ICP-MS, 11: Liati et al, 2011, U-Pb zircon LA-ICP-MS, 12: Arkadakskiy et al. 2003, U-Pb zircon TIMS

2.6.2 Timing of HP/UHP metamorphism

Four distinct age groups for HP metamorphism have been reported in the literature for the RM. These are 1) Late Jurassic ca. 150 Ma, 2) Late Cretaceous ca. 73 Ma, 3) Early Eocene ca. 51 Ma, and 4) Late Eocene ca. 42 Ma, as shown in Figure 2-7. These ages have been interpreted as reflecting either a Late Jurassic UHP metamorphic event and resetting by post peak metamorphism and fluid rock interaction (Turpaud and Reischmann, 2010), or multiple HP/UHP events spanning the Jurassic to the Eocene. All 4 age groups have been recognised in HP zircon domains from across the massif, with pressure conditions established through index mineral inclusions, the lack of a Eu anomaly and unfractionated CI-normalised HREE profiles (Liati et al., 2011). This suggests that all 4 age clusters are geologically significant, and any one of them could be attributed to the UHP metamorphic event. This topic will be discussed further in section 2.8 with respect to geodynamic implications, and in chapter 5 and 6 incorporating new Sm-Nd garnet geochronological data.

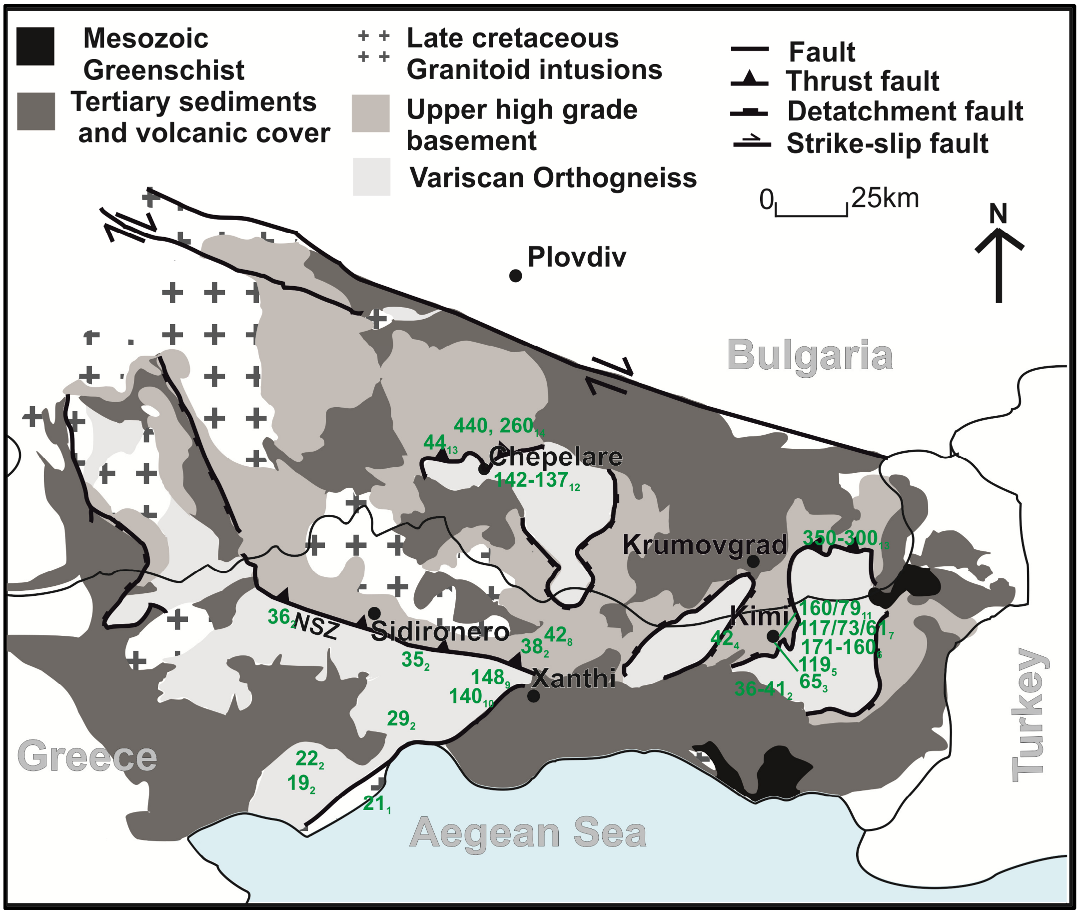

Figure 2-7: Summary of proposed metamorphic ages from across the Rhodope Massif: 1: Dinter et al. 1995, U-Pb zircon and ^{40}Ar/^{39}Ar Mica, 2: Lips et al. 2000, ^{40}Ar/^{39}Ar Mica, 3: Mposkos and Wawrzenitz, 1995, Rb-Sr Mica, 4: Mposkos and Krohe, 2000, K-Ar, 5: Wawrzenitz and Mposkos 1998, Sm-Nd WR-Grt-CPX, Rb-Sr mica, 6: Wawrzenitz and Krohe, 1998, Rb-Sr mica, 7: Liati et al. 2002, U-Pb zircon SHRIMP, 8: Liati and Gebauer 1999, U-Pb zircon SHRIMP, 9: Liati, 2005, U-Pb Shrimp, 10: Reischmann and Kostoplous, 2002, Sm-Nd Grt-Wr, 11: Bauer et al. 2007, U-Pb zircon SHRIMP , 12: Bosse et al. 2010, U-Th-Pb Monazite LA-ICP-MS, 13: Kirchenbauer et al., 2012 Lu-Hf Grt, 14: Arkadisky et al., 2003, U-Pb Zircon

2.7 Area of Study

For this project two areas within the RM were selected for study (Figure 2-5). The first is a recently re-mapped (at 1:50000 scale) area of the Central Rhodope Mts. in the vicinity of the town of Chepelare with exposure of the Upper high grade basement along the Chepelare Shear Zone (Sarov, 2004). The second area is in the vicinity of Krumovgrad in the Eastern Rhodope Mts. This area has been recently mapped by the Gold exploration company Dundee Precious Metals, who supported and advised our fieldwork in this area. This study area is close to the well-studied Kimi complex of the Greek Rhodope Massif, and was chosen to allow both further understanding of the geology of the Eastern Rhodope Mts., and to allow direct comparisons between the East and Central Rhodope Mts. to be made. A full list of sample localities with GPS coordinates can be found in appendix A.

2.7.1 Geology of the Central Rhodope Mts., Bulgaria

Chepelare is ~ 100km south of the city of Plovdiv, Bulgaria's 2nd largest city. It is located on the edge of the Arda dome in the Central Rhodope Mts, one of the three metamorphic core complexes seen across the RM. Orthogneiss in this region has been divided into two distinct units, Arda 1 and Arda 2, separated by a high strain shear zone – the Chepelare Shear Zone (CSZ). The Arda 1 sub unit is part of the lowermost tectonic unit seen across the RM. Forming the core of the dome, it is composed of Early Permian orthogneiss with a late collisional calc alkaline granitic protolith (Cherneva and Georgieva, 2005).

The Chepelare Shear Zone (CSZ)) occurs in a ~ 2 km wide zone along the north and eastern flanks of the dome, marking the boundary between the Arda 1 and Arda 2 subunita (Sarov, 2004). It is composed of upper high grade basement units, locally referred to as the Variegated Formation (VF). Marble is the most abundant lithology, found alongside kyanite-garnet schist and amphibolite (Figure 2-8). The latter two lithologies will be discussed in detail in chapters 3 and 4 respectively. A syn-metamoprhic thrust fault has been mapped as marking the upper boundary of the CSZ, although field evidence for this is unclear (Burg, 2011, Ricou et al., 1998). The lower boundary with the Arda 1 gneiss is not observed anywhere in the field area. Foliation in the host gneiss is consistently in the same orientation as the units of the Variegated Formation suggesting that emplacement of this package occurred prior to the late stage Eocene metamorphic overprint and formation of the core complex. On the basis of proposed UHP conditions for garnet-kyanite schist samples (Kostopoulos et al., 2003), and a common stratigraphy the CSZ has been viewed as a continuation of the Nestos Shear Zones in recent studies (Jahn-Awe et al., 2010, Jahn-Awe et al., 2012, Nagel et al., 2011, Turpaud and Reischmann, 2010).

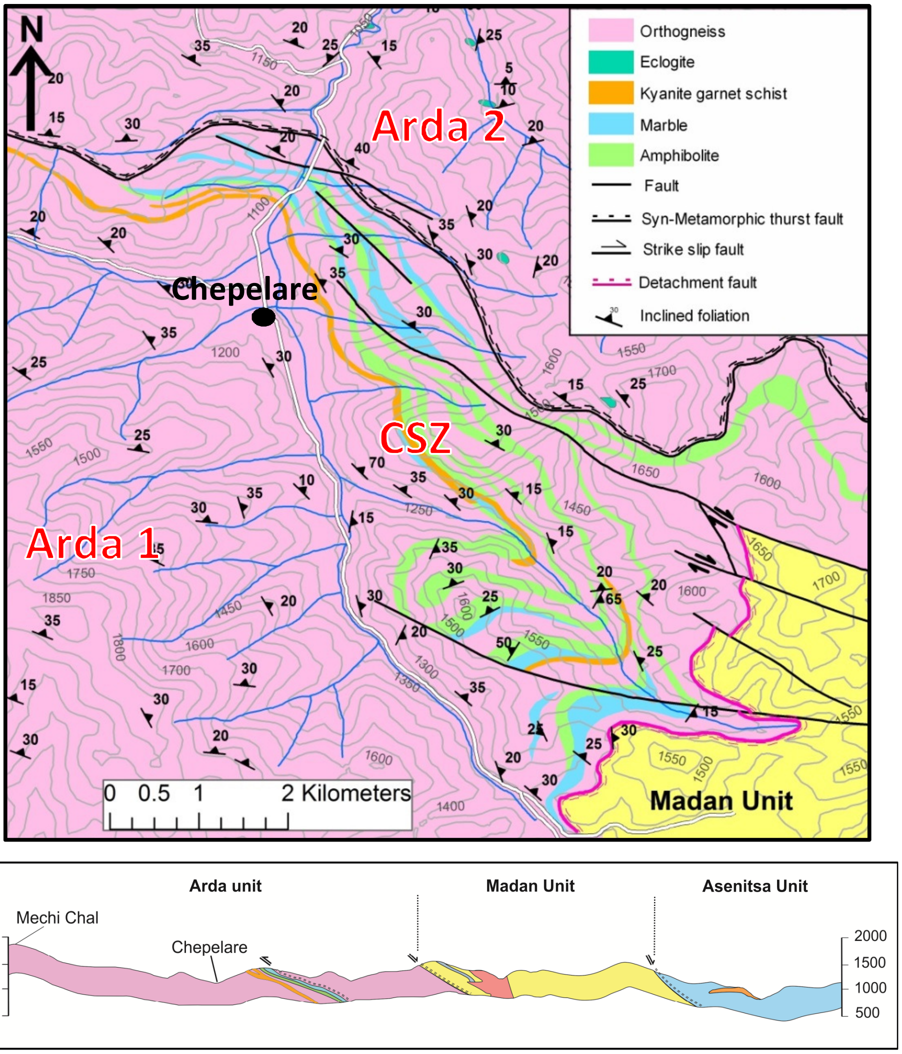

Figure 2-8: Simplified map of the geology in the vicinity of the town of Chepelare in the Central Rhodope Mts. Bulgaria, and schematic cross section running N-S through the Arda dome (redrawn from Sarov et al. 2004)

U-Pb zircon dating of the Arda 2 subunit has revealed a Late Carboniferous protolith,age with bulk rock geochemical studies suggesting an evolved volcanic arc origin (Cherneva and Georgieva, 2005). Eclogite boudins are found throughout the formation, with an increased concentration at the base. The reason for this is unclear, although work on the Starcevo Unit, analogous to the Arda 2 unit along the Eastern extent of the Arda dome, has revealed heterogeneity within this formation with contrasting P-T-t condition for distinct horizons (Jahn-Awe et al., 2012). The Arda 2 unit has been attributed to the middle allochthon of the upper high grade basement unit, analogous to the Rhodope Terrane in the hanging wall of the Nestos Shear Zone (Jahn-Awe et al., 2010, Nagel et al., 2011, Turpaud and Reischmann, 2010). The exact reasoning behind this link is unclear, and will be discussed further in Chapter 6.

Exposure of VF units is limited across the CSZ. Many of the best samples come from abandoned mines and exploration trenches, which prevents a clear understanding of the outcropping style of a number of units. Despite this, a few sites preserve key relationships, and a similar repetition of units combined with consistent structural measurements between outcrops has resulted in the proposed sheet like structures that surround Chepelare (Figure 2-8), an observation that is not necessarily intuitive at outcrop scale.

2.7.2 Geology of the Eastern Rhodope Mts.

Krumovgrad is a town in the Eastern Rhodope Mts, approximately 110 km SE of Plovdiv, and 10km north of the Greek border. A large area (35 km x 20 km) was studied south of this town, spanning from the village of Ivaylovgrad near the Turkish border to the east, to the village of Egrek, 1 km north of the Greek border. The regional geology is dominated by the Byala-Reka and Kesebir-Kechors late-Alpine extensional domes that expose the Variscan lower high grade basement unit across the region (Mposkos and Wawrzenitz, 1995, Peytcheva and Von Quadt, 1995). The lower high grade basement unit is restricted to the core of the dome structures, forming the footwall of a detachment fault system that is easily identified at outcrop scale. The hanging wall is composed of upper high grade basement units: meta-igneous and metasedimentary rocks, eclogite boudins and metaophiolite lenses, essentially analogous to the VF of the Central Rhodope Mts., although with the addition of large amounts of ultramafic material (Bonev et al., 2013, Bonev et al., 2006, Daieva et al., 2007, Haydoutov et al., 2004).

The first microdiamond discovery in the RM was found within a metapelite from the Kimi complex, ~ 5 km south of the study area (Mposkos and Kostopoulos, 2001). The Kimi Complex is proposed to occupy the highest structural level of the RM basement units (Upper allochthon), the result of Cenozoic extensional tectonics (Krohe and Mposkos, 2002). The extent of this UHP unit in the Bulgarian Rhodopes, and relationship with the middle allochthon in Bulgaria is currently unconstrained, and will be discussed with reference to studies of meta-mafic units in Chapter 4.

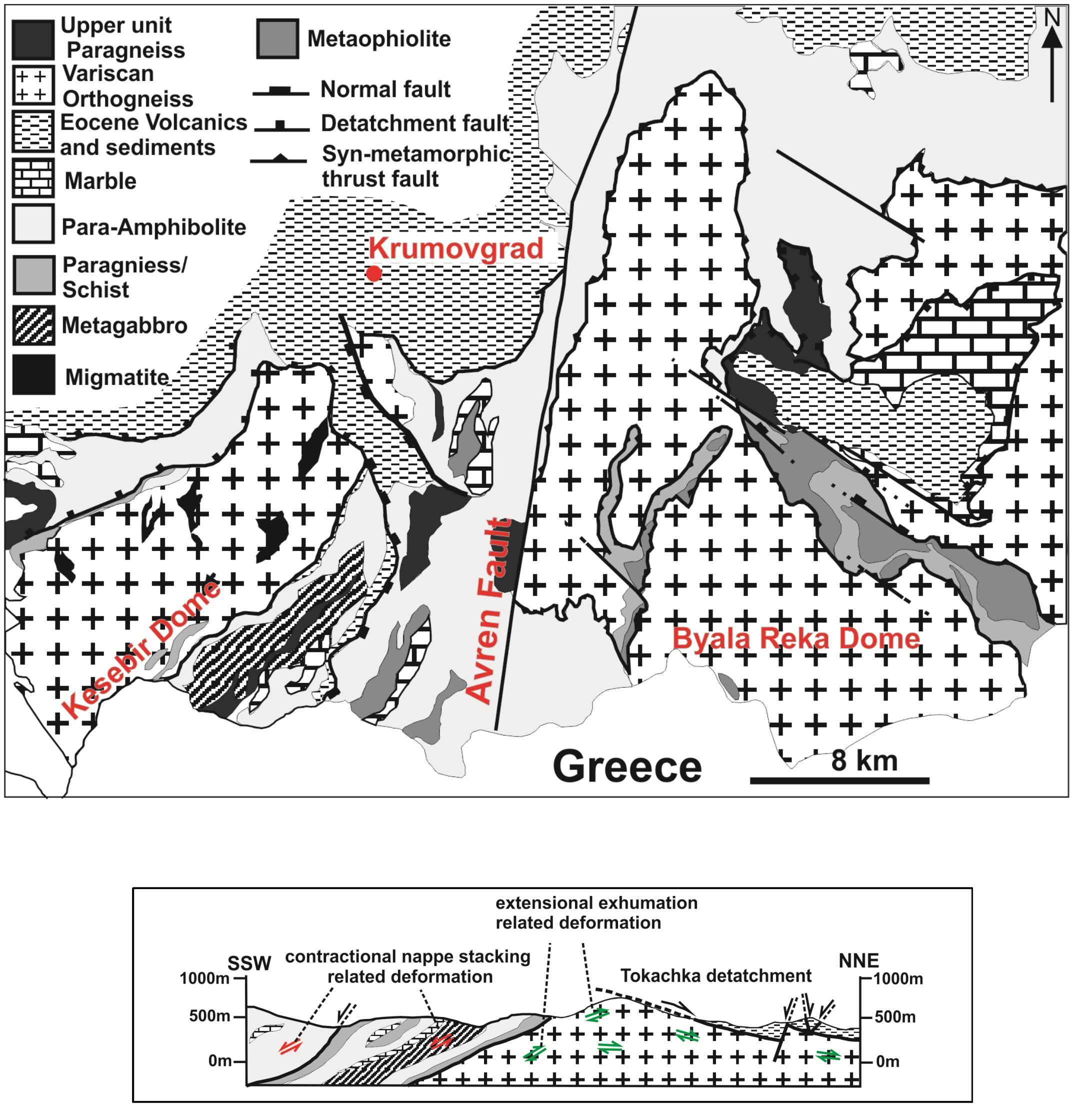

Figure 2-9: Simplified geological map of the Eastern Rhodope Mts. in the vicinity of the town of Krumrovgard, and schematic cross section through the Kesebir dome based on map of Bonev (2006)

2.8 Proposed geodynamic models for the evolution of the Rhodope Massif

The restriction of upper allochthon (UHP?) units in the Central Rhodope Mts. to a melange zone along the Chepelare and Nestos Shear Zones has been used to place constraints on the geodynamic evolution of the Rhodope Massif. The Nestos Shear Zone was originally believed to mark a suture between Variscan granite of the Lower allochthon and the Jurassic units of the middle allochthon/ Rhodope Terrane. In this scenario the UHP units form in the Jurassic subduction zone associated with arc magmatic protolith, and samples experienced a prolonged single subduction-exhumation cycle, with accretion ages ranging from the Jurassic through to the Eocene (Krenn et al., 2010, Ricou et al., 1998, Turpaud and Reischmann, 2010).

Alternatively, the NSZ represents a stretching fault at the base of a collapsing orogenic wedge. This model, suggested by Nagel et al. (2011) is based on the lower allochthon occupying an external position in the Hellenide Nappe Stack, exposed beneath an orogenic scale out of sequence thrust (the NSZ), which extends underneath the Cretaceous nappe pile west of the RM, reaching the surface between the Pindos Zone and the external hellenides**.** The NSZ acts as a major shear zone, emplacing the orogenic wedge (including the middle allochthon) on top of the lower allochthon during the Eocene. Widespread horizontal extension in the hanging wall, the result of slab roll back resulted in exhumation of the middle allochthon. The upper allochthon is not involved in this Eocene subduction-exhumation event, but fragments are entrapped between the upper and lower allochthon during the course of Cenozoic thrusting, explaining the occurrence of UHP metapelites both within the Nestos Shear Zone (sandwiched between the middle and lower allochthon), and directly above the lower allochthon in the Kimi complex of the Eastern Rhodope Mts.

Both of these models are built upon observations made along the Nestos Shear Zone, and do not take into account observations from the Central Rhodope Mts. As such, they will both be discussed in relation to the findings of this study from the Bulgarian Central Rhodope Mts. in chapter 6.

Chapter 3 Petrogenesis of Kyanite-Garnet schist units from the Rhodope Massif

3.1 Introduction

Metapelites are present throughout the upper high grade basement unit of the RM. They are the only unit to preserve evidence of UHP conditions, with 3 microdiamond localities known across the region (Mposkos and Kostopoulos, 2001, Perraki et al., 2006, Schmidt et al., 2010). Microdiamonds are found only as inclusions within garnets from metapelites (locally referred to as either kyanite-garnet gneiss or schist) within the upper high grade basement unit seen across the RM, as described in chapter 2.

This chapter focuses on kyanite-garnet schist from the vicinity of Chepelare in the central Rhodope Mts. General UHP conditions have been proposed for this area by Kostopoulos et al. (2003) on the basis of exsolved quartz and rutile inclusions in garnet, however these features have since been shown to reflect high temperatures of garnet formation and are not definitive of UHP conditions (Chopin and Ferraris, 2003). A subsequent study by Georgieva et al. (2007) instead suggested that metapelites in the vicinity of Chepelare experienced HP conditions on the basis of GASP and GRAIL barometry, and underwent melting during HP granulite facies metamorphism. To date there has been no evidence of key UHP indicator minerals (microdiamond or coesite) or thermobarometric investigations that indicate UHP conditions. In this chapter I will present the first detailed petrological and geochemical study of metapelites from the Central Rhodope Mts., discuss their P-T history and contrast with the existing UHP localities of the RM.

3.2 Analytical methods

The following section is a summary of the analytical techniques used in this study. Bulk rock major and trace element concentrations of representative kyanite schist samples were measured using ICP-AES and ICP-MS at Royal Holloway College, University of London in 2011, following flux fusion with $LiBO_2$ for ICP-AES, and dissolution in a HF and $HClO_4$ mix for ICP-MS. Further bulk rock trace element concentrations were measured via ICP-MS at the Open University in 2013, following dissolution in a HF-HNO_3 mix. Textures and particularly small mineral inclusions (<50 µm) were investigated at the University of Leeds on a FEI Quanta 650 FEG-ESEM. The chemical composition of the major rock forming minerals was determined via an electron probe micro analyser (EPMA) analysis at the University of Leeds, using a JEOL 8230 EPMA. A range of analytical conditions were used, optimised for individual mineral targets, with spot sizes ranging between 2µm and 5µm and an accelerating voltage of 15kV. . Laser Raman Spectroscopy was conducted at the University of Leeds using a Renishaw 2000 Raman

Microscope with a HeNe laser at 633nm. The laser was focused using the x50 objective lens to a 2-3 µm spot, and was operated at 100% power.

3.3 Field relationships

In this study, 18 samples of kyanite garnet schist were collected from the RM; 15 from the Central Rhodope Mts. in the vicinity of Chepelare, and 3 from the Eastern Rhodope Mts. south of the town of Krumovgrad. Locations of all specimens collected can be found in appendix A. In Chepelare, all samples of kyanite garnet schist are found within the VF of the Chepelare Shear Zone, part of the upper high grade basement unit (upper allochthon) discussed in chapter 2. Exposure of these units is poor, with many of the specimens coming from abandoned exploration trenching or river beds. Of the 13 Chepelare specimens studied 2 were donated by the Bulgarian museum of natural history, Sofia. Only the general vicinity of these samples is known, as no co-ordinates were recorded in the museum archives.

The exact shape and extent of most bodies is unclear. Outcrops are found in close association with amphibolite, marble and gneiss units, but often contacts are masked by vegetation or eroded material. Where seen in situ, the pervasive foliation in the kyanite-garnet schist follows that of the host gneiss (Figure 3-1a). Alteration is widespread, and units can often be distinguished from the surrounding gneiss by an intense rust colouration and a heavily weathered fine grained matrix. In some extreme cases, heavily altered garnet is the only preserved mineral, and the entire matrix has weathered to an indistinguishable clay rich mud.

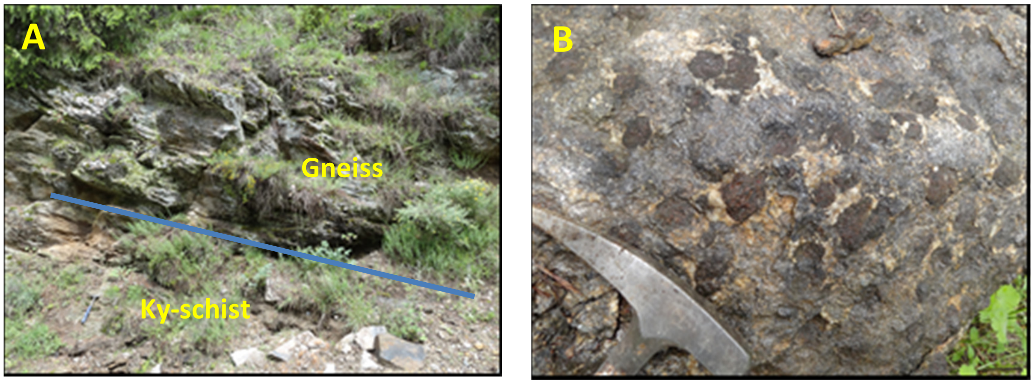

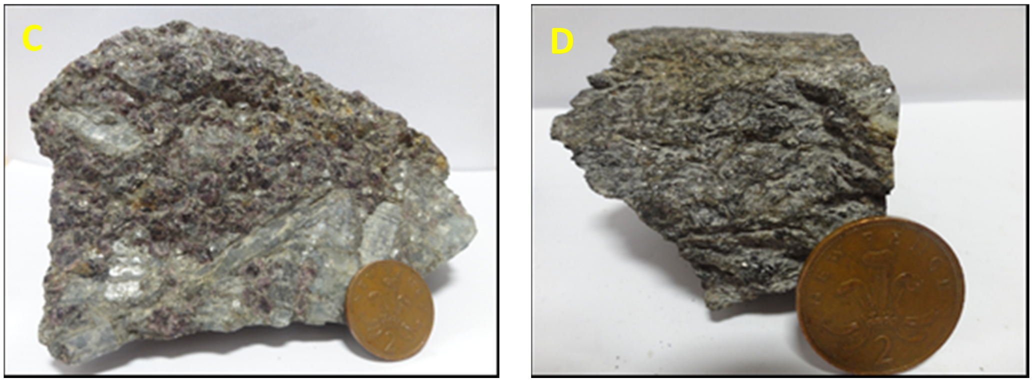

Figure 3-1: Photographs of kyanite schist outcrop in the field, and hand specimens of the studied samples. A: Outcrop of kyanite schist and host gneiss, B: Outcrop of quartz rich ky-grt schist end member with large garnet crystals (sample 2-1-11), C: Museum specimen of ky-grt schist with elongated kyanite crystals (sample 26-1-10), D: Biotite rich ky-grt schist specimen with a well-defined schistosity (sample 3-1-10).

Widespread mineralogical variation is observed between individual samples. Specimens can be grouped in terms of garnet size or colour, and relative abundance of key index minerals. Garnet colour can varies between light pink and a dark purple and size varies from <1mm to > 2cm. Kyanite ranges from small, hard to distinguish needles < 1cm in length, to large crystals up to 7 cm long (figure 1b,c). Some samples display a clear schistosity defined by biotite (figure 1d), whereas others have a quartz and feldspar rich matrix, or no matrix at all (figure 1c). In this study, the abundance of biotite and prevalence of a schistose texture was used to group the samples into 4 distinct sub groups.

3.4 Sample Petrography

13 kyanite garnet schist thin sections were examined from the Central Rhodope Mts. All samples contain abundant garnet and kyanite porphyroblasts of variable shape and size. Broadly speaking, each of the samples can be classified into one of four sub groups (Table 3-1). These are: 1) samples with a schistose texture defined by elongated biotite crystals (biotite rich matrix), 2) like group 1, but with associated quartz and plagioclase feldspar (quartz rich matrix), 3) samples with no visible matrix, where the sample is composed entirely of interlocking garnet and kyanite crystals (phaneritic samples), and 4) Samples dominated by quartz with no visible garnet (quartz dominated samples)

Sample	**2-1-10**	**3-1-10**	**25-1-10**	**26-1-10**	**27-1-10**	**2-1-11**	**28-1-11**
Biotite rich matrix		x					
Quartz rich matrix	x		x		x	x	x
Phaneritic sample				x			
Quartz dominated sample							
Sample	**33-1-11**	**35-1-11**	**38-1-11**	**47-1-11**	**5-1-12**	**13-1-12**	**-**
Biotite rich matrix	x		x				-
Quartz rich matrix					x		-
Phaneritic sample				x			-
Quartz dominated sample		x				x	-

Table 3-1 Summary of end member mineralogical and textural classifications for kyanite garnet schist samples from the vicinity of Chepelare

3.4.1 Biotite rich matrix subgroup

This suite of samples is dominated by large garnet and kyanite poikiloblastic porphyroblasts. The garnets range in size from ~100 µm - 7mm, are subhedral to anhedral in shape, and are often heavily retrogressed and fractured or fragmented (Figure 3-2a), with biotite and chlorite concentrated along the fractures. They contain abundant inclusions of quartz, rutile and biotite alongside rarer inclusions of muscovite, apatite, zircon, monazite and carbon phases (graphite/diamond). Multiphase inclusions are present in a large number of garnet crystals, with common associations being quartz + kyanite + biotite, quartz + muscovite + biotite and muscovite + quartz (Figure 3-3 b). Exsolved, orientated needles of rutile and biotite alongside rods of quartz are commonly observed (Figure 3-2b). Smaller (< 300 µm) garnet crystals and the rims of the larger crystals are often have a lower inclusion density, and crystals rims are frequently replaced by biotite and chlorite (Figure 3-2a, Figure 3-3a).

Kyanite forms large (up to 3mm in length) prismatic crystals that are often strongly deformed, exhibiting fragmentation, kink banding and undulose extinction (Figure 3-2c,Figure 3-3c). Inclusions of zircon, rutile, biotite and muscovite are common. Kyanite crystals are commonly strongly retrogressed, with rims exhibiting replacement by sericite (Figure 3-2d). The matrix of samples is dominated by platy biotite crystals that define a well-developed foliation and provides the observed schistose texture (Figure 3-2b). Biotite wraps around the garnet and kyanite porphyroblasts, and is commonly retrogressed to chlorite and kaolinite (Figure 3-2b,g). In areas it is closely associated with fibrous sillimanite (Figure 3-2e), and pockets of decussate biotite and quartz occur throughout the matrix, again outlined by the platy biotite (Figure 3-2f). Further quartz occurs in both pockets associated with kyanite (Figure 3-2g) and bands that follow the pervasive foliation (Figure 3-2h), ranging in size from a few crystals ~100 µm long to cm wide vein like structures that cut through samples. Plagioclase, rutile, K-feldspar, white mica, apatite and pyrite are also all present in small amounts throughout the matrix. A TiO_2

phase occurs as intergrowths with both muscovite and K-feldspar (Figure 3-3d) as inclusions in kyanite and in the matrix of samples.

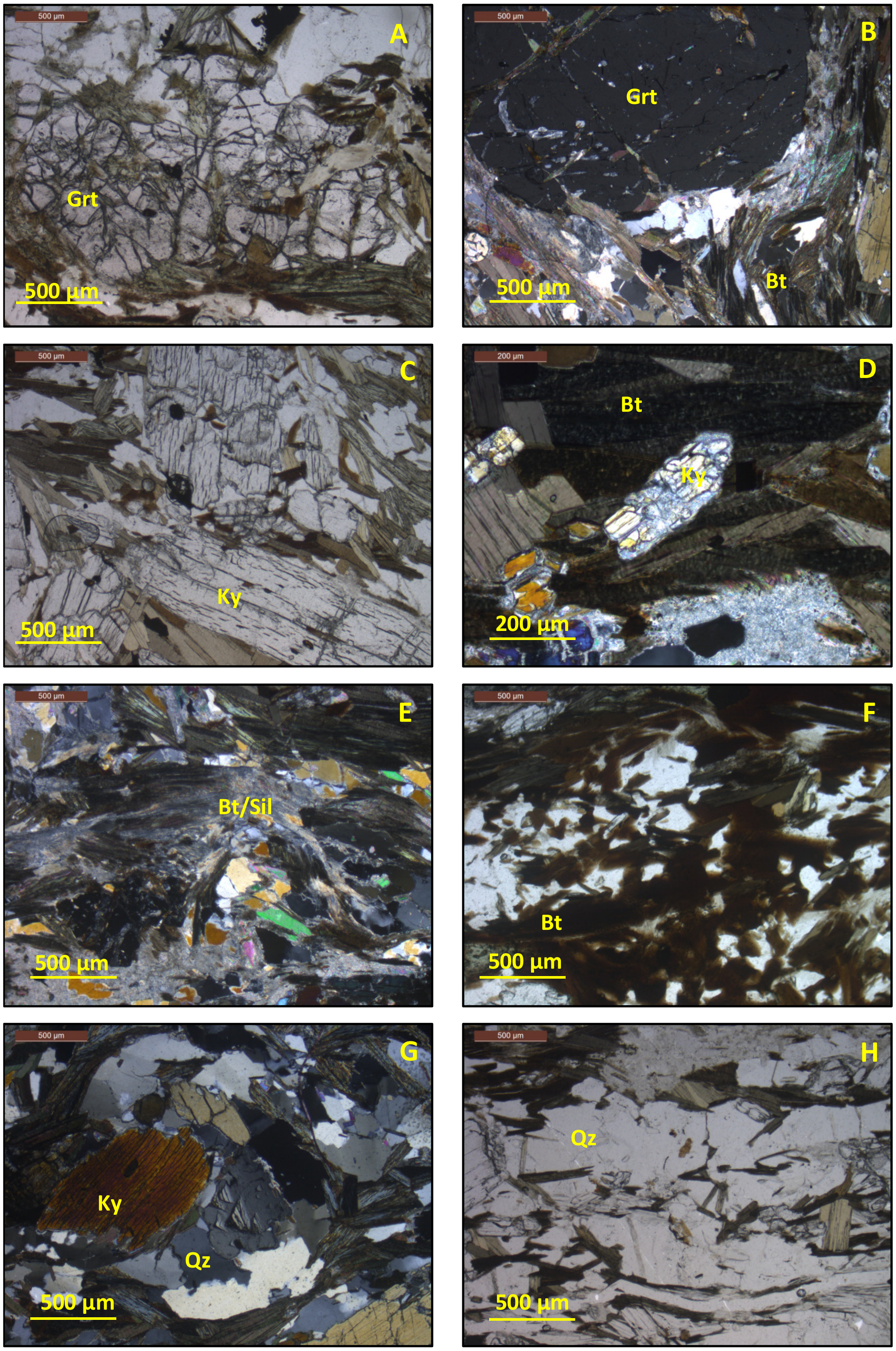

Figure 3-2: Photomicrographs of sample 3-1-10. A: dismembered garnet with biotite/chlorite matrix, B: intact garnet with exsolved needles of rutile and biotite matrix wrapping around crystal, C: large prismatic kyanite crystal, D: heavily retrogressed kyanite crystal showing breakdown to sericite, E: silimanite – biotite intergrowth in matrix, F: decussate biotite and quartz intergrowth, G: biotite wrapping around quartz and kyanite pocket, H: quartz lenses within matrix

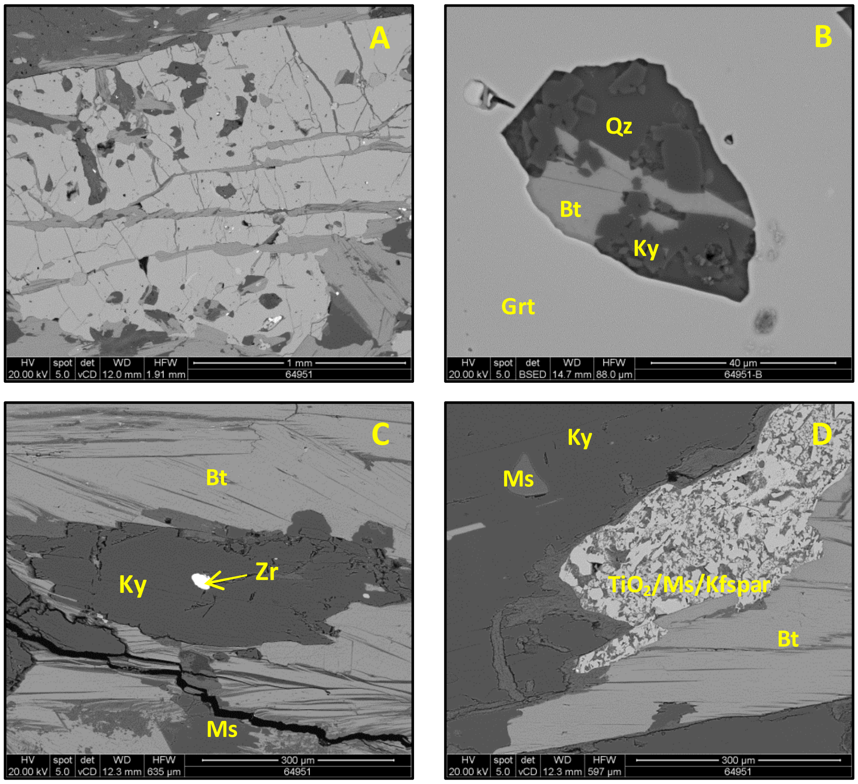

Figure 3-3: Back scatter electron images from sample 3-1-10. A: heavily fractured large garnet crystal, B: multiphase inclusion within garnet, C: heavily embayed kyanite crystal, D: TiO2 – K-feldpsar intergrowth associated with Quartz and biotite

3.4.2 Quartz rich matrix samples

This group is characterized by very large garnets, up to 2.5 cm in diameter. These grains are often deformed, with multiple aligned fractures and biotite filled cracks, and a characteristic biotite halo (Figure 3-4a,b). Inclusions are abundant, broadly the same as the biotite rich matrix samples but with the addition of chlorite. Swarms of orientated quartz rods are clearly visible (Figure 3-4 c), and the rims of crystals are often inclusion free. Smaller fragments of garnet occur in association with decussate biotite and quartz, forming pockets within the matrix.

Large kyanite porphyroblasts exhibit limited deformation and resorbtion (Figure 3-4d), although some do exhibit kink banding and undulose extinction. Some of the smaller crystals are heavily retrogressed, exhibiting retrogression to sericite (Figure 3-4 d,e,f). There is no preferred orientation for kyanite crystals. Unlike the biotite rich subgroup there is no foliation defined by matrix biotite; instead the samples have a more gneissose appearance. The matrix is dominated by quartz, which occurs in two forms. Most widespread is interlocking quartz grains ~ 100 – 500 µm in diameter that exhibit undulose extinction, bulging and grain boundary migration (Figure 3-4g). The remainder is recyrstallised quartz with a granoblastic mortar texture (Figure 3-4h), often found in close association with biotite and chlorite (Figure 3-4i, j).

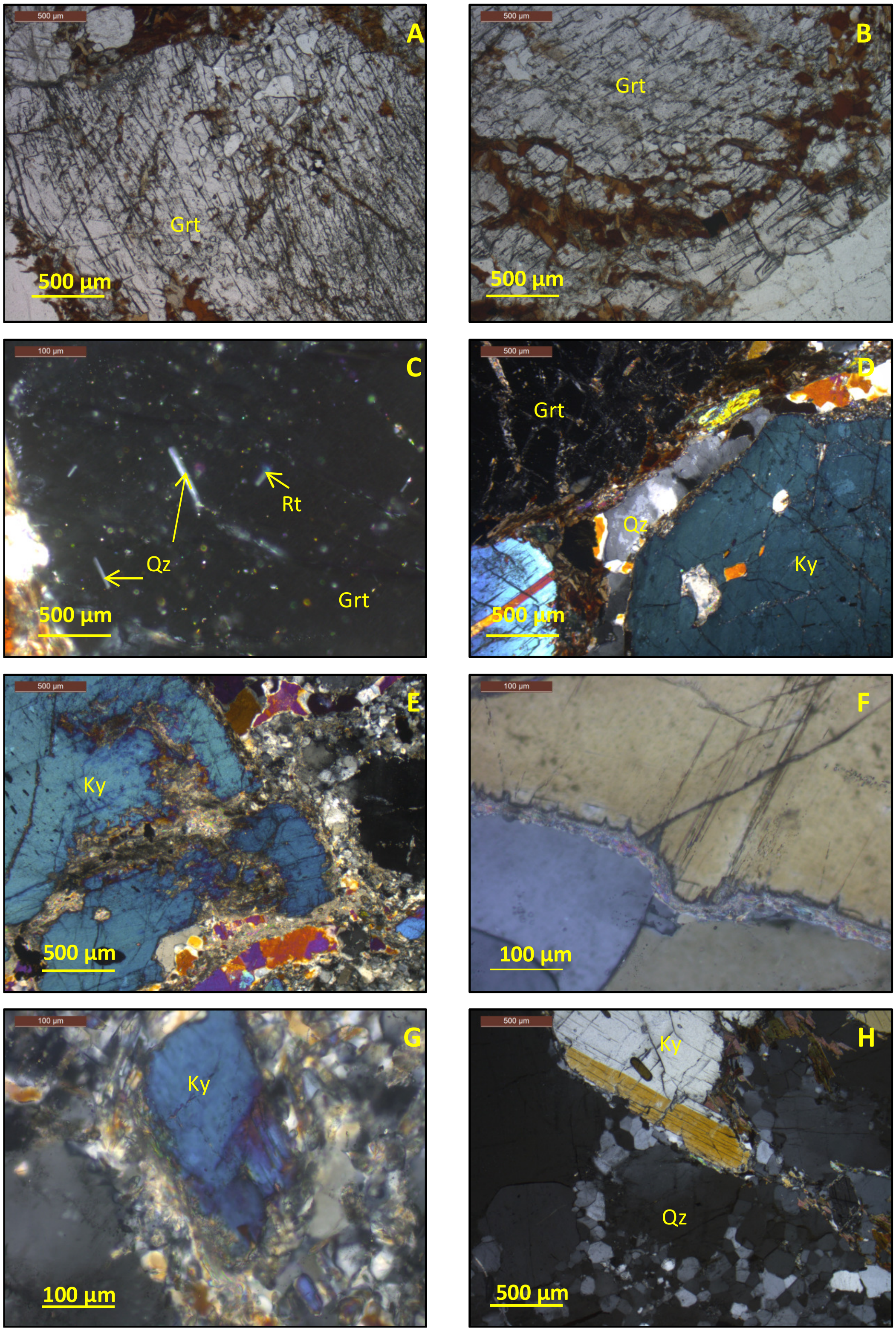

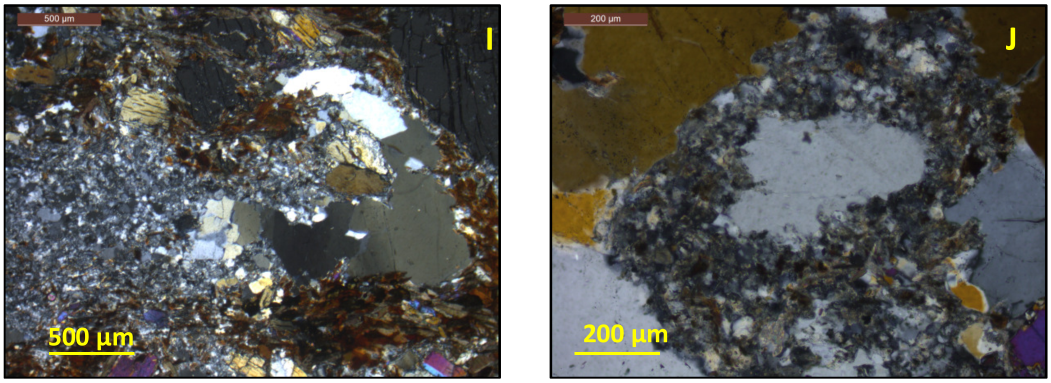

Figure 3-4: Photomicrographs of sample 27-1-10, a quartz rich end member. A and B: large heavily fractured garnet crystals retrogressed by biotite, C: quartz rods and rutile needles exsolved within garnet, D: retrogressed garnet and kyanite, with quartz lense in matrix, E: Heavily altered kyanite, F: Kyanite breakdown to sericite,hosted by quartz matrx G: matrix kyanite breaking down to silimanite/sericite, H: crystalline quartz rich, I: fine grained recrystallised matrix, J: recrystallised quartz crystal

3.4.3 Phaneritic sub group

This subgroup contains no visible matrix. It is predominantly garnet and kyanite, with biotite, chlorite, rutile and sericite infilling the intergranular space. Garnets range in size from 500 µm to 10 mm, and despite intense fracturing remain largely intact. Few inclusions are observed (Figure 3-5a) although rutile exsolution is common and restricted to garnet cores. Garnet rims are inclusion free (Figure 3-5a). Kyanite forms large deformed porphyroblasts, with common kink banding, undulose extinction (Figure 3-5b) and no preferred crystal orientation. Sericite is observed along numerous kyanite grain boundaries (Figure 3-5c). Small pockets of fine grained aggregates of quartz and decussate biotite occur throughout the matrix (Figure 3-5d).

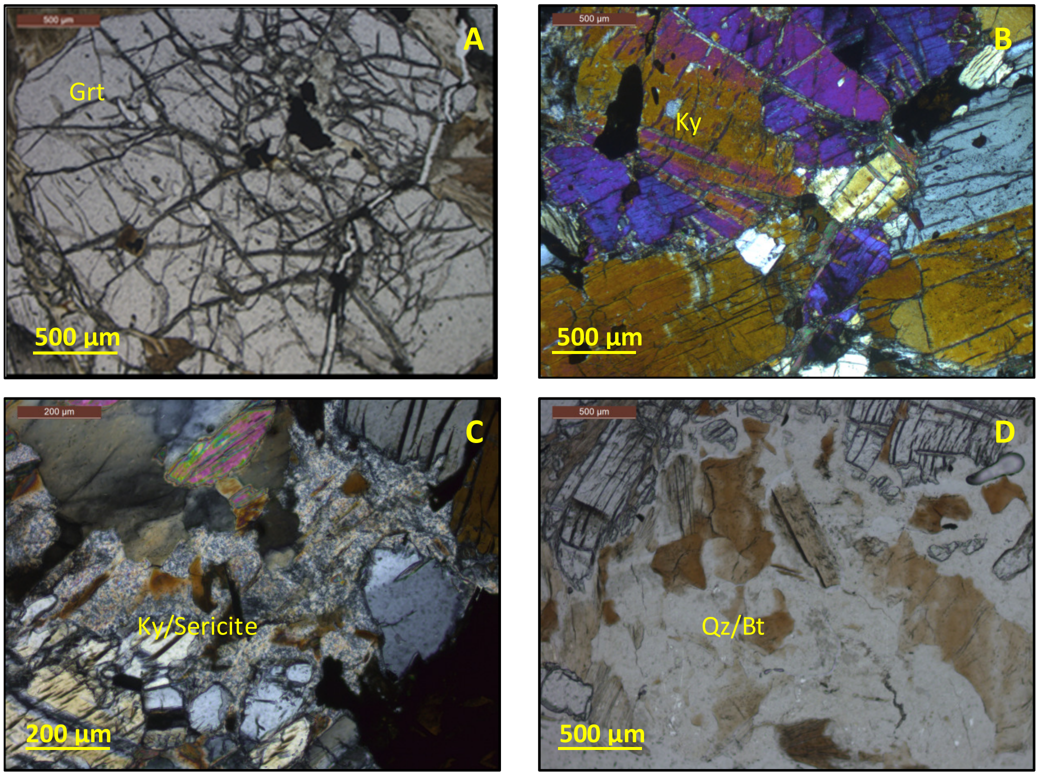

Figure 3-5: Photomicrographs of sample 47-1-11. A: intact, relatively inclusion free garnet, B: interlocking kyanite crystals, C: corroded kyanite breaking down to sericite, D: decussate biotite and quartz

3.4.4 Quartz dominated subgroup

These two samples are very quartz rich, with smaller amounts of biotite and no visible garnet. Apatite grains are widespread. Biotite is largely restricted to pockets within the thin section, forming intergrowths with quartz and rutile (Figure 3-6a). Kyanite is very rare, occurring as very small (< 500 µm) heavily retrogressed crystal fragments surrounded by a rim of biotite and rutile (Figure 3-6b).

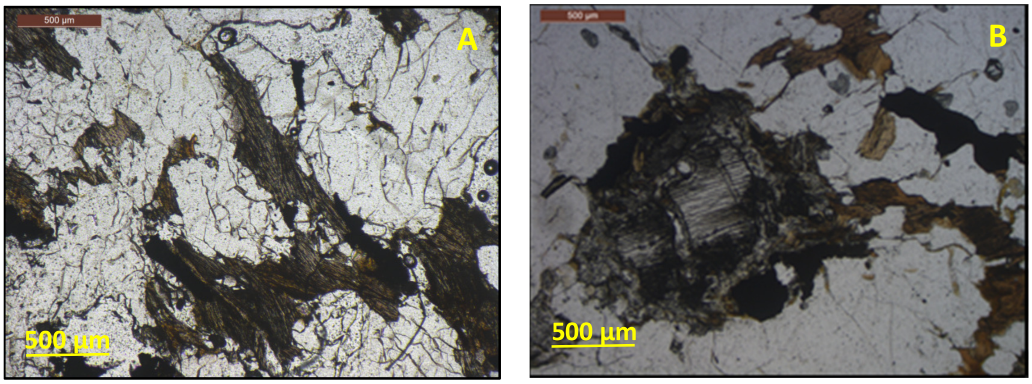

Figure 3-6: Photomicrographs of sample 35-1-11. A: Quartz and biotite matrix, B: Heavily retrogressed kyanite surrounded by quartz.

3.5 Mineral Chemistry

3.5.1 Garnet

The major element chemistry of garnet from 4 Central Rhodope samples was analysed. Results are presented in Table 3-2, and are displayed in Figure 3-7. All garnets are almandine rich ($\text{Alm}_{68\text{-}80}$), and display wide ranges of grossular ($\text{Gross}_{0.7\text{-}7.4}$), pyrope ($\text{Pyp}_{6.8\text{-}22.9}$) and spessartine ($\text{Sps}_{0.8\text{-}6.6}$) content. The range in composition within individual samples is significantly smaller than that observed between samples, with only small degrees of core-rim variation. Sample 3-1-10, a biotite rich sample has the lowest pyrope content and highest spessartine content of all samples analysed. In addition, for two samples (2-1-11 and 27-1-10), polished wafers of large (~ 2cm in diameter) garnets cut through the geometric core were prepared. These were mapped on the electron microprobe (Figure 3-8**)**. All 4 of the samples preserve Ca zonation, and three preserve Mn zonation. In sample 27-1-10 analyses were collected along a traverse at 25 µm intervals (Figure 12a). Core- rim variation in both the spessartine ($\text{Sps}_{0.9\text{-}2}$) and grossular ($\text{Gros}_{2\text{-}9}$) content is seen. Almandine and pyrope content vary within the crystal ($\text{Alm}_{66\text{-}72}$, $\text{Pyp}_{21\text{-}27}$), but with no systematic pattern (figure 12b).

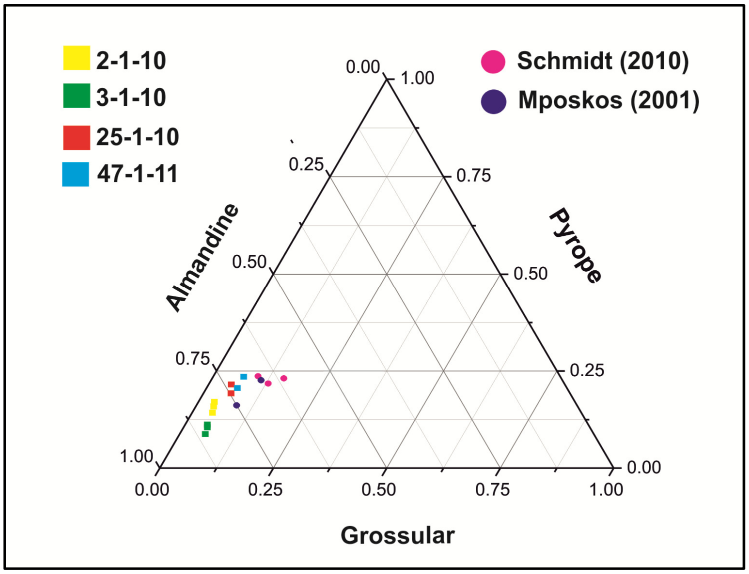

Figure 3-7: Ternary diagram of garnet composition for kyanite-garnet schist samples from the Central Rhodope Mts. UHP samples from the Kimi complex (Mposkos and Kostopoulos, 2001) and Sidironero complex (Schmidt et al., 2010) are plotted for comparison

	3-1-10			**2-1-10**			**25-1-10**		**47-1-11**	
	Core	**middle**	**Rim**	**Core**	**middle**	**rim**	**Core**	**rim**	**core**	**Rim**
SiO_2	37.09	37.13	37.02	37.68	37.60	37.50	37.55	37.54	37.59	37.36
TiO_2	0.01	0.01	0.02	0.01	0.01	0.01	0.03	0.06	0.00	0.01
Al_2O_3	21.02	21.10	21.05	21.05	20.95	21.03	21.32	21.26	21.26	21.20
Cr_2O_3	0.01	0.01	0.03	0.02	0.00	0.01	0.01	0.02	0.02	0.02
Fe_2O_3	0.22	0.06	0.01	0.51	0.60	0.36	0.74	0.68	0.41	0.52
FeO	35.88	35.93	36.01	35.32	35.47	35.91	32.53	32.96	31.18	32.14
MnO	1.69	1.72	2.36	0.46	0.49	0.56	0.74	0.83	0.69	0.89
MgO	2.73	2.66	2.18	4.35	4.04	3.63	5.28	4.77	5.78	5.04
CaO	1.73	1.77	1.70	1.25	1.46	1.51	2.15	2.39	2.58	2.67
Total	100.35	100.48	100.39	100.65	100.63	100.52	100.35	100.52	99.52	99.86
Si	2.99	2.99	2.99	3.00	3.00	3.00	2.97	2.97	2.98	2.97
Ti	0.00	0.00	0.00	0.00	0.00	0.00	0.00	0.00	0.00	0.00
Al	2.00	2.00	2.00	1.97	1.97	1.98	1.99	1.99	0.02	0.03
Cr	0.00	0.00	0.00	0.00	0.00	0.00	0.00	0.00	0.00	0.00
Fe^{3+}	0.01	0.00	0.00	0.03	0.04	0.02	0.04	0.04	0.02	0.03
Fe^{2+}	2.42	2.42	2.43	2.35	2.36	2.40	2.15	2.18	2.07	2.14
Mn	0.12	0.12	0.16	0.03	0.03	0.04	0.05	0.06	0.05	0.06
Mg	0.33	0.32	0.26	0.52	0.48	0.43	0.62	0.56	0.68	0.60
Ca	0.15	0.15	0.15	0.11	0.12	0.13	0.18	0.20	0.22	0.23
Total	8.01	8.01	8.00	8.00	8.00	8.00	8.01	8.01	8.01	8.02
Mg#	11.88	11.65	9.73	17.96	16.87	15.27	22.44	20.50	24.62	21.59
pyp	10.97	10.69	8.77	17.22	16.04	14.47	20.96	18.94	22.93	20.10
gros	4.36	4.63	4.77	3.03	3.34	3.87	4.53	5.34	6.03	6.00
alm	80.19	80.27	80.91	78.19	78.70	79.93	71.24	72.35	68.16	70.22
Sps	3.86	3.93	5.40	1.03	1.11	1.27	1.66	1.88	2.0275	1.5628
n	18	14	34	5	4	11	18	33	11	7

Table 3-2: Summary of EPMA analyses of garnet from kyanite garnet schist from the vicinity of Chepelare. Pyp: Pyrope content, Gross: Grossular content, Alm: Almandine content, Sps: Spessartine content

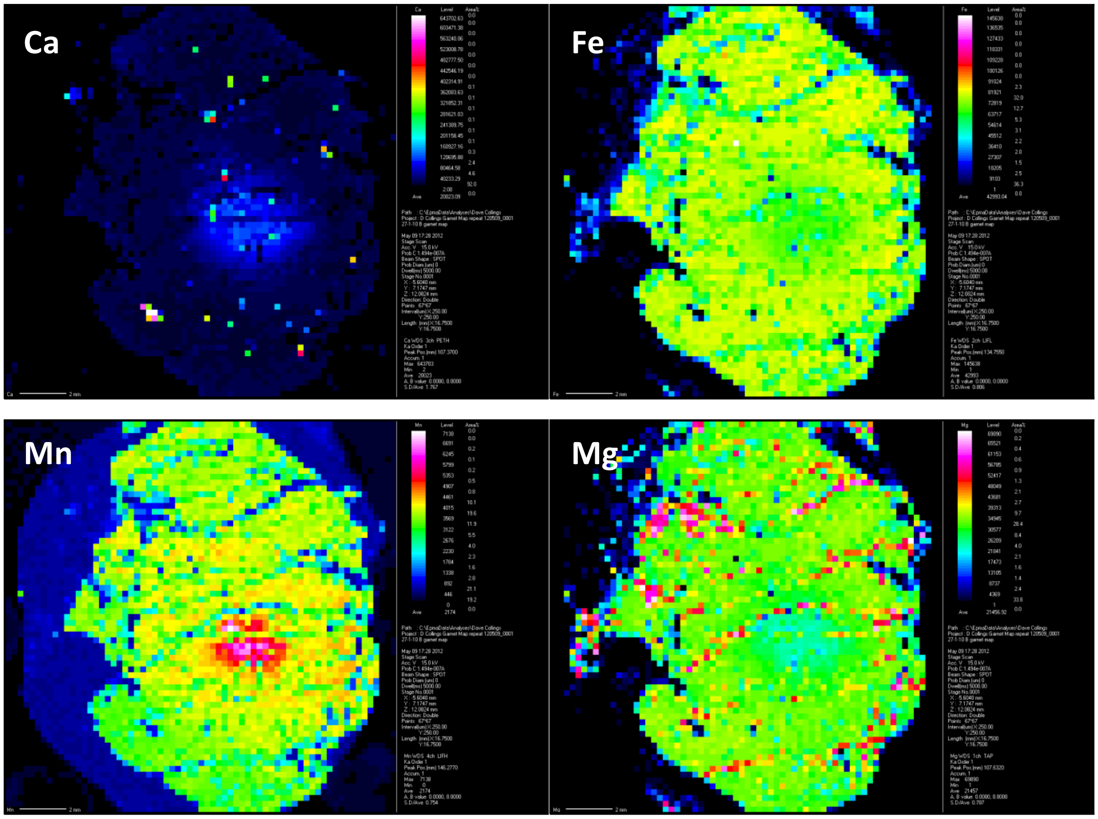

Figure 3-8: WDS elemental distribution maps of single garnet wafer ~ 2.5 cm in diameter from sample 27-1-10. The sample was mapped with 250 µm spacing between points.

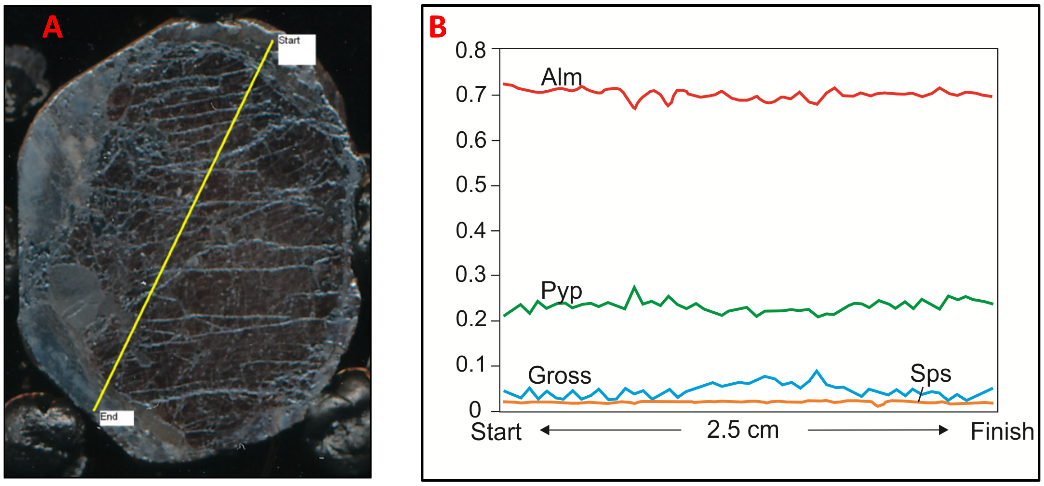

Figure 3-9, A: Scanned image of mapped garnet wafer from sample 27-1-10. Length of yellow line – 2.5 cm. B: Plots of garnet compositional variations across sample 27-1-10. Individual zones from this crystal were dated via Sm/NdO+ garnet geochronology and are discussed in chapter 5.

3.5.2 White mica

Results of white mica analyses from samples 25-1-10 and 3-1-10 are presented in Figure 3-10. White mica inclusions in garnet from sample 3-1-10 were divided into 4 distinct sub-groups: 1) those fully included in garnet, 2) those associated with cracks though the garnet, 3) those part of a multiphase inclusion, 4) those large (> 400 µm). All analysed crystals are muscovite/phengite, with small amounts of paragonite and negligible Margarite. Paragonite content is varied, and although no trends are recognised between individual subgroups, two distinct populations of white mica are seen when Si atoms per formula unit is plotted against Na/(Na+K) (Figure 3-10a)**.**

Si content ranges between 3.03 and 3.63 a/fu, suggesting a variable phengite component of samples. This is reflected on Figure 3-10b**,** where Si, Fe^{2+} and Mg^{2+} exhibit strong correlation with Al^{VI} and Al^{IV} in all analyses, indicating a broad range of compositions controlled by the phengite substitution reacton: $\mathbf{Si^{IV} + (Fe^{2+},Mg)^{VI} = Al^{IV} + Al^{VI}}$ (Guidotti and Sassi, 2002). Although absolute Ti concentrations are very small, two distinct populations can be identified on the basis of Si and Ti content of grains, with the more phengitic Si rich grains (Si content up to 3.6 a/fu) containing no measureable Ti (Figure 3-10c). All muscovite found in association with kyanite is of the Ti rich category. All analyses from sample 25-1-10 are Ti poor (max measured 0.015 a/fu), but display a wide range of Si contents (Si = 3.05 – 3.4 a/fu).

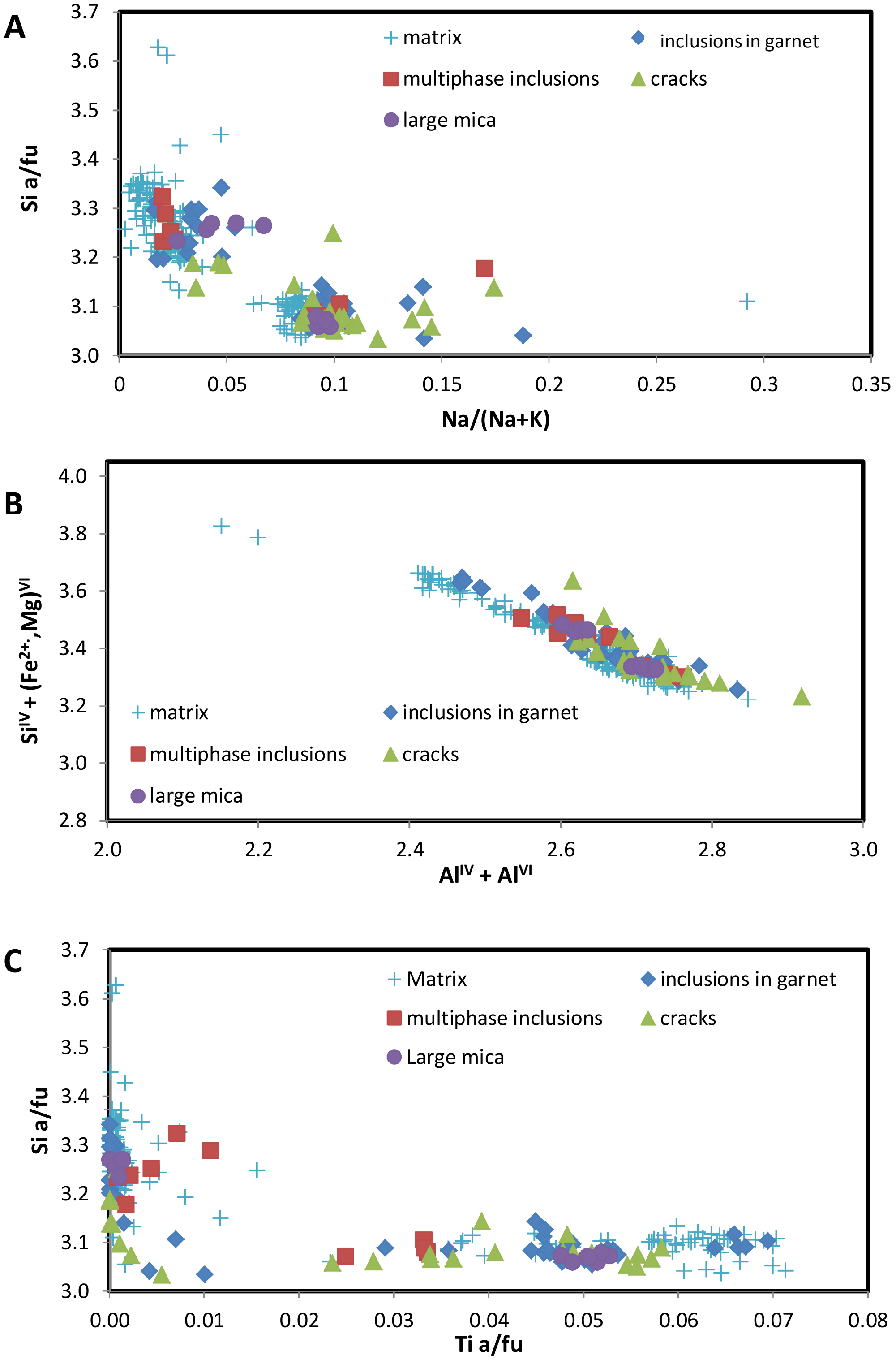

Figure 3-10: chemical analyses of white mica from sample 3-1-10. A: Plot of Si a/fu vs Na/(Na+K) showing two distinct sub groups. B: Plot of $Si^{IV} + (Fe^{2+},Mg)^{VI}$ vs $Al^{IV} + Al^{VI}$ showing strong correlation indicating phengite substitution is controlling the chemistry of the white mica. C: Plot of Si a/fu vs Ti a/fu, highlighting the two distinct populations on the basis of Ti content. (a/fu = atoms per formula unit).

		3-1-10															25-1-10		
		Inclusion in Grt			**Large Incl in Grt**			**Crack in Grt**			**Multiphase incl**			**Matrix**			**Matrix**		
		avg	*max*	*min*	*avg*	*max*	*min*	*avg*	*max*	*min*	*avg*	*max*	*min*	*avg*	*max*	*min*	*avg*	*max*	*min*
Oxide Wt %	**SiO_2**	*47.25*	*50.88*	*45.23*	*47.52*	*50.34*	*45.58*	*46.24*	*49.68*	*44.66*	*48.17*	*50.20*	*45.93*	*48.53*	*56.47*	*44.27*	*48.70*	*51.85*	*47.07*
	TiO_2	*0.56*	*1.38*	*0.00*	*0.59*	*1.05*	*0.00*	*0.57*	*1.15*	*0.00*	*0.30*	*0.67*	*0.02*	*0.37*	*1.41*	*0.00*	*0.06*	*0.20*	*0.00*
	Al_2O_3	*33.76*	*36.29*	*31.52*	*34.22*	*34.57*	*33.90*	*34.36*	*37.49*	*32.58*	*34.13*	*35.04*	*32.64*	*33.43*	*36.53*	*28.29*	*34.05*	*35.66*	*31.76*
	FeO	*2.78*	*4.00*	*1.98*	*2.43*	*2.88*	*1.77*	*2.72*	*6.03*	*1.54*	*2.10*	*2.73*	*1.42*	*1.68*	*2.85*	*0.49*	*1.85*	*2.97*	*1.08*
	MnO	*0.05*	*0.15*	*0.00*	*0.04*	*0.15*	*0.00*	*0.06*	*0.13*	*0.00*	*0.03*	*0.11*	*0.00*	*0.02*	*0.09*	*0.00*	*0.02*	*0.06*	*0.00*
	MgO	*0.66*	*1.12*	*0.32*	*0.56*	*0.71*	*0.30*	*0.58*	*1.03*	*0.29*	*0.59*	*0.83*	*0.38*	*0.73*	*1.26*	*0.22*	*1.26*	*1.88*	*0.85*
	CaO	*0.13*	*0.89*	*0.00*	*0.12*	*0.27*	*0.04*	*0.14*	*0.71*	*0.04*	*0.21*	*0.74*	*0.00*	*0.16*	*0.97*	*0.00*	*0.04*	*0.24*	*0.00*
	Na_2O	*0.54*	*1.26*	*0.10*	*0.52*	*0.71*	*0.16*	*0.66*	*1.09*	*0.18*	*0.45*	*1.00*	*0.11*	*0.30*	*1.65*	*0.02*	*0.29*	*0.48*	*0.05*
	K_2O	*9.28*	*10.06*	*7.70*	*9.46*	*10.17*	*8.45*	*9.28*	*10.11*	*7.37*	*9.19*	*10.23*	*7.40*	*9.58*	*11.08*	*6.08*	*10.43*	*10.99*	*9.53*
	H_2O	*4.50*	*4.61*	*4.40*	*4.52*	*4.62*	*4.45*	*4.47*	*4.58*	*4.38*	*4.53*	*4.58*	*4.48*	*4.52*	*4.69*	*4.36*	*4.58*	*4.65*	*4.49*
	total	*99.52*			*99.99*			*99.08*			*99.69*			*99.31*			*101.27*		
Cations to 12 O, OH	**Si**	*3.15*	*3.34*	*3.03*	*3.15*	*3.27*	*3.06*	*3.09*	*3.25*	*3.03*	*3.19*	*3.32*	*3.07*	*3.22*	*3.63*	*3.04*	*3.19*	*3.35*	*3.12*
	Al	*0.85*	*0.97*	*0.66*	*0.85*	*0.94*	*0.73*	*0.91*	*0.97*	*0.75*	*0.81*	*0.93*	*0.68*	*0.78*	*0.96*	*0.37*	*0.81*	*0.88*	*0.65*
	Al	*1.80*	*1.89*	*1.73*	*1.82*	*1.89*	*1.77*	*1.81*	*1.95*	*1.75*	*1.85*	*1.89*	*1.81*	*1.83*	*1.94*	*1.75*	*1.81*	*1.88*	*1.73*
	Ti	*0.03*	*0.07*	*0.00*	*0.03*	*0.05*	*0.00*	*0.03*	*0.06*	*0.00*	*0.02*	*0.03*	*0.00*	*0.02*	*0.07*	*0.00*	*0.00*	*0.01*	*0.00*
	Cr	*0.00*	*0.00*	*0.00*	*0.00*	*0.00*	*0.00*	*0.00*	*0.00*	*0.00*	*0.00*	*0.00*	*0.00*	*0.00*	*0.00*	*0.00*	*0.00*	*0.00*	*0.00*
	Fe^{2+}	*0.16*	*0.22*	*0.11*	*0.13*	*0.16*	*0.10*	*0.15*	*0.34*	*0.08*	*0.12*	*0.15*	*0.08*	*0.09*	*0.16*	*0.03*	*0.10*	*0.16*	*0.06*
	Mn	*0.00*	*0.01*	*0.00*	*0.00*	*0.01*	*0.00*	*0.00*	*0.01*	*0.00*	*0.00*	*0.01*	*0.00*	*0.00*	*0.01*	*0.00*	*0.00*	*0.00*	*0.00*
	Mg	*0.07*	*0.11*	*0.03*	*0.06*	*0.07*	*0.03*	*0.06*	*0.10*	*0.03*	*0.06*	*0.08*	*0.04*	*0.07*	*0.13*	*0.02*	*0.12*	*0.19*	*0.08*
	Ca	*0.01*	*0.06*	*0.00*	*0.01*	*0.02*	*0.00*	*0.01*	*0.05*	*0.00*	*0.01*	*0.05*	*0.00*	*0.01*	*0.07*	*0.00*	*0.00*	*0.02*	*0.00*
	Na	*0.07*	*0.16*	*0.01*	*0.07*	*0.09*	*0.02*	*0.09*	*0.14*	*0.02*	*0.06*	*0.13*	*0.01*	*0.04*	*0.21*	*0.00*	*0.04*	*0.06*	*0.01*
	K	*0.79*	*0.86*	*0.65*	*0.80*	*0.87*	*0.71*	*0.80*	*0.87*	*0.64*	*0.78*	*0.87*	*0.62*	*0.81*	*0.96*	*0.51*	*0.87*	*0.93*	*0.78*
		n = 42			*n = 12*			*n = 25*			*n = 10*			*n = 186*			*n = 17*		

Table 3-3: Summary of EPMA data for white mica from samples 3-1-10 and 2-1-10

3.5.3 Biotite

A study was conducted on biotite from the three petrological end members; samples 3-1-10 (biotite rich), 25-1-10 (quartz rich) and 47-1-11 (phaneritic), Analyses have been divided into inclusions within garnet (inclusion, crack, multiphase inclusion and exsolution) and matrix (garnet rim and matrix samples). Results are summarised in Table 3-4 and Table 3-5.

In samples 3-1-10 large variations are seen in the Mg# of biotite crystals. Inclusions within garnet having the highest values, which likely the result of retrograde exchange reactions. Ti content has previously been shown to increase as a function of metamorphic grade (Guidotti, 1984). Although little within sample variation in Ti content is seen, biotite from samples 25-1-10 have higher Ti content, alongside higher Mg# than biotite from samples 3-1-10, indicating formation at higher metamorphic grades.

		3-1-10																	
		Exsolution (n = 2)			**Multiphase (n = 4)**			**Crack (n = 10)**			**inclusion in grt (n = 2)**			**Matrix (n = 6)**			**Garnet rim (n = 33)**		
		avg	**max**	**min**	**avg**	**max**	**min**	**avg**	**max**	**min**	**avg**	**max**	**min**	**avg**	**max**	**min**	**avg**	**max**	**min**
Oxide wt%	**SiO_2**	34.48	34.50	34.46	35.03	35.17	34.87	35.12	37.86	34.38	35.42	35.78	35.06	35.04	35.41	34.75	34.59	35.74	33.62
	TiO_2	1.66	1.66	1.65	2.38	2.44	2.29	2.08	2.43	1.56	1.83	1.84	1.81	2.62	2.97	2.30	2.06	3.02	1.40
	Al_2O_3	20.49	20.57	20.42	20.40	20.47	20.23	20.56	24.08	19.74	21.37	21.58	21.17	19.61	19.91	19.47	20.29	22.19	19.16
	Cr_2O_3	0.02	0.04	0.00	0.03	0.05	0.00	0.02	0.05	0.00	0.02	0.03	0.01	0.01	0.04	0.00	0.02	0.06	0.00
	FeO	23.63	23.63	23.63	21.28	21.64	20.84	21.74	23.42	17.69	20.63	20.94	20.32	23.00	23.67	22.63	23.06	24.64	19.82
	MnO	0.11	0.13	0.10	0.05	0.08	0.02	0.08	0.10	0.05	0.09	0.10	0.08	0.04	0.06	0.01	0.09	0.33	0.03
	MgO	7.02	7.05	7.00	8.16	8.38	7.96	7.57	9.04	5.81	8.37	8.56	8.17	7.20	7.35	7.03	7.10	7.55	6.13
	CaO	0.03	0.04	0.02	0.02	0.02	0.01	0.02	0.05	0.00	0.04	0.06	0.02	0.00	0.01	0.00	0.04	0.66	0.00
	Na_2O	0.32	0.32	0.32	0.28	0.29	0.28	0.28	0.34	0.20	0.31	0.31	0.31	0.27	0.30	0.23	0.27	0.32	0.20
	K_2O	8.75	8.81	8.69	9.02	9.04	9.00	8.80	9.00	8.66	8.84	8.88	8.80	8.88	9.01	8.74	8.74	9.06	7.70
	H_2O	3.92	3.93	3.92	3.97	3.98	3.97	3.96	4.09	3.91	4.01	4.02	4.00	3.94	3.98	3.91	3.92	3.95	3.86
	total	*100.44*			*100.63*			*100.23*			*100.92*			*100.61*			*100.17*		
Cations to 12 O, OH	**Si**	2.63	2.64	2.63	2.64	2.65	2.63	2.66	2.77	2.63	2.65	2.67	2.63	2.66	2.68	2.64	2.64	2.71	2.58
	Al^{iv}	1.37	1.37	1.36	1.36	1.37	1.35	1.34	1.37	1.23	1.35	1.37	1.33	1.34	1.36	1.32	1.36	1.42	1.29
	Al^{vi}	0.48	0.48	0.48	0.46	0.47	0.45	0.50	0.85	0.42	0.53	0.56	0.50	0.42	0.45	0.40	0.47	0.70	0.40
	Ti	0.10	0.10	0.10	0.14	0.14	0.13	0.12	0.14	0.09	0.10	0.10	0.10	0.15	0.17	0.13	0.12	0.17	0.08
	Cr	0.00	0.00	0.00	0.00	0.00	0.00	0.00	0.00	0.00	0.00	0.00	0.00	0.00	0.00	0.00	0.00	0.00	0.00
	Fe^{2+}	1.51	1.51	1.51	1.34	1.37	1.31	1.38	1.49	1.08	1.29	1.31	1.27	1.46	1.50	1.44	1.47	1.57	1.26
	Mn	0.01	0.01	0.01	0.00	0.01	0.00	0.00	0.01	0.00	0.01	0.01	0.00	0.00	0.00	0.00	0.01	0.02	0.00
	Mg	0.80	0.80	0.80	0.92	0.94	0.90	0.86	1.02	0.63	0.93	0.96	0.91	0.82	0.83	0.79	0.81	0.86	0.70
	Ca	0.00	0.00	0.00	0.00	0.00	0.00	0.00	0.00	0.00	0.00	0.00	0.00	0.00	0.00	0.00	0.00	0.05	0.00
	Na	0.05	0.05	0.05	0.04	0.04	0.04	0.04	0.05	0.03	0.05	0.05	0.05	0.04	0.04	0.03	0.04	0.05	0.03
	K	0.85	0.86	0.85	0.87	0.87	0.87	0.85	0.87	0.83	0.84	0.85	0.84	0.86	0.87	0.85	0.85	0.88	0.75
	OH	2.00	2.00	2.00	2.00	2.00	2.00	2.00	2.00	2.00	2.00	2.00	2.00	2.00	2.00	2.00	2.00	2.00	2.00
	Mg#	35	35	35	41	42	40	38	44	35	42	42	42	36	37	35	35	37	32

Table 3-4: Summary of biotite EPMA analyses from sample 3-1-10

		25-1-10									47-1-11					
		Matrix (n = 38)			Crack (n = 6)			Inclusion (n = 6)			Matrix (n = 4)			decussate (n = 3)		
		avg	max	min	avg	max	min	avg	max	min	avg	max	min	avg	max	min
Oxide wt%	SiO_2	35.86	36.89	32.86	36.22	37.06	35.28	36.22	37.06	35.28	35.90	36.06	35.80	35.54	35.76	35.31
	TiO_2	3.82	4.61	2.59	3.31	4.49	2.71	3.31	4.49	2.71	2.37	2.45	2.30	1.76	1.98	1.33
	Al_2O_3	17.95	19.26	16.11	18.33	18.63	18.14	18.33	18.63	18.14	17.89	18.24	17.70	18.28	18.31	18.26
	Cr_2O_3	0.02	0.06	0.00	0.02	0.05	0.00	0.02	0.05	0.00	-	-	-	-	-	-
	FeO	17.12	19.59	14.74	17.12	18.44	16.32	17.12	18.44	16.32	16.54	16.80	16.32	18.14	18.60	17.35
	MnO	0.03	0.08	0.00	0.03	0.06	0.00	0.03	0.06	0.00	0.03	0.04	0.01	0.07	0.08	0.05
	MgO	11.37	12.52	10.28	11.96	12.24	11.60	11.96	12.24	11.60	12.27	12.41	12.17	11.26	11.54	10.97
	CaO	0.07	1.83	0.00	0.00	0.01	0.00	0.00	0.01	0.00	-0.01	0.01	-0.03	0.03	0.04	0.00
	Na_2O	0.15	0.29	0.08	0.18	0.22	0.14	0.18	0.22	0.14	0.25	0.27	0.22	0.07	0.33	-0.42
	K_2O	7.99	9.23	6.24	7.85	8.32	7.27	7.85	8.32	7.27	8.71	8.80	8.52	8.31	8.67	8.04
	H_2O	3.96	4.04	3.72	4.00	4.03	3.96	4.00	4.03	3.96	3.95	3.96	3.94	3.91	3.93	3.89
	total	*98.41*			*99.08*			*99.08*			*97.91*			*97.37*		
Cations to 12 O, OH	Si	2.68	2.72	2.60	2.68	2.71	2.64	2.68	2.71	2.64	2.72	2.73	2.72	2.73	2.75	2.71
	Al^{iv}	1.32	1.40	1.28	1.32	1.36	1.29	1.32	1.36	1.29	1.28	1.28	1.27	1.27	1.29	1.25
	Al^{vi}	0.26	0.33	0.17	0.27	0.29	0.24	0.27	0.29	0.24	0.33	0.35	0.31	0.38	0.42	0.35
	Ti	0.21	0.26	0.15	0.18	0.25	0.15	0.18	0.25	0.15	0.14	0.14	0.13	0.10	0.11	0.08
	Cr	0.00	0.00	0.00	0.00	0.00	0.00	0.00	0.00	0.00	0.00	0.00	0.00	0.00	0.00	0.00
	Fe^{2+}	1.07	1.25	0.91	1.06	1.15	1.00	1.06	1.15	1.00	1.05	1.06	1.04	1.16	1.19	1.12
	Mn	0.00	0.01	0.00	0.00	0.00	0.00	0.00	0.00	0.00	0.00	0.00	0.00	0.00	0.01	0.00
	Mg	1.27	1.38	1.15	1.32	1.36	1.27	1.32	1.36	1.27	1.39	1.40	1.38	1.29	1.32	1.25
	Ca	0.01	0.15	0.00	0.00	0.00	0.00	0.00	0.00	0.00	0.00	0.00	0.00	0.00	0.00	0.00
	Na	0.02	0.04	0.01	0.03	0.03	0.02	0.03	0.03	0.02	0.04	0.04	0.03	0.01	0.05	-0.06
	K	0.77	0.88	0.60	0.75	0.79	0.70	0.75	0.79	0.70	0.84	0.85	0.82	0.81	0.85	0.78
	OH	1.99	2.00	1.97	1.99	1.99	1.99	1.99	1.99	1.99	2.00	2.00	2.00	2.00	2.00	2.00
	Mg#	54.18	60.14	48.31	55.44	56.47	54.00	55.44	56.47	54.00	56.93	57.12	56.46	52.52	54.24	51.42

Table 3-5: Summary of biotite EPMA analyses from samples 25-1-10 and 47-1-11

3.6 Constraining P-T conditions

3.6.1 Petrological constraints on P-T conditions

To date there has been no reported direct evidence of UHP conditions (either coesite or microdiamond inclusions) in the Bulgarian part of the Central Rhodope Mts. Previous studies of Chepelare metapelites have suggested HP/UHP conditions (Georgieva et al., 2007, Kostopoulos et al., 2003) on the basis of observed exsolution of rutile, polyphase inclusions in garnet. This has also been recognised in this study (Figure 3-11a,b), but in addition microdiamond inclusions have been found in garnet, establishing UHP conditions for the area.

A promising inclusion was identified on the SEM (Figure 3-12a), confirmed as carbon using EDS spectroscopy and fluorescence was observed using the cathodeluminescence detector. Further Laser Raman spectroscopy investigation identified the inclusion as diamond, with the characteristic raman spectra peak at 1333.2 cm^{-1} (Figure 3-12d). Metamorphic microdiamonds are commonly associated with graphite, which acts as a clear test to discriminate from contamination of diamonds from a polishing paste (Perraki et al., 2009). Although a very broad peak around 1580 cm^{-1} (the main peak for graphite) is observed on the Raman spectra, this is too broad to definitively be graphite and rule out contamination by diamond polishing paste.

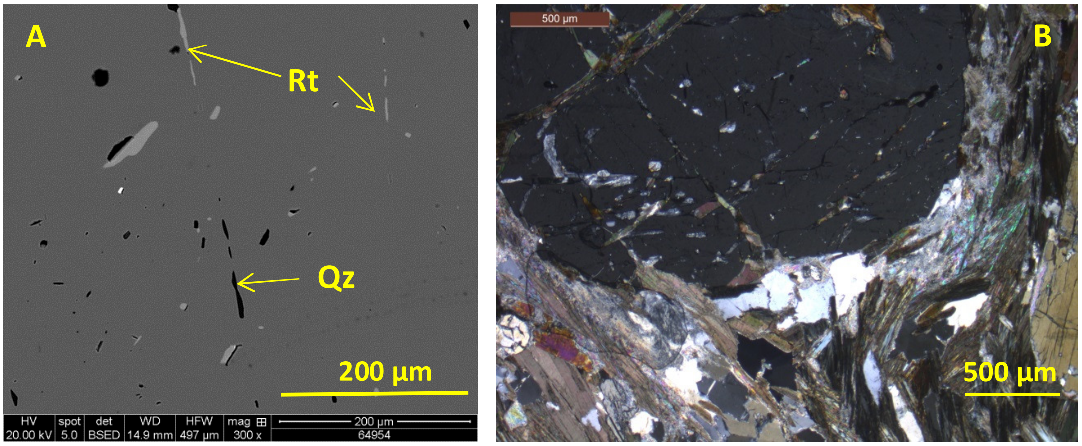

Figure 3-11: A: Back scatter electron image of exsolved rutile and quartz rods from sample 2-1-10, B: Photomicropgraph of rutile exsolition from sample 3-1-10

Two methods were employed to ensure that the microdiamond was not an artefact from the polishing process. Firstly a study was conducted on the SEM of the diamond polishing paste itself. This revealed that the shape of the synthetic diamonds used was euhedral without the distinctive stepped cleavage observed in the diamond inclusion (Figure 3-12c). In addition diamond pastes containing only 10 µm, 3µm and 1 µm were used in the polishing process i.e. the diamond inclusion of interest is not any of these sizes.

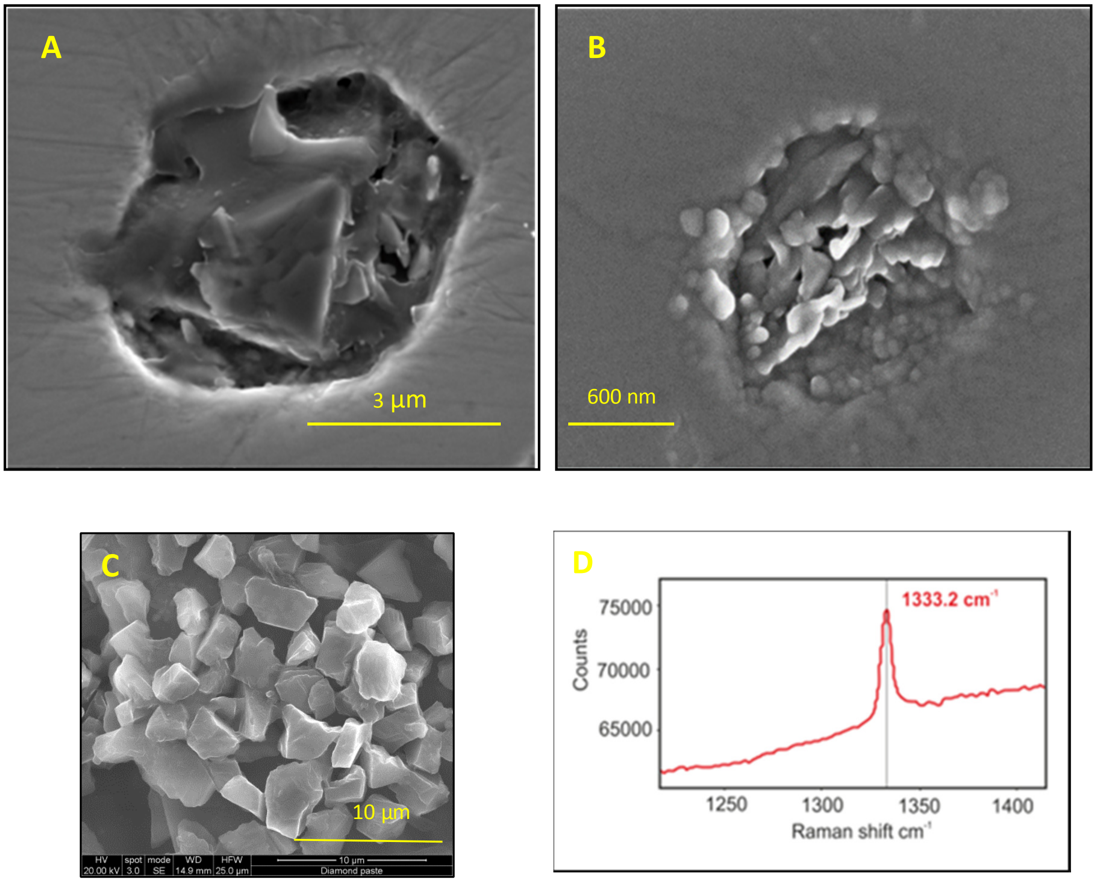

Figure 3-12: A: SEM image of microdiamond inclusion from sample 3-1-10, B: SEM image of carbon inclusion that fluoresced under CL light from sample 3-1-10, C: SEM image of diamond polishing paste, D: Laser raman spectra from microdiamond.

Secondly, a polished block of garnet separates from the same sample was prepared and polished with 0.3 µm alumina rather than diamond paste. A small carbon inclusion (Figure 3-12b) (< 1 µm) fluoresced under cathodoluminescence, revealing that it is not graphite. The texture of this inclusion resembles partially graphitised microdiamonds from the Kokchetav massif (Korsakov et al., 2010b) and the results of experimental studies on UHP diamond crystallisation performed by Dobrzhinetskaya et al. (2013). The small size of the inclusion , however rendered it unsuitable for confirmation by laser raman spectroscopy. These observations suggest that kyanite-garnet schist from the Chepelare area experienced pressures of at least 4 GPa, and reached depths in the crust in excess of 100 Km.

3.6.2 Thermobarometry

The complex petrological associations described in section 3.4 complicate establishing equilibrium assemblages for thermobarometry. As a result, reconstructing the peak P-T conditions and the overall P-T path of these samples is challenging. A large number of published thermometers and barometers are also unsuitable for the expected pressures and temperatures for this assemblage. In this section a selection of the most appropriate thermobarometers have been applied.

3.6.3 Geothermometry

3.6.3.1 Zr in rutile thermometry

Peak temperatures experienced by the kyanite-garnet schists have been determined using the Zr in rutile thermometer of Zack et al. (2004). This thermometer is based upon the the empirical relationship between Zr concentration in rutile and temperature of metamorphism. The Zr content of rutile is buffered by the reactions: $\mathbf{SiO_2 + ZrO_2 = ZrSiO_4}$ and $\mathbf{SiO_2 + Ti_2ZrO_6 = 2TiO_2 + ZrSiO_4}$. ZrO_2 (baddelyite) and Ti_2ZrO_6 (srilankite) have not been found in association with quartz in nature, and as such these equations are not considered equilibrium assemblages. Instead, quartz, rutile and zircon, the most common phases in the SiO2-TiO_2-ZrO_2 system, are used as the basis for this thermometer (Zack et al., 2004).

Temperatures are calculated via the equation: **T °C = 127.8 x ln (Zr in ppm) -10**

This relationship is pressure independent, removing a degree of uncertainty often associated with geothermometry. Rutile grains from different settings in samples 3-1-10 and 25-1-10 were analysed, and results are presented in Table 3-6. Rutile exsolved from garnet was ignored, as this will not have equilibrated with quartz and zircon. The EPMA was optimised for analysis of trace amounts of Zr, with analysis performed simultaneously on 3 spectrometers. The average Zr contents of all sub groups range between 350 and 560 ppm, equating to temperatures of 760 – 810 $\pm$ 50 °C. No distinction can be made between inclusions and matrix grains in either sample.

Contamination by neighbouring zircon crystals can skew the calculated temperatures to unrealistically high values. As such, Si concentration of rutile grains is suggested as a suitable proxy to test the degree of contamination (Zack et al., 2004). Si concentrations range between 20 and 15800 ppm. The reason for this variation is unclear; although contamination is possible, another explanation is differences in background measurements between runs on the electron microprobe - the result of a lack of a suitable Si standard for such small concentrations. On plots of calculated temperature vs Si concentration no correlation is observed, and if all analyses with Si > 200 ppm are ignored there is no change to the average calculated temperature, suggesting that zircon contamination has had a negligible effect on Zr content in rutile.

Rutile loaction		3-1-10			25-1-10		
		Si (ppm)	Zr (ppm)	T °C	Si (ppm)	Zr (ppm)	T°C
Garnet	**Average**	2152	353	759	227	564	807
	Max	15840	527	814	1440	1270	932
	Min	90	210	691	50	300	739
crack	**Average**	1499	412	776	80	352	760
	Max	2486	778	867	150	410	781
	Min	656	302	740	30	250	715
multi-phase	**Average**	1317	442	790	76	362	764
	Max	2624	522	813	100	380	771
	Min	752	379	770	50	340	756
matrix with kyanite	**Average**	50	437	789	47	358	762
	Max	90	510	810	160	430	788
	Min	20	390	774	0	290	735
Matrix with biotite	**Average**	-	-	-	82	391	774
	Max	-	-	-	180	450	794
	Min	-	-	-	10	320	748

Table 3-6: Overview of all Zr in rutile thermometry analyses from samples 3-1-10 and 25-1-10

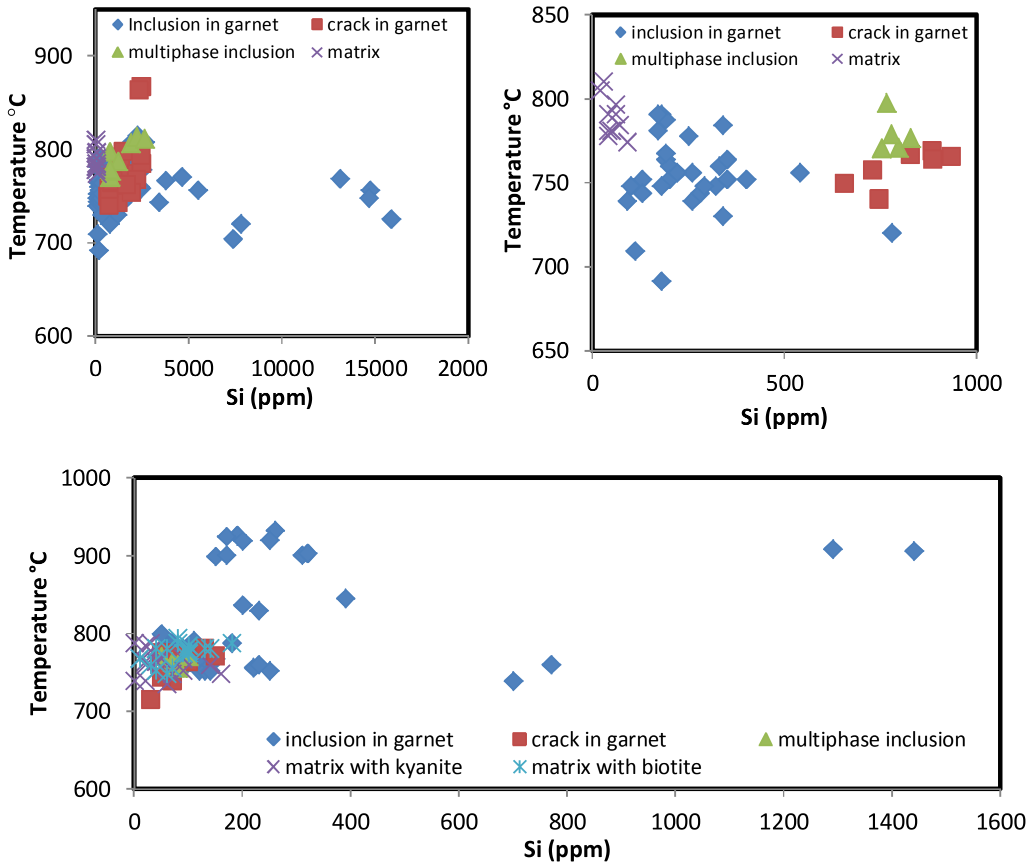

Figure 3-13, A: Plot of temperature vs Si for sample 3-1-10, B: Same as plot A, but restricted to Si content < 1000 ppm, C: Plot of temperature vs Si for sample 25-1-10

3.6.3.2 Garnet Biotite thermometry

The garnet-biotite Fe-Mg exchange thermometer was also used to constrain metamorphic temperatures. The relationship between temperature and Fe-Mg content of coexisting garnet and biotite was first recognised by Kretz (1959), and the first experimental thermometer was published by Ferry and Spear (1978) based on the equation: **Almandine + Phlogopite = Pyrope + Annite**. Subsequent work has refined this thermometer, by expanding the effective temperature range of the thermometer and taking into account the effect of elements such as Ti and Al^{VI} in biotite and Ca and Mn in garnet. Accordingly, a number of different calibrations now exist for this thermometer. The calibration by Bhattacharya et al. (1992) has been shown to be little affected by pressure variations, and has been used in this study, although results from other calibrations are presented for comparison (Table 3-7). Temperatures have been calculated at pressures of both 40 and 10 kbar for samples 25-1-10 and 3-1-10.

Analyses from the rim of garnets at 40 Kbar in sample 25-1-10 yield temperatures between 630 and 740 ºC, with an average of 671 ºC. In sample 3-1-10, the average from the same setting is 608 ºC, with a narrower range of 563 – 628 ºC. All analyses in sample 3-1-10 fall within this range irrespective of petrological setting. In both samples, inclusions of biotite within garnet yield lower temperatures than garnet rim analyses, as expected from the effects of diffusion between biotite inclusions and garnet.

A

			B92-HW	B92-GS	Dasg91	FS78	HS82	PL83	T76	HL77
3-1-10, p = 40 kbar	rim (n = 10)	average	608.5	604.3	726.1	729.3	747.9	686.3	859.9	707.3
		max	628.3	627.8	763.0	759.5	779.3	702.1	886.0	727.3
		min	563.5	553.7	681.4	652.1	672.0	645.2	792.6	655.5
	inclusion (n = 6)	average	606.9	613.5	722.1	706.0	725.4	674.3	839.9	692.0
		max	624.5	629.2	755.1	739.4	761.8	691.9	868.9	714.3
		min	593.3	599.1	689.3	679.1	699.2	660.0	816.5	674.0
	matrix	**average**	**678**	**684**	**842**	**852**	**870**	**747**	**963**	**786**
3-1-10, p = 10 kbar	rim (n = 10)	average	587.4	576.9	584.1	613.0	633.4	604.7	643.5	605.7
		max	606.7	599.5	617.5	639.7	661.5	619.2	664.6	623.7
		min	543.7	528.3	548.8	544.8	566.3	567.1	589.1	559.3
	Inclusion (n = 6)	average	586.2	586.7	583.2	592.4	613.6	593.8	627.4	592.1
		max	603.3	601.6	611.7	621.9	646.5	609.8	650.8	612.0
		min	573.0	573.1	554.0	568.6	589.8	580.7	608.5	575.9
	matrix	**average**	**655**	**653**	**684**	**722**	**742**	**660**	**727**	**676**

B			B92-HW	B92-GS	Dasg91	FS78	HS82	PL83	T76	HL77
25-1-10, p = 40 kbar	rim (n = 20)	average	671.3	689.1	882.1	812.4	835.0	727.6	929.7	760.4
		max	741.3	757.3	1055.0	970.2	992.9	799.2	1056.0	854.8
		min	630.1	649.7	802.5	730.9	747.6	687.5	861.6	708.7
	inclusion (n = 3)	average	639.4	659.2	819.4	747.0	766.6	695.1	874.8	718.6
		max	662.8	680.8	862.8	795.8	816.0	720.1	916.5	750.5
		min	603.0	625.2	746.8	674.4	690.8	657.5	812.4	670.8
25-1-10, p = 10 kbar	rim (n = 20)	average	649.0	659.6	729.0	686.4	711.6	642.5	700.0	653.4
		max	716.7	723.7	881.2	826.0	852.0	708.1	802.2	738.0
		min	608.9	622.2	659.2	614.4	632.7	605.8	644.9	607.0
	inclusion (n = 3)	average	618.1	631.3	675.0	628.6	650.3	612.8	655.6	615.9
		max	640.7	651.7	711.9	671.8	694.2	635.7	689.3	644.5
		min	582.7	599.2	612.2	564.5	582.3	578.4	605.1	573.0

Table 3-7: A: Garnet-biotite thermometry results from sample 3-1-10, B: results from sample 25-1-10. Rim: Temperatures calculated using Garnet and Biotite pairs at the rims of crystals, inclusion: temperatures calculated using biotite inclusions in garnet and neighbouring garnet composition, matrix: temperatures calculated using average garnet core and matrix biotite composition, B92: Bhattacharya et al. (1992) , Das91: Dasgupta et al. (1991), FS78: Ferry and Spear (1978), HS82: Hodges and Spear (1982), PL83: Perchuk and Lavrent'Eva (1983), T76: Thompson (1976), HL77: Holdaway and Lee (1977)

Calculated temperatures using garnet-biotite pairs are likely blocking temperatures, owing to the effects of retrograde diffusion at the rims of garnet. As such, the average core of garnet compositions, combined with matrix biotite not in contact with garnet was used to calculate temperatures for sample 3-1-10. All calibrations yielded higher temperatures, closer to the range of values determined using the Zr in rutile thermometer. This calculation was not possible in sample 25-1-10, owing to the lack of matrix biotite not in equilibrium with garnet.

3.6.4 Geobarometry

Constraining peak pressure for the metapelites has proved to be problematic. The diverse mineral assemblage and uncertainty surrounding co-existing mineral phases questions the applicability of continuous net transfer equilibria barometers, such as GASP (garnet – Al_2SiO_5-quartz-plagioclase) and GRAIL (garnet-rutile- Al_2SiO_5-ilmenite-quartz) to these samples. Previous studies have reported pressures of 12-14 kbar for Chepelare metapelite samples, significantly below the peak pressures suggested by the microdiamond inclusion.

Studies have attempted to use phengite chemistry to place geobarometric constraints on pressures experienced. The Si content of phengite has been shown to increase with increasing pressure, although absolute values are dependent on the both the composition of the sample and the equilibrium assemblage. As such, it has not been calibrated as a barometer. Models produced for the assemblage, garnet + kyanite + phengite + quartz (the peak assemblage inferred from petrological observations) do however suggest that phengite with Si a.fu > 3.5 formed at pressures > 30 kbar (Massonne and Szpurka, 1997). Accordingly, the Si content of phengite in sample 3-1-10 could indicate UHP conditions.

The Ti content of phengite has been proposed as a single element barometer suitable for samples that experienced UHP conditions based on the equilibrium $^{VI}Ti^{IV}Al–^{VI}Al^{IV}Si$ exchange in muscovite and phengite in equilibrium with rutile and quartz/coesite (Auzanneau et al., 2010). The pressure dependence of this exchange has since been questioned (Chambers and Kohn, 2012), and results of this study indicate that the most phengitic muscovite crystals do not contain enough Ti to be suitable for geobarometry using the Auzanneau et al. (2010) calibration.

3.7 Whole Rock Geochemistry

The major elemental concentrations of three samples, and trace elemental concentrations of four samples from the vicinity of Chepelare were analysed. Results are presented in Table 3-8. These samples are representative of the biotite and quartz rich matrix end members described in section 3.4. On a chondrite normalised REE diagram (Figure 3-14), all samples display strong LREE enrichment, and a relatively flat HREE profile, with a slight negative Eu anomaly. A plot of selected elements normalised to the GLOSS reference model for subducted sediment (Plank and Langmuir, 1998) is presented in Figure 3-15. The GLOSS reference model is predominantly composed of terrigenous material, with a small biogenic component (approximately 17%). The composition is therefore akin to that of upper continental crust, and consequently is not a true representation of the protolith for the metapelites. Normalisation of these samples to GLOSS does however effectively distinguish elemental variations between samples. Although all samples exhibit general enrichment relative to GLOSS, strong depletions in Ca, Na, Sr, Mn, Dy and to a lesser extent Si and Ba are observed. Cs, Rb and K display widespread variation between all samples.

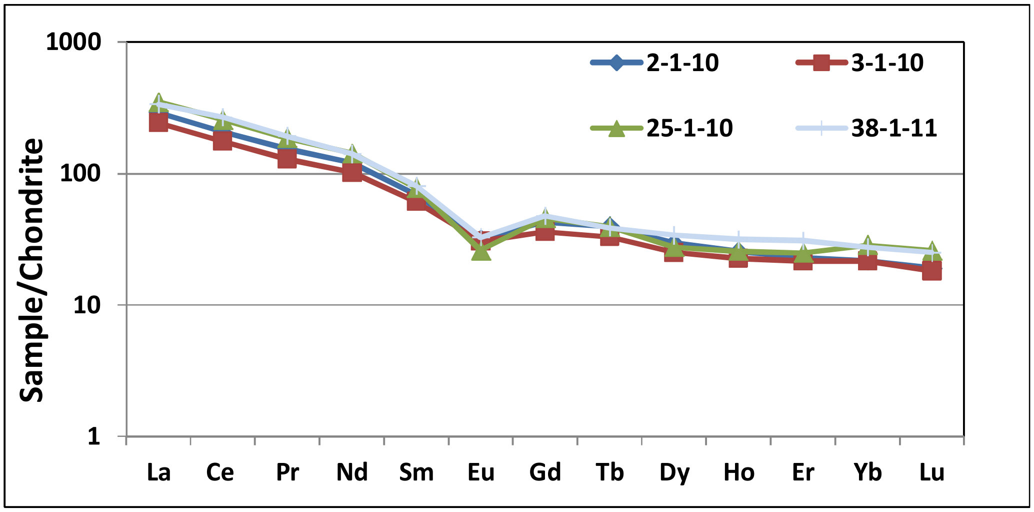

Figure 3-14: Chondrite normalised REE diagram. Sample is normalised to Boynton (1985) values.

		2-1-10	3-1-10	25-1-10	38-1-11
ICP-AES (Wt%)	**SiO_2**	48.71	52.05	49.41	-
	Al_2O_3	28.18	24.11	27.18	-
	FeO	12.89	11.03	16.18	-
	MgO	2.94	2.49	3.45	-
	MnO	0.11	0.13	0.23	-
	CaO	0.41	0.31	0.89	-
	K_2O	3.54	3.57	1.33	-
	Na_2O	0.31	0.09	0.17	-
	TiO_2	1.49	1.24	1.19	-
	P2O5	0.11	0.12	0.13	-
ICP-AES (ppm)	**Li**	13.33	59.89	14.46	21.01*
	Sc	24.99	25.19	30.59	14.77*
	Tl	0.76*	0.97*	0.38*	-
	V	130.41	148.86	85.33	129.66*
	Cr	78.19	94.18	62.14	96.09*
	Co	27.72	29.30	24.38	26.35*
	Ni	64.28	68.94	48.90	71.44*
	Cu	34.45	32.97	29.00	42.97*
	Zn	141.90	154.50	143.02	99.46*
	Rb	175.65*	193.49*	56.75*	13.39*
	Sr	66.03	14.84	20.28	170.76*
	Y	54.65	47.79	53.40	29.20*
	Mg #	0.19	0.18	0.18	

		2-1-10	3-1-10	25-1-10	38-1-11
	Zr	213.06	184.10	192.79	1.82*
	Nb*	36.66*	26.77*	28.96*	0.28*
	Cs*	1.49*	7.92*	2.45*	0.05*
	Ba	685.55	591.44	212.11	523.40*
ICP-MS (ppm)	**La**	89.94	75.21	108.09	40.42
	Ce	166.21	141.21	206.95	86.96
	Pr	18.66	15.67	22.66	9.92
	Nd	71.87	60.70	85.42	37.18
	Sm	13.43	11.87	15.08	7.40
	Eu	2.32	2.25	1.91	1.63
	Gd	11.13	9.29	11.84	5.79
	Tb	1.87	1.56	1.86	0.84
	Dy	9.52	8.03	8.87	4.94
	Ho	1.83	1.62	1.84	1.04
	Er	4.84	4.51	5.21	3.06
	Tm	0.72	0.68	0.86	2.98
	Yb	4.53	4.51	5.95	0.45
	Lu	0.61	0.59	0.83	0.07
	Hf	5.79	5.07	5.17	0.04
	Ta	2.62	1.95	2.60	12.17
	Th	30.90	26.19	42.06	11.44
	U	3.18	3.27	3.06	1.60

Table 3-8: Whole rock ICP-AES and ICP-MS measurements for kyanite garnet schist units from the Central Rhodope Mts. in the vicinity of chepelare . * highlights measurements made via ICP-MS

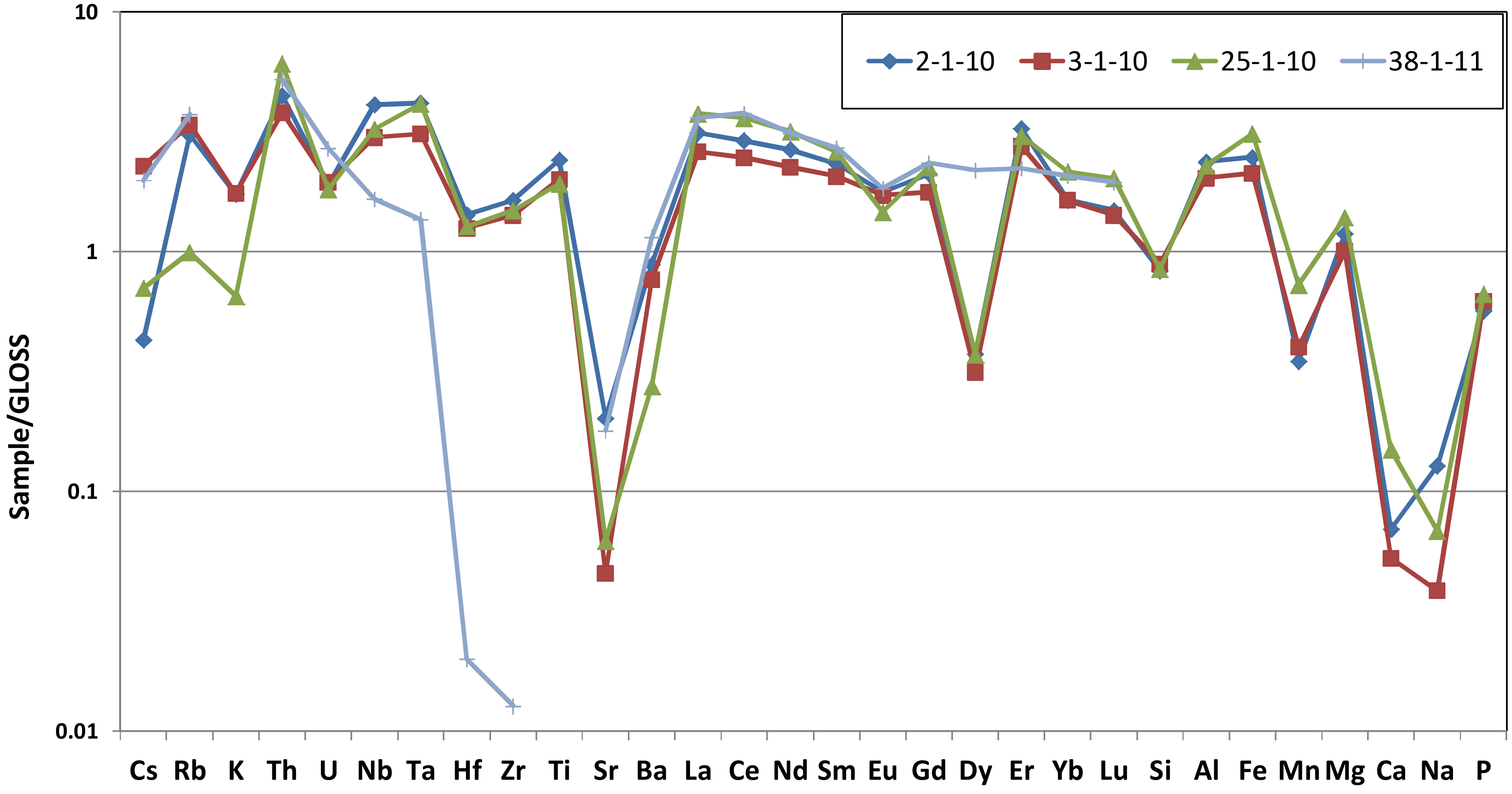

Figure 3-15: GLOSS normalised kyanite garnet schist samples from the Central Rhodope Mts. GLOSS normalsing values from Plank and Langmuir (1998)

3.8 The Eastern Rhodope metapelites

To facilitate comparisons between metapelites from the Eastern and Central Rhodope Mts, a preliminary study was conducted on metapelites from the Bulgarian part of the Eastern Rhodope Mts, in the vicinity of the town of Krumovgrad. Three samples were collected from the northern flank of the Kesebir dome, within the upper high grade basement unit. All were heavily migmatised, with abundant quartz and plagioclase throughout samples. Sample 11-1-11 was the only kyanite bearing sample, and as such was thought most likely to preserve remnants of the HP assemblage. This sample was therefore characterised petrographically and whole rock trace element concentrations were analysed.

Sample 11-1-11 does not fall into any of the petrological categories discussed for the Central Rhodope metapelites. The sample is very heterogeneous, with biotite, garnet and kyanite largely restricted to distinct zones within the sample (Figure 3-16a). The remainder of the matrix is predominantly large crystals (> 500 µm in diameter) of plagioclase and quartz (Figure 3-16b,c,d,e). Garnets are heavily fractured and retrogressed, ranging in size from ~ 50 µm – 1mm (Figure 3-16b,c,d,e). The majority of crystals are inclusion poor (Figure 3-16b,e), but examples of rutile and quartz exsolution (as described in the Chepelare samples) are seen (Figure 3-16d). Where present, inclusions are not restricted to specific garnet zones. In Figure 3-16d inclusions are restricted to the core, but in numerous examples pockets of inclusions are seen at the rims of crystals (Figure 3-16e). It is not possible to delineate two distinct garnet populations.

Biotite is prevalent, closely associated with garnet and kyanite, but preserves no preferred orientation (Figure 3-16c). Kyanite crystals are largely elongated in the same orientation, heavily retrogressed and exhibit no evidence of kink banding or undulose extinction. Quartz and plagioclase are pervasive across the section. These crystals are well formed, and often contain inclusions of biotite, and surround small fragments of heavily retrogressed kyanite and garnet crystals (Figure 3-16f).

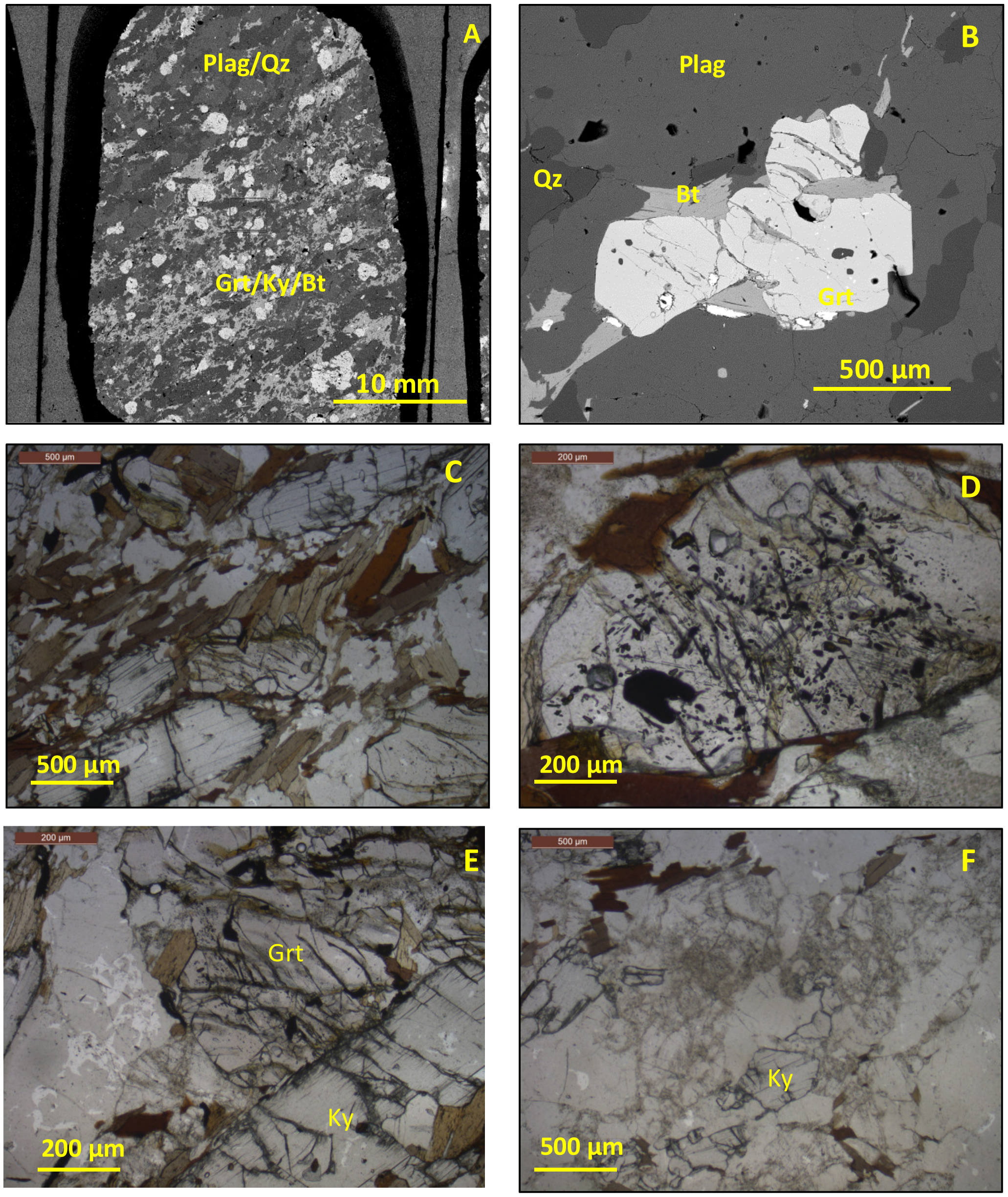

Figure 3-16: A: Backscatter montage of sample 11-1-11 highlighting the quartz and plagioclase rich areas, B: Heavily retrogressed garnet crystal surrounded by plagioclase and quartz crystals, C: Kyanite and garnet crystals found in association with biotite and quartz, D: Small inclusion rich garnet with distinctive rutile exsolution in core, E: Large, well-formed kyanite crystal alongside small, fractured, garnet crystal with inclusions concentrated at the crystal rim, F: Heavily retrogressed kyanite surrounded by large plagioclase and quartz crystals.

Bulk rock trace element concentrations of sample 11-1-11 are presented in Table 3-9**,** and a plot of this sample normalised to the GLOSS reference material is presented in Figure 3-17**.** Three additional metapelite analyses from the Greek part of the Eastern Rhodope Mts, previously reported in (Cornelius, 2008), are plotted for comparison. Unlike the three samples from the Greek Rhodope Mts., widespread deviation from GLOSS is observed for sample 11-1-11, with large depletions of Cs, Rb, Nb and Ta. The REE all exhibit concentrations similar to GLOSS. Sr concentrations are the closest to GLOSS of all samples analysed in this study.

Sample 11-1-11					
Element	**Conc. (ppm)**	**Element**	**Conc. (ppm)**	**Element**	**Conc. (ppm)**
Li	49.4	**Zr**	1.7	**Tb**	1.8
Sc	42.8	**Nb**	14.8	**Dy**	10.9
V	115.0	**Cs**	6.9	**Ho**	2.3
Cr	99.1	**Ba**	889.2	**Er**	6.5
Co	58.1	**La**	104.3	**Tm**	5.7
Ni	118.1	**Ce**	216.2	**Yb**	0.8
Cu	130.0	**Pr**	23.4	**Lu**	0.1
Zn	190.0	**Nd**	84.2	**Hf**	0.9
Rb	214.0	**Sm**	15.7	**Ta**	26.6
Sr	58.5	**Eu**	2.4	**Th**	36.0
Y	63.4	**Gd**	12.3	**U**	4.5

Table 3-9: Whole rock trace elemental data measured for sample 11-1-11

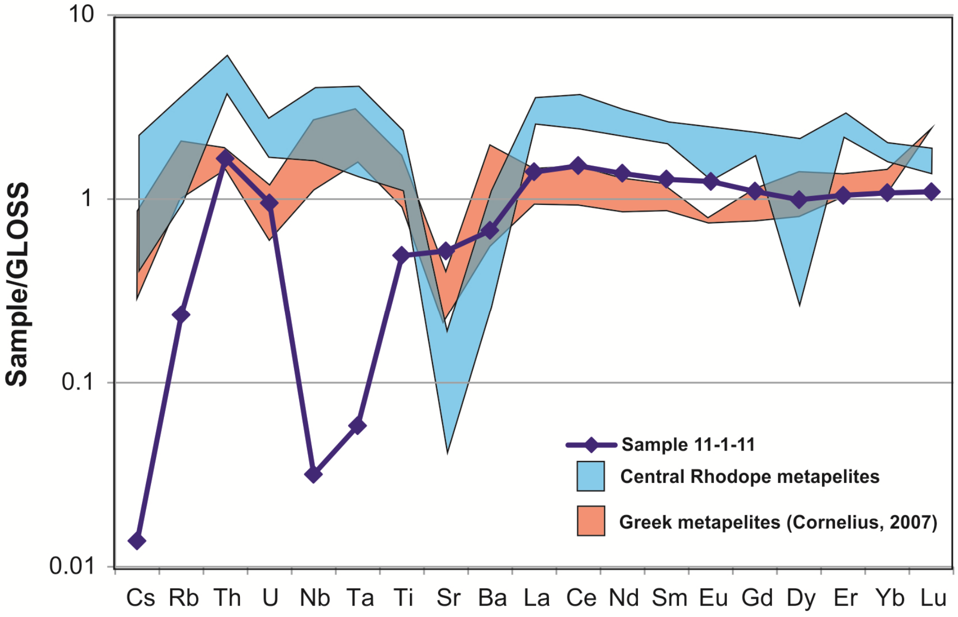

Figure 3-17: Selected trace elements from sample 11-1-11 normalised to GLOSS (Plank and Langmuir, 1998). Blue field: GLOSS normalised profiles for Central Rhodope metapelites, Red field: GLOSS normalised profiles for published UHP metapelites from the Greek Rhodope Mts. from Cornelius (2008)

3.9 Discussion

3.9.1 Protolith and Peak metamorphic conditions

On the basis of K:Na, Al:Mg and Fe:Ca ratios these samples have an illite rich protolith (Gaudette et al., 1966), such as a continental shelf clay. Little of the prograde metamorphic growth history is preserved, however textural observations and inclusions within garnet indicate a common high pressure mineral assemblage of garnet + kyanite + phengite +

quartz + rutile for all samples. This peak pressure assemblage is widely recognised in UHP metapelites across the RM (Mposkos et al., 2010, Mposkos and Liati, 1993, Schmidt et al., 2010), representing a minimum of upper amphibolite metamorphic conditions, with pressures > 18 kbar (Bucher and Grapes, 2011). Diamond inclusion in almandine rich garnets from across the RM however indicate that metapelites in this region experienced pressures in excess of 3.5 GPa.

Pseudosection modelling has previously suggested that this assemblage does not represent the true UHP assemblage, owing to the lack of expected clinopyroxene and coesite under UHP conditions (Schmidt et al., 2010). Instead, the observed assemblage is proposed to represent either portions of continental crust that experienced UHP conditions under metastable condition, or is the product of a HP metamorphic overprint event which obliterated the peak metamorphic record. The large deviations between samples relative to GLOSS reported in this study (Figure 3-15 & Figure 3-17) demonstrate the complex open system behaviour experienced by this suite of metapelites samples. As such, reconstructing an effective bulk rock composition is problematic, and it is unsurprising that the peak assemblage modelled by Schmidt et al. (2010) does not agree with petrographic observations.

As discussed in chapter 2, a common link between metapelites samples of the upper high grade basement has been proposed for the NSZ and CSZ samples on the basis of common lithological and stratigraphic observations between the two areas (Jahn-Awe et al., 2010, Mposkos et al., 2010, Nagel et al., 2011, Turpaud and Reischmann, 2010). This new microdiamond discovery adds credence to this proposal. Implications of this new discovery, combined with new garnet geochronology data constraining the timing of the UHP metamorphic event presented in chapter 5 will be discussed in chapter 6.

3.9.2 Partial melting of metapelites across the RM

The widespread occurance of quartzofeldspathic material in the matrix of metapelite samples, commonly observed cross cutting the pervasive biotite foliation, indicates that these samples have undergone exhumation related partial melting. This is reflected in the low bulk rock SiO_2 concentrations (ranging between 45 – 50 Wt%) , which are the same range as metapelites from Connemara, Western Ireland that are interpreted as restites following extensive melt removal under H_2O saturated upper amphibolite facies conditions (Yardley and Barber, 1991). Multiphase inclusions in garnet of kyanite + quartz + muscovite (Figure 3-3b) are further evidence of crystallisation following partial melting of phengite inclusions (Zheng et al., 2011), and have been previously reported from the Kimi complex of the Greek Rhodope Mts. complex (Mposkos et al., 2009).

In a previous study of metapelites from the Kimi complex, the lack of a negative Eu anomaly on chondrite normalise REE profiles was used as evidence for the addition of anatectic melt from an external source (Bauer et al., 2007). All samples analysed in this study do preserve a negative Eu anomaly, indicating that any leucocratic material originated from within the sample as a result of partial melting. Under water saturated conditions metapelites can melt via the following congruent melting reactions:

Qtz + Kfs + Pl + H2O = melt and **Ms + Qz + Pl + Bt + H2O = melt**

The relevance of water saturated melting reactions during subduction zone metamorphism has been questioned (Clemens and Vielzeuf, 1987), owing to the low porosity of high grade metamorphic rocks. Yardley and Barber (1991) however demonstrated in Connemara that with a supply of H_2O and heat from contemporaneous calc alkaline intrusions, widespread water saturated melting is feasible.

At low pressures muscovite breaks down in the presence of quartz via the following reactions:

1) **1Ms + 1 Ann + 3 Qtz = 1 Alm + 2 Kfs + 2 H_2O**
2) **Ms + Qtz = Kfs + Als + H_2O**

The subsequent water produced can then further fuel water saturated melting. Although water saturated melting can occur, most melt forming reactions in metapelites occur at higher pressures under granulite facies conditions via dehydration melting of muscovite and/or biotite via the following reactions

Ms + Pl + Qtz = Als + Kfs + melt, **Bt + Als + Qz = grt + kfs + melt** and **Bt+ Pl+ Als + Qtz = Grt +kfs + melt**

Biotite reactions have been shown to generate significantly more melt than muscovite breakdown, but generally occur at higher temperatures, in the range of 750 – 850 °C (Clemens and Vielzeuf, 1987). As a consequence of partial melting and melt extraction, the restite would have a higher modal abundance of the mafic phases aluminosilicate, biotite and garnet (Bucher and Grapes, 2011).

The widespread stability of phengite under UHP pressures limits the extent of prograde dehydration and melting reactions (Hermann, 2003). Much of the partial melting recorded in UHP rocks is instead believed to result from hydrate mineral breakdown where temperatures are > 800 °C during isothermal decompression. Evidence for this is seen at a number of UHP localities worldwide, with UHP samples from the Dabie-Sulu UHP belt and

Kokchetav massif both indicating a granulite facies overprint post-dating the peak metamorphic event (Zheng et al., 2011).

In metapelites under UHP conditions, phengite is the main host of Cs, Rb and Ba (Spandler and Pirard, 2013). Concentrations of Cs are highly varied in the samples analysed, ranging between 0.05 and 8ppm, indicative of varying degrees of phengite dehydration melting between samples. Although a positive correlation is obverved between Cs and Rb, (as expected by the experiments of Spandler and Pirard (2013)), larger Cs than Rb depletions are observed relative to GLOSS in all samples (Figure 3-15 & Figure 3-2). This fractionation could be the result of residual phengite preferentially retaining Rb, which is a better fit in the interlayer cation space owing to its ionic radius (Busigny et al., 2003, Hermann and Rubatto, 2009). This same fractionation process has however been documented in the presence of aqueous fluids (Melzer and Wunder, 2000), questioning the extent melting has on the observed profiles. The Cs concentrations and Cs/Rb ratios do correlate well with petrological observations; the two biotite end member samples have the highest Cs concentrations and low Cs/Rb values, indicating a smaller degree of mica dehydration melting in these samples. Alternatively, the variation relative to GLOSS is simply the result of variation in sample protolith, accounting for the widespread mineralogical variation observed between samples. This alternative view is not supported by large observed intersample variation, especially between the Central and Eastern Rhodope samples, and the same trends (albeit with no general enrichment) are observed when samples are normalised to Pelagic Clay frpm IODP hole 801 rather than the GLOSS refrence material.

Large depletions in Ca, Na and Sr relative to GLOSS are seen in all of the Central Rhodope metapelites samples, indicating the likely removal of plagioclase feldspar from these samples as a result of partial melting. Cs and Sr are both highly incompatible elements, and experimental studies have recognised a strong correlation between these two elements in the melt if widespread partial melting occurs (Hermann and Rubatto, 2009). No correlation is observed between Cs and Sr in any of the samples analysed, indicating that although biotite and phengite dehydration melting has occurred upon exhumation (to varying degrees), a prior melting event could also have occurred, unless the Sr concentrations are a function of either the protolith composition or hydrothermal alteration. A prior melting event would explain the phaneritic “museum” samples, with no observed leucocratic material (they would essentially be restites prior to exhumation) and could act as the required trigger for exhumation. The source of water required for this earlier melting is hard to explain.

Sample 11-1-11 from the Eastern Rhodope Mts. is the only sample to exhibit large depletions in Nb and Ta relative to GLOSS, with an increased Nb depletion relative to Ta. Rutile is the major host of these two phases in metapelites (Spandler and Pirard, 2013). Although often viewed as a refractory insoluble phase, solubility is greatly increased in the presence of hydrous silicate melts (Dickinson Jr and Hess, 1985), and is highly temperature dependent (Hayden and Watson, 2007). Experimental studies have indicated residual rutile remaining in the sample will preferentially fractionate Ta over Nb (Hermann and Rubatto, 2009), accounting for the observed trend on Figure 3-17**.** This suggests that sample 11-1-11 experienced either a higher degree of metamorphism, or a subsequent high temperature melting event, which is in keeping with the increased amount of leucocratic material observed in this sample (section 3.8)**.**

When compared to existing published data on Greek metapelites (Cornelius, 2008), the observed trends are not consistent. SiO_2 concentrations from these samples are all consistently higher, indicating lower degrees of partial melting in-keeping with the higher concentrations of Na, Ca and Sr relative to the Chepelare samples. The Cs concentrations are however not as high as the biotite rich samples from Chepelare, suggesting either some degree of partial melting, or variations in the original protolith chemistry of samples. Ultimately a lot still remains unknown about the behaviour of trace elements during partial melting and interaction with aqueous fluids during subduction zone metamorphism (Zheng et al., 2011). The petrological variations observed between samples do appear to reflect contrasting melting histories between samples, but it is difficult to place constraints on the exact cause of melting, or when in the P-T path melting occurred

3.9.3 Implications of observations for P-T evolution of RM metapelites

A previous study of metapelites from the Greek portion of the RM reported petrological evidence for multiple garnet and kyanite populations related to distinct HP metamorphic events (Mposkos et al., 2010). Although the euhedral, fracture free, inclusion poor garnet zones identified in the quartz rich sample 27-1-10 (Figure 3-4**)** could represent a later stage of garnet growth, this is rare and not widely recognised across samples. The lack of contrasting inclusion populations and the uniform garnet chemistry within samples indicates one garnet porphyroblast population and correspondingly one (U)HP garnet forming metamorphic event.

The large variation in pyrope content observed between samples can be attributed to contrasting temperatures experienced between samples. In experimental studies investigating metapelitic garnet compostion at sub arc depths pyrope content increased with increasing temperature, coupled with a slight decrease in Grossular content (Hermann and Spandler, 2008). This explains the apparent correlation between pyrope content and amount of matrix biotite, as the biotite rich samples underwent less partial melting than their quartz rich counterparts. This could explain the preservation of microdiamond in garnets with the lowest pyrope content; the decreased amount of partial melting aided preservation of the diamond.

Much of the post peak metamorphic history has been destroyed as a result of the partial melting. The two distinct populations of white mica identified in sample 3-1-10 can be correlated with different stages of the samples history. The high Si, phengitic white mica are remnants of prograde metamorphism/peak metamorphic event. This is reflected in the low Na/(Na+K) ratios, which although not calibrated as a barometer is indicative of formation under high pressures (Guidotti and Sassi, 2002). Retrograde muscovite can form from aluminosilicate when in contact with a Ks feldspar ruch melt via the reaction: **Musc + Qz = Al_2SiO_5 + Kspar + Liquid** (Spear et al., 1999). This would explain the higher Ti contents observed in this population, with Ti concentration an indicator of metamorphic grade of muscovite formation (Guidotti and Sassi, 2002). It is difficult to link these two populations to textural settings, with both populations found within the matrix and as inclusions in garnet.

Coronas of retrograde biotite surrounding garnet porphyroblasts have likely formed via the reaction: **Grt + Musc = Al_2SiO_5 + Bt + Qz**, explaining the widespread occurrence of fibrolitic silimanite in close association with biotite and quartz throughout the matrix of samples. The absence of staurolite in samples indicates a “hot” exhumation path at temperatures exceeding the stability field of staurolite, in-keeping with the evidence of phengite and biotite dehydration melting as a result of isothermal decompression.

3.10 Chapter Summary

- There is compelling evidence for a new UHP locality in the vicinity of the town of Chepelare, in the Central Rhodope Mts.
- Like all previous microdiamond discoveries in the region, all evidence of UHP conditions is restricted to inclusions within almandine rich garnets from metapelites.
- These samples have a complicated metamorphic history. Very little of the prograde history is preserved, and there is evidence for variable degrees of partial melting between samples.

- The relationship with existing UHP localities across the massif is unclear, and will be discussed further with reference to timings of events in chapter 5.

Chapter 4 : Petrogenesis of Metabasic units of the Rhodope Massif

4.1 Introduction

Amphibolites and eclogites are widespread throughout the Rhodope Massif, with outcrops being reported from a number of locations in both the upper and lower high grade basement unit (Mposkos et al., 2012, Liati and Mposkos, 1990). Given the complex polymetamorphic history of the RM (Liati et al., 2011) this is unsurprising, but does create serious difficulties when attempting to correlate units across the RM. A number of studies have utilised both bulk rock geochemistry and geochronology to place constraints on the protolith and metamorphic history of these metabasic lithologies , but in many cases these yielded contradicting results (Bonev et al., 2006, Daieva et al., 2007, Georgieva et al., 2010, Haydoutov et al., 2004, Kirchenbaur et al., 2012, Kolcheva and Eskenazy, 1988). Consequently, the evolution of the Rhodope Massif remains unclear.

In this chapter I present a detailed petrographic and geochemical study of eclogites and amphibolites from the upper high grade basement of both the Central and Eastern Rhodope Mts. Particular attention has been paid to bulk rock trace element and radiogenic isotope geochemistry to constrain the protolith of units. These results have been incorporated with existing geochemical and geochronological datasets to unravel the complex history of these units, Identify differences between middle and upper allochthon units and discuss the implications for the evolution of the Rhodope Massif.

4.2 Analytical Techniques

Bulk rock major element concentrations of samples were measured using ICP-AES at Royal Holloway College, University of London following flux fusion with $LiBO_{2.}$ Bulk rock trace element concentrations were measured using ICP-MS at both Royal Holloway College, University of London (2011), and the Open University (2013). The 2011 samples were digested in a HF-$HClO_4$ mix, whereas the 2013 samples were digested in a HF-HNO_3 mix. Textures and particularly small mineral inclusions (<50 µm) were investigated at the University of Leeds on a FEI Quanta 650 FEG-ESEM. The chemical composition of the major rock forming minerals was determined via electron microprobe analysis at the University of Leeds, using a JEOL 8230 electron probe micro-analyser (EPMA). A range of analytical conditions were used, optimised for each target mineral. Spot sizes range between 1µm and 5µm, and an accelerating voltage of 15kV was used. Bulk rock Sr and Nd isotopic measurements were made using a TRITON thermal ionisation mass spectrometer at the

University of Leeds. Details of the sample preparation, analytical procedure and quality control measures can be found in appendix B.

4.3 Metabasic samples of the Central Rhodope Mts.

4.3.1 Overview of previous research

4.3.1.1 Metabasic samples from the Arda 2 Gneiss

Eclogites in the Central Rhodope Mts. were first identified in the Arda 2 gneiss (middle allochthon) of the upper high grade basement unit in the 1980's (Kolcheva and Eskenazy, 1988). In that study, bulk rock major and trace elemental data was used to infer a MORB like protolith, despite strong deviations from the typical N type MORB patterns. All samples exhibited strong LREE enrichment, which was interpreted as arising from a combination of migmatisation, (widespread evidence for which is seen in both eclogite samples and the host gneiss), and inheritance from the protolith. As such, the eclogites were classified as E or P type MORB, gravitating towards basalts with a more alkaline affinity. Subsequent studies have dated these eclogites as Neoproterozoic, with Lu-Hf garnet-omphacite dating yielded an age of 567.3 Ma (Savov et al., 2007), and U-Pb zircon dating yielding three distinct metamorphic growth zones at 560 Ma, 440 Ma and 265Ma, followed by a high grade metamorphic event at 38 Ma (Arkadakskiy et al., 2003).

Recent work has instead suggested an island arc origin for eclogites from within the upper high grade basement (Kirchenbaur et al., 2012). Of four samples analysed from across the Central Rhodope Mts. (including one from the Chepelare Shear Zone), three preserved negative Nb and Ta anomalies and unradiogenic Nd and Hf isotope signatures, which is inconsistent with a MORB protolith. The anomalous sample from the Kardzali unit (to the East of the Arda dome) was interpreted to have experienced a partial melting event earlier in the samples history, distorting the geochemical profile. On the basis of equilibrium assemblage diagrams modelled using the Theriak-Domino program, these samples were estimated to have experienced peak pressures in the region of 20 – 25 kbar, and temperatures > 600 °C.

Lu-Hf dating of these samples using garnet whole-rock pairs produced Eocene ages ranging between 42.8 and 44.6 Ma, with the exception of the anomalous Kardzali sample which yielded 126 Ma, and a Sm-Nd garnet–whole-rock- pyroxene age of 109 Ma (Kirchenbaur et al., 2012). The authors argue that these Eocene ages are not the result of a thermal resetting event, and are instead due to a distinct, short lived, HP Cenozoic subduction event. The Early Cretaceous age is harder to resolve, but is in keeping with the published 119 Ma age of a metagabbro unit from the Eastern Rhodope Mts. (Wawrzenitz and Mposkos, 1997).

The significance of these age populations will be discussed in chapter 5 alongside new geochronological data. The important observation is that on the basis of both geochemical and geochronological data there appears to be two distinct populations of eclogites in the Central Rhodope Mts. The extent of these populations and their relationship to the metabasic units of the Variegated Formation in the nearby Chepelare Shear Zone is unclear, and as such is one of the main motivations for this chapter.

4.3.1.2 Metabasic units from within the Variegated Formation (Chepelare Shear Zone)

Little work has been performed on Amphibolite units from the VF in the vicinity of Chepelare. Previous studies have attempted to draw correlations between amphibolites of the VF from the central and Eastern Rhodope Mts, highlighting a common boninitic/Island arc tholeite protolith for units across the RM (Daieva et al., 2007). This study however focused on samples from the Madan-Davidkovo antiform, ~80 km east of Chepelare, and the relationship to samples in the HP/UHP Chepelare Shear Zone is unclear. A recent preliminary study on a garnet amphibolite sample from within the Chepelare Shear Zone suggested a MORB protolith, alongside minimum P-T constraints of 12-14 kbars and 700 – 750 °C (Georgieva et al., 2010). As a result a common formation history with the Arda 2 metabasic units was tentatively suggested, although there is currently insufficient evidence to evaluate this claim.

4.3.2 Field sampling

In this study, a total of 29 metabasic samples were collected in the Central Rhodope Mts. in the vicinity of Chepelare. These have been divided into two groups, those from within the Arda 2 Gneiss, and those from the VF of the Chepelare Shear Zone. Sample locations can be found in appendix A.

4.3.2.1 Metabasic samples from Arda 2 gneiss

15 samples from within the gneiss of the Arda 2 subunit, north of the Chepelare Shear Zone were sampled. Although present throughout this unit, there is a larger concentration at the base directly above the Chepelare Shear Zone. All outcrops occur as boudins, wrapped by the pervasive foliation in the host gneiss (Figure 4-1a-d). These boudins range in size from less than 1m to greater than 10m in diameter. They are very hard and dense, often weathering proud of the host gneiss. Garnets, when present are always clear, ranging in size from < 1 mm to 6mm, in a uniformly green matrix largely dominated by amphibole. There is no evidence in any hand samples for the preservation of omphacite.

Samples have undergone variable degrees of retrogression, with migmatisation and segregation of garnets into distinct zones commonly observed.

Figure 4-1: A-D Field photographs of eclogite boudins outcropping north of the Chepelare Shear Zone within the Arda 2 Gneiss

4.3.2.2 Metabasic samples from within the Chepelare Shear Zone

14 metabasic samples from within the variegated formation of the CSZ were collected. They are found in close association with both metapelites and marbles, mapped as continuous sheets along the edge of the Arda dome in 2 km wide zone. Like the metapelites of chapter 3, direct contacts with surrounding units are often unclear or obscured. As such, it is difficult to ground truth the interpretation portrayed on the geological map of the area. Outcrops vary greatly in style from large pods that are heavily migmatised (Figure 4-2a,b) to units conformable with surrounding metapelites and marble. (Figure 4-2c). Garnet is clearly visible in some samples (Figure 4-2d), but only makes up a small proportion of most samples. The unclear boundaries of the Chepelare Shear Zone complicate distinguishing VF and Arda samples.

Figure 4-2, A and B: Migmatized amphibolite boudin within the VF, C: Amphibole outcrop conformable with overlying marble, D: Garnet bearing amphibolite from within the VF

4.3.3 Central Rhodope Mts. Petrology

4.3.3.1 Metabasic samples from the Arda 2 garnet gneiss

Four contrasting garnet morphologies are seen amongst the 11 Arda 2 garnet bearing metabasite samples. Small (<500 µm diameter), anhedral, and relatively inclusion poor garnet crystals are seen in 4 samples (Figure 4-3a,b), whilst a further 4 samples exhibit large (up to 4mm diameter), subhedral garnets with inclusions restricted to the cores of crystals (Figure 4-3c,d). In both of these subgroups garnets constitute 20-40% of the sample, and are almandine rich (Alm_{41-54}), although the larger crystals have a higher pyrope content (up to Pyp_{35}). The chemistry of these crystals is overviewed in detail in section 4.3.5.1.

In the large, inclusion rich garnets, inclusions are restricted to the cores of crystals. Quartz, amphibole and plagioclase inclusions are the most common, but omphacite (Figure 4-4a) and orientated needles of rutile (Figure 4-3d) are observed, alongside apatite, ilmenite and zircon. In sample 22-1-10, a quartz inclusion was found surrounded by distinct radial fracturing (Figure 4-4b). This phenomenon is often associated with the breakdown of coesite upon exhumation, but without the distinctive glassy rim is not definitive evidence for prior UHP conditions.

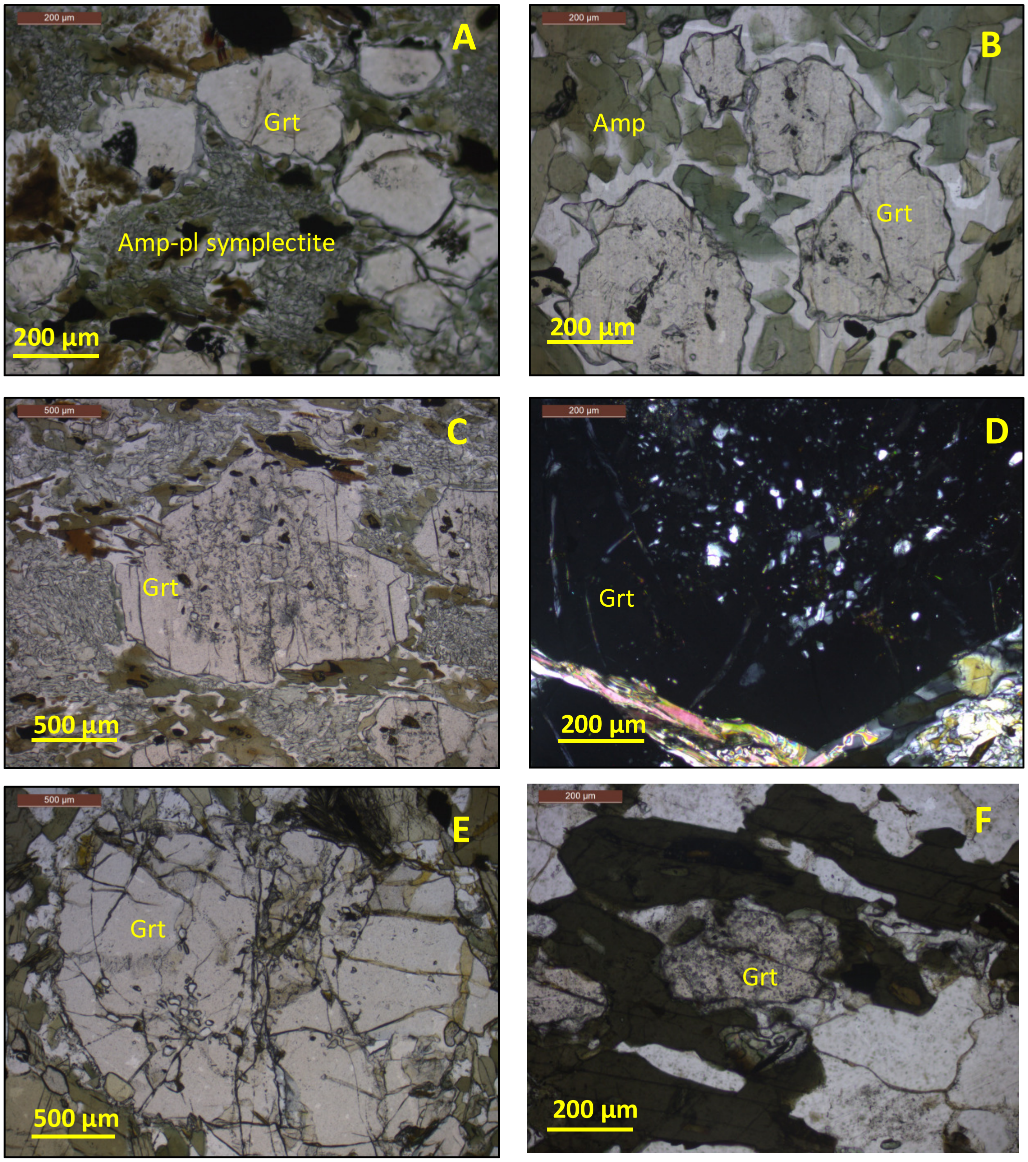

Figure 4-3: Photomicrographs of garnets and inclusions from Arda 2 metabasic samples .A: Small inclusion poor garnet hosted by amphibole-plagioclase symplectite (sample 22-1-10), B: Small inclusions poor garnets hosted by amphibole-plagioclase intergrowth (sample 31-1-11) C:Large inclusion rich garnet (sample 36-1-11), D: Quartz inlcusions and exsolved rutile needles in garnet (sample 36-1-11), E: Large resorbed inclusion poor garnet (sample 45-1-11), F: Heavily resorbed inclusion rich garnet (40-1-11)

Of the remaining samples, 1 contains large (up to 2mm diameter) inclusion poor garnets (Figure 4-3e), which constitute ~ 10 % of the sample. The remaining two contain only rare fragments of heavily retrogressed inclusion rich garnet (Figure 4-3f). Sample 45a-1-11 is unique among all samples studied from the Central Rhodope Mts., containing rare poikoblastic kyanite porphyroblasts alongside the garnet porphyroblasts (Figure 4-4c,d).

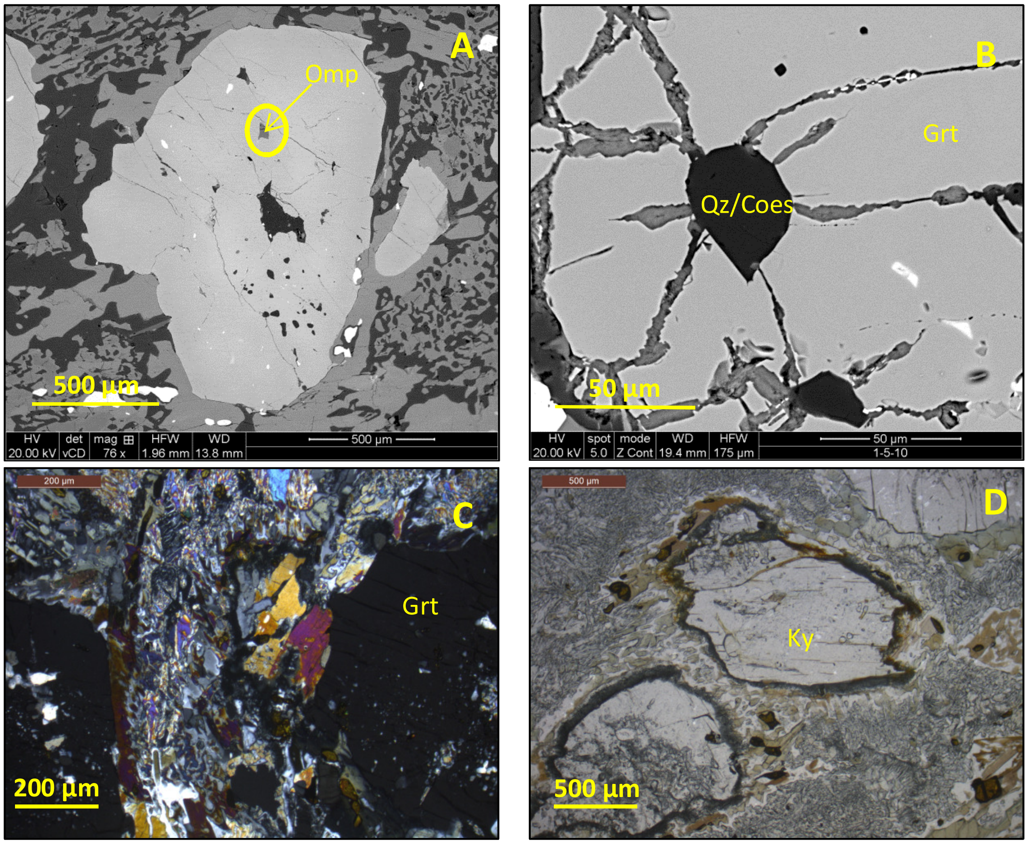

Figure 4-4: indicators of HP metamorphism in Arda 2 garnet bearing samples A: Omphacite inclusion in garnet from sample 36-1-11, B: Possible coesite inclusion from sample 22-1-10.C: Kyanite crystal in contact with garnet, sample 45a-1-11, D: Kyanite porphyroblasts in sample 45a-1-11

The matrix of all samples is composed of plagioclase, amphibole and diopside, although large differences are seen in sample textures. Most are symplectites of either amphibole and plagioclase or diopside and plagioclase, with variations in the scale of symplectic intergrowth observed between samples (Figure 4-3a,c,Figure 4-5b,d,f). Retrogression of amphibole to both chlorite and biotite is commonly observed Figure 4-5f), alongside extensive quartz veining (Figure 4-5e). Two samples (45-1-11 and 44-1-11) have granoblastic matrices composed of interlocking subhedral amphibole and plagioclase crystal, 100 – 500 µm in diameter (Figure 4-5a,c). No retrogression to biotite is seen in these samples.

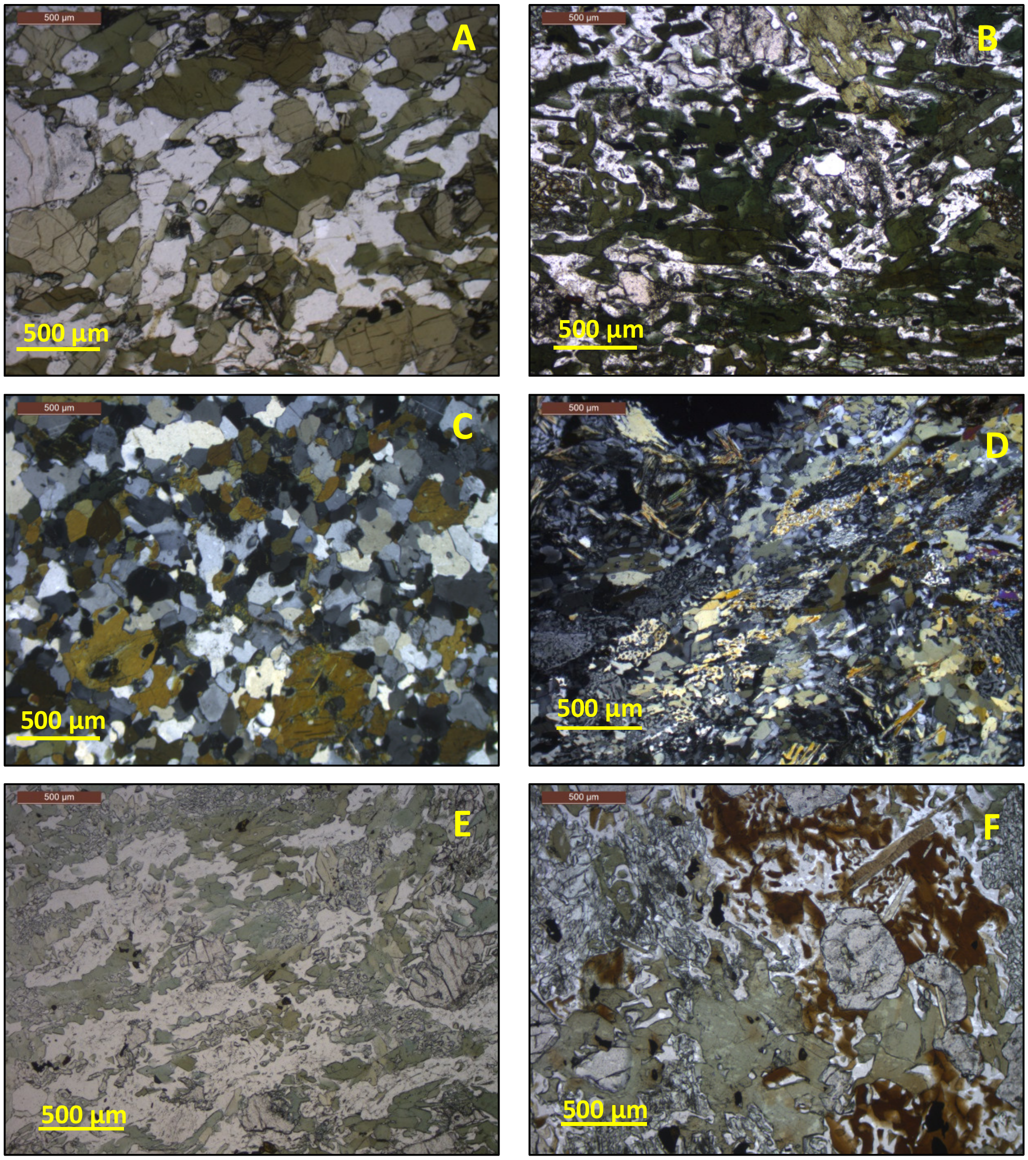

Figure 4-5: Photomicrographs of matrix of garnet bearing samples within the Arda gneiss of the Central Rhodope Mts. A: Large subhedral amphibole crystals (sample 45-1-11), B: Large resorbed elongated amphibole, with small garnet fragments (sample 23-1-10),C: : Granoblastic matrix of sample 44-1-11 composed of amphibole, plagioclase and quartz, D: Diopside rich symplectite from sample 12-1-13, E: Extensive quartz veining in sample 12-1-13,F: Biotite rich matrix in sample 36-1-11 . ,

4.3.3.1.1 Petrological evidence for Eclogite facies metamorphism

The assemblage garnet+amphibole+plagioclase is not characteristic for eclogite, as by definition, eclogite should have the assemblage garnet + omphacite, with no plagioclase present (Bucher and Grapes, 2011). The discovered omphacite inclusions in garnet (Jd$_{35-42}$(Figure 4-4a)), alongside the possible presence of coesite inclusions in garnet (Figure 4-4b) indicates that at least some of these samples were eclogites, with extensive retrogression through amphibolite and greenschist facies. The abundance of plagioclase – diopside symplectites, plagioclase-amphibole symplectites and amphibole rich areas can be explained through progressive hydration related retrograde metamorphism of omphacite, a phenomenon seen in a number of eclogite localities worldwide (Carswell, 1990). It is unclear whether variable degrees of exhumation related hydration is the sole cause for the inter-sample variation observed within these samples, or instead contrasting P-T histories and/or protoliths are contributing factors. Kyanite porphyroblasts in sample 45a-1-11(Figure 4-4c,d) indicate higher peak metamorphic temperatures than other samples, possibly forming as a result of anorthite breakdown under high pressure conditions.

4.3.3.2 Arda 2 non garnet bearing metabasic samples

Unlike the garnet bearing samples, significantly less variation is observed in this group. Amphibole, plagioclase and to a much lesser extent quartz are the main constituents of all samples, and variation is largely a function of grain size, and degree of deformation Amphibole ranges in size from ~ 2mm in the coarsest sample to ~ 100 µm in the finest (Figure 4-6a,b). Where present, quartz is largely restricted to either veins that cut through the sample, or in close association with biotite, forming intergrown pockets throughout the matrix (Figure 4-6d). In all, except sample 11-1-3, biotite and amphibole form a pervasive foliation throughout the matrix (Figure 4-6c).

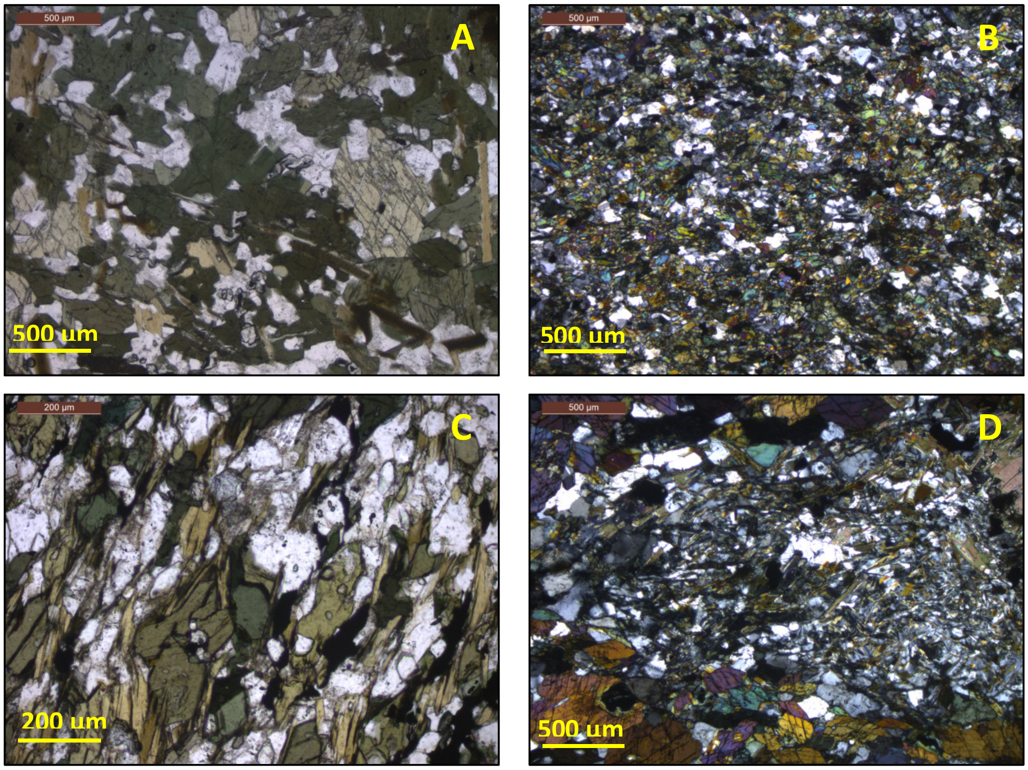

Figure 4-6 A: Garnet free amphibolite with large amphibole crystal from sample 36a-1-11, B: Fine grained amphibole and plagioclase from sample 11-1-13, C: Foliation defined by elongated amphibole crystals in sample 41-1-11, D: Pocket of intergrown biotiote and quartz in an otherwise granoblastic amphibolite, sample 3-1-13.

4.3.3.3 Garnet bearing metabasic samples from within the Chepelare Shear Zone

Like their Arda counterparts, widespread mineralogical and textural variation is seen amongst the four garnet amphibolite samples collected from the Variegated Formation. Sample 3-1-11 closely resembles many of the garnet amphibolites boudins found within the Arda gneiss (described in section 4.3.3.1), containing abundant small, inclusion free garnets, < 500 µm in diameter, often with a halo of plagioclase (Figure 4-7a,b). The matrix is predominantly amphibole and plagioclase, with small pockets of quartz (Figure 4-7a) and areas of symplectic intergrowth. Accessory titanite, ilmenite, apatite and magnetite are common. Sample 6-1-13 is similar, but with larger, well-formed amphibole crystals up to 3mm in diameter (Figure 4-7c) and epidote veins cross cutting the sample (Figure 4-7d).

Sample 1-1-11 contains little garnet. Although identified in the field and visible in hand specimen, no crystals were identified in the thin section. It is composed of interlocking crystals of amphibole, plagioclase and quartz 100 µm – 2mm in diameter, with no preferred orientation (Figure 4-7e). Titanite, apatite and magnetite are all common accessory minerals. The sample is cut by thick (~ 5mm) quartzofeldspathic veins, containing fragments of matrix amphibole/epidote, and quartz crystals that preserve evidence of dynamic recrystallisation (Figure 4-7f).

Sample 30a-1-11 is unique amongst the garnet bearing amphibolite samples, owing to the presence of calcite throughout the matrix closely associated with amphibole, plagioclase and epidote (Figure 4-7g). Only one, 4mm diameter garnet occurs within the thin section. This crystal appears different to all garnets observed in the RM, being large and anhedral with inclusions of plagioclase, calcite and zoisite but without the characteristic mass of small inclusions (<10 µm) commonly observed in this study (Figure 4-7h).

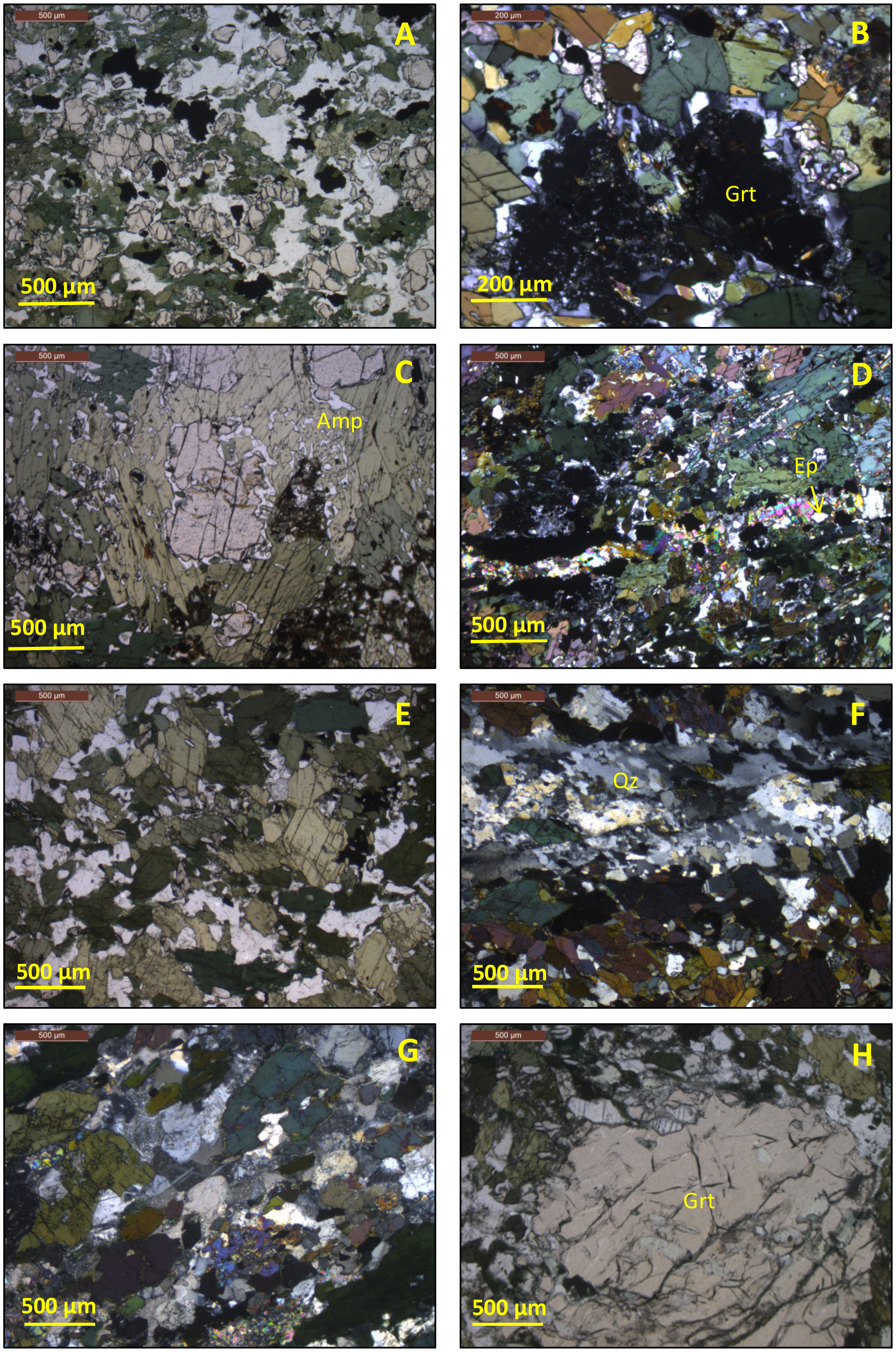

Figure 4-7: Photomicrographs of garnet bearing amphibolites from within the VF. A: Small inclusion free, resorbed garnets, sample 3-1-11, B: Close up of resorbed garnet with plagioclase halo, sample 6-1-13, C: Large euhedral amphibole crystals, sample 6-1-13, D: Epidote vein through amphibole rich matrix, sample 6-1-13, E: Interlocking amphibole crystals with no preferred orientation from sample 1-1-11, F: Quartz vein cross-cutting through sample 1-1-11, G: Calcite and epidote rich matrix, sample 30a-1-11, H: Heavily resorbed garnet with quartz and zoisite inclusions, sample 30a-1-11

4.3.3.4 Garnet free amphibolites within the Chepelare Shear Zone

This suite forms a diverse group within the Variegated Formation., but samples range from hornblendites composed entirely of interlocking amphibole crystals (Figure 4-8a) to amphibolites with varying proportions of amphibole and plagioclase (Figure 4-8b,c,d). Some samples have large amounts of epidote (Figure 4-8c), and contain veins of quartz and k-feldspar both following (Figure 4-8b) and cross cutting the foliation (Figure 4-8d).

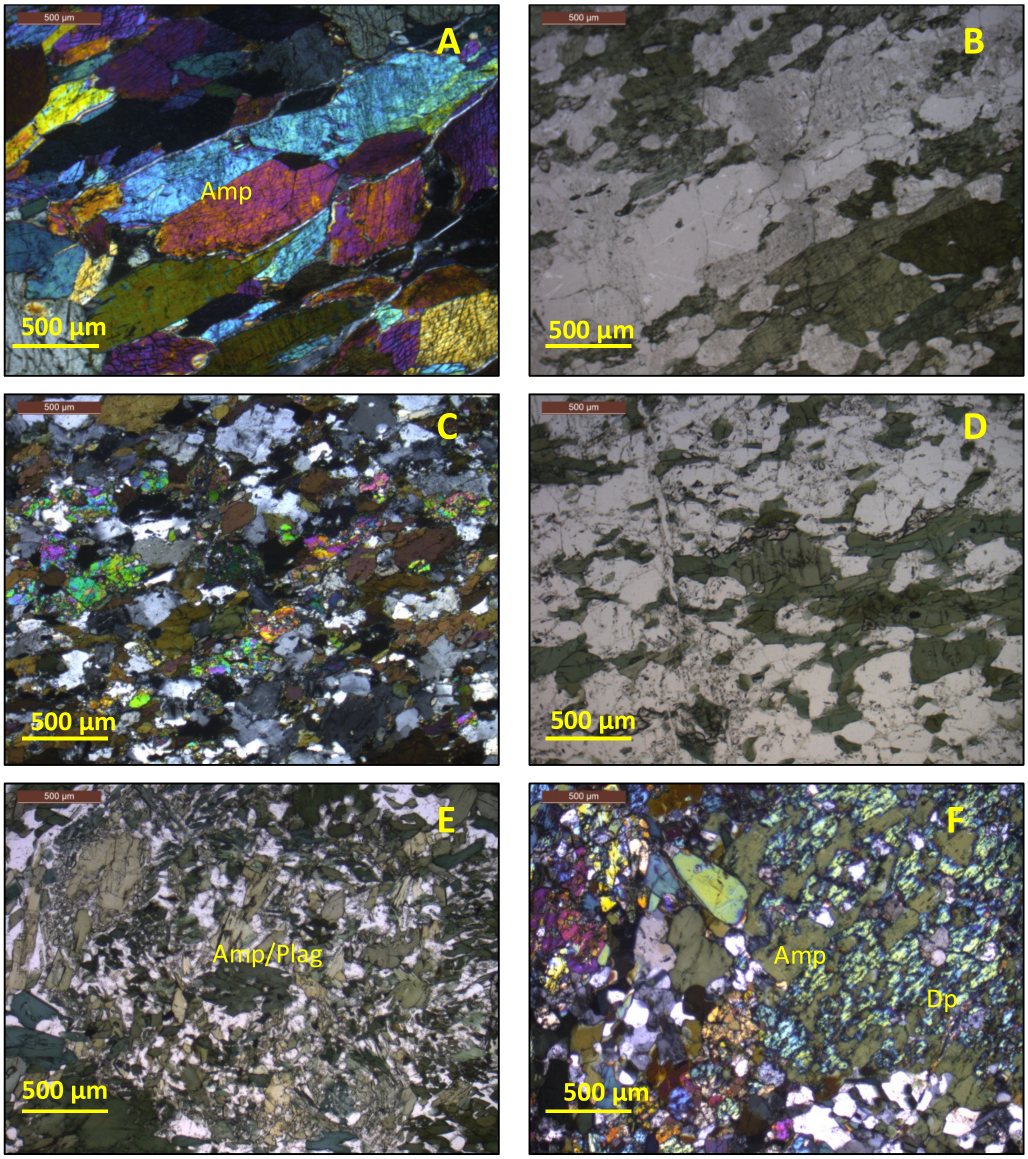

Figure 4-8: Photomicrographs of non-garnet bearing samples from the VF, in the vicinity of Chepelare. A: Interlocking amphibole crystals of sample 39-1-11, B: Elongated amphibole and plagioclase crystals with quartz vein following samples foliation, sample 9-1-13, C: epidote rich matrix of sample 2-1-3, D: Quartz vein cross cutting the foliation in sample 1-1-3, E: Plagioclase-amphibole intergrowth of sample 5-1-13, F: Epitaxial overgrowth of amphibole on diopside, sample 5-1-13.

Samples 34-1-11 and 5-1-13 contain distinctive pockets of amphibole-plagioclase intergrowths outlined by larger (up to 1mm in length) amphibole crystals, giving the appearance of a former porphyroblast that has undergone severe retrogression (Figure 4-8). These two samples also contain large amounts of diopside (30-40%), with the amphibole crystals occurring as epitaxial overgrowths on the pyroxene (Figure 4-8f).

4.3.4 Implications of petrographic observations

The study of the Arda 2 metabasic units indicates that at least some of the garnet bearing samples are prior eclogites that have undergone retrogression through amphibolite facies. Textural evidence in the non-garnet bearing samples suggests the presence of former garnet porphyroblasts, possibly reflecting more severe greenschist facies retrograde metamorphism. Garnet with rare omphacite inclusions and the matrix kyanite from sample 45a-1-11 are likely the only remnants of the peak metamorphic assemblage within these units. There is no clear evidence to suggest that the garnet bearing metabasic samples from the VF experienced eclogite facies metamorphism. The two samples which resemble the garnet bearing units of the Arda 2 gneiss do however have rare amphibole-plagioclase symplectites. The remaining samples are characterised by an increased greenschist facies overprint, and presence of calcite in sample 30a-1-11 suggests interaction with the adjacent marble units of the VF. Two of the garnet free samples exhibit textural evidence of former garnet porphyroblasts, which combined with the remnant diopside likely represents remnants of a previous, higher grade assemblage. No such evidence is seen in the other garnet free amphibolites.

4.3.5 Central Rhodope Mts. Mineral Chemistry

4.3.5.1 Garnet

The major element chemistry of garnets from 5 samples is presented in Table 4-1. 3 samples are from within the Arda 2 gneiss, and 2 are from within the VF of the CSZ. A graphical representation of the garnet composition is presented in Figure 4-9**.** Garnets from eclogite within the Arda unit are all almandine rich (Alm_{50-41}). A large range in pyrope content is observed between samples (Pyp_{35-17}), compensated by variations in almandine content. Limited variation in grossular content occurs ($Gross_{25-19}$). Samples 31-1-11 and 36a-1-11 preserve slight increases in pyrope content from core to rim, accompanied by a decrease in almandine content. In sample 45a-1-11 a slight increase in almandine content is observed from core to rim, which is offset by a decrease in grossular content.

Garnets from amphibolite within the VF are significantly more varied in major element chemistry than their Arda counterparts. Sample 3-1-11 has almandine rich garnets with significant pyrope content ($Alm_{55}Pyp_{20}Gross_{20}$), whereas sample 30a-1-11, although still almandine rich has a higher grossular content and lower pyrope conent ($Alm_{53}Pyp_{10}Gross_{28}$). This sample has the highest spessartine content of any analysed in this study (Sps_5). No core to rim variation is seen in either of the VF samples.

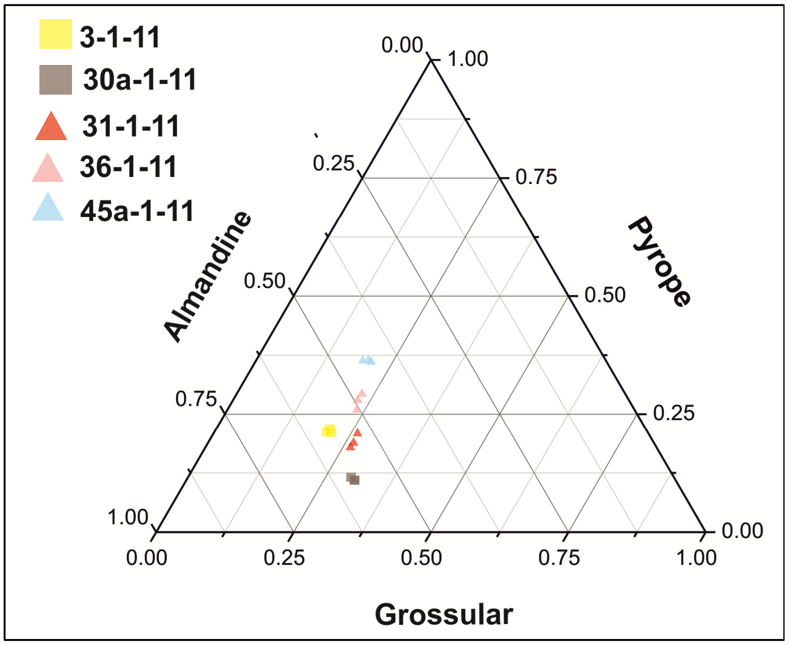

Figure 4-9: A graphical representation of garnet composition for metabasic samples from the Central Rhodope Mts. Square: Sample from VF, Triangle: Arda samples.

4.3.5.2 Amphibole

The major element chemistry of amphibole was measured for 8 samples; 6 from within the VF, and 2 from within the Arda gneiss. A summary of all results is presented in Table 4-2. Following the Leake et al. (1997) classification scheme, all amphiboles analysed are calcic, with $Ca_B \geq 1.5$. All analyses are plotted on the relevant classification diagrams (Figure 4-10a,b), with the division based on the $(Na+K)_A$ content of each analysis.

The majority of samples cluster along the tschermakite - magnesiohornblende boundary. 3 samples, all from the VF (1-1-11, 30-1-11 and 9-1-13) record a broader spectrum of compositions, extending throughout the magnesiohornblende field, and for 9-1-13 into the actinolite field. 4 samples (2 from Arda, 2 from VF) have amphibole with a sufficiently high $(Na+K)_A$ value to plot on the second classification diagram, although sample 30a-1-11 is the only sample in which all analyses meet this criteria. Samples 30-1-11, 30a-1-11 and 31-1-11 have ${}^{VI}Al > Fe^{3+}$, and are therefore all pargasite – ferropargasite, whereas sample 41-1-11 is predominantly magnesiohastingite. A clear positive trend is seen on plots of $(Na+K)_A$ vs A_{IIV} and Ti vs Al^{IV} (Figure 4-11), likely reflecting the broad range of amphibole compositions seen in Figure 4-10, the result of edenite and tschemrakite substitution reactions which vary as a function of metamorphic grade (Spear, 1993).

A		31-1-11			36-1-11			45a-1-11		
		Rim	Mid	Core	Rim	Mid	Core	Rim	Mid	Core
Oxide wt%, O by stoichiometry	SiO_2	38.49	38.45	38.36	38.93	38.82	38.79	39.63	39.73	39.80
	TiO_2	0.23	0.57	0.09	0.06	0.06	0.09	0.06	0.21	0.08
	Al_2O_3	21.10	21.10	20.88	21.28	21.47	21.31	21.86	21.81	21.86
	Cr_2O_3	0.02	0.01	0.01	0.01	0.00	0.01	0.05	0.05	0.02
	Fe_2O_3	0.75	0.64	0.90	-	-	-	0.80	0.81	0.93
	FeO	23.52	24.27	24.04	23.72	24.49	24.26	20.04	19.80	19.55
	MnO	0.82	0.95	0.99	0.44	0.44	0.51	0.49	0.45	0.47
	MgO	5.12	4.42	4.48	7.30	6.57	6.87	9.30	9.28	9.25
	CaO	9.74	9.63	9.89	8.13	8.36	8.15	8.04	8.34	8.63
	total	99.79	100.03	99.65	99.87	100.19	99.99	100.27	100.48	100.59
	Fe=FeO	24.20	24.85	24.85	-	-	-	20.77	20.52	20.39
Cations to 12 O	Si	3.00	3.00	3.01	3.01	3.00	3.00	3.00	3.00	3.00
	Ti	0.01	0.03	0.01	0.00	0.00	0.00	0.00	0.01	0.00
	Al	1.94	1.94	1.93	1.94	1.96	1.94	1.95	1.94	1.94
	Fe^{3+}	0.04	0.04	0.05	-	-	-	0.05	0.05	0.05
	Fe^{2+}	1.53	1.58	1.58	1.53	1.58	1.57	1.27	1.25	1.23
	Mn	0.05	0.06	0.07	0.03	0.03	0.03	0.03	0.03	0.03
	Mg	0.59	0.51	0.52	0.84	0.76	0.79	1.05	1.04	1.04
	Ca	0.81	0.81	0.83	0.67	0.69	0.68	0.65	0.67	0.70
	total	7.99	7.98	7.99	8.02	8.02	8.02	8.00	8.00	8.00
	Mg#	27.87	24.37	24.88	35.39	32.30	33.44	45.26	45.51	45.76
	And	2.23	1.90	2.81	0.00	0.00	0.00	2.29	2.30	2.65
	Pyp	20.02	17.35	17.65	28.93	25.78	27.21	35.10	35.02	34.76
	Sps	1.83	2.11	2.24	1.00	0.97	1.15	1.04	0.97	1.01
	Gross	25.14	25.36	25.22	23.14	23.60	23.13	19.37	20.18	20.61
	Alm	50.72	53.26	52.04	46.91	49.63	48.48	42.02	41.38	40.92
	n	17	18	10	20	12	9	8	23	11

B		3-1-11			30a-1-11		
		Rim	Mid	Core	Rim	Mid	Core
Oxide wt%, O by stoichiometry	SiO_2	38.33	38.28	38.33	37.94	37.95	37.89
	TiO_2	0.04	0.05	0.04	0.12	0.16	0.21
	Al_2O_3	21.08	21.00	20.95	20.57	20.41	20.37
	Cr_2O_3	0.01	0.01	0.01	0.02	0.03	0.04
	Fe_2O_3	1.09	1.24	1.25	1.01	1.14	1.24
	FeO	25.26	25.29	25.01	24.49	24.26	24.05
	MnO	0.58	0.62	0.55	2.06	2.13	2.24
	MgO	5.10	5.10	5.25	2.65	2.59	2.54
	CaO	8.59	8.53	8.59	10.86	11.03	11.20
	total	100.07	100.11	99.97	99.71	99.71	99.77
	Fe=FeO	26.24	26.41	26.13	25.39	25.29	25.16
Cations to 12 O	Si	2.99	2.99	2.99	3.01	3.01	3.00
	Ti	0.00	0.00	0.00	0.01	0.01	0.01
	Al	1.94	1.93	1.93	1.92	1.91	1.90
	Fe^{3+}	0.06	0.07	0.07	0.06	0.07	0.07
	Fe^{2+}	1.65	1.65	1.63	1.62	1.61	1.59
	Mn	0.04	0.04	0.04	0.14	0.14	0.15
	Mg	0.59	0.59	0.61	0.31	0.31	0.30
	Ca	0.72	0.71	0.72	0.92	0.94	0.95
	total	8.00	8.00	8.00	7.99	7.99	7.99
	Mg#	26.46	26.42	27.22	16.16	15.99	15.85
	And	3.20	3.67	3.67	3.04	3.44	3.74
	Pyp	19.86	19.88	20.45	10.52	10.33	10.11
	Sps	1.28	1.37	1.22	4.65	4.83	5.06
	Gross	20.81	20.23	20.34	27.91	28.07	28.16
	Alm	54.83	54.83	54.29	53.83	53.23	52.80
	n	15	13	8	5	12	4

Table 4-1: Summary of EPMA analyses of garnet from the Central Rhodope Mts. A: Samples from within the Arda gneiss, B: Samples from within the Variegated Formation

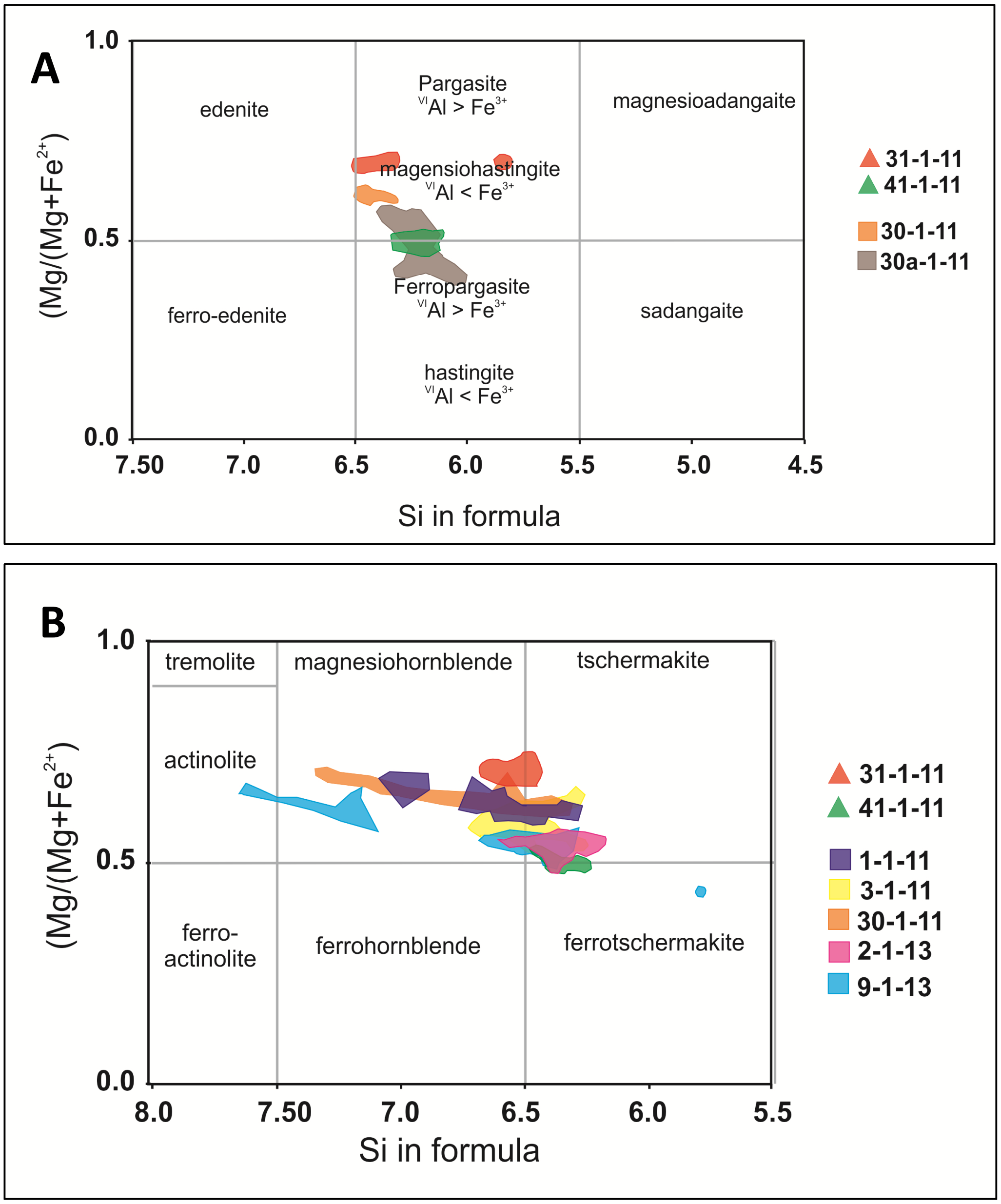

Figure 4-10: Classification diagrams to show changes in the chemistry of calcic amphiboles, after Leake et al. (1997), A:Amphibole analyses where $Ca_B \geq 1.5$, $(Na+K)_A < 0.5$, $Ca_A < 0.5$, B: Amphibole analyses where $Ca_B \geq 1.5$, $(Na+K)_A \geq 0.5$, $Ti < 0.5$. Triangles: samples from within Arda gneiss, square: VF samples

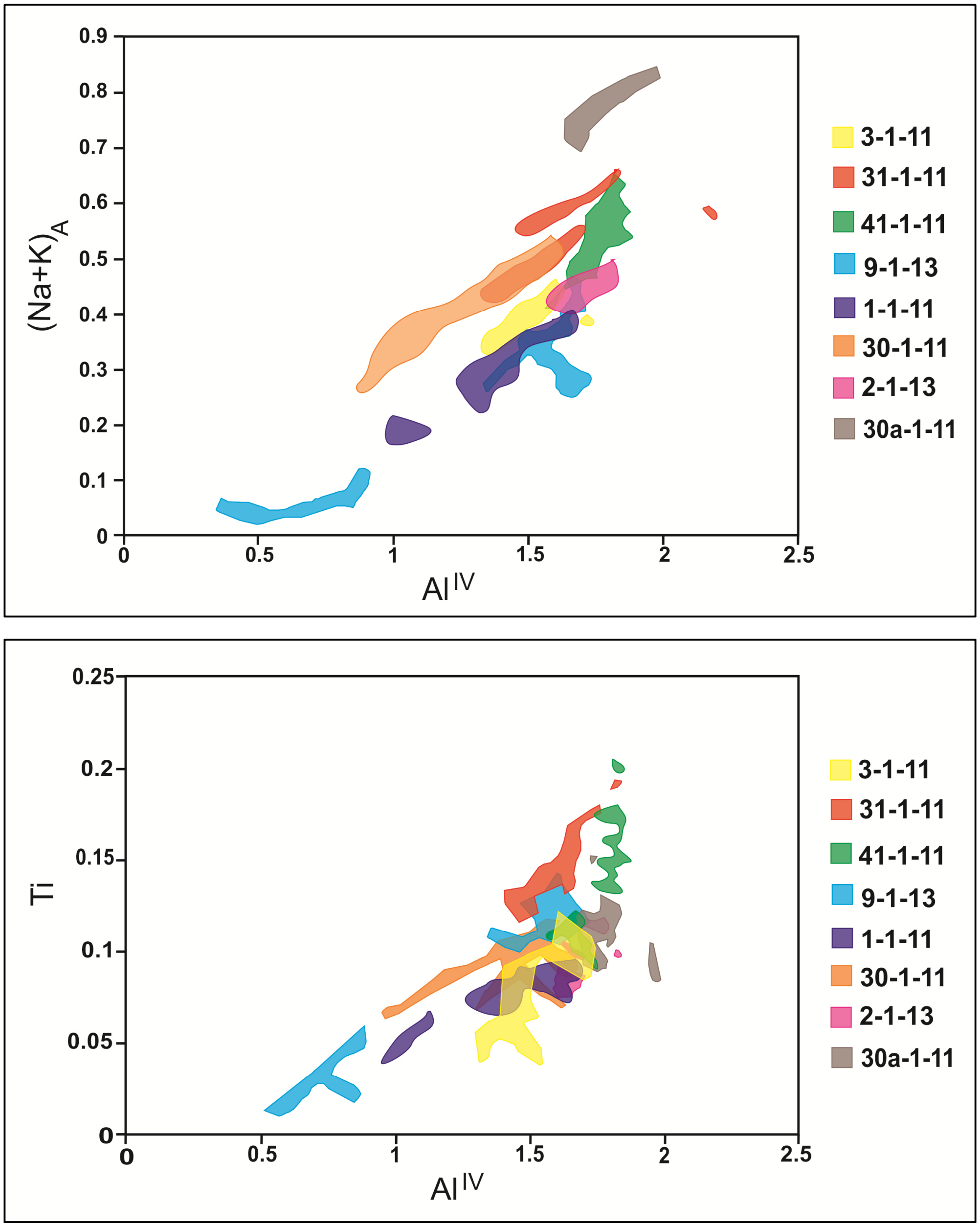

Figure 4-11: Plots of amphibole chemistry for central rhodope metabasic samples. A: Plot of $(Na+K)_A$ vs Al^{IV}, B: Plot of Ti vs Al^{IV}

A

		Arda			
		31-1-11		**41-1-11**	
	Sample	**core**	**rim**	**core**	**rim**
Oxide wt%, O by stoichiometry	**SiO_2**	44.7	43.9	40.9	41.3
	TiO_2	1.0	1.2	1.4	1.2
	Al_2O_3	12.0	12.5	12.1	11.5
	Cr_2O_3	0.1	0.0	0.0	0.0
	Fe_2O_3	3.4	3.2	6.2	6.5
	FeO	9.8	10.4	14.9	14.9
	MnO	0.1	0.1	0.4	0.3
	MgO	13.1	12.6	8.2	8.3
	CaO	11.6	11.6	11.5	11.6
	Na_2O	1.8	1.9	1.5	1.5
	K_2O	0.6	0.7	1.3	1.1
	F	0.0	0.0	0.0	0.0
	Cl	0.0	0.0	0.0	0.0
	H2O*	2.0	2.0	2.0	2.0
	Total	100.3	100.1	100.2	100.1
Cations to 23O	**Si**	6.5	6.4	6.2	6.3
	Ti	0.1	0.1	0.2	0.1
	Al	2.1	2.2	2.2	2.1
	Fe^{3+}	0.4	0.3	0.7	0.7
	Fe^{2+}	1.2	1.3	1.9	1.9
	Mn	0.0	0.0	0.0	0.0
	Mg	2.8	2.7	1.8	1.9
	Ca	1.8	1.8	1.9	1.9
	Na	0.5	0.5	0.5	0.4
	K	0.1	0.1	0.2	0.2
	Total	15.5	15.5	15.6	15.6
	n	21	20	23	25

B

		VF											
		1-1-11		**3-1-11**		**30-1-11**		**30a-1-11**		**2-1-13**		**9-1-13**	
	Sample	**core**	**rim**	**core**	**rim**	**core**	**rim**	**Core**	**Rim**	**core**	**rim**	**core**	**rim**
Oxide wt%, O by stoichiometry	**SiO_2**	43.1	44.8	44.6	44.1	44.6	46.2	41.5	41.7	40.9	41.2	44.6	43.3
	TiO_2	0.8	0.7	0.6	0.7	0.8	0.8	1.0	1.0	0.8	0.8	0.9	1.5
	Al_2O_3	11.9	9.6	11.5	11.5	11.4	9.4	13.1	12.8	11.9	11.1	11.4	10.3
	Cr_2O_3	0.0	0.0	0.0	0.0	0.0	0.0	0.0	0.1	0.0	0.0	0.0	0.0
	Fe_2O_3	6.2	6.2	4.4	4.6	3.2	3.2	2.2	2.4	7.2	6.8	5.2	5.1
	FeO	11.2	11.3	13.2	13.3	11.7	11.4	16.2	15.7	12.9	13.2	13.3	13.0
	MnO	0.3	0.3	0.2	0.2	0.3	0.3	0.3	0.3	0.4	0.4	0.4	0.4
	MgO	10.4	11.2	10.9	10.6	11.6	12.5	9.1	9.4	8.4	8.6	9.5	9.3
	CaO	11.7	11.9	11.6	11.6	12.1	12.2	11.8	11.8	10.9	11.1	11.4	10.9
	Na_2O	1.6	1.3	1.5	1.6	1.5	1.3	2.1	2.0	1.3	1.2	1.1	1.0
	K_2O	0.2	0.2	0.1	0.1	0.7	0.7	1.1	1.2	1.3	1.3	1.0	0.9
	F	0.0	0.0	0.0	0.0	0.1	0.1	0.0	0.0	0.0	0.0	0.0	0.0
	Cl	0.0	0.0	0.0	0.0	0.0	0.0	0.0	0.0	0.0	0.0	0.0	0.0
	H2O*	2.0	2.0	2.0	2.0	2.0	2.0	2.0	2.0	1.9	1.9	2.0	2.0
	Total	99.4	99.4	100.8	100.5	100.0	99.9	100.5	100.3	97.9	97.7	100.8	97.6
Cations to 23O	**Si**	6.4	6.6	6.5	6.5	6.6	6.8	6.2	6.3	6.3	6.4	6.6	6.6
	Ti	0.1	0.1	0.1	0.1	0.1	0.1	0.1	0.1	0.1	0.1	0.1	0.2
	Al	2.1	1.7	2.0	2.0	2.0	1.6	2.3	2.3	2.2	2.0	2.0	1.9
	Fe^{3+}	0.7	0.7	0.5	0.5	0.4	0.3	0.2	0.3	0.8	0.8	0.6	0.6
	Fe^{2+}	1.4	1.4	1.6	1.6	1.4	1.4	2.0	2.0	1.7	1.7	1.6	1.7
	Mn	0.0	0.0	0.0	0.0	0.0	0.0	0.0	0.0	0.1	0.1	0.0	0.0
	Mg	2.3	2.5	2.4	2.3	2.5	2.7	2.0	2.1	1.9	2.0	2.1	2.1
	Ca	1.9	1.9	1.8	1.8	1.9	1.9	1.9	1.9	1.8	1.8	1.8	1.8
	Na	0.5	0.4	0.4	0.5	0.4	0.4	0.6	0.6	0.4	0.4	0.3	0.3
	K	0.0	0.0	0.0	0.0	0.1	0.1	0.2	0.2	0.3	0.2	0.2	0.2
	Total	15.4	15.3	15.4	15.4	15.5	15.4	15.8	15.8	15.4	15.4	15.3	15.3
	n	8	23	12	20	22	14	13	15	5	10	9	16

Table 4-2: Summary of EPMA analyses of amphibole from the Central Rhodope Mts. A: Samples from within the Arda Gneiss. B: Samples from within the VF

4.3.5.3 Plagioclase

The major element chemistry of plagioclase from 8 samples across the central Rhodope Mts. was measured; 6 from within the VF and 2 from within the Arda unit. A summary of all results is presented in Table 4-3. With the exception of sample 3-1-11, all analysed plagioclase from within the VF are andesine ($Ab_{59\text{-}68}An_{30\text{-}40}$), and most exhibit some degree of core-rim variation, with slightly elevated Ab content in crystal cores. Plagioclase from sample 3-1-11 is labradorite ($Ab_{44}An_{56}$) and exhibits no appreciable zoning. The two samples from the Arda unit have elevated Ab contents when compared to the VF samples. Plagioclase from sample 31-1-11 is andesine ($Ab_{68}An_{31}$), whereas plagioclase from sample 41-1-11 is oligoclase ($Ab_{69\text{-}71}$, $An_{27\text{-}30}$).

4.3.6 Central Rhodope Mts. Thermobarometry

As discussed in section 4.3.4, little of the peak metamorphic assemblage is preserved in the metabasic units of the Central Rhodope Mts. This presents a real problem when attempting to constrain the prograde P-T path of samples, as with the absence of phengite inclusions in garnet there is no suitable mineral assemblage to constrain peak pressures or temperatures experienced by these samples. If all of the amphibole and plagioclase represents the product of omphacite breakdown, these phases were not in equilibrium with the garnet, and thermobarometers such as the garnet-honrblende thermometer (Ravna, 2000) and the garnet-amphibole-plagioclase-quartz barometer (Kohn and Spear, 1990) will yield meaningless P-T estimates for these samples. This is demonstrated with garnet-hornblende thermometry suggesting temperatures range between 490 and 670 °C, and GAPQ barometry pressures between 9 and 12 kbar. Constraints can however be placed on the retrograde path using amphibole-plagioclase thermobarometry.

4.3.6.1 Amphibole – Plagioclase Thermometer

The amphibole-plagioclase thermometer of Blundy and Holland (1990) is the most widely used geothermometer for amphibolite facies metabasic units. The thermometer is based on temperature dependent changes to the Al^{iv} content of an amphibole crystal coexisting with plagioclase in a silica saturated environment, following the equilibrium **Edenite + Quartz = Tremolite + Albite**. This original calibration has been refined to account for non-ideal mixing within amphibole, and the coupled substitution of Ca in the A site and Al in the tetrahedral site of amphibole (Holland and Blundy, 1994). Amphibole-plagioclase pairs measured from the matrix of samples were used to calculate temperatures; results therefore represent a minimum temperature for formation of these minerals. Calculated

A		**31-1-11**		**41-1-11**	
		core	**rim**	**core**	**rim**
Oxide Wt%, O by stoichiometry	**SiO_2**	60.9	60.8	61.4	60.6
	TiO_2	0.0	0.0	0.0	0.0
	Al_2O_3	25.3	25.3	23.8	24.2
	FeO	0.2	0.3	0.2	0.3
	MnO	0.0	0.0	0.0	0.0
	MgO	0.0	0.0	0.0	0.0
	CaO	6.5	6.5	5.8	6.4
	Na_2O	8.0	8.0	8.4	8.1
	K2O	0.2	0.2	0.3	0.2
	TOTAL	101.2	101.1	99.9	99.9
Cations to 8O	Si	2.7	2.7	2.7	2.7
	Al	0.0	0.0	1.2	1.3
	Ti	1.3	1.3	0.0	0.0
	Fe	0.0	0.0	0.0	0.0
	Mn	0.0	0.0	0.0	0.0
	Mg	0.0	0.0	0.0	0.0
	Ca	0.3	0.3	0.3	0.3
	Na	0.7	0.7	0.7	0.7
	K	0.0	0.0	0.0	0.0
	Total	5.0	5.0	5.0	5.0
	Or	1.1	1.1	1.5	1.2
	Ab	68.3	68.1	71.4	69.0
	An	30.6	30.7	27.1	29.8
	n	6	19	8	23

B		**1-1-11**		**3-1-11**		**30-1-11**		**30a-1-11**		**2-1-13**		**9-1-13**	
		core	**rim**	**core**	**rim**	**core**	**rim**	**core**	**rim**	**core**	**rim**	**core**	**rim**
Oxide Wt%, O by stoichiometry	**SiO_2**	59.1	58.4	54.3	54.1	59.8	60.1	60.9	59.7	58.3	57.1	57.2	56.9
	TiO_2	0.0	0.0	0.0	0.0	0.0	0.0	0.0	0.0	0.0	0.0	0.0	0.0
	Al_2O_3	26.1	26.6	29.7	30.0	24.7	24.6	25.2	26.0	25.7	26.4	26.3	26.6
	FeO	0.1	0.3	0.3	0.5	0.1	0.2	0.1	0.3	0.2	0.3	0.1	0.2
	MnO	0.0	0.0	0.0	0.0	0.0	0.0	0.0	0.0	0.0	0.0	0.0	0.0
	MgO	0.0	0.0	0.0	0.0	0.0	0.0	0.0	0.0	0.0	0.0	0.0	0.0
	CaO	7.9	8.5	11.7	11.9	7.0	6.7	6.4	7.3	6.2	6.7	6.5	6.9
	Na_2O	7.3	7.0	5.1	5.0	7.8	8.0	8.0	7.6	7.2	6.9	6.7	6.8
	K2O	0.1	0.1	0.0	0.0	0.3	0.2	0.2	0.2	0.2	0.2	0.5	0.2
	TOTAL	100.8	101.0	101.3	101.7	99.6	99.9	100.9	101.2	97.8	97.5	97.3	97.6
Cations to 8O	**Si**	2.6	2.6	2.4	2.4	2.7	2.7	2.7	2.6	2.7	2.6	2.6	2.6
	Al	0.0	0.0	0.0	0.0	1.3	1.3	0.0	0.0	1.4	1.4	1.4	1.4
	Ti	1.4	1.4	1.6	1.6	0.0	0.0	1.3	1.4	0.0	0.0	0.0	0.0
	Fe	0.0	0.0	0.0	0.0	0.0	0.0	0.0	0.0	0.0	0.0	0.0	0.0
	Mn	0.0	0.0	0.0	0.0	0.0	0.0	0.0	0.0	0.0	0.0	0.0	0.0
	Mg	0.0	0.0	0.0	0.0	0.0	0.0	0.0	0.0	0.0	0.0	0.0	0.0
	Ca	0.4	0.4	0.6	0.6	0.3	0.3	0.3	0.3	0.3	0.3	0.3	0.3
	Na	0.6	0.6	0.4	0.4	0.7	0.7	0.7	0.6	0.6	0.6	0.6	0.6
	K	0.0	0.0	0.0	0.0	0.0	0.0	0.0	0.0	0.0	0.0	0.0	0.0
	Total	5.0	5.0	5.0	5.0	5.0	5.0	5.0	5.0	5.0	5.0	5.0	5.0
	Or	0.6	0.5	0.2	0.2	1.4	1.2	1.3	1.1	1.3	1.3	2.9	1.2
	Ab	62.1	59.4	44.1	43.3	65.9	67.5	68.2	64.6	67.0	64.1	63.0	63.1
	An	37.3	40.2	55.7	56.5	32.7	31.3	30.4	34.3	31.8	34.6	34.1	35.7
	n	3	23	3	17	9	20	2	14	5	10	8	24

Table 4-3: Summary of EPMA analyses of plagioclase from the Central Rhodope Mts. A: Samples from the Arda Gneiss, B: samples from the VF

values are presented in Table 4-4. Average temperatures for samples are consistently between 650 – 730 °C, irrespective of mineralogy or geographical location.

	sample	(n)	Avg T	max	min	stdvev
VF	1-1-11	17	723	738	694	11
	3-1-11	17	787	838	745	29
	30-1-11	15	655	714	547	54
	30a-1-11	14	731	794	701	24
	2-1-13	8	731	749	712	11
	9-1-13	15	668	711	569	46
Arda	31-1-11	17	714	815	663	32
	41-1-11	17	738	757	718	10

Table 4-4: Results for the amphibole – plagioclase thermometer of Holland and Blundy (1994). Temperature is reported in °C.

4.3.6.2 Amphibole-Plagioclase barometer

To address the lack of barometers for mafic lithologies which do not contain garnet, Bhadra and Bhattacharya (2007) calibrated a barometer based on the reaction **Tremolite + Tschermakite + 2 Albite = 2 Pargasite + 8 Quartz.** This was based on experimental data in the range 1 – 15 kbar and 650 to 950 °C. Pressures have been calculated for the same amphibole-plagioclase pairs used for geothermometry, and results are presented in Table 4-5. A wide range of pressures are produced for all samples; VF values range between 2.4 and 17.1 Kbar, and Arda samples range between 2 and 10 Kbar.

		n	Avg P	max	min	stdev
VF	**1-1-11**	22	9.6	10.7	7.3	0.8
	3-1-11	17	13.3	17.1	10.4	2.1
	30-1-11	15	5.2	8.0	2.4	1.9
	30a-1-11	14	6.6	14.2	4.4	2.5
	2-1-13	8	9.0	10.4	8.0	0.9
	9-1-13	10	8.1	9.5	5.5	1.2
Arda	**31-1-11**	17	5.0	10.0	2.0	2.0
	41-1-11	23	7.2	8.8	5.6	0.8

Table 4-5 : Pressures estimated using the barometer of Bhadra and Bhattacharya (2007). All values been calculated using temperatures calculated by the Holland and Blundy (1994) thermometer. All pressures are reported in Kbar.

4.3.6.3 Summary of key observation and implications for P-T history of samples

The composition of garnets from the Arda 2 gneiss samples confirms the petrographical interpretation that some of these were once eclogites. Two of the samples have pyrope contents sufficiently high enough to be characterised as group B eclogites by the Coleman et al. (1965) classification scheme. The large range in pyrope content would however indicate contrasting P-T histories between samples. Garnets from the two samples of the VF have lower pyrope contents, and it is unclear whether they represent Group C eclogites or instead garnet amphibolites. The increased anorthite content seen in sample 3-1-11 is characteristic of a higher metamorphic grade, reflected in the pressure determined via amphibole-plagioclase barometry. This combined with large variations in amphibole composition confirms the contrasting P-T histories for VF samples.

4.3.7 Whole Rock Geochemistry

The whole rock trace element chemistry of 29 metabasic samples from the Central Rhodope Mts. was measured. These samples have been divided into VF and Arda, and further subdivided based on the presence or absence of garnet. Results for VF samples are presented in Table 4-6 and Arda samples in Table 4-7 .

4.3.7.1 Discrimination diagrams

Amphibolite can have a wide range of protoliths ranging from mixtures of decarbonated calcite/dolomite and pelites to metabasic basalt/dolerite (Leake, 1964). Field relationships indicate an igneous protolith for samples, with no intercalation with other units, or preservation of sedimentary structures. This interpretation is reflected in Cr-Ni-Ti concentrations, which in many samples are too high to be derived from a sedimentary protolith (Leake, 1964). Accordingly, all amphibolites are assumed to be derived from an igneous protolith.

A number of discrimination diagrams, based on both major and trace element chemistry have been proposed for establishing the original tectonic setting of igneous units eg. Pearce and Cann (1973). Many of these diagrams utilise elements such as Ti and V, which are generally viewed as immobile elements during metamorphism (Cann, 1970, Floyd and Winchester, 1978), and as such are suitable for constraining the protolith of metabasic units.

Subsequent work has since shown that element mobility is not simply a reflection of rock type or metamorphic grade, and there are instead a large number of mineralogical and fluid based controls on elemental mobility (Humphries, 1984). Given the complex tectonic history experienced by these metabasic samples, it is a large assumption that elements have remained immobile and the samples preserve a true geochemical record of the protolith. This has been combatted through using a number of different discrimination diagrams which utilise different ‘immobile’ elements. The general trend displayed on these diagrams is therefore much more significant than indiviudal results.

These were revisited by Vermeesch (2006), who applied discriminant analysis to refine the fields of these classic discrimination diagrams. These are presented in Figure 4-12. All suggest MORB as the main protolith for these units. The diagrams that utilise more mobile elements such as Eu and Sr exhibit a wider scatter between samples, with some samples plotting in the ocean island basalt and island arc basalt fields. No distinction on the basis of geography (Arda vs VF) or mineralogy can be seen in any of these diagrams.

	No Garnet									Garnet				
	30-1-11	**34-1-11**	**37-1-11**	**4-1-12**	**1-1-13**	**2-1-13**	**5-1-13**	**7-1-13**	**9-1-13**	**1-1-11**	**3-1-11**	**30a-1-11**	**1-1-12**	**6-1-13**
Li	10.5	17.5	19.1	5.5	5.8	3.2	20.7	14.6	9.8	13.7	7.7	17.0	9.5	8.6
Sc	45.3	49.2	13.0	32.8	27.7	27.1	53.4	29.9	35.1	43.6	47.4	37.6	42.2	70.2
Ti	8345.3	7549.6	6077.5	6898.2	5292.3	5806.3	6076.4	13474.0	10751.9	9555.0	18893.7	6790.6	13207.9	16925.5
V	354.1	306.8	135.2	218.8	162.8	263.0	336.7	282.3	256.1	391.3	464.3	225.7	414.4	623.6
Cr	159.2	390.6	22.3	320.7	187.8	13.9	327.9	31.6	132.9	110.0	32.1	291.3	83.4	170.8
Mn	1525.5	1975.1	954.6	1106.8	910.7	1002.9	2183.5	1250.5	1556.4	1770.0	2129.1	1089.2	1808.3	2902.7
Co	46.3	43.7	14.8	35.3	30.4	23.2	39.8	34.3	39.0	51.1	49.3	45.1	50.3	68.7
Ni	66.7	135.0	12.4	40.3	48.9	10.4	91.6	25.9	9.5	63.6	25.4	133.2	50.8	92.6
Cu	135.8	21.0	3.1	23.8	45.0	35.0	7.5	37.8	37.9	51.1	12.5	79.3	59.8	184.6
Zn	105.1	156.5	83.8	76.6	58.9	73.7	129.8	83.9	90.6	112.2	132.7	76.0	126.1	172.7
Ga	17.5	20.9	22.8	16.8	18.8	17.5	21.1	20.4	21.1	17.3	19.3	15.5	20.2	21.7
Rb	12.6	22.1	143.4	27.4	14.0	13.5	16.5	43.6	20.9	2.5	10.9	17.1	4.8	14.8
Sr	152.2	97.2	351.9	212.9	182.9	206.9	73.5	277.5	252.0	108.2	46.9	279.8	109.1	97.5
Y	36.6	54.4	23.7	30.4	33.8	25.1	49.6	41.0	35.1	41.5	76.6	27.3	51.4	76.4
Zr	11.4	13.5	5.3	8.6	8.4	9.2	11.2	13.0	11.0	10.0	8.0	10.3	12.8	18.8
Nb	3.3	30.9	19.3	4.2	6.1	1.9	39.8	15.6	6.2	3.8	9.9	2.5	4.8	7.7
Mo	0.4	0.5	0.5	0.3	0.3	0.3	0.3	0.6	5.1	0.5	1.9	0.3	0.5	1.1
Sn	1.9	12.6	5.3	2.4	4.5	1.4	13.8	5.0	3.6	2.0	2.5	1.1	2.3	3.0
Sb	0.2	0.2	0.1	0.1	0.0	0.2	0.2	0.1	0.2	0.2	0.1	0.2	0.1	0.4
Cs	0.5	0.5	7.5	2.0	0.5	2.4	0.3	0.8	3.2	0.3	0.8	7.8	0.4	0.7
Ba	44.1	150.9	715.4	119.6	109.9	120.2	87.7	278.2	93.2	18.7	20.1	31.6	35.6	73.8
La	4.3	6.6	50.2	9.9	18.5	7.1	3.6	27.3	12.9	4.7	12.9	3.7	5.8	9.1
Ce	11.7	16.6	105.6	22.4	39.6	17.1	10.5	62.5	30.0	12.9	34.3	10.5	17.6	25.9
Pr	1.9	2.4	12.2	3.1	5.2	2.4	1.9	8.1	4.1	2.1	5.2	1.7	3.0	4.2
Nd	9.6	10.8	44.7	13.7	21.1	11.2	10.5	32.4	18.1	10.8	25.7	8.7	15.3	20.3
Sm	3.4	4.0	8.6	3.8	5.2	3.3	4.6	7.7	5.0	3.9	8.7	2.9	5.2	6.4
Eu	1.1	1.0	1.7	1.1	1.3	1.0	1.0	1.8	1.4	1.3	2.5	1.1	1.8	1.6
Gd	4.6	5.6	6.3	4.3	5.5	3.6	6.4	7.4	5.7	5.2	11.0	3.7	6.9	8.1
Tb	0.8	1.2	0.9	0.8	0.9	0.6	1.2	1.2	1.0	1.0	1.9	0.7	1.2	1.7

	No Garnet									Garnet				
	30-1-11	**34-1-11**	**37-1-11**	**4-1-12**	**1-1-13**	**2-1-13**	**5-1-13**	**7-1-13**	**9-1-13**	**1-1-11**	**3-1-11**	**30a-1-11**	**1-1-12**	**6-1-13**
Dy	5.7	8.1	4.3	4.8	5.5	3.9	7.9	7.0	6.2	6.4	12.1	4.3	8.1	11.7
Ho	1.3	1.9	0.8	1.0	1.2	0.8	1.7	1.4	1.4	1.5	2.6	1.0	1.8	2.6
Er	3.8	5.6	2.1	3.0	3.3	2.4	4.9	3.8	3.8	4.3	7.4	2.7	5.2	7.6
Yb	3.5	5.4	1.7	2.8	2.9	2.2	4.7	3.3	3.4	4.1	6.7	2.5	4.8	7.1
Lu	0.5	0.8	0.2	0.4	0.4	0.3	0.7	0.5	0.5	0.6	1.0	0.4	0.7	1.1
Hf	0.6	1.1	0.3	0.5	0.5	0.5	1.2	0.7	0.6	0.6	0.6	0.5	0.8	1.0
Ta	0.2	1.8	1.3	0.4	0.5	0.2	3.9	1.1	0.6	0.2	0.5	0.2	0.3	0.4
Pb	4.9	4.6	14.5	5.6	5.6	11.9	4.8	2.6	7.0	1.6	1.6	4.8	8.7	4.5
Th	0.4	2.0	14.2	2.8	7.3	2.4	0.3	3.9	3.1	0.4	1.4	0.3	0.4	0.5
U	0.3	1.2	3.4	0.9	2.2	1.3	0.3	0.6	1.1	0.2	0.7	1.2	0.2	0.5

Table 4-6: Whole rock trace and REE element concentrations for VF metabasic samples from the Central Rhodope Mts. All were measured using ICP-MS at the Open University, summer 2013, and are reported as ppm.

	No Garnet				Garnet										
	32-1-11	**36a-1-11**	**41-1-11**	**3-1-13**	**22-1-10**	**23-1-10**	**36-1-11**	**40-1-11**	**42-1-11**	**44-1-11**	**45-1-11**	**14-1-12**	**15-1-12**	**11-1-13b**	**12-1-13**
Li	21.9	34.6	16.1	10.9	12.5*	6.3*	21.4	14.1	25.8	18.0	5.3	20.9	13.7	21.3	6.0
Sc	17.6	29.6	30.5	31.4	31.4*	39.8*	30.0	28.7	63.4	39.9	35.5	42.8	49.1	26.9	33.2
Ti	8740	10910	16889	8870	13132*	14438*	10021	15031	27435	3376	10013	8423	23439	9391	3626
V	218.0	268.2	345.1	235.8	239.0*	334.6*	289.3	294.4	600.0	344.8	304.0	304.0	747.9	235.2	210.7
Cr	342.7	70.5	30.5	242.5	209.6*	129.7*	74.9	10.7	143.9	52.2	203.0	363.1	123.8	270.3	250.9
Mn	1145.2	1468.4	1438.9	1188.1			1712.6	1716.8	4475.8	1374.2	1534.0	1646.2	2566.8	1320.5	791.3
Co	48.4	57.2	34.4	42.2	39.0*	43.4*	73.2	32.1	81.8	38.2	44.2	50.1	75.3	53.5	42.1
Ni	153.6	96.7	21.3	112.4	150.9*	53.8*	110.9	12.6	101.3	28.5	23.0	119.5	101.4	58.8	113.2
Cu	64.7	11.5	32.9	23.0	55.1*	72.6*	90.7	41.7	64.6	28.0	33.3	9.6	287.7	38.3	154.2
Zn	79.2	101.7	95.8	87.2	123.9*	140.3*	127.1	113.5	227.1	80.8	98.4	86.9	178.7	83.8	53.6
Ga	15.6	20.0	20.6	17.0	-	-	22.7	21.5	37.7	14.5	20.2	16.8	26.5	17.5	14.9
Rb	28.3	113.2	53.7	16.3	13.5	14.5	25.9	72.3	36.9	2.8	11.7	1.0	13.6	15.4	4.6
Sr	166.2	279.3	188.6	132.9	164.6*	350.5*	267.1	211.2	550.7	86.6	149.5	256.8	638.5	257.6	583.8
Y	18.3	23.9	53.2	33.6	52.4*	33.3*	23.0	49.7	70.5	15.3	33.5	35.8	40.1	23.1	13.2

	No Garnet				**Garnet**										
	32-1-11	**36a-1-11**	**41-1-11**	**3-1-13**	**22-1-10**	**23-1-10**	**36-1-11**	**40-1-11**	**42-1-11**	**44-1-11**	**45-1-11**	**14-1-12**	**15-1-12**	**11-1-13b**	**12-1-13**
Zr	9.4	13.3	7.7	10.6	204.6*	165.3*	14.0	9.8	13.9	7.0	17.2	17.0	11.4	9.0	5.2
Nb	4.5	8.3	11.3	2.9	4.5	19.0	7.9	12.1	21.8	0.2	3.9	2.6	17.4	3.7	1.4
Mo	0.4	1.1	1.0	0.4	-	-	0.5	1.7	2.9	0.2	0.2	0.3	1.1	0.4	0.2
Sn	2.6	2.6	2.5	1.7	-	-	3.1	3.8	3.5	0.4	1.9	1.6	2.8	1.7	1.6
Sb	0.1	0.2	0.1	0.2	-	-	0.1	0.1	0.3	0.1	0.1	0.1	0.2	0.2	0.0
Cs	1.2	7.7	1.7	1.3	0.5	0.8	1.3	2.0	2.0	0.5	0.1	0.1	0.7	0.9	0.4
Ba	507.1	139.3	375.3	71.1	89.0*	260.8*	112.8	464.2	256.6	26.4	104.5	12.4	114.3	86.7	79.8
La	7.7	10.3	29.6	6.6	9.9	16.1	8.1	29.4	30.4	1.1	8.9	5.1	14.2	8.6	4.8
Ce	20.6	26.0	66.5	17.2	25.9	34.8	20.8	67.2	73.5	3.1	21.5	13.8	34.7	21.7	12.6
Pr	2.9	3.9	8.8	2.7	4.0	4.9	3.1	8.6	10.3	0.5	3.2	2.3	5.2	3.0	1.9
Nd	13.5	18.0	37.7	13.2	20.0	23.4	14.4	35.9	45.6	2.8	14.5	11.6	24.3	13.7	8.6
Sm	3.6	4.7	9.3	4.1	5.8	6.4	4.0	8.8	11.8	1.2	4.3	3.8	6.9	3.6	2.3
Eu	1.2	1.6	2.6	1.4	1.7	2.0	1.4	2.5	3.6	0.4	1.4	1.3	2.4	1.3	0.8
Gd	3.8	4.3	9.8	4.9	6.1	6.0	4.3	8.9	12.1	1.8	5.2	5.0	7.4	4.1	2.3
Tb	0.6	0.7	1.5	0.9	1.2	1.0	0.7	1.4	2.0	0.3	0.9	0.9	1.2	0.7	0.4
Dy	3.9	4.1	9.0	5.4	6.8	5.4	4.1	8.3	12.0	2.4	5.8	5.7	6.9	4.2	2.2
Ho	0.8	0.9	1.9	1.2	1.5	1.1	0.9	1.7	2.5	0.6	1.3	1.3	1.4	0.9	0.5
Er	2.2	2.3	5.1	3.3	3.8	2.8	2.3	4.7	6.9	1.7	3.6	3.5	3.8	2.5	1.4
Yb	1.9	2.1	4.2	2.9	4.1	2.7	2.0	4.0	6.1	1.6	3.2	3.2	3.2	2.3	1.3
Lu	0.3	0.3	0.6	0.4	0.5	0.4	0.3	0.6	0.9	0.2	0.5	0.5	0.5	0.3	0.2
Hf	0.5	0.7	0.5	0.6	3.8	4.1	0.6	0.6	0.5	0.4	0.8	0.9	0.6	0.4	0.3
Ta	0.2	0.7	0.9	0.3	0.3	1.1	0.4	0.8	1.1	0.1	0.3	0.2	1.0	0.2	0.2
Pb	5.2	8.2	4.1	4.9	-	-	3.0	5.3	3.5	4.3	4.9	1.8	3.8	2.0	3.2
Th	0.9	0.6	6.8	0.6	0.9	1.5	0.6	7.9	1.6	0.3	1.4	0.3	1.0	0.4	0.4
U	0.2	0.9	1.3	0.2	0.4	0.5	0.3	1.6	0.4	0.1	0.6	0.2	0.3	0.1	0.3

Table 4-7 Whole rock trace and REE element concentrations for Arda metabasic samples from the Central Rhodope Mts. With the exception of samples 22-1-10 and 23-1-10, all were measured using ICP-MS at the Open University, summer 2013, and are reported as ppm. Samples 22-1-10 and 23-1-10 were measured at Royal Holloway in 2011, and values marked with a * were measured using an ICP-AES rather than ICP-MS.

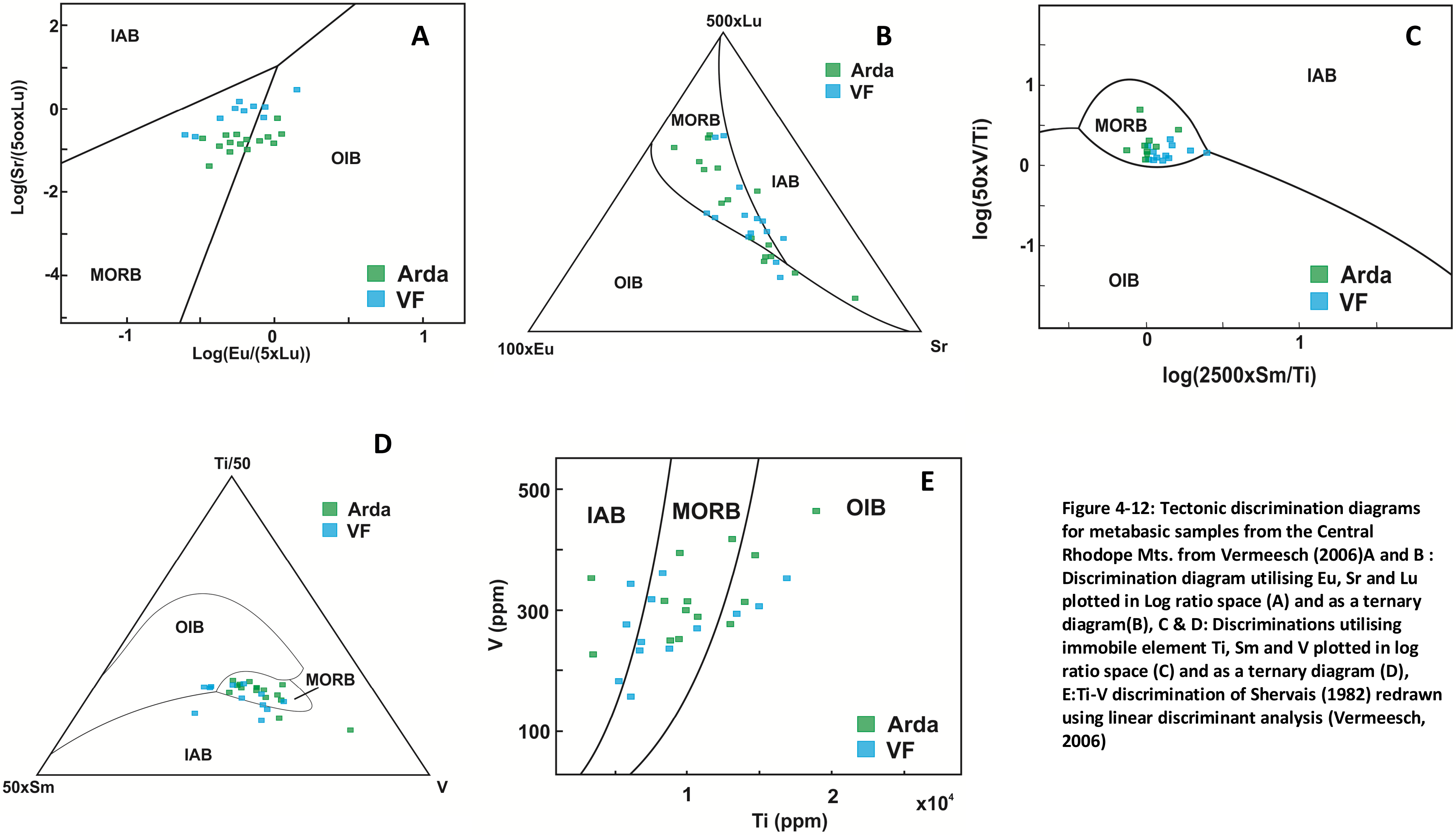

Figure 4-12: Tectonic discrimination diagrams for metabasic samples from the Central Rhodope Mts. from Vermeesch (2006)A and B : Discrimination diagram utilising Eu, Sr and Lu plotted in Log ratio space (A) and as a ternary diagram(B), C & D: Discriminations utilising immobile element Ti, Sm and V plotted in log ratio space (C) and as a ternary diagram (D), E:Ti-V discrimination of Shervais (1982) redrawn using linear discriminant analysis (Vermeesch, 2006)

4.3.7.2 Chondrite normalised REE diagrams

Chondrite normalised REE diagrams are presented for all samples in Figure 4-13. Garnet bearing samples within the VF all show flat profiles (Figure 4-13a), many with a slight negative Eu anomaly.(Eu/Eu*) which ranges from 0.7 to 0.9. Only sample 30a-1-11 has no Eu anomaly. Non garnet bearing samples are more varied, ranging from LREE depleted to those with a distinct LREE enrichment, although most appear to have a similar flat profile to the garnet bearing samples (Figure 4-13b). $(La/Sm)_N$ range from 0.5 to 3.7. All samples have a negative Eu anomaly, with (Eu/Eu*) ranging from 0.6 to 0.9.

Garnet bearing samples within the Arda unit vary greatly. Like the Non garnet VF samples, they range from extremely LREE enriched, to LREE depleted with $(La/Sm)_N$ ratios ranging from 0.6 to 2.1 (Figure 4-13c). Eu anomalies are rare; where present they are negligible with (Eu/Eu*) ~ 0.9. Non garnet bearing samples from the Arda gneiss are generally LREE enriched, with one flat profile (Figure 4-13d). $(La/Sm)_N$ ratios range from 1 to 2. Where present Eu anomalies are small, wth Eu/Eu* ranging from 0.82-0.95.

4.3.7.3 MORB normalised trace element diagrams

N-MORB normalised trace element diagrams are presented in Figure 4-14 . A feature of all samples analysed at the Open University in 2013 is a strong depletion in Zr and Hf. Rather than being indicative of an island arc source setting, these patterns are likely the result of incomplete dissolution of zircon during digestion, explaining the lack of depletions in samples analysed at Royal Holloway College, University of London in 2011.

Garnet bearing samples from within the VF all have a broadly similar trace element pattern, characterised by flat profiles for the HFSE (with the exception of Zr and Hf), and deviations form MORB for the LILE (Figure 4-14a). Non garnet bearing samples exhibit more variation (Figure 4-14b). Like the garnet bearing samples, the more compatible HFSE are uniformly flat, and a large spread of values are observed for the LILE. This suite however exhibits a larger range of Nb-Ta concentrations. Although most preserve some degree of negative anomaly, sample 30-1-11 closely resembles the garnet bearing units, and samples 5-1-13 and 34-1-11 preserve positive anomalies.

Garnet bearing samples from within the Arda unit exhibit the same degree of variation as the non-garnet bearing VF sample, with a large spread in Nb, Ta and LILE concentrations (Figure 4-14c). This suite also has the largest range of absolute concentrations for each element. Of the 4 non-garnet bearing samples from the Arda unit, 3 preserve negative Nb-Ta anomalies (Figure 4-14). All have uniformly flat HFSE and enriched LILE concentrations.

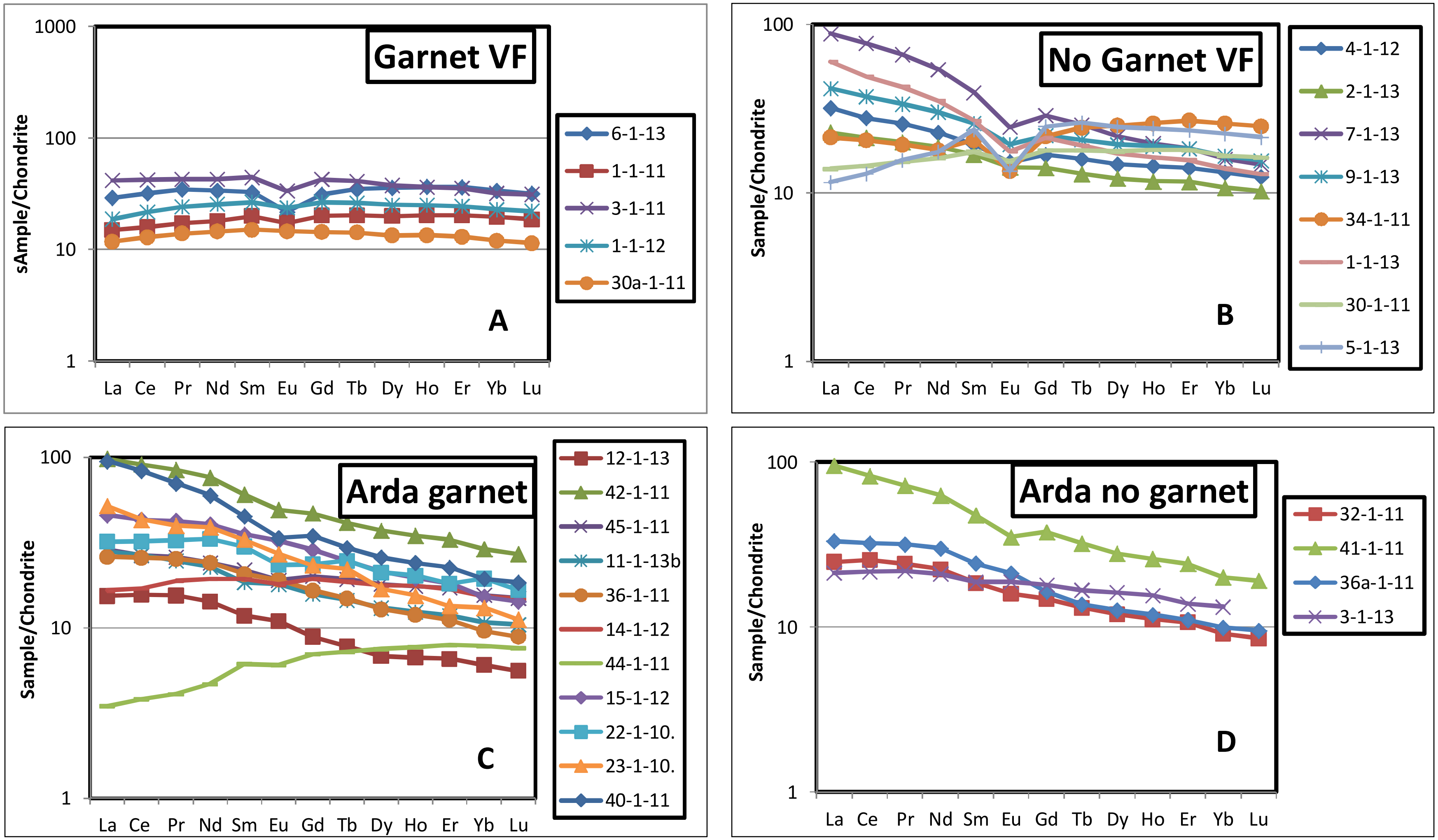

Figure 4-13: Chondirte normalised REE diagrams for Arda and VF samples from the Cenrtal Rhodope Mts. Normalising values from Boynton (1985)

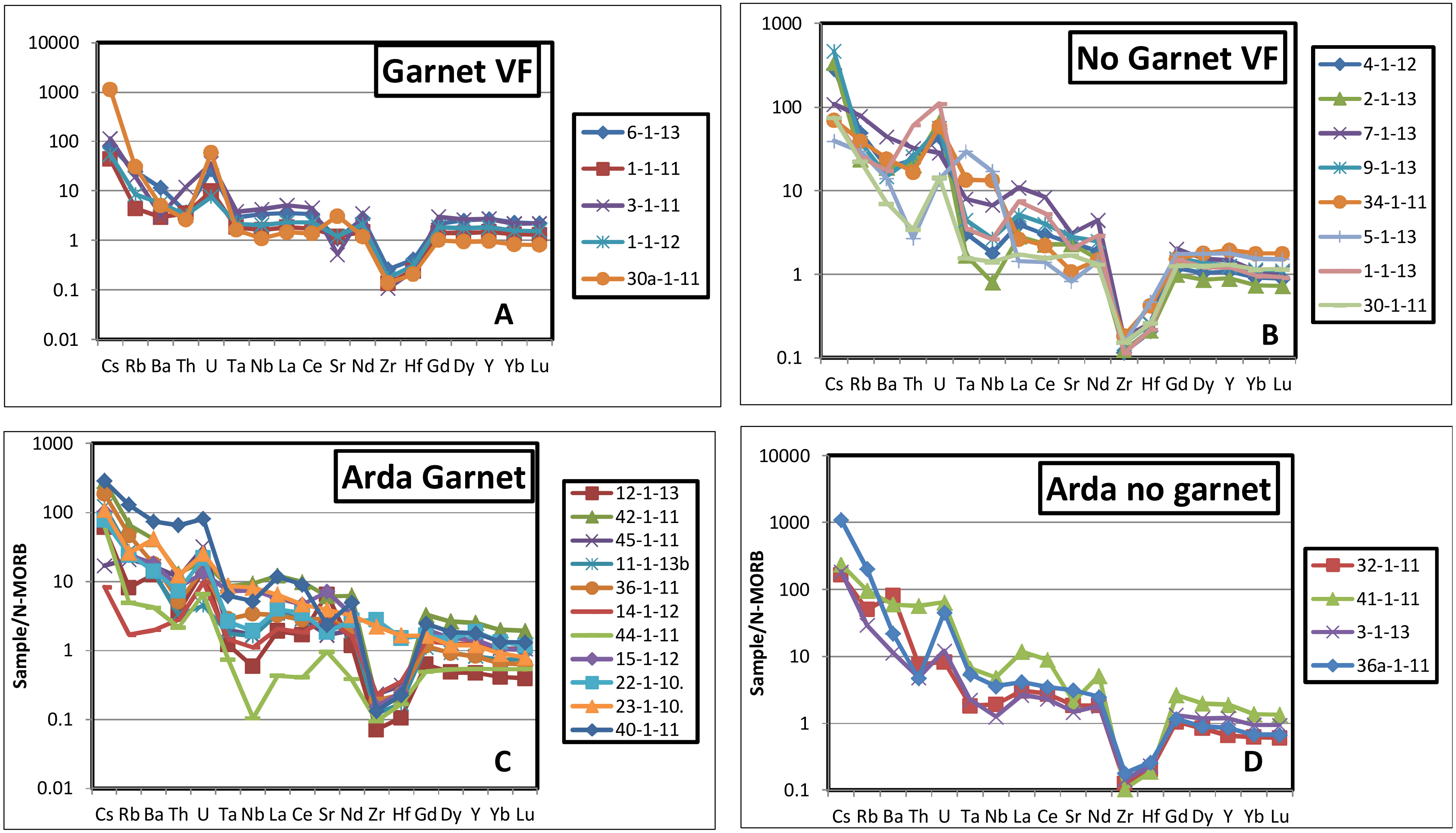

Figure 4-14: N-MORB normalised trace element diagrams for Arda and VF samples from the Central Rhodope Mts. Normalising values from McDonough and Sun (1995)

4.3.7.4 Radiogenic Isotope Geochemistry

Bulk rock Sr and Nd isotope measurements were made on 12 samples from the Central Rhodope Mts. to further constrain the tectonic setting of sample protoliths. Details of the analytical procedure are described in appendix B. ^{87}Sr/^{86}Sr isotope ratios were deemed unsuitable for constraining tectonic settings; a large range of *f*Rb values (between -0.18 – 11.05) indicates varying degrees of enrichment relative to CHUR, likely the result of interaction with the gneiss of the Arda dome. Results for the Sr isotope study can be found in appendix B. ^{143}Nd/^{144}Nd isotope ratios are presented in Table 4-8. Details of the effect of sample age on calculated initial values and the calculation of ε_{Nd} and *f*Sm can be found in appendix B.

		Sample	^{143}Nd/^{144}Nd	Initial ^{143}Nd/^{144}Nd	ε^{t}_{Nd}	*f*Sm
Arda	Garnet	1-22-10	0.512847 ± 6	0.512211	5.50	-0.10
		1-23-10	0.512721 ± 4	0.512123	3.78	-0.16
		36-1-11	0.512788 ± 6	0.512181	4.92	-0.14
		40-1-11	0.512469 ± 4	0.511937	0.14	-0.25
		44-1-11	0.512934 ± 6	0.512006	1.49	0.31
		45-1-11	0.512696 ± 3	0.512053	2.43	-0.09
	No Grt	36a-1-11	0.512785 ± 9	0.512216	5.60	-
		41-1-11	0.512488 ± 7	0.511950	0.41	-0.24
VF	Garnet	1-1-11	0.512975 ± 6	0.512620	5.93	0.10
		3-1-11	0.512692 ± 7	0.512357	0.80	0.04
		30a-1-11	0.512876 ± 7	0.512543	4.42	0.04
	No Grt	34-1-11	0.512531 ± 5	0.512163	-3.00	0.14

Table 4-8: Overview of Nd isotope results for metabasic samples from the Central Rhodope Mts. Protolith formation ages of 550 Ma for Arda samples, and 250 Ma for VF samples have been used to calculate the initial values. These are based on reported ages in the literature (Burg, 2011).

All of the samples analysed have low *f*Sm values, indicating that any interaction with crustal material had a limited effect on Nd isotope signature. Two groups of samples can be identified on the basis of ε^{t}_{Nd} in the Arda 2 samples. Most have positive values (2.43 – 5.5) indicative of samples originating from a depleted mantle source region and a subsequent MORB protolith. The lower ε^{t}_{Nd} of samples 40-1-11 and 41-1-11 are indicative of an increased crustal component. The same range of high and low ε^{t}_{Nd} samples is seen in the VF samples.

4.3.7.5 Key findings of geochemical analysis

Trace elemental discrimination diagrams indicate a MORB protolith for all of the metasbasic samples of the Central Rhodope Mts. Chondrite normalised REE and MORB normalised trace element profiles however indicate a variable SSZ input for samples, which is confirmed through variations in $^{143}Nd/^{144}Nd$ isotope ratios.

All metabasic units from the Arda 2 gneiss display characteristics of this SSZ input, suggesting an E-MORB/island arc basalt protolith. The only sample with a distinct N-MORB REE profile (44-1-11), has the highest fSm value of all samples analysed, indicating this anomalous REE pattern may be as a result of interaction with surrounding lithologies. The two samples with the highest $(La/Sm)_N$ (40-1-11 and 41-1-11) exhibit low to negative ε^t_{Nd} values indicative of an increased crustal component, strongly indicating an Island arc protolith for these samples.

Garnet bearing samples from within the VF all have flat REE profiles, and lack the characteristic negative Nb-Ta anomalies, indicating a reduced SSZ input. This is reflected in the $^{143}Nd/^{144}Nd$ isotope for two samples, with positive ε^t_{Nd} valus indicative of formation from a depleted mantle source region, typical of N-MORB. The low ε^t_{Nd} value for sample 3-1-11 likely reflects a small degree of crustal contamination rather than a contrasting protolith. The non-garnet bearing amphibolite samples from the VF exhibit a wide range of geochemical characteristics, indicating an amalgamation of Island arc/E-MORB and N-MORB protoliths.

4.3.8 Discussion of Central Rhodope metabasic samples

This study has demonstrated widespread petrographical and geochemical variation between metabasic samples of the Arda 2 gneiss and the Variegated Formation., to the extent that a common formation history for these two formations is unlikely.

Despite the petrographical differences between the Arda 2 metabasic samples, geochemical analysis indicates a common protolith of E-MORB/Island arc basalt for these units, supporting the findings of Kirchenbaur et al. (2012). The variation in pyrope content in garnet of these samples suggests contrasting P-T histories, explaining the observed petrographical differences. On this basis, without two contrasting protoliths for samples it is difficult to explain the conflicting age data reported in the literature (Arkadakskiy et al., 2003, Kirchenbaur et al., 2012, Savov et al., 2007).

Eocene thermal resetting of the garnet could explain the Cenozoic ages reported by Kirchenbaur et al. (2012). In their study the garnets dated from the Arda 2 unit lack Mn, Ca and Fe core-rim variation, and a LA-ICP-MS study indicated diffusion of Lu across the crystals. The authors attributed this to a subsequent near peak metamorphic event, owing to virtually identical Cenozoic ages across the Central Rhodope Mts. in samples that do preserve Lu zonation across crystals.

A Cenozoic HP metamorphic event is hard to reconcile with existing studies of the host Arda 2 orthogneiss. There is no evidence for an Eocene eclogite facies event in this unit (Cherneva and Georgieva, 2005), with all Eocene zircon ages restricted to discordant leucsomes associated with amphibolite facies migmatisation (Ovtcharova et al., 2002, Peytcheva et al., 2004). Studies of the Western Gneiss Region of Norway have however demonstrated the difficulties involved in establishing the peak metamorphic condition experienced by felsic lithologies such as orthogneiss (Carswell and Cuthbert, 2003). Further geochronological investigations of the Arda 2 metabasic samples and petrological studies of the host Arda 2 gneiss are required to fully understand the extent and conditions experienced during the Cenozoic.

There is no evidence to suggest that the garnet amphibolite units of the Variegated formation from the CSZ experienced eclogite facies conditions, suggesting a metamorphic history unrelated to both their kyanite-garnet schist counterparts (described in chapter 3), and the metabasic units hosted by the Arda 2 gneiss described in this study. The contrasting P-T conditions and protoliths described in this study indicate that the sheet like structure mapped for amphibolite units in the vicinity of Chepelare (Sarov, 2004) may be an over simplification, and instead the area is a true melange of lithologies with contrasting protliths and P-T histories.

4.4 Metabasic samples of the Eastern Rhodope Mts.

4.4.1 Overview of existing research

Eclogites are widespread throughout both the upper and lower high grade basement units of the Eastern Rhodope Mts., occurring in a variety of different stratigraphic and structural settings. Outcrop morphologies include lenses, sheet like structures concordant with marbles and gneiss and as metagabroic dykes (Liati and Mposkos, 1990). Samples from the two terranes can be distinguished on the basis of contrasting metamorphic grade, with the lower unit samples experiencing peak P-T conditions of 17 Kbar and 620 °C (although pressures up to 21 Kbar for kyanite eclogites), and the upper unit samples experiencing higher temperatures, and pressures in excess of 20 Kbar (Liati and Mposkos, 1990, Mposkos et al., 2012, Baziotis et al., 2008). Most samples underwent severe retrogression upon exhumation in amphibolite facies (534 °C, 8 Kbar), destroying most evidence of the high pressure assemblage (Liati and Mposkos, 1990, Mposkos et al., 2012).

All eclogites were proposed to share a common protolith of tholeitic basalt (Liati, 1986, Mposkos and Perdikatsis, 1989), although subsequent work on samples from the lower high grade basement has questioned this interpretation. Two distinct populations of eclogite have been recognised in the Kechros Complex of the lower high grade basement unit of the Greek Eastern Rhodope Mts. on the basis of bulk rock geochemistry. Low Fe-Ti eclogites, with strong LREE enrichment, and a negative Nb anomaly are thought to originate in a rift related tectonic setting, whereas high Fe –Ti eclogites have more MORB like REE and trace element profiles, and are interpreted to have formed during partial melting in an extensional oceanic environment (Baziotis and Mposkos, 2010, Mposkos et al., 2012). Eclogites from within the Kimi complex of the upper high grade basement unit have been shown to have formed via fractional crystallisation of tholeitic magmas (Baziotis et al., 2008). These units are commonly cross cut by tonalitic-trondhjemitic dykes, which are interpreted as the product of partial melting of mafic material at the base of the thickened continental crust during the early tertiary – essentially being akin to modern adakites, but forming in a collision environment (Baziotis et al., 2008).

Studies of metabasic units from the VF of the Bulgarian upper high grade basement suggest a supra-subduction zone origin for all units. Protoliths range from boninite/island arc tholeite (Daieva et al., 2007, Haydoutov et al., 2004) through to MORB (Bonev et al., 2006), suggesting the metabasic suite is recording the full evolution of a subduction zone and associated back are rifting (Bonev et al., 2006). Estimated P-T conditions on the basis of conventional thermobarometry are 6-2 kbars and 520 - 630 °C, with the exception of a metagabbro sample from Bubino, which yielded granulite facies conditions of 11-5 Kbar, and 780-680 °C (Haydoutov et al., 2004). There is no indication that any of the Bulgarian samples are retrogressed eclogite, and as such the relationship to metabasic samples described from the Greek Rhodopes is unclear.

Like in the Central Rhodope Mts., the age of both the protolith and of metamorphism remains very unclear. Zircons from the granulite facies Bubino metagabbro described in Haydoutov et al. (2004) have been dated via U-Pb SHRIMP dating (Carrigan et al., 2003). Cores yielded ages of 572 ± 5Ma, and the rims of many crystals yielded Variscan ages of ~300 – 350 Ma. This Neoproterozoic formation age has been used as evidence for a Variscan aged suture zone separating the VF from the underlying Varsican aged orthogneiss of continental origin from the Bela-Reka dome (Haydoutov et al., 2004).

Recently discovered Ordovician metabasic units from the village of Egrek in the Avren Synform support this interpretation (Bonev et al., 2013).

U-Pb zircon dating of eclogite units from the Kimi complex however yielded magmatic Permian cores with HP metamorphic rims, suggesting eclogite facies metamorphism between 160 and 195 Ma (Bauer et al., 2007). Some rims were dated at 115 Ma, and 79 Ma, both of which have been attributed to metamorphic overprint events. Permo-Triassic protolith ages have also been reported from eclogites of the Kechros complex (Liati and Fanning, 2005), where the age of eclogite metamorphism has been placed sometime between the late Jurassic and Late Cretaceous (Liati and Mposkos, 1990), but remains poorly constrained (Mposkos et al., 2012). Ultimately the relationship between the Neo-Proterozoic Bubino Gabbro, and the Permian metabasic units of the Kimi complex and the Kechros dome remain unclear.

4.4.2 Field sampling

In this study, 15 samples were collected from across the Bulgarian part of the Eastern Rhodope Mts (Figure 4-17). With the exception of sample 19-1-11, all samples outcrop as part of the upper high grade basement unit, predominantly along the flanks of the Byala Reka and Kesebir domes. This is the same tectonic setting as the samples described in the Haydoutov et al. (2004) study.

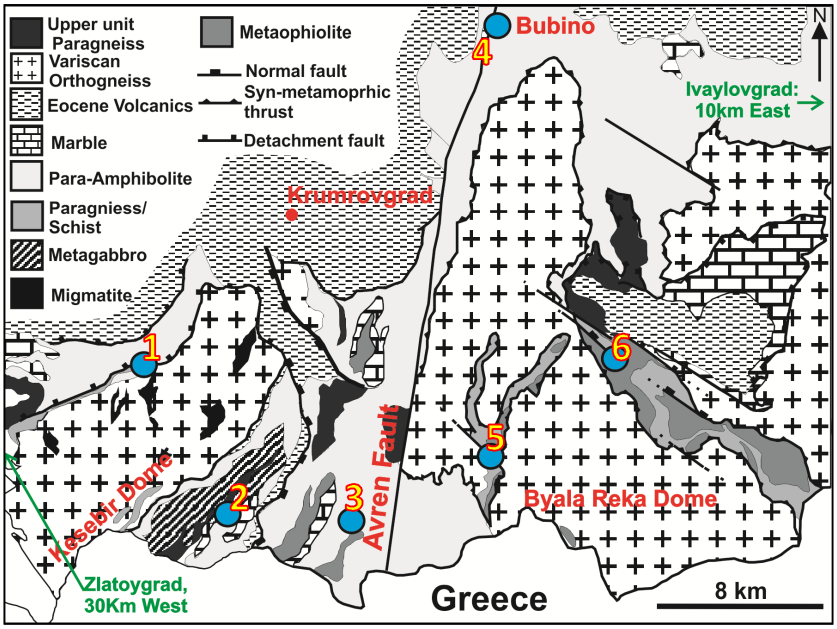

Figure 4-15: Simplified geological map of the Eastern Rhodopes Mts. Sampled localities are highlighted in blue. 1:15-1-11, 2: 9-1-10, 14-1-02, 24-1-02, 3: 8-1-10, 4: 4-1-10, 6a-1-10, 6b-1-10, 5:19-1-11, 6: 18-1-11. Additional samples collected, but not lying within the area of this map are shown in green, Ivaylovgrad: 26-1-11, 27-1-11, Zlatoygrad: 4-1-11, 7-1-11

As in the Central Rhodope Mts. vegetation and poor outcrop exposure limit detailed observations on the morphology of units and their relationship to surrounding lithologies. This is particularly true at Bubino, where 4 samples were collected along a river bed over a distance of ~ 200m. Despite this, most samples within the Avren Synform and flanks of the metamorphic domes appear to have a sheet like structure, sandwiched between mylonitized gneiss, and are found in close association with ultramafic bodies and often marble (Figure 4-16a). Samples from Ivaylovgrad (26-1-11 and 27-1-11) are instead large boudins, found within the walls of the dam (Figure 4-16e.f).

Some of the amphibolites encountered within the VF appear to have a clear sedimentary origin. Fine intercalations of amphiblolite with marble and gneiss are observed (Figure 4-16c), suggesting a flysch like origin. Boudinaged amphibolite is also seen sandwiched between marble layers, appearing to preserve primary sedimentary characteristics (Figure 4-16d). These outcrops were all extensively weathered, and were therefore not sampled for geochemical analysis.

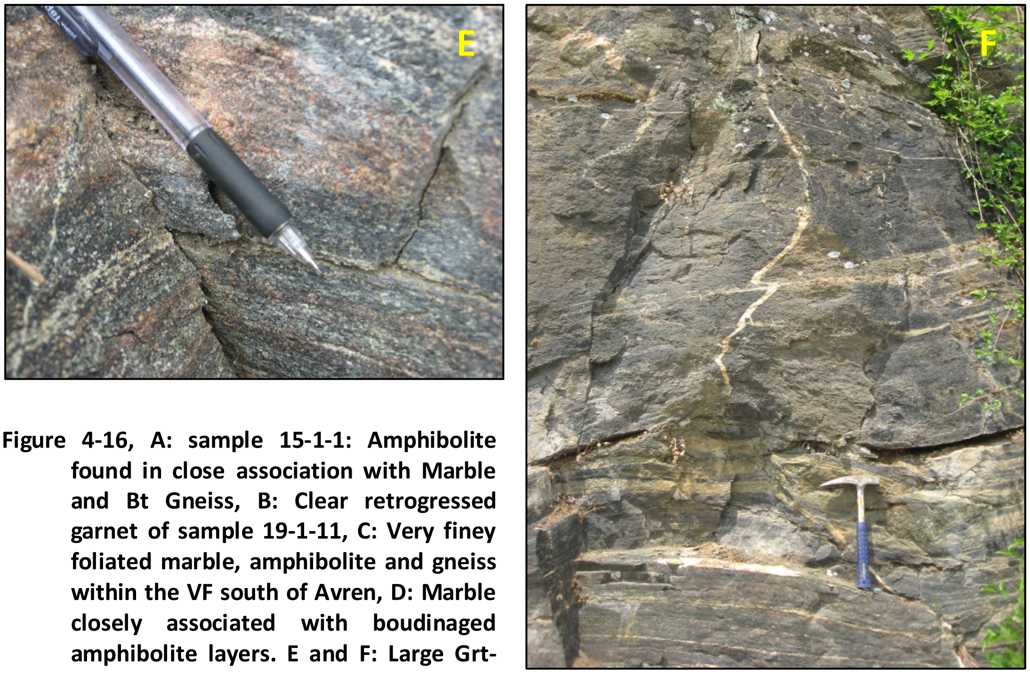

Figure 4-16, A: sample 15-1-1: Amphibolite found in close association with Marble and Bt Gneiss, B: Clear retrogressed garnet of sample 19-1-11, C: Very finey foliated marble, amphibolite and gneiss within the VF south of Avren, D: Marble closely associated with boudinaged amphibolite layers. E and F: Large Grt-Amphibolite boudins from the Ivaylovgrad dam.

4.4.3 Petrography

The samples have been grouped on the basis of geographical location; Bubino, Ivalylovgard, the flanks of the Byala-Reka and Kesbir domes and Zlatovgrad. Each of these locations will be discussed in turn.

4.4.3.1 Bubino

Large variation is seen over a very short distance in the river running north of Bubino. Furthest from the village is sample 4-1-10, a weakly foliated, possibly banded, amphibolite. Anhedral amphibole crystals up to 2mm in length, together with biotite and chlorite make up ~50% of the sample, alongside accessory diopside, zoisite and epidote (Figure 4-17a). The remainder of the sample is anhedral, sericitized plagioclase and deformed quartz preserving evidence of bulging and sub grain recrystallisation (Figure 4-17a,b).

Samples 6a and 6b-1-10 are from the same outcrop but have very different textures. 6a-1-10 is composed almost entirely of anhedral elongated amphibole crystals, up to 4mm long, with pockets of quartz and plagioclase (Figure 4-17c). Sample 6b-1-10 instead has a fine grained matrix, predominantly made of amphibole, with a mortar like texture (Figure 4-17d). Distinct areas are dominated by plagioclase and quartz, again with a mortar texture, forming pockets throughout the amphibole rich matrix (Figure 4-17e,f). Larger amphibole and quartz porphyroblasts are seen throughout the sample (Figure 4-17f).

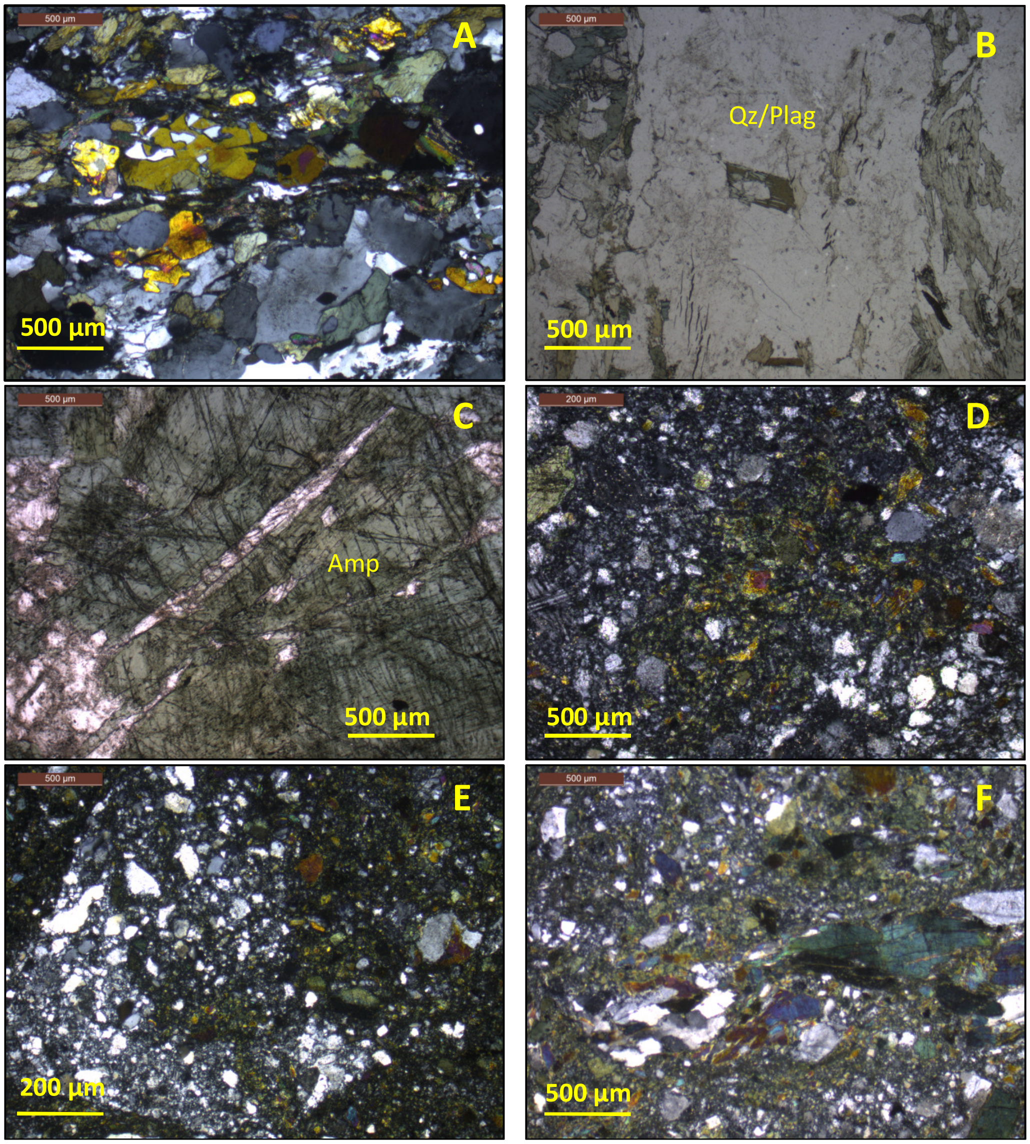

Figure 4-17: Photomicrographs of Bubino amphibolite samples. A: Anherdral amphibole and sericitisized plagioclase alongside dynamically recrystallised quartz from sample 4-1-10, B: Quartz and plagioclase band in sample 4-1-10, C: Large anhedral amphibole crystal, sample 6a-1-10, D: fine grained amphibole rich matrix, sample 6b-1-10, E: pocket of fine grained felsic material, sample 6b-1-10, F: Larger amphibole, plagioclase and quartz crystals surrounded by fine grained matrix, sample 6b-1-10

4.4.3.2 Byala-Reka and Kesebir domes

4 garnet bearing amphibolites were studied from the flanks of the two metamorphic domes: samples 7b-1-02, 12-1-02, 18-1-11 and 19-1-11. With the exception of 12-1-02 all contain poikioblastic garnet porhyroblasts, alongside a pervasive foliation defined by amphibole and epidote, that post-dates garnet formation (Figure 4-18a,b). Garnets are heavily fractured and resorbed, containing abundant inclusions of epidote and clinozoisite (Figure 4-18,d). The matrix is predominantly amphibole and epidote, with areas of heavily coroded poikioblastic plagioclase crystals (Figure 4-18). Epidote crystals can reach up to

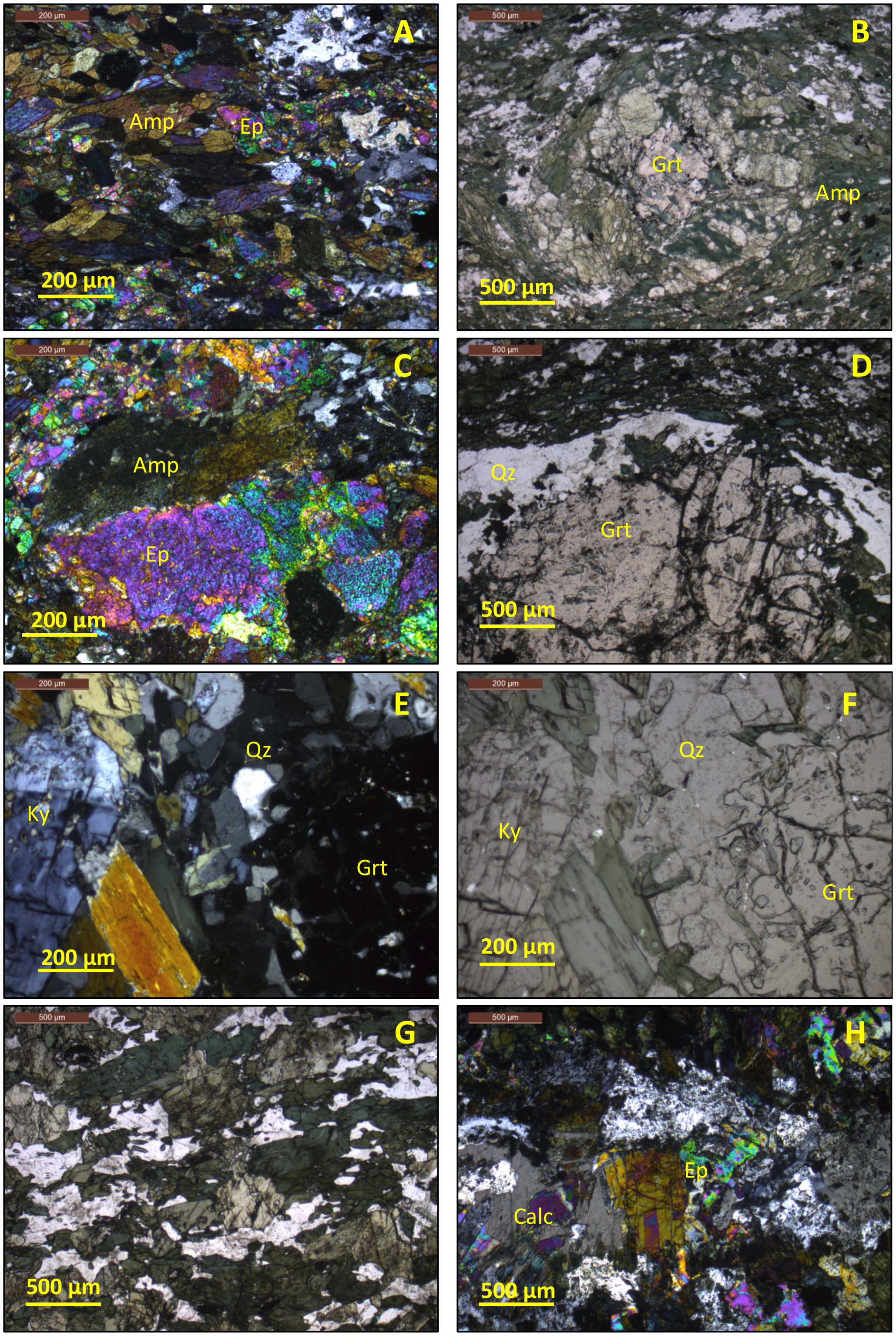

Figure 4-18: Photomicrographs of samples from flanks of the Byala-Reka and Kesebir domes. A: Foliation defined by amphibole and epidote crystal, alongside large resorbed porphyroblastic plagioclase crystals from sample 19-1-11, B: Resorbed garnet and associated amphibole and chlorite surrounded wrapped by foliated amphibole in sample 19-1-11, C: Large amphibole crystal altering to epidote in sample 19-1-11, D: Large inclusion rich fractured and resorbed garnet, surrounded by quartz vein parallel to foliation in sample 18-1-11, E & F: Resorbed kyanite crystal and small, strongly resorbed garnet from sample 12-1-02, G: Anhedral, orientated amphibole and strongly resorbed plagioclase from sample 8-1-10, H: Calcite, plagioclase and epidote rich vein of sample 15-1-11.

1mm in diameter and are seen forming form amphibole (Figure 4-18c). Quartz veins parallel to foliation are common, displaying evidence of dynamic recrystallisation (Figure 4-18d). Sample 12-1-02 is unique amongst all mafic samples from the Eastern Rhodope Mts., due to heavily resorbed kyanite porphyroblasts throughout the matrix (Figure 4-18e,f). Garnet is rare, and where present crystals are small and highly resorbed, containing inclusions of quartz (Figure 4-18e,f).

Samples 8-1-10, 9-1-10 and 15-1-11 are the 3 non-garnet bearing samples from this area. Samples 8-1-10 and 15-1-11 have a clear foliation defined by amphibole and chlorite crystals, which range from elongated and prismatic to anhedral in shape (Figure 4-18g). A series of discontinuous quartz veins run parallel to the foliation. Poikioblastic anhedral plagioclase crystals are common, containing inclusions of zoisite/epdiote. A large (3mm thick) calcite, epidote and plagioclase vein is seen cross cutting sample 15-1-11(Figure 4-18h). Sample 9 -1-10 is predominantly plagioclase and quartz. These crystals form spherical pockets outlined by amphibole and chlorite, up to 1 cm in diameter.

4.4.3.3 Ivaylovgrad

The two samples from Ivaylovgrad are very different. Sample 26-1-11, from the dam wall contains small (<300 µm) euhedral-subhedral inclusion poor garnets within a matrix of predominantly large (up to 2mm diameter), subhedral, amphibole and clinopyroxene (augite/diopside) crystals (Figure 4-19a,b). There are many examples of garnet included within amphibole crystal. Areas of the matrix contain clinozoisite – plagioclase symplectites (Figure 4-19b). Epidote is present, but restricted to a vein network that cross-cuts the entire sample. Sample 27-1-11 closely resembles the garnet-amphibolites from the flanks of the metamorphic domes. Garnets are anhedral (Figure 4-19c), and a clear foliation is defined by elongated prismatic amphibole crystals, and associated epidote and poikioblastic plagioclase (Figure 4-19d).

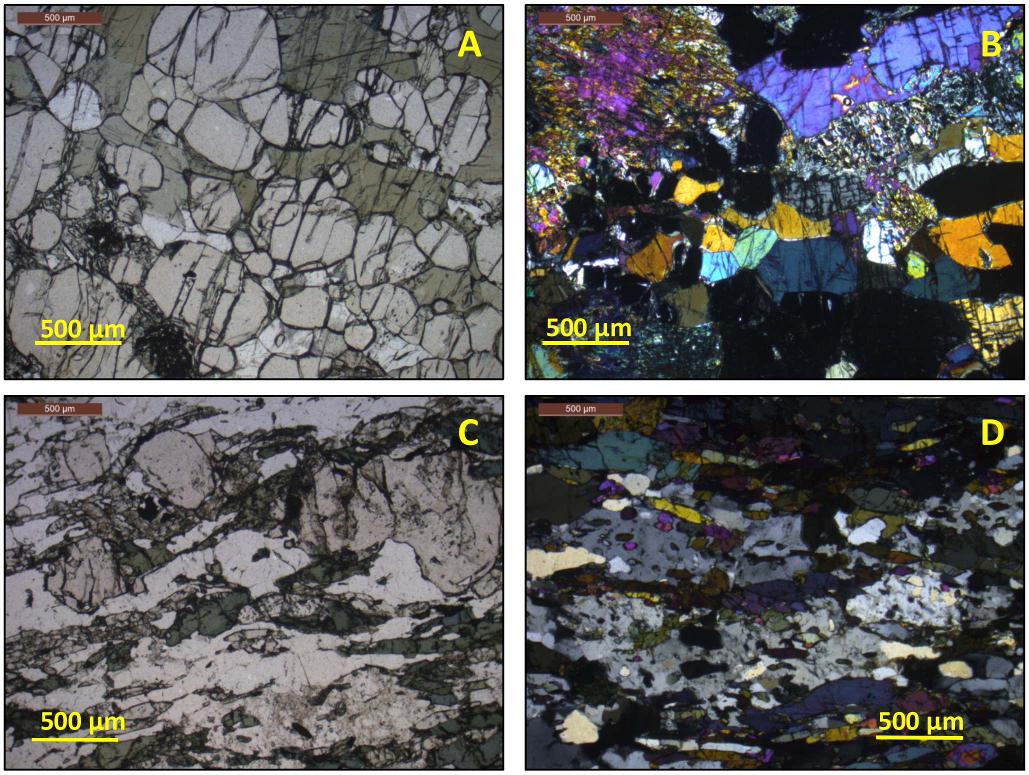

Figure 4-19: Photomicrographs of eclogite samples from Ivaylovgrad. A: Small subhedral inclusion free garnets, hosted by larger subhedral amphibole crystals (sample 26-1-11), B: Diopside and amphibole crystals, alongside small inclusion free garnet and clinozoisite plagioclase symplectite (sample 26-1-11), C: Elongated amphibole and chlorite crystals, small resorbed inclusion poor garnets and foliation parallel quartz veins (sample 27-1-11), D: Poikioblastic anhedral plagioclase crystals, alongside elongated amphibole crystals (sample 27-1-11).

4.4.3.4 Zlatovgrad

Samples 4-1-11 and 7-1-11 come from Zlatovgrad, an area of the upper high grade basement unit 30 km NW of the Kesebir dome. Both samples are composed of elongated, foliated amphibole and plagioclase. In sample 4-1-11 amphibole and plagioclase are coarse grained and subhedral, ~1 mm in length (Figure 4-20a). Sample 7-1-11 is fine grained, and contains a number of discontinuous quartz veins parallel to the sample foliation (Figure 4-20b).

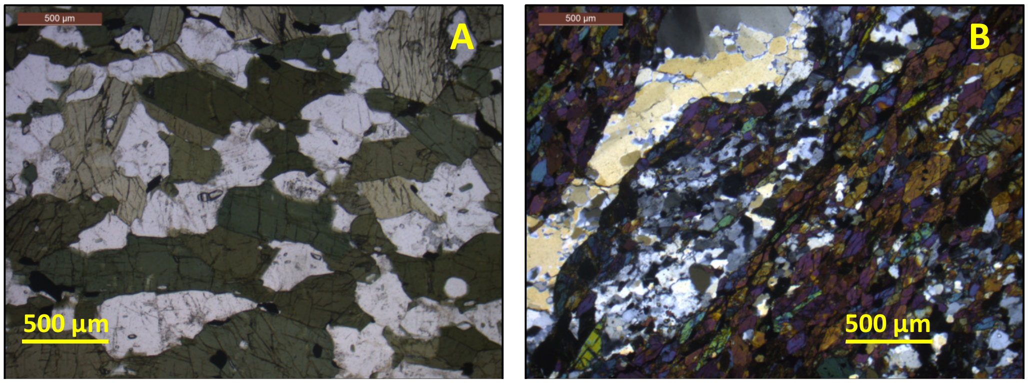

Figure 4-20: Photomicrographs of samples from Zlatovgrad. A: Coarse grained elongated amphibole and plagioclase crystals (sample 4-1-11), B: Fine grained elongated amphibole, and foliation parallel quartz vein (sample 7-1-11).

4.4.3.5 Implications of petrographical observations

Widespread petrographical variation is seen amongst the metabasic samples of the Bulgarian Eastern Rhodope Mts. Some samples, such as those from Bubino exhibit no evidence of a HP garnet-amphibolite/eclogite facies metamorphic event. Here, the observed petrographic differences are likely a result of contrasting protoliths and post metamorphic deformation. Sample 26-1-11, from Ivaylovgrad, is the only sample which texturally resembles the eclogites from the Central Rhodope Mts. The clinozoiste-plagioclase symplectites in this sample could represent a further degree of retrogression following the hydration of omphacite. Kyanite porphyroblasts in sample 12-1-02 also indicate a previous HP metamorphic event, likely from the breakdown of anorthite. No omphacite, or amphibole-plagioclase/diopside-plagioclase symplectite which would indicate eclogite facies conditions were found in any of the samples

Varying degrees of retrogression in greenschist facies between samples is recorded, with both epidote and clinozoisite commonly seen both as veins and constituent parts of the matrix. Veining of calcite and epidote in some samples likely reflects differing degrees of interaction with other units of the upper high grade basement unit.

4.4.4 Mineral Chemistry and Thermobarometry

4.4.4.1 Garnet

The major element chemistry of garnets from 4 samples was measured from the Eastern Rhodope Mts. (2 from the Avren Synform, 1 from Egrek and 1 from Ivaylovgrad). Results are presented in Table 4-9, and a graphical representation of the garnet composition for each sample is presented in Figure 4-21. All analysed garnets from the Eastern Rhodope Mts. are almandine rich ($Alm_{43.3\text{-}59.1}$). Large variation is seen in both pyrope ($Pyp_{5.9\text{-}25}$) and spessartine ($Sps_{1.2\text{-}8.9}$) content, but grossular is consistent in all samples ($Gross_{22.3\text{-}29.3}$). No consistent variation is seen between the core and rim in any sample. The most pyrope rich sample (26-1-11 from the Ivaylovgrad dam) is also the sample with lowest almandine and spessartine content.

		19-1-11			26-1-11				12-1-02		7b-1-02	
		Rim	Mid	Core	Rim	Mid	Core	Small	rim	core	rim	core
Oxide wt%, O by stoichiometry	SiO_2	37.5	37.5	37.4	39.0	39.0	39.0	39.0	38.2	38.1	37.3	37.4
	TiO_2	0.2	0.1	0.2	0.0	0.0	0.0	0.0	0.1	0.1	0.1	0.1
	Al_2O_3	20.8	20.8	20.8	21.5	21.6	21.5	21.4	21.7	21.6	21.0	21.1
	Cr_2O_3	0.0	0.0	0.0	0.0	0.0	0.0	0.0	0.0	0.1	0.0	0.0
	Fe_2O_3	1.4	1.4	1.4	0.8	0.8	0.8	0.8	0.0	0.1	0.6	0.7
	FeO	26.5	27.0	25.9	20.5	20.5	20.4	20.3	23.9	23.6	25.1	25.6
	MnO	3.4	3.2	3.9	0.6	0.5	0.6	0.5	3.4	3.8	2.8	3.3
	MgO	1.5	1.6	1.4	6.5	6.7	6.7	6.2	4.0	4.0	3.5	2.9
	CaO	9.9	9.7	10.1	10.9	10.7	10.7	11.5	8.6	8.6	8.4	8.6
	total	101.1	101.2	101.0	99.9	99.9	99.8	99.8	100.0	99.9	98.9	99.6
	Fe=FeO	27.8	28.2	27.1	21.3	21.2	21.1	21.0	23.9	23.7	25.7	26.2
Cations to 12 O	Si	3.0	3.0	3.0	3.0	3.0	3.0	3.0	3.0	3.0	3.0	3.0
	Ti	0.0	0.0	0.0	0.0	0.0	0.0	0.0	0.0	0.0	0.0	0.0
	Al	1.9	1.9	1.9	1.9	2.0	2.0	1.9	2.0	2.0	2.0	2.0
	Cr	0.0	0.0	0.0	0.0	0.0	0.0	0.0	0.0	0.0	0.0	0.0
	Fe^{3+}	0.1	0.1	0.1	0.0	0.0	0.0	0.0	0.0	0.0	0.0	0.0
	Fe^{2+}	1.8	1.8	1.7	1.3	1.3	1.3	1.3	1.6	1.6	1.7	1.7
	Mn	0.2	0.2	0.3	0.0	0.0	0.0	0.0	0.2	0.3	0.2	0.2
	Mg	0.2	0.2	0.2	0.7	0.8	0.8	0.7	0.5	0.5	0.4	0.3
	Ca	0.8	0.8	0.9	0.9	0.9	0.9	0.9	0.7	0.7	0.7	0.7
	total	8.0	8.0	8.0	8.0	8.0	8.0	8.0	8.0	8.0	8.0	8.0
	Mg#	9.0	9.2	8.6	36.1	36.8	37.1	35.1	23.1	23.3	19.9	16.9
	And	4.2	4.1	4.1	2.4	2.3	2.4	2.5	0.0	0.3	1.9	2.0
	pyp	5.9	6.2	5.5	24.9	25.6	25.8	23.7	15.8	15.8	14.0	11.7
	Sps	7.7	7.2	8.9	1.2	1.2	1.3	1.2	7.5	8.4	6.3	7.4
	Gross	24.2	23.4	24.8	27.5	27.2	26.9	29.3	24.1	23.8	22.3	22.6
	alm	58.1	59.1	56.6	43.8	43.7	43.5	43.3	52.4	51.6	55.5	56.3
	n	12	19	13	22	26	13	8	8	7	7	6

Table 4-9: Summary of EPMA analyses of garnet from the Eastern Rhodope Mts.

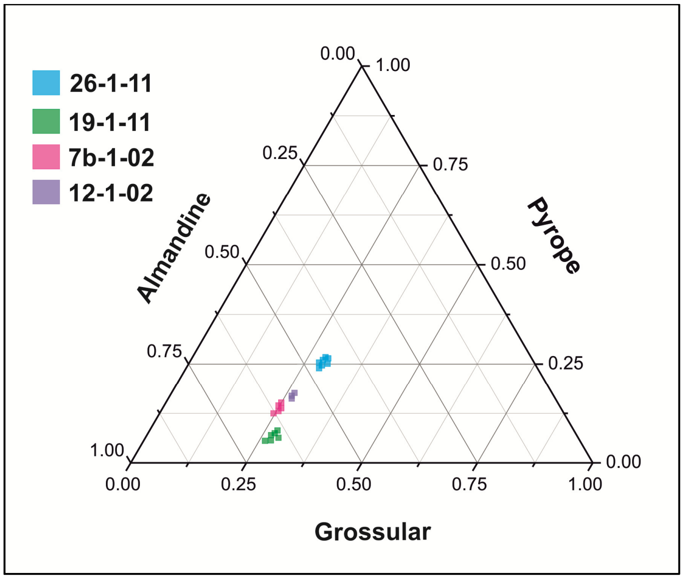

Figure 4-21: Ternary diagram showing garnet compositions for Eastern Rhodope metabasic samples

4.4.4.2 Amphibole

The major element chemistry of amphibole was measured for 7 samples from across the Eastern Rhodope Mts. A summary of all results is presented in Table 4-10. Following the Leake et al. (1997) classification scheme, all amphiboles analysed during this study are calcic, with $Ca_B \geq 1.5$. All analyses are plotted on the relevant classification diagrams (Figure 4-22a,b), with the division being based on the $(Na+K)_A$ content of each analysis.The majority of samples have a broad range of compositions spanning the tschermakite and magnesio-hornblende fields. Samples 4-1-10, 8-1-10 and 26-1-11 all contain some crystals with an elevated $(Na+K)_A$ content, plotting in the pargasite field. Sample 26-1-11 contains the broadest range of amphibole compositions of all analysed samples. In addition, some analyses plot in the actinolite and edenite fields. Like the amphibole analyses from the Central Rhodope Mts. a strong correlation is observed between both $(Na+K)_A$ and Al_{IV} and Ti and A_{lIV} (Figure 4-23), again reflecting the broad spectrum of metamorphic grades under which these amphiboles formed (Spear, 1993).

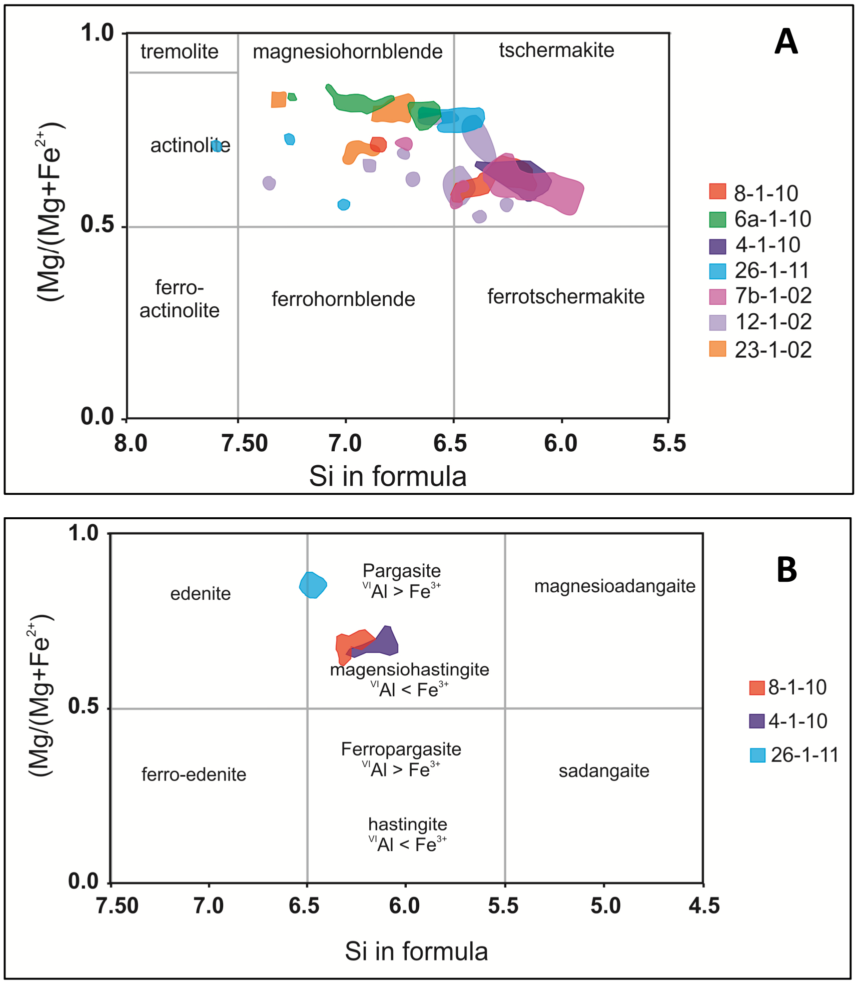

Figure 4-22: Classification of calcic amphibole using diagrams from Leake et al. (1997). A: analyses with CaB ≥ 1..5, $(Na+K)_A < 0.5$ & $Ca_A < 0.5$, B: Amphibole analyses where $Ca_B \geq 1.5$, $(Na+K)_A$, ≥ 0.5 & Ti < 0.5

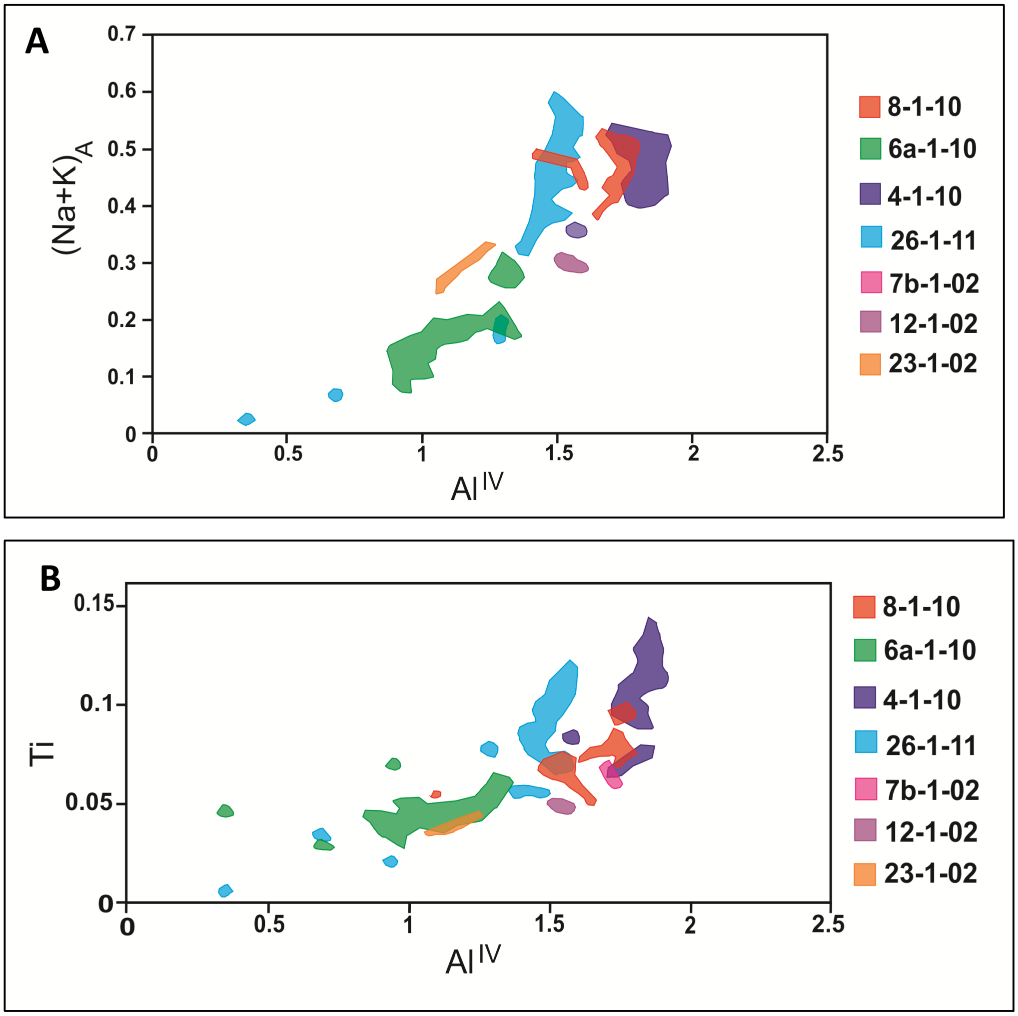

Figure 4-23: Plot of amphibole mineral chemistry. A: Plot of $(Na+K)_A$ vs Al^{IV}, B: Plot of Ti vs AlI^{V}

		Bubino				Avren Synform						Ivaylovgrad			
		4-1-10		6a-1-10		8-1-10		7b-1-02		12-1-02		23-1-02		26-1-11	
		core	rim	core	rim	core	rim	core	rim	core	rim	core	rim	core	rim
Oxide wt%, O by stoichiometry	SiO_2	40.2	40.7	48.0	46.8	42.2	42.2	42.5	42.7	44.5	44.8	47.0	48.3	45.4	45.7
	TiO_2	1.0	0.8	0.4	0.5	0.7	0.6	0.6	0.6	0.4	0.4	0.4	0.3	0.9	0.7
	Al_2O_3	16.2	14.3	7.9	9.7	13.4	13.0	14.0	13.7	14.5	14.1	11.1	9.4	13.3	13.5
	Cr_2O_3	0.0	0.0	0.1	0.1	0.0	0.1	0.0	0.0	0.1	0.1	0.1	0.3	0.0	0.0
	Fe_2O_3	5.3	5.4	6.0	6.1	5.3	5.1	6.0	6.0	4.2	4.1	4.1	3.6	2.2	2.8
	FeO	9.6	10.7	4.6	5.3	10.1	10.7	10.7	10.6	8.3	9.0	6.9	6.8	7.4	6.6
	MnO	0.3	0.4	0.2	0.2	0.2	0.2	0.3	0.4	0.3	0.3	0.3	0.2	0.0	0.1
	MgO	8.2	8.6	15.4	14.5	10.7	10.5	10.5	10.7	11.8	11.6	13.9	14.8	14.2	14.2
	CaO	12.6	12.1	11.5	11.3	11.4	11.6	10.9	10.7	11.5	11.6	11.5	11.7	11.8	11.7
	Na_2O	1.6	1.5	1.2	1.5	1.8	1.7	1.9	1.9	1.6	1.6	1.7	1.4	2.4	2.2
	K_2O	0.9	0.7	0.2	0.2	0.7	0.6	0.2	0.3	0.3	0.3	0.5	0.3	0.1	0.1
	F	0.0	0.0	0.0	0.0	0.0	0.0	0.0	0.0	0.0	0.0	0.0	0.0	0.0	0.0
	Cl	0.0	0.0	0.0	0.0	0.0	0.0	0.0	0.0	0.0	0.0	0.0	0.0	0.0	0.0
	H_2O*	2.0	2.0	2.1	2.1	2.0	2.0	2.0	2.0	2.0	2.0	2.0	2.0	2.1	2.1
	Total	98.0	97.2	97.5	98.4	98.5	98.3	99.9	99.8	99.6	100.1	99.7	99.3	99.8	99.8
Cations to 23O	Si	6.1	6.2	7.0	6.8	6.3	6.3	6.3	6.3	6.4	6.5	6.8	6.9	6.5	6.5
	Al iv	1.9	1.8	1.0	1.2	1.7	1.7	1.7	1.7	1.6	1.5	1.2	1.1	1.5	1.5
	Al vi	0.9	0.8	0.3	0.4	0.7	0.6	0.7	0.7	0.9	0.9	0.6	0.5	0.7	0.8
	Ti	0.1	0.1	0.0	0.1	0.1	0.1	0.1	0.1	0.0	0.0	0.0	0.0	0.1	0.1
	Cr	0.0	0.0	0.0	0.0	0.0	0.0	0.0	0.0	0.0	0.0	0.0	0.0	0.0	0.0
	Fe3+	0.6	0.6	0.6	0.7	0.6	0.6	0.7	0.7	0.5	0.4	0.4	0.4	0.2	0.3
	Fe2+	1.2	1.4	0.6	0.6	1.3	1.3	1.3	1.3	1.0	1.1	0.8	0.8	0.9	0.8
	Mn	0.0	0.0	0.0	0.0	0.0	0.0	0.0	0.1	0.0	0.0	0.0	0.0	0.0	0.0
	Mg	1.8	1.9	3.3	3.1	2.4	2.3	2.3	2.3	2.6	2.5	3.0	3.2	3.0	3.0
	Ca	2.0	2.0	1.8	1.8	1.8	1.9	1.7	1.7	1.8	1.8	1.8	1.8	1.8	1.8
	Na	0.5	0.4	0.3	0.4	0.5	0.5	0.5	0.6	0.5	0.4	0.5	0.4	0.7	0.6
	K	0.2	0.1	0.0	0.0	0.1	0.1	0.0	0.1	0.1	0.0	0.1	0.1	0.0	0.0
	Total	15.4	15.4	15.1	15.2	15.5	15.5	15.4	15.4	15.3	15.3	15.3	15.2	15.5	15.4
	n	13	16	19	15	12	14	3	4	5	7	5	5	9	18

Table 4-10: Summary of amphibole EPMA analyses from across the Eastern Rhodope Mts.

4.4.4.3 Plagioclase

The major element chemistry of plagioclase from 7 samples from across the Eastern Rhodope Mts. was measured. A summary of all results is presented in Table 4-12. Plagioclase from all samples is albite rich ($Ab_{65.9-80.3,}$ $An_{18.9-37.7}$), and display a consistent albite enrichment in the core of crystals relative to the rim. Plagioclase from samples 26-1-11 and 12-1-02 are andesine, and all other analyses are oligoclase. One crystal of bytownite ($Ab_{15.6}An_{84.3}$) was analysed in sample 12-1-02.

4.4.4.4 Eastern Rhodope Mts. Thermobarometry

The lack of distinct indicators for eclogite facies metamorphism in all samples from the Eastern Rhodope Mts. could indicate a larger range of valid geothermobarometers for this suite of samples. Preliminary tests conducted using the garnet-hornblende thermometer (Ravna, 2000) and the garnet-amphibole-plagioclase-quartz barometer (Kohn and Spear, 1990) however yielded low pressure and temperature estimates (temperatures between 400 and 560 °C and pressures between 7.5 and 11 Kbar) indicating that garnet was not in equilibrium with plagioclase or amphibole in these samples. As such, pressures and temperatures were calculated using the amphibole-plagioclase thermobarometers described in section 4.3.6. The composition of adjacent minerals from the matrix of samples was used for calculations, resulting in minimum estimates for pressures and temperatures experienced by samples. Results are presented in Table 4-11. Temperatures calculated using the Holland and Blundy (1994) amphibole-plagioclase thermometer range between 580 and 710 °C, and pressures calculated using the Bhadra and Bhattacharya (2007) amphibole-plagioclase barometer range between 2.5 and 12.2 Kbar.

A	n	average	max	min	stdev
4-1-10	9	679.3	708.5	648.8	20.9
6a-1-10	10	622.5	657.3	583.0	25.4
8-1-10	11	671.1	693.1	649.1	13.8
26-1-11	12	680.0	693.8	646.9	13.8

B	n	average	max	min	stdev
4-1-10	9	7.0	10.0	5.8	1.4
6a-1-10	9	4.9	6.0	2.5	1.1
8-1-10	11	9.8	12.2	8.2	1.5
26-1-11	12	7.8	8.9	6.3	1.0

Table 4-11: Summary of thermobarometric results for Eastern Rhodope Metabasic samples. All temperatures are reported in °C, and all pressures are reported in Kbar. A: Temperature estimates determined using the amphibole plagioclase thermometer of Holland and Blundy (1994), B: Pressures estimated using the amphibole-plagioclase barometer of Bhadra and Bhattacharya (2007).

	Bubino				**Avren Synform**						**Ivaylovgrad**			
	4-1-10		**6a-1-10**		**8-1-10**		**7b-1-02**		**12-1-02**		**23-1-02**		**26-1-11**	
	core	**rim**	**core**	**rim**	**core**	**rim**	**core**	**rim**	**core**	**rim**	**core**	**rim**	**core**	**rim**
SiO_2	63.4	62.2	63.4	62.7	62.1	61.3	63.2	62.2	60.8	59.3	63.4	62.7	48.1	48.0
TiO_2	0.0	0.0	0.0	0.0	0.0	0.0	0.0	0.0	0.0	0.0	0.0	0.0	0.0	0.0
Al_2O_3	23.0	24.1	23.2	23.5	24.0	24.5	22.8	23.3	24.9	25.6	23.1	23.1	26.1	25.3
FeO	0.1	0.2	0.1	0.2	0.1	0.2	0.2	0.4	0.1	0.2	0.1	0.2	0.3	0.1
MnO	0.0	0.0	0.0	0.0	0.0	0.0	0.0	0.0	0.0	0.0	0.0	0.0	0.0	0.0
MgO	0.0	0.0	0.0	0.0	0.0	0.0	0.0	0.0	0.0	0.0	0.0	0.0	0.2	0.0
CaO	4.1	5.0	4.1	4.5	5.1	5.7	4.1	4.7	6.2	7.1	4.2	4.3	15.6	16.0
Na_2O	9.6	9.1	9.6	9.3	9.0	8.8	9.3	9.1	8.2	7.7	9.4	9.3	4.3	4.6
K_2O	0.2	0.2	0.1	0.2	0.2	0.2	0.1	0.1	0.1	0.1	0.1	0.2	0.0	0.0
TOTAL	100.4	100.8	100.5	100.4	100.6	100.7	99.7	99.8	100.4	100.1	100.4	99.9	94.6	94.1
Si	2.9	2.8	2.8	2.8	2.7	2.7	2.8	2.8	2.7	2.6	2.8	2.8	2.3	2.4
Al	1.2	1.3	1.2	1.2	1.2	1.3	0.0	0.0	0.0	0.0	0.0	0.0	0.0	0.0
Ti	0.0	0.0	0.0	0.0	0.0	0.0	1.2	1.2	1.3	1.3	1.2	1.2	1.5	1.5
Fe	0.0	0.0	0.0	0.0	0.0	0.0	0.0	0.0	0.0	0.0	0.0	0.0	0.0	0.0
Mn	0.0	0.0	0.0	0.0	0.0	0.0	0.0	0.0	0.0	0.0	0.0	0.0	0.0	0.0
Mg	0.0	0.0	0.0	0.0	0.0	0.0	0.0	0.0	0.0	0.0	0.0	0.0	0.0	0.0
Ca	0.2	0.2	0.2	0.2	0.2	0.3	0.2	0.2	0.3	0.3	0.2	0.2	0.8	0.8
Na	0.8	0.8	0.8	0.8	0.8	0.8	0.8	0.8	0.7	0.7	0.8	0.8	0.4	0.4
K	0.0	0.0	0.0	0.0	0.0	0.0	0.0	0.0	0.0	0.0	0.0	0.0	0.0	0.0
Total	5.0	5.0	5.0	5.0	5.0	5.0	5.0	5.0	5.0	5.0	5.0	5.0	5.1	5.1
Or	1.1	1.1	0.8	0.9	1.2	1.3	0.5	0.4	0.6	0.6	0.8	0.9	0.1	0.0
Ab	79.8	75.9	80.3	78.2	75.1	72.7	79.9	77.3	69.7	65.5	79.7	78.9	66.7	65.9
An	19.0	22.9	18.9	20.9	23.7	26.0	19.6	22.3	29.6	33.9	19.5	20.2	33.2	34.0
n	3	10	9	13	8	11	5	3	13	15	6	6	14	12

Table 4-12: Summary of plagioclase EPMA analyses from the Eastern Rhodope Mts.

4.4.4.5 Summary of key observation and implications for P-T history of samples

The range of pyrope content of garnet seen across the area confirms the petrographic observations, with sample 26-1-11 appearing the most eclogitic sample in section 0, and correspondingly having the highest pyrope content of the garnets analysed. The two samples with the highest pyrope contents have the broadest range of amphibole compositions, spanning tschermakite to actinolite, indicating prolonged retrograde metamorphism under amphibolite – greenschist facies conditions. This could explain the lack of evidence beyond garnet composition for HP metamorphism. The lack of variation between remaining samples, in both mineral composition and P-T estimates indicates pervasive amphibole facies metamorphism for all samples across the Eastern Rhodope Mts.

4.4.5 Bulk rock Geochemistry

The whole rock major element chemistry of 5 metabasic samples and trace element chemistry of 12 metabasic samples from the Eastern Rhodope Mts. were measured. Major element concentrations are presented in Table 4-13 and trace and REE concentrations are presented in Table 4-14.

	Bubino			Avren	Egrek
Sample	**4-1-10.**	**6a-1-10.**	**6b-1-10.**	**8-1-10.**	**9-1-10.**
SiO_2	62.4	49.6	51.7	51.3	57.3
Al_2O_3	13.7	8.9	15.6	13.9	16.6
FeO	7.3	10.6	10.0	12.0	8.0
MgO	3.7	15.3	6.9	7.7	4.6
MnO	0.1	0.2	0.2	0.2	0.2
CaO	6.4	10.7	9.7	9.7	6.7
K_2O	1.2	0.3	0.2	0.6	0.3
Na_2O	3.3	1.5	3.6	2.7	5.2
TiO_2	1.0	0.4	0.9	1.3	0.9
P_2O_5	0.3	0.0	0.1	0.1	0.2

Table 4-13: Major element composition of 5 metabasic samples from the Eastern Rhodope Mts, measure via ICP-AES. All values are reported as Wt. %.

4.4.5.1 Discrimination diagrams

For the same reasons outlined in section 4.3.7.1, an igneous protolith has been assumed for all samples. As with the metabasic samples from the Central Rhodope Mts., a number of different discrimination diagrams have been used to constrain the protolith of individual samples (Figure 4-24). A diverse range of protoliths are suggested on the Hf-Th-

Ta and Zr-Nb-Y diagrams (Figure 4-24a,b), encompassing MORB, island arc basalts and within plate basalt. This is not reflected in the discrimination diagrams of Vermeesch (2006) drawn using linear discriminant analysis (Figure 4-24c-f). The diagrams utilising the immobile elements Ti,V and Sm (Figure 4-24c,e,f) all suggest that protoliths are either MORB or IAB, with a larger population of MORB samples. The restriction of all samples to the IAB field on the Eu-Lu-Sr diagram (Figure 4-24d) is likely the result of the increased mobility of these elements relative to Ti, V and Sm, rather than being a true reflection of the protolith.

	Li	Sc	TiO2 (Wt%)	V	Cr	Co	Ni	Cu	Zn	Rb	Sr	Y	Zr	Nb	Cs	Ba
4-1-10*	1.9	21.6	1.0	128.7	93.4	22.2	223.2	52.4	72.4	17.8	166.6	49.3	210.4	14.9	0.3	246.0
6a-1-10*	5.7	27.4	0.4	219.9	953.5	34.9	386.2	14.4	95.3	5.6	28.7	12.6	23.1	0.6	0.2	37.7
6b-1-10*	1.8	34.2	0.9	269.8	206.7	31.7	72.7	22.2	68.1	3.2	184.6	25.7	51.1	0.8	0.5	75.1
8-1-10*	27.6	43.7	1.3	295.6	208.0	31.7	65.9	50.8	95.7	7.1	206.3	34.7	83.2	4.4	0.2	41.7
9-1-10*	4.4	25.7	0.9	150.9	119.6	18.4	40.4	60.4	98.4	1.9	232.2	27.6	199.2	56.4	0.2	419.8
4-1-11	9.0	39.1	1.9	354.0	87.5	47.1	48.6	8.4	60.5	4.2	165.7	38.3	14.5	6.8	0.1	60.5
7-1-11	23.8	43.7	2.2	400.6	90.4	44.2	54.0	56.1	117.9	6.1	115.4	51.0	4.8	3.6	0.0	34.1
15-1-11	5.7	32.4	0.9	243.8	52.9	41.6	49.8	109.3	66.7	5.2	313.9	15.8	7.3	1.9	0.0	47.4
18-1-11	10.2	44.8	1.8	322.3	146.4	61.4	87.5	82.7	94.0	8.8	343.0	31.0	6.7	8.6	0.8	30.7
19-1-11	9.6	41.6	2.3	312.1	92.9	53.3	62.1	114.9	108.2	9.1	161.4	34.3	5.2	11.1	1.7	110.2
26-1-11	9.0	51.9	1.3	568.1	8.5	64.5	9.7	185.3	97.3	8.4	106.0	7.3	2.6	5.6	0.3	60.5
27-1-11	9.1	35.3	0.6	260.8	81.7	36.4	32.0	7.7	108.7	2.7	149.2	25.3	5.6	0.8	0.0	46.2

	La	Ce	Pr	Nd	Sm	Eu	Gd	Tb	Dy	Ho	Er	Yb	Lu	Hf	Ta	Th	U
4-1-10*	59.8	114.5	13.9	59.0	13.5	2.3	10.8	1.6	7.9	1.6	4.7	5.2	0.7	5.7	0.9	10.4	1.2
6a-1-10*	0.9	3.2	0.6	3.2	1.1	0.5	1.4	0.3	1.9	0.4	1.2	1.3	0.2	0.7	0.1	0.4	0.3
6b-1-10*	4.0	9.1	1.5	8.3	2.9	1.0	3.1	0.7	4.0	0.9	2.3	2.5	0.4	1.6	0.1	0.9	0.3
8-1-10*	4.4	10.5	1.7	9.1	3.3	1.1	3.9	0.9	5.3	1.2	3.3	3.6	0.5	2.2	0.3	0.3	0.2
9-1-10*	21.8	40.8	5.5	24.2	5.5	1.5	4.9	1.1	4.5	1.0	2.7	2.9	0.4	7.3	3.5	6.1	1.4
4-1-11	7.7	20.6	3.2	15.1	4.8	1.5	5.7	1.0	6.3	1.4	3.8	3.6	0.5	0.8	0.4	0.7	0.2
7-1-11	5.4	16.3	2.8	14.2	5.0	1.7	6.8	1.2	8.0	1.8	5.0	4.6	0.7	0.3	0.3	0.3	0.1
15-1-11	3.8	9.7	1.5	7.4	2.3	0.8	2.5	0.4	2.6	0.6	1.6	1.4	0.2	0.4	0.2	0.4	0.1
18-1-11	8.7	21.1	3.1	14.3	4.3	1.4	5.1	0.9	5.3	1.1	3.1	2.8	0.4	0.3	0.4	0.6	0.2
19-1-11	10.5	26.6	4.0	18.4	5.3	1.8	6.0	1.0	6.2	1.2	3.5	2.9	0.4	0.3	0.5	0.9	0.3
26-1-11	0.3	1.0	0.2	1.2	0.6	0.6	1.0	0.2	1.3	0.3	0.9	0.8	0.1	0.2	8.2	0.0	0.0
27-1-11	5.6	12.6	1.8	8.6	2.7	0.9	3.3	0.6	3.9	0.9	2.6	2.3	0.3	0.4	0.1	1.2	0.6

Table 4-14: Whole rock trace and REE concentrations for Eastern Rhodope Metabasic samples. Samples marked with * were analysed at RHUL, all remaining samples were analysed at the Open University, summer 2013.

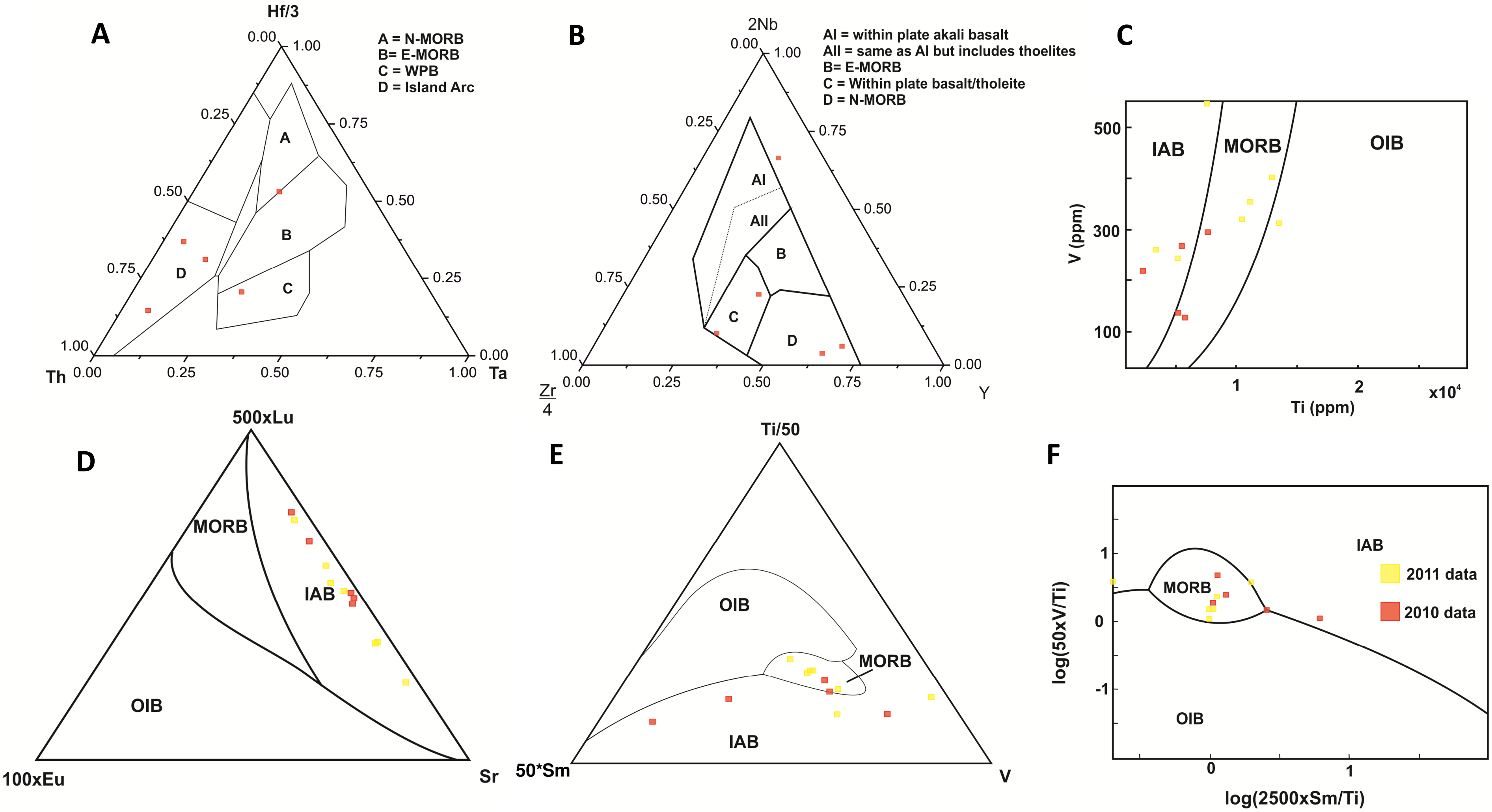

Figure 4-24 Tectonic discrimination diagrams for metabasic samples from the Eastern Rhodope Mts. A: 2010 samples plotted on Th-Hf-Ta discrimination diagram of Wood (1980), B :2010 sample plotted on Zr-Nb-Y diagram of Meschede (1986), C: Ti-V discrimination of Shervais (1982) redrawn using linear discriminant analysis (Vermeesch, 2006), D: Ternary discrimination diagram utilising Eu, Sr and Lu (Vermeesch, 2006) E & F: Discrimination diagrams utilising immobile element Ti, Sm and V plotted as a ternary diagram (E) and in log ratio space (F) (Vermeesch, 2006). MORB: Mid Ocean Ridge Basalt, OIB: Ocean Island Basalt, IAB: Island Arc Basalt

4.4.5.2 Chondrite normalised REE diagrams

Chondrite normalised REE diagrams for all of the Eastern Rhodope metabasic units are presented in Figure 4-25. Patterns range from strongly LREE depleted with a positive Eu anomaly to strongly LREE enriched with a negative Eu anomaly. $(La/Sm)_N$ ratios range from 0.3 to 2.8. All samples from the Avren Synform have flat to LREE enriched profiles. Sample 26-1-11 from the Ivaylovgrad dam wall exhibits the strongest LREE depletion ($(La/Sm)_N$ = 0.35), closely followed by sample 6a-1-10 from Bubino ($(La/Sm)_N$ = 0.54). Samples from Bubino exhibit the largest variation from a single area with $(La/Sm)_N$ ranging between 0.54 and 2.8. With the exception of samples 26-1-11 and 4-1-10, little to no Eu anomaly is seen in any of the samples, with Eu/Eu* ranging between 0.7 and 1.2.

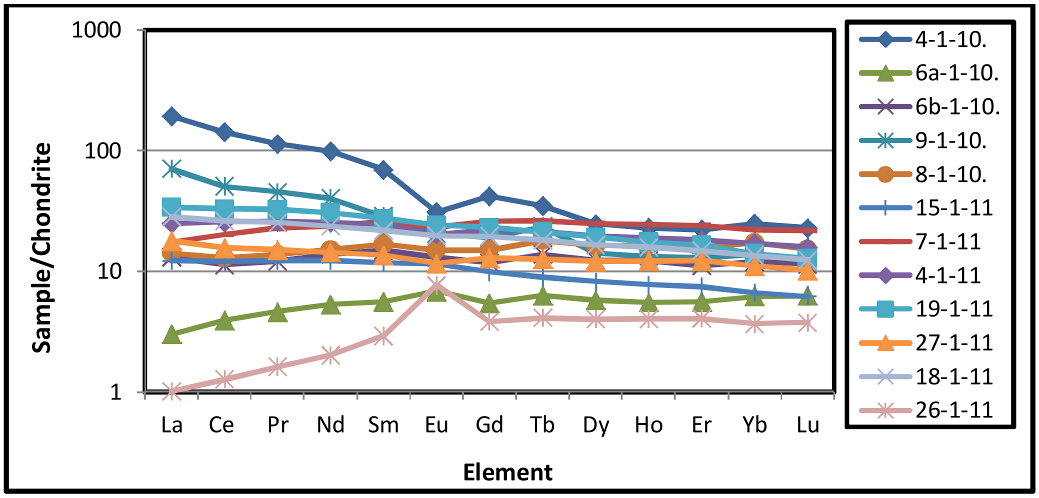

Figure 4-25: Chondrite normalised REE diagram for metabasic samples from across the Eastern Rhodope Mts. Normalising values from Boynton (1985)

4.4.5.3 MORB normalised trace element diagrams

N-MORB normalised trace element diagrams, with elements plotted in order of increasing compatability are presented in Figure 4-26**.** As with the Central Rhodope samples, most analyses from the Open University in 2013 exhibit strong Zr and Hf depletions, attributed to incomplete zircon dissolution. HFSE profiles are uniformly flat, but concentrations relative to MORB vary greatly. There is no distinct pattern for the LILE; widespread variation is seen in both the absolute concentration of individual elements and their behaviour relative to neighbouring elements. Approximately half of the samples preserve a negative Nb-Ta anomaly relative to U and La. Sample 26-1-11 is unique with a strong enrichment in Ta, U and Th depletions, and the lowest overall concentration of HFSE. At Bubino, widespread variation is seen from within the same outcrop. Sample 6a-1-10 has a uniformly flat HFSE profile, with some of the lowest concentrations, whereas sample 6b-1-

10 has a strong negative Nb-Ta anomaly, and HFSE concentrations akin to N-MORB. There is no correlation between $(La/Sm)_{\text{Chondrite normalised}}$ and $(La/Nb)_{\text{MORB normalised}}$.

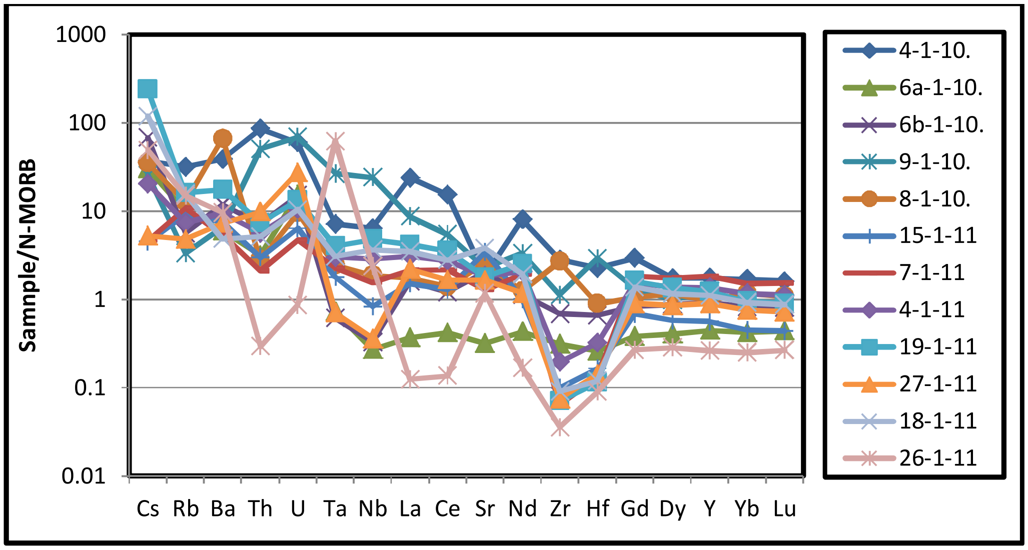

Figure 4-26: N-MORB normalised trace element data from across the Eatsern Rhodope Mts. Normalising values from McDonough and Sun (1995)

4.4.5.4 Radiogenic Isotope geochemistry

Whole rock Sr and Nd isotope measurements were made on 11 samples from across the Eastern Rhodpe Mts. As with the Central Rhodope Mts. samples, large variation was seen in *f*Rb values, indicating crustal contamination. Results of the Sr isotope can be found in appendix B. Nd isotope measurements are presented in Table 4-15.As a result of unclear protolith ages, initial ratios have been calculated for protolith ages of both 570 Ma and 250 Ma.

	Sample	$^{143}Nd/^{144}Nd$	570 Ma		250 Ma		*f*Sm
			initial	ε^{t}_{Nd}	initial	ε^{t}_{Nd}	
Avren Synform	1-14-02	0.512884 ± **7**	0.512053	2.92	0.512520	3.98	0.13
	1-24-02	0.512986 ± **18**	0.512171	5.22	0.512629	6.10	0.11
	1-8-02	0.512780 ± **16**	0.511910	0.12	0.512399	1.61	0.18
	8-1-10	0.512987 ± **5**	0.512172	5.24	0.512630	6.12	0.11
	9-1-10	0.512508 ± **4**	0.511990	1.70	0.512281	-0.68	-0.30
Ivaylovgrad	23-1-02	0.512608 ± **6**	0.511953	0.97	0.512321	0.09	-0.11
	27-1-11	0.512750 ± **7**	0.512049	2.85	0.512443	2.48	-0.05
Bubino	4-1-10	0.512385 ± **5**	0.511866	-0.72	0.512158	-3.09	-0.29
	6a-1-10	0.512934 ± **6**	0.512160	5.01	0.512595	5.44	0.05
	6b-1-10	0.512940 ± **4**	0.512152	4.85	0.512595	5.44	0.07
Zlatovgrad	4-1-11	0.512932 ± **7**	0.512221	6.20	0.512620	5.94	-0.03

Table 4-15: Summary of Nd isotope data for Eastern Rhodope metabasic samples

Irrespective of the formation age used, large variations are seen in ε^t_{Nd} values, with Neoproterozoic protolith ages yielding ε^t_{Nd} values between -0.7 and 5.2, and Triassic ages yielding ε^t_{Nd} between -3.1 and 6.1. There is no geographical pattern to this variation, with samples from the same area yielding contrasting ε^t_{Nd} values. This indicates contrasting protoliths and/or formation ages between samples across the Eastern Rhodope Mts.

4.4.5.5 Synthesis of whole rock geochemistry

Geochemical analysis of the Eastern Rhodope metabasic units indicates a broad array of protoliths. Tectonic discrimination diagrams, trace element geochemistry and Nd isotopes all indicate protoliths ranging from N-MORB through to island arc basalts. This is particularly apparent on the REE plots, with $(La/Sm)_N$ ranging from 0.3 to 2.8. At first glance, there is no obvious trend in sample protolith on the basis of geographical location, with contrasting protoliths from the same area. Samples 6a-1-10 and 6b-1-10 from Bubino are essentially the same outcrop, reflected in the near identical ε^t_{Nd} values, yet large differences are observed in the REE and trace element geochemical profiles. The LREE depleted profile of sample 6a-1-10 is characteristic of an N-MORB protolith, whereas sample 6b-1-10 has a flat REE profile and a distinct negative Nb-Ta anomaly indicative of an increased SSZ component. The same contrasting protolith characteristics are seen in samples from Ivaylovgrad (26-1-11 and 27-1-11).

Of the samples from the Avren Synform and the flanks of the Byala-Reka and Kesebir domes, with the exception of sample 9-1-10 from Egrek, there is less indication of a SSZ input. These samples have flat REE profiles $(La/Sm)_N$ ranging between 0.67 and 1.23, no negative Nb and Ta anomaly on the MORB normalised trace element diagram, and positive ε^t_{Nd} values indicative of a MORB protolith. This would suggest that two distinct populations of metabasic samples can be identified across the Eastern Rhodope Mts.; one suite of samples where SSZ units are juxtaposed against MORB, and a second suite of MORB samples that lack this distinctive SSZ signature.

4.4.6 Discussion of metabasic samples from the Eastern Rhodope Mts.

This study has demonstrated the diverse and complex evolution of metabasic samples from across the Eastern Rhodope Mts. Few distinctions can be made between samples on the basis of petrographic observations; likely the result of the complex metamorphic history and variable P-T conditions experienced by samples. Sample geochemistry does however provide valuable information regarding protoliths across the Eastern Rhodope Mts.

Protoliths associated with a SSZ environment from Bubino are in keeping with bonninites previously reported from this area by Haydoutov et al. (2004). The diversity reported from the same outcrop at Bubino in this study (samples 6a-1-10 and 6b-1-10) does however indicate the juxtaposition of oceanic crust from contrasting tectonic settings. This same trend of contrasting MORB and SSZ signatures is seen for the two Ivaylovgrad samples (26-1-11 and 27-1-11) and in the metabasic samples studied by Bonev et al. (2013) from the eastern flank of the Kesebir-Kardamos dome, in the vicinity of Egrek. Sample 9-1-10, also from Egrek, shares some of the SSZ characteristics with LREE enrichment and a low ε^{t}_{Nd} value. U-Pb zircon dating of these outcrops suggests Neoproterozoic (Carrigan et al., 2003) and Ordovician (Bonev et al., 2013) formation ages, with Carboniferous, Jurassic and Eocene metamorphic overprints. On this basis, these outcrops in Bulgaria appear to record a distinct Variscan metamorphic cycle, and were used as evidence for a Variscan aged suture between the upper and lower high grade basement by Haydoutov et al. (2004).

The existence of a second, distinct population of metabasic samples with a stronger MORB affinity from the Avren Synform is supported by existing geochronological data. The oldest age of zircon from eclogite in the adjacent Kimi Complex of the Greek Rhodope Mts. is 288 Ma, and the youngest reported age of inherited zircon in the associated UHP metapelites is 300 Ma (Bauer et al., 2007). These younger zircon ages from the Kimi Complex indicate a history postdating both formation and metamorphism of samples from Bubino and Egrek, and raise doubts concerning the existence of a Variscan suture between the upper and lower high grade basement units of the Eastern Rhodope Mts.

How the Kimi Complex relates to the upper high grade basement of the Bulgarian Eastern Rhodope Mts. is poorly constrained. The Kimi Complex is mapped as a distinct tectonic slice separated from neighbouring regions by large scale Late Eocene/Oligocene detachment faults (Krohe and Mposkos, 2002). A clear tectonic contact, observed in the field, marks the boundary between the upper high grade basement and gneiss of the Byala-Reka dome, likely the continuation of the basal detachment fault of the Kimi complex. The western extent of the Kimi complex into Bulgaria is however unclear, and a number of different faults (normal, thrust and detachment) have been mapped throughout the Avren Synform, which could mark the boundary between the middle and upper allochthon. If the MORB samples of the Avren Synform represent a continuation of the Kimi Complex into Bulgaria, this would explain the contrasting metabasite populations identified in this study.

Jahn-Awe et al. (2010) however did not separate the Kimi Complex from the remainder of the upper high grade basement unit of the Eastern Rhodope Mts. In their study all units were attributed to the upper allochthon, and the boundary with the lowermost allochthon was proposed to represent a Cenozoic suture. The heterogeneous nature of metabasic units of the upper high grade basement of the Eastern Rhodope Mts. presented in this study suggests the grouping of all units together is an over simplification, and further work is required to establish the limits of the pre and post Variscan metamorphic units of the Eastern Rhodope Mts.

4.5 Comparison of metabasic samples from the Central and Eastern Rhodope Mts.

A link between the metabasic units of the Central and Eastern areas on the basis of shared stratigraphic relationships and boninitic/Island arc protoliths has previously been proposed (Daieva et al., 2007). This connected history is reinforced by the discovery of microdiamond inclusions in garnet from metapelitic units from across the RM (Mposkos and Kostopoulos, 2001, Schmidt et al., 2010). Exact linkages are however complicated by contrasting stratigraphic terminology between studies, and a wide array of proposed formation and metamorphic ages for individual units (See chapter 5).

This chapter has highlighted the varied nature of the metabasic units over a small area in the central Rhodope Mts. There is a clear distinction between the VF and Arda units on the basis of both geochemistry and field relationships that reinforces the previously reported conflicting geochronological data. This same distinction of two populations is observed in the Eastern Rhodope Mts. As such, there is a population of Pre-Mesozoic metabasic samples unrelated to the UHP metamorphic event across the RM.

Contrasting protoliths are seen within this Pre-Mesozoic group of samples. The MORB nature of many of the Pre-Mesozoic samples from the Eastern Rhodope Mts., combined with an increased amount of associated ultramafic units relative to the Central Rhodope Mts. could reflect increased preservation of oceanic crust/sheeted dyke complex, essentially the basement units of a more complete ophiolite succession. The Arda units of the Central Rhodope Mts. would then represent only the overlying island arc portion of the oceanic crust. In that sense the entire life cycle of a Variscan subduction-exhumation event is recorded in this suite of samples. This scenario is hard to reconcile with the reported Eocene eclogite ages reported by Kirchenbaur et al. (2012), unless their garnet-whole rock

Lu-Hf ages are recording exhumation and emplacement processes rather than the peak metamorphic event.

A MORB protolith is recognised across the RM for all garnet bearing amphibolite samples within the VF. This common protolith, combined with the shared UHP conditions for metapelites as reported in chapter 3, requires a novel exhumation mechanism to emplace the 'melange' at different stratigraphic levels across the massif. The mechanism proposed by Mposkos et al. (2010)**,** whereby all units of the VF are part of the same subducting slab, and the current stratigraphy of the Central Rhodope Mts. is the result of fragments of the Upper Allochthon being caught beneath the lower Allochthon during Cenozoic thrusting is a viable scenario. The timing of this subduction event and the associated peak metamorphic event is a controversial topic, and will be discussed in detail in chapter 5.

4.6 Chapter Summary

- Two contrasting populations of metabasic units have been identified in both the Central and Eastern Rhodope Mts.
- An older, Pre-Mesozoic population records a diverse range of protoliths incorporating both MORB and SSZ protoliths
- A second group of metabasic samples with MORB protoliths are found within the VF, in close association with the UHP units. There is no indication that these samples experienced the same UHP conditions as the associated metapelites
- Common links between both populations have been recognised across the Rhodope Massif

Chapter 5 : Timing of UHP metamorphism across the Rhodope Massif

5.1 Introduction

As alluded to in chapter 2, the timing of UHP metamorphism across the Rhodope Massif is unclear. A number of different ages have been proposed in the literature, ranging from 171 Ma to 40 Ma, and 4 viable time periods have been suggested for the UHP metamorphic event across the RM (Liati et al., 2011). In this chapter, I report new Sm-Nd garnet ages for the metapelites from the Central and Eastern Rhodope Mts. studied in chapter 3. I discuss the validity of these new ages and their implication for the tectonic evolution of the Rhodope Massif.

5.2 Overview of existing geochronolgical data

5.2.1 The Rhodope Massif

In recent years a large number of geochronological studies have been conducted across the Rhodope Massif, utilising a variety of different dating techniques. A summary of all existing age data for the age of the metamorphic event across the RM is presented in Table 5-1, and presented as a histogram in Figure 5-1

Age (Ma)	Error (±Ma)	Rock Type	Location	Dating technique	Reference
567		Eclogite	C-RM BG	Lu-Hf Grt-Omp	(Savov et al., 2007)
~300		Metagabbro	E-RM BG	U-Pb zircon	(Carrigan et al., 2003)
~300		Eclogite	C-RM BG	Lu-Hf Grt-Omp	(Savov et al., 2007)
~186		metapelite	C-RM GC	U-Pb Monazite	(Reischmann and Kostopoulos, 2002b)
171	1	metapelite	E-RM GC	U-Pb zircon	(Bauer et al., 2007)
~160		Eclogite	E-RM GC	U-Pb zircon	(Bauer et al., 2007)
160	1	Metapelite	E-RM GC	U-Pb zircon	(Bauer et al., 2007)
153	13	Amphibolite	C-RM GC	Sm-Nd Grt	(Kostopolous, in Burg (2011))
~150		Garnet Gneiss	E-RM GC	U-Pb zircon	(Liati et al., 2011)
~150		Metapelite	C-RM BG	U-Pb Monazite	(Didier et al., 2012)
148.8	2.2	Paragneiss	C-RM GC	U-Pb zircon	(Liati, 2005)
147.2	4.7	Paragneiss	C-RM GC	U-Pb zircon	(Liati, 2005)
143.4	3.3	Eclogite	C-RM GC	U-Pb zircon	(Liati, 2005)
~140		Metapelite	C-RM BG	U-Pb monazite	(Bosse et al., 2010)
140	4	Metapelite	C-RM GC	Sm-Nd Grt	(Reischmann and Kostopoulos, 2002b)
~130		Metapelite	C-RM GC	U-Pb zircon	(Krenn et al., 2010)
126	0.7	Eclogite	C-RM BG	Lu-Hf Grt	(Kirchenbaur et al., 2012)

Age (Ma)	Error (±Ma)	Rock Type	Location	Dating technique	Reference
119	3.5	Garnet-Pyroxenite	E-RM GC	Sm-Nd Grt	(Wawrzenitz and Mposkos, 1997)
117	1.9	Garnet amphibolite	E-RM GC	U-Pb zircon	(Liati et al., 2002)
~115		Eclogite	E-RM GC	U-Pb zircon	(Bauer et al., 2007)
82.8	1.3	Paragneiss	C-RM GC	U-Pb zircon	(Liati, 2005)
79	3	Eclogite	E-RM GC	U-Pb zircon	(Bauer et al., 2007)
~77		Pegmatites	C-RM GC	U-Pb zircon	(Bosse et al., 2009)
73.9	0.8	Garnet Gneiss	E-RM GC	U-Pb zircon	(Liati et al., 2011)
73.5	3.4	Grt Amphibolite	E-RM GC	U-Pb zircon	(Liati et al., 2002)
72.9	1.1	Pyroxenite	E-RM GC	U-Pb zircon	(Liati et al., 2002)
71.4	1.1	Orthogneiss	E-RM GC	U-Pb zircon	(Liati et al., 2011)
55.9	7.2	Orthogneiss	C-RM BG	U-Pb zircon	(von Quadt et al., 2006)
51	1	Garnet Amphibolite	C-RM GC	U-Pb zircon	(Liati and Fanning, 2005)
~50		Metapelite	C-RM BG	U-Pb monazite	(Didier et al., 2012)
49.1	6	Metagabbro	E-RM BG	U-Pb zircon	(Bonev et al., 2010a)
~43		Eclogite	C-RM BG	Lu-Hf Grt	(Kirchenbaur et al., 2012)
42.4	1.4	Pyroxenite	C-RM GC	U-Pb zircon	(Liati et al., 2011)
42.2	0.9	Amp Eclogite	C-RM GC	U-Pb zircon	(Liati et al., 2002)
42.1	1.2	Pegmatites	C-RM BG	U-Pb Monazite	(Bosse et al., 2009)
~40		Leucosome	C-RM GC	U-Pb zircon	(Liati et al., 2002)
~40		Metapelite	C-RM BG	U-Pb Monazite	(Bosse et al., 2010)
39.7	1.2	Lecuosome	C-RM GC	U-Pb zircon	(Liati, 2005)
38.1	0.8	Garnet Amphibolite	C-RM GC	U-Pb zircon	(Liati, 2005)

Table 5-1: Summary of all available published metamorphic ages for the Rhodope Massif. E-RM: Eastern Rhodope Mts., C-RM: Central Rhodope Mts., GC: Greece, BG: Bulgaria, OMP: omphacite, Grt: Garnet.

It is clear from both Table 5-1 and Figure 5-1 that pulses in metamorphic activity have occurred during the formation of the RM. Accordingly, recreating the history of the RM and placing constraints on the timing of the UHP metamorphic event(s), particularly for the oldest units is extremely difficult. A recent review paper (Liati et al., 2011) further refined the pulses shown in Figure 5-1 to suggest 4 HP events, all of which are possible for the age of UHP metamorphism. These are ca. 150 Ma, ca. 73 Ma, ca. 51 Ma and ca, 42 Ma. As shown in Table 5-1, the majority of ages are U-Pb zircon dates. Although a very robust chronometer, with a high closure temperature that results in geological meaningful ages (Lee et al., 1997), it has the additional complication of inheritance, and the complexity of multiple metamorphic rims on single grains. In recent year this has been combated via trace element analysis, which has been used to distinguish magmatic and metamorphic zones within individual crystals. Zircon that formed under high pressure conditions has been shown to have a flatter REE profile and a smaller negative Eu anomaly than their magmatic counterparts (Rubatto, 2002). Zircons from all four of the possible UHP age groups have these HP indicators, and as such constraining the UHP event through zircon geochronology is problematic (Liati et al., 2011).

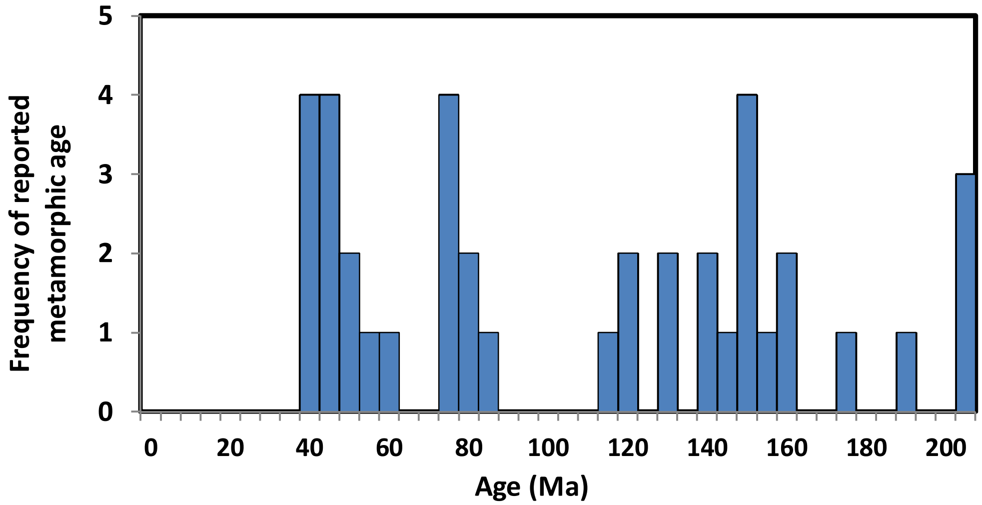

Figure 5-1: Histogram of ages displayed in Table 5-1. The 3 distinct post Variscan episodes of (U)HP metamorphism are shown, with peaks focused around ca. 150 Ma, 80 Ma & 45 Ma. Bin size: 5 Ma.

In the Liati et al. (2011) study the Jurassic (ca. 150 Ma) was favoured as the most likely time for UHP metamorphism, due to the lack of extensive recrystallization of the ca. 150 Ma zircon domain, which would be expected with subsequent UHP metamorphism. They do however concede that a Jurassic UHP event fails to explain the preservation of microdiamond inclusions and exsolution textures within garnets in the same samples, and all four periods are possible candidates for the timing of UHP metamorphism.

Studies attempting to date garnet, the only host of UHP indicators across the RM yield largely contrasting results, with ages ranging from 567 Ma, to 40 Ma. The Neoproterozoic and Carboniferous ages from metabasic samples are interpreted as relicts of the Pan African and Hercynian Orogeny (Carrigan et al., 2005, Savov et al., 2007) which have been correlated with ages from ophiolite successions in the Balkan Terrane to the North (Savov et al., 2001). These are therefore unrelated to the UHP metamorphic event. The remaining garnet ages broadly coincide with the pulses recognised in the zircon record. The majority of these studies have focused on dating eclogite. Only one study has dated garnets from a

UHP metapelite unit in the RM (Reischmann and Kostopoulos, 2002b), which yielded a 140 Ma age.

One anomaly is a 119 Ma age reported from a garnet pyroxenite body in the Kimi complex, which was interpreted as the timing of eclogite facies metamorphism (Wawrzenitz and Mposkos, 1997). The only similar reported age is 117 Ma reported for oscillatory zircon domains from a garnet rich mafic rock (Liati et al., 2002), which was interpreted as the time of crystallisation of a (U)HP cumulate. The relationship between these mid-Cretaceous ages and the proposed (U)HP events remains unclear.

5.2.2 Geochronology of the Bulgarian Central Rhodope Mts.

Significantly less geochronological work has been performed on the Bulgarian Central Rhodope Mts. relative to the rest of the Rhodope Massif. The oldest ages in the Central Rhodope Mts. come from eclogite samples hosted by the Arda 2 gneiss. Neoproterozoic protolith ages are recorded in the cores of zircons from two samples: U-Pb TIMS dating of zircons from a gabbroic eclogite yielded ages of ~ 610 Ma, whereas zircons from a basaltic eclogite yielded ages of ~ 560 Ma, 440 Ma and 265 Ma (Arkadakskiy et al., 2003). These ages, alongside a Carboniferous metamorphic overprint have also been replicated in eclogites from the Central Rhodope Mts. and the Ograzhden Mts. to the west, dated via Lu-Hf Grt-Omph geochronology (Savov et al., 2007). These dates have been used, in conjunction with Variscan zircon rims from the Eastern Rhodope Mts. (Carrigan et al., 2003), to infer a widespread Variscan HP metamorphic event across the entire RM. The relationship between these Neoproterozoic eclogites and the HP/UHP units of the UHP units of the VF, as discussed in chapter 4, is currently unconstrained (Burg, 2011).

On the basis of Y concentrations two populations of monazite have been identified in metapelities from the Chepelare Shear Zone (Bosse et al., 2010, Didier et al., 2012). Monazite inclusions in garnet and kyanite are uniformly depleted in Y, where matrix crystals have strong Y enrichment in the rim, likely the result of garnet resorbtion. These two zones reveal distinctly different ages; Y poor regions produced ^{208}Pb/^{232}Th ages between 130 and 155 Ma, whereas Y rich regions produced Cenozoic ages between 40 and 50 Ma. These Cenozoic ages are inkeeping with monazite dates from pegmatites hosted by felsic gneiss within the Variegated Formation, interpreted as the formation age of this body (Bosse et al., 2009). In the same study, U-Pb zircon dating did not reveal such a clear story, with Triassic zircon cores surrounded by complex Late Cretaceous overgrowth patterns. These were interpreted as relicts from one or more Mesozoic metamorphic cycles (Bosse et al., 2009).

As discussed in chapter 4, Cenozoic ages are also reported from eclogite samples within the Chepelare Shear Zone (Kirchenbaur et al., 2012). In this study, Lu-Hf garnet-whole rock dating yielded ages of 45 Ma. Fission track dating of zircons and apatites from gneiss and associated migmatites from the Central Rhodope Mts. also all yield Eocene – Oligocene ages, ranging from 35 – 20 Ma (Wüthrich, 2009). It remains unclear whether these ages represent a regional cooling event from amphibolite to greenschist facies (Burg, 2011), or an Eocene HP subduction exhumation cycle (Nagel et al., 2012).

5.3 Sample selection

In this study, 5 kyanite-garnet schist samples from the vicinity of Chepelare were chosen for Sm-Nd garnet geochronology in the TIMS facility at Boston University. These samples were selected to encompass the three main petrographic end members described in detail in chapter 3. Samples 3-1-10 and 38-1-11 both have a strong foliation defined by biotite, samples 27-1-10 and 2-1-11 both have a quartz rich matrix with little biotite, and sample 47-1-11 is one of the samples donated by the Bulgarian Natural History Museum with no visible matrix. A map showing the location of each sample is presented in Figure 5-2. In addition, one kyanite-garnet schist sample (sample 11-1-11) and a layered serpentinised garnet peridotite sample (sample 22-1-11) were dated from the Bulgarian part of the Kimi complex in the Eastern Rhodope Mts. 6 garnet amphibolite and eclogite samples were also prepared for Sm-Nd garnet dating, but unfortunately their partial dissolution technique (See section 5.5.1) could not be perfected and no meaningful ages were produced. In addition, zircons were extracted and dated from a metagabbro sample in the Eastern Rhodope Mts. (sample 8-1-12).

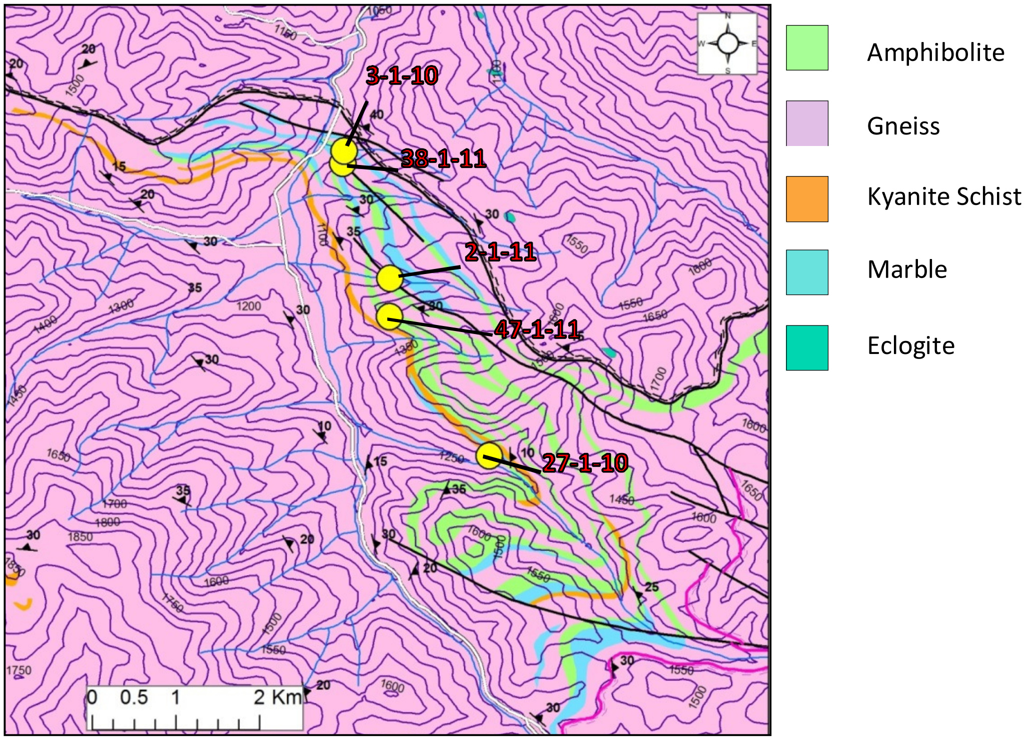

Figure 5-2: Geological map in the vicinity of Chepelare in the Central Rhodope Mts. Location of dated kyanite-garnet schist samples are highlighted

5.4 Overview of garnet geochronology

5.4.1 Why date garnet?

Garnet is a key metamorphic mineral that occurs over a wide range of conditions and in a diverse array of tectonic settings. It generally records prograde growth conditions, and often preserves chemical and age zonation upon exhumation (Baxter and Scherer, 2013). As such, dating the age of garnet crystals is a powerful tool to aid understanding the formation history of a sample. In addition, provenance issues associated with dating of inclusions such as zircon or monazite are removed

A large variety of methods have bee used to date garnets over the years. Early studies attempted to use the U-Pb and Rb-Sr systems (Mezger et al., 1989, Christensen et al., 1989). These were shown to be inappropriate, largely due to vast numbers of inclusions and element mobility in crustal fluids (Sousa et al., 2013). As a result, ^{176}Lu – ^{176}Hf and ^{147}Sm - ^{143}Nd have become the isotope systems of choice for dating the age of a garnet crystal (Baxter and Scherer, 2013). This is the result of ubiquitous HREE enrichment of garnet resulting in high Sm/Nd and Lu/Hf ratios. Both systems are widely used, and tend to complement each other with their own distinct advantages and disadvantages, which are discussed in section 5.4.2

5.4.2 Common problems associated with garnet geochronology

There are a number of issues related to garnet geochronology that need to be addressed in order to correctly interpret garnet ages. These are summarised below

1) Isotope systematics: garnet strongly fractionates Sm over Nd and Lu over Hf – the basis for both systems acting as viable geochronometers. The Lu fractionation is stronger than Sm, resulting in very high Lu/Hf parent daughter ratios, especially in the core of garnets. This has been suggested as a possible explanation for older ages produced for the Lu-Hf system relative to the Sm-Nd system for the same garnet crystals (Skora et al., 2009).

This problem can be exacerbated by the effects of resorption of the garnet crystal (Smit et al., 2010). During resorption, Lu concentrations are raised in the rim of the relict crystal, whereas Hf, due to its incompatible nature is lost from the crystal. This redistribution of Lu and Hf produces ages that are markedly younger than the garnet crystallisation age (Kelly et al., 2011). Conversely, intracrystalline diffusion of Lu relative to Hf can lead to anti clockwise rotation of the isochron, and apparent older ages (Kohn, 2009). A combination of these two factors has been suggested as the reason behind the large spread in ages observed in some Lu-Hf data sets (Anczkiewicz et al., 2012). This is less of a problem for the Sm-Nd system, as there is a much smaller difference in diffusion rate between Sm and Nd (Baxter and Scherer, 2013).

2) Inclusions: The presence of inclusions rich in Hf (rutile, zircon) and Nd (monazite) results in the measurement of artificially high concentrations for these elements in garnet. The consequence of this is a small spread in the parent/daughter isotopes, and as a result a large uncertainty associated with the calculated age. Partial dissolution techniques can be been used to dissolve such inclusions in garnet, therefore removing their effect from the garnet analysis (Dewolf et al., 1996, Anczkiewicz and Thirlwall, 2003, Pollington and Baxter, 2011). Although applicable to the Sm/Nd system where no preferential leaching of Sm vs Nd or vice versa occurs (Pollington and Baxter, 2011), it has been shown that leachates preferentially leach Lu relative to Hf, rendering partial dissolution inappropriate for Lu-Hf dating (Scherer et al., 2000). Instead, techniques that involve preferential dissolution of garnet relative to refractory minerals such as zircon and rutile have been established (Lagos et al., 2007).

3) Thermal resetting: For garnets that experience temperatures > 700 °C, diffusional resetting of their age starts to become a problem. It is widely accepted that the Lu-Hf system has a higher closure temperature than the Sm-Nd system, and retains age information at higher temperatures. Many authors have attempted to put an exact temperature on the effective closure temperature of the Sm-Nd system, and published estimates range from 480 – 900 °C (Smit et al., 2013). The concept of closure temperature is however misleading. It is dependent on a number of factors including, size, composition, exhumation rate. A recent study by Baxter and Scherer (2013), using published kinetic diffusion data for Nd in garnet (Tirone et al., 2005), demonstrated that it would take 360 Ma to reset the age of a 5 mm garnet heated to 700 °C. A 1 mm diameter garnet would only take 14 Ma to reset under the same conditions. As such, it is impossible to assign a single temperature, and a number of different factors have to be evaluated to place the Sm-Nd garnet age of high temperature (>700 °C) in context. As shown in chapter 3, metapelites from the vicinity of Chepelare have experienced temperatures in the range of 750 – 850 °C, and as such the impact of closure temperature on the garnet ages will be discussed in detail in section 5.8.1.

5.4.3 Advantage of analysis of garnet as NdO+

The increased ionisation efficiency of NdO+ relative to Nd metal has long been recognised, making the method ideally suited for the analysis of material of small/limited sample size (DePaolo and Wasserburg, 1976, Lugmair et al., 1976). Conventional techniques however to supply a source of oxygen (i.e. an oxygen bleed valve and/or silica gel) result in much poorer precision for NdO^+ analyses when compared to Nd^+. A recent advance in the analysis of very small aliquots (< 10 ng) of Nd via Thermal Ionisation Mass spectrometry has occurred through the use of a Ta_2O_5 phosphoric acid slurry during loading to act as the required oxygen source (Harvey and Baxter, 2009).

Prior to the work of Harvey and Baxter (2009) the best reported external precision for a NdO^+ was 22 ppm (2σ RSD) on a 10-15 ng load of La Jolla standard (Amelin and Rotenberg, 2004). This is significantly higher than the best measurements made with Nd^+, where external precision can be as low as 2ppm (2σ RSD) on a 300 – 500 ng load (Caro et al., 2006). Using the new technique of Harvey and Baxter (2009), studies have demonstrated that 1-10 ng Nd samples yield $^{143}Nd/^{144}Nd$ with 10-20ppm (2σ RSD) precision (Pollington and Baxter, 2011, Dragovic et al., 2012).

5.5 Laboratory technique

5.5.1 Sample preparation and partial dissolution

Samples were crushed using a steel hammer and anvil, from which approximately 0.1 g of garnet were picked and inspected via binoclular microscope to limit the amount of non-garnet material included. The garnet then underwent further hand crushing in a tungsten carbide mortar and pestle to a grain size between 106 µm and 63 µm**,** using a 140-230 mesh sieve. Typical mass loss during this final preparation stage was 50 – 60%. Samples were then processed using a frantz magnetic separator running at 0.5, before a final hand picking stage to ensure only garnet remained.

The garnet samples then underwent a three step partial dissolution procedure to remove all remaining inclusions. This procedure is largely based on that reported by Baxter et al. (2002) but has been modified after subsequent studies (Pollington and Baxter, 2011, Dragovic et al., 2012) and a number of tests on samples from this study. 1 ml of HF was added to samples, before heating on a hotplate at 120 °C for 60 minutes in closed beakers. Samples were ultrasonicated for 5 minutes for every 10 minutes spent on the hotplate. The leachate was then decanted prior to a series of washing and decanting steps using 1.5 N HCl and Milli-Q water. Once dry, 1ml of 1.5N HCl and 2ml of conc $HClO_4$ was added and the samples were heated again in closed beakers for an hour at 150 °C. Samples were ultrasonicated for 5 minutes before and after this heating step. After the final ultrasonication, the beaker is attached to an elbow still and left to dry overnight on a hotplate at 150 °C. Once dry, the wash, ultrasonicate and decant steps using 1.5 N HCl and Milli-Q water were repeated. 2ml of 7N HNO_3 was then added to the samples, which were then heated in closed beakers on a hotplate at 120 °C for 180 minutes. All samples were ultrasonicated for 5 minutes after every 55 minutes on the hotplate. The HNO_3 was then decanted, and the wash, ultrasonicate and decant steps using 1.5 N HCl and Milli-Q water were repeated. The final stage involves partial dissolution in aqua regia. 2ml of 6 N HCl and 500 µl of concentrated HNO_3 were added to samples, which were then ultrasonicated for 5 minutes. Samples were heated in closed beakers on a hotplate for 50 minutes at 120 °C. Following a final ultrasonication for 5 minutes, the wash, ultrasonicate and decant steps using 1.5 N HCl and Milli-Q water were repeated.

Samples were then dried, weighed and inspected under a microscope to ensure that only optically clean garnet remained. Any impurities were removed via handpicking, although their presence was extremely rare. This partial dissolution method, although effective, results in significant volume loss of garnet. On average 45-60% of the sample is lost, which when combined with the initial ~ 50% loss during hand crushing/sieving, results in up to 80% total sample loss during sample preparation.

5.5.2 Chemical separation of Sm and Nd

Once clean, samples underwent full dissolution following a similar process to that described in Harvey and Baxter (2009). Samples were dissolved in 2 ml of HF on a hotplate at ~ 120 °C. Once dissolved, the solutions were dried down and then re-dissolved in a mix of 2ml conc. HNO_3 and 1 ml 6 N HCl. Once dissolved, these samples were again dried down and re-dssolved in a mix of 4ml 1.5 N HCl and 1ml 6N HNO_3. This dissolution procedure failed to fully dissolve whole rock samples owing to the large abundance of kyanite in each sample. As a result, these samples were digested using Parr 4749 general purpose acid digestion bombs in an oven. The same sequence of chemical digestion was used, but samples were left for longer times in the oven to ensure full dissolution. Upon dissolution these samples were again dried down, ready for spiking and chromatographic separation. A mixed ^{147}Sm-^{150}Nd spike was used on all samples. Samples were passed through a series of three columns to separate Nd and Sm. The first column contained a cation exchange resin (AG50w-X4) to remove all Fe from the sample, as Fe has previously been shown to overwhelm the subsequent columns, resulting in a poor yield (Pollington and Baxter, 2011). The second column is a teflon microcloumn containing Eichrom TRU-spec resin to isolate the rare earth elements, before a final 2-methyl lactic acid (MLA) column to separate Sm and Nd. MLA columns are used in preference to LN-spec columns to ensure complete separation of Pr from Nd.

5.5.3 Dating of individual zones from a single garnet crystal

4 large garnet crystals were extracted from kyanite garnet schist samples from the Central Rhodope Mts.; 2 from sample 27-1-10 and 2 from sample 2-1-11. These were cut through the geometric centre of the crystal, and polished to form a 2mm thick wafer. Samples were mapped for Ca, Mg, Fe and Mn via EPMA at the University of Leeds (see Figure 5-3A). A grid spacing of 250 µm was used for all samples. The probe was operated at an accelerating voltage of 15Kv, a probe current of 150 nA and a counting time of 5s for each of the 4 major cations.

The best sample was selected for micro sampling at Boston University, following the procedure outlined in Pollington and Baxter (2011) and Dragovic et al. (2012). Using the Mn elemental map, 5 zones were defined and drilled using a NewWave MicroMill. The garnet wafer was attached to a graphite block using Crystal Bond, a substance that is easily dissolved in acetone and has low concentrations of Nd. The block was surrounded by a water tight Teflon ring which allows drilling whilst the sample is submerged in milli-Q water, both ensuring a neat trench and preservation of the diamond drill bit (Figure 5-3B). Multiple traverses are made of each trench, with each pass drilling 50 µm deep. 5 trenches were drilled to isolate the 5 garnet zones (Figure 5-3A). Once extracted, each zone underwent the same hand crushing, magnetic separation and partial dissolution technique as described in section 5.5.1.

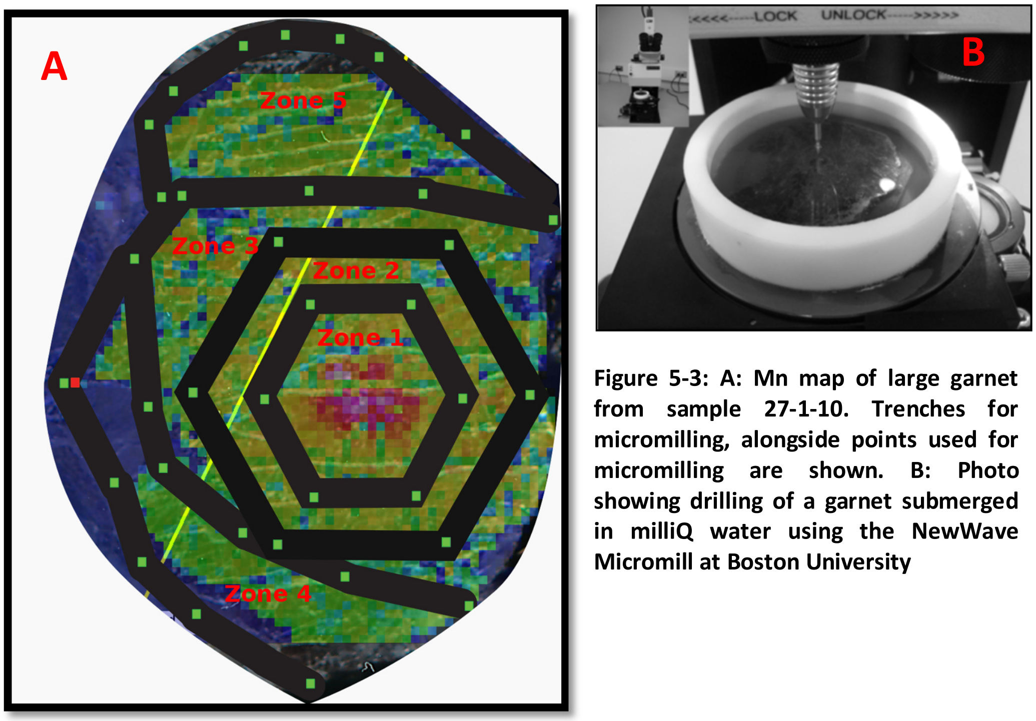

Figure 5-3: A: Mn map of large garnet from sample 27-1-10. Trenches for micromilling, alongside points used for micromilling are shown. B: Photo showing drilling of a garnet submerged in milliQ water using the NewWave Micromill at Boston University

5.5.4 Analytical technique

All samples were analysed at the TIMS facility at Boston University, using a multicollector Thermo Finnigan TRITON mass spectrometer. Nd separates were loaded onto single Re filaments using 1µl of 2 M HNO_3 with 2 µl of H_3PO_4 and Ta_2O_5 activator slurry, as described in Harvey and Baxter (2009). The triton was run in static mode with amplifier rotation, and Nd was measured as NdO^+. In-house Nd standard solution (Ames metal) yielded a mean of $^{143}Nd/^{144}Nd=0.5121318 \pm 0.000016$ (31 ppm, 2 RSD, n=35), and in house Sm standard solution yielded a mean $^{147}Sm/^{152}Sm$ of 0.560820 ± 0.000021 (39ppm, 2 RSD, n=28) over the duration of sample analysis for this study. Whole procedural blanks ranged between 13.4 and 26.1 pg for Nd, and around 3.3 pg for Sm. The blank value for samples that were bombed using acid digestion vessels was measured at 171 pg. This high blank value is the result of contamination restricted to this sample, and is unlikely to be representative of the other samples that were 'bombed'. Unfortunately the Sm blank value could not be calculated, due to a combination of a poor yield from the MLA columns and high pressure when run on the Triton. 3 column blanks ranged between 12 and 20 pg for Nd, and were consistently 1.6 pg for Sm.

5.6 Results – Central Rhodope Mts.

5.6.1 Bulk Garnet Separates

The isotopic compositions of 5 bulk garnet separates are presented in Table 5-3. Multiple repeats were conducted on samples 47-1-11 and 3-1-10, the diamond bearing sample. With the exception of sample 47-1-11, all samples yielded good $^{147}Sm/^{144}Nd$ (>1.0), and low Nd concentrations < 0.5 ppm, suggesting successful elimination of contaminating inclusions. Calculated garnet ages range between 70.3 and 99.6 Ma (Table 5-2). All ages were calculated using the Isoplot Program (Ludwig, 2003).

A	Age	Error
38-1-11	80.6	3.0
27-1-10	89.3	6.0
3-1-10	70.3	2.4
3-1-10 2	70.8	2.7
2-1-11	89.7	2.3
47-1-11	91.5	4.6
47-1-11 2	99.6	5.3

B	Age	Error	MSWD
3-1-10	70.5	1.9	0.08
47-1-11	95	73	8

Table 5-2: A: Age data calculated from 2 point isochrons for kyanite-garnet schist samples from the vicinity of Chepelare. B: Age data calculated using 3 point isochrons (multiple bulk garnet separates)

There are a number of disadvantages to utilising two point iscohrons as used in this technique. Two point isoschrons always define a perfect line, so there is no check on the degree of geological scatter and adherence to isochron assumptions. They do however have the advantage that there is no chance of introducing phases into the isochron that may have formed at different times within the sample; isotopic equilibrium on a two point isochron is significantly more likely. In this study, 2 point isochrons were constructed for all samples studied. In addition, multiple garnet separates were processed for two samples, samples 3-1-10 and 47-1-11, which allowed the construction of multipoint isochrons in addition to the 2-point iscohrons (Figure 5-4).

The isochron for sample 3-1-10 (Figure 5-4a) has a very low MSWD of 0.08, reflecting overestimation of analytical uncertainties in the calculation of the isochron. The high

MSWD value for sample 47-1-11 (Figure 5-4b) is the result of the large error associated with the garnet analyses in this samples, and subsequent increased scatter on the ischron. Despite this, both of these multipoint isochrons do replicate the same ages (within error) as the 2-point isochrons, significantly increasing confidence in the technique used. The reason for the larger error associated with sample 47-1-11 is unclear. Both garnet separates have higher Nd concentrations than the other samples (Table 5-3). Extra time in HF for the 2nd garnet separate actually had the inverse effect of lowering the ^{147}Sm/^{144}Nd ratio. This could be the result of near complete dissolution off all silicate inclusions, resulting in the undesired effect of the HF attacking the garnet that remains, therefore lowering the measured ^{147}Sm/^{144}Nd ratio. Alternatively, there was simply a Nd rich inclusion that the partial dissolution technique failed to eliminate in both analyses, in which case the older (ca. 90 Ma) age for this sample should not be trusted.

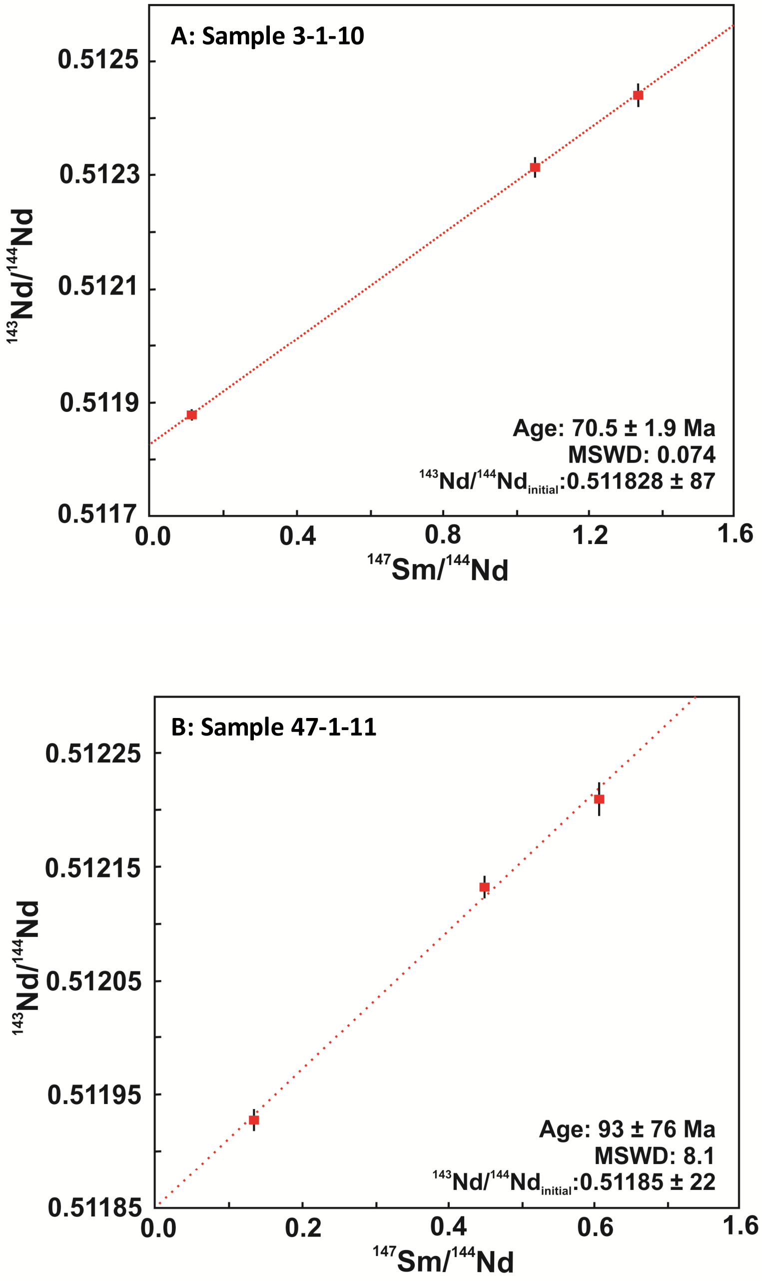

Figure 5-4: A: 3 point iscohron calculated for sample 3-1-10, the diamond bearing sample from Chepelare, Central Rhodope Mts. B: 3 point isochron calculated for sample 47-1-11, the phaneritic "museum" sample, also from Chepelare.

Sample	Sm (ppm)	Nd (ppm)	ng Nd loaded	^{147}Sm/^{144}Nd	± 2 S.E. (ppm)	^{143}Nd/^{144}Nd	± 2 S.E. (ppm)
38-1-11 Grt	1.026	0.367	13.1	1.690875	0.000389	0.512771	0.000030
27-1-10 Grt	1.749	0.498	6.7	2.122316	0.000788	0.513150	0.000079
3-1-10 Grt 1	0.457	0.208	4.4	1.331532	0.000306	0.512441	0.000017
3-1-10 Grt 2	0.537	0.309	9.6	1.049758	0.000085	0.512314	0.000015
2-1-11 Grt	0.837	0.375	10.3	1.351216	0.000430	0.512598	0.000013
47-1-11 Grt 1	1.006	1.005	18.9	0.605892	0.000207	0.512212	0.000012
47-1-11 Grt 2	0.792	1.065	16.9	0.449974	0.000050	0.512135	0.000008
38-1-11 WR	17.392	94.458	72.99	0.111374	0.000026	0.511938	0.000007
27-1-10 WR	10.822	70.294	69.36	0.093124	0.000021	0.511965	0.000006
3-1-10 WR	8.304	45.382	49.21	0.110683	0.000012	0.511879	0.000008
2-1-11 WR	11.950	64.308	78.35	0.112403	0.000026	0.511871	0.000014
47-1-11 WR	2.538	11.294	48.40	0.135933	0.000031	0.511930	0.000008

Table 5-3: Sm-Nd isotope data collected for both whole rock samples and garnet separates. BG: Bulk garnet separate, WR: Whole rock

Sample	Sm (ppm)	Nd (ppm)	ng Nd loaded	^{147}Sm/^{144}Nd	± 2 S.E. (ppm)	^{143}Nd/^{144}Nd	± 2 S.E. (ppm)
27-1-10 Z1	1.184	0.483	6.52	1.482306	0.000547	0.512406	0.000011
27-1-10 Z2	0.410	0.228	1.10	1.090185	0.000467	0.512454	0.000043
27-1-10 Z3	0.818	0.412	3.28	1.201346	0.000313	0.512556	0.000021
27-1-10 Z4	0.927	0.629	10.22	0.891774	0.000307	0.512405	0.000017
27-1-10 Z5	1.046	0.598	3.34	1.058207	0.000243	0.512490	0.000021
27-1-10 P1	3.632	14.675	5.12	0.149733	0.000042	0.511899	0.000013
27-1-10 P5	36.791	220.6	158.4	0.100879	0.000023	0.511846	0.000005

Table 5-4: Sm-Nd isotope data for single zoned garnet crystal. Z1-Z5 correspond to zones 1- 5 defined in Figure 5-3, P1 and P5: Garnet powders collected during hand crushing of zones 1 and 5

5.6.2 Single Zoned Crystal

Results from dating of the five garnet zones from the same large garnet crystal (sample 27-1-10) are reported in Table 5-4. At first glance these ages appear wrong, as it is obviously impossible to have a garnet core younger than its rim. Zone 5 was run through columns at a later date, ensuring there was no mix up in the column chemistry, and these calculated ages are correct for each zone processed.

A younger age for the garnet core is difficult to explain. Commonly, artificially young ages in Sm/Nd garnet geochronology are the result of incomplete removal of younger monazite inclusions during partial dissolution. As the two inner zones underwent the same partial dissolution procedure as the three outer zones, and both have high ^{147}Sm/^{144}Nd values this appears unlikely. A resistant retrograde mineral unique to the garnet core, such as allanite, could explain the anomaly, but none have been identified as inclusions in garnet from the thin section of this sample.

Resorption and recrystallization of the core during retrograde metamorphism, akin to formation of atoll garnet, would explain the age profile, but this is not reflected in thin section textures, and is not in keeping with the prograde zonation preserved in garnet crystals. Younger garnet cores have previously been recognised in garnets form Gore Mountain, in the Adirondack highlands of upstate New York (Mezger et al., 1992). In this study, they attributed the resetting of the core to the result of a denser inclusion population effectively decreasing the grain size and facilitating resetting more easily than the rim. Although possible, it is hard to envisage this occurring when the rims of the crystal preserve no evidence of resetting to this 40 Ma age. Alternatively, a shift in the whole rock ^{143}Nd/^{144}Nd occurred between growth of the core and the outer zones. The partial melting and subsequent open system behaviour described in Chapter 3 could facilitate this, assuming melting and new garnet growth occurred simultaneously. This is the favoured explanation for the anomalous core ages. Alternatively physical mixing of different sample populations (e.g. in a cataclasite) could account for a shift in the whole rock ^{143}Nd/^{144}Nd. If this occurred, any petrological evidence has been destroyed through subsequent HP/HT metamorphism.

Because of the close fit of all the garnet ages (with the exception of zone 1), a series of multi point isochrons were constructed. Results are displayed in Table 5-4, and all calculated multipoint isochrons are displayed in Figure 5-6. All yield ages in the vicinity of the 84 Ma, with the best fit (MSWD of 0.85) coming from the combination of zones 3, 4 and 5 with the WR measurement, yielding an age of 82.9 ± 2 Ma.

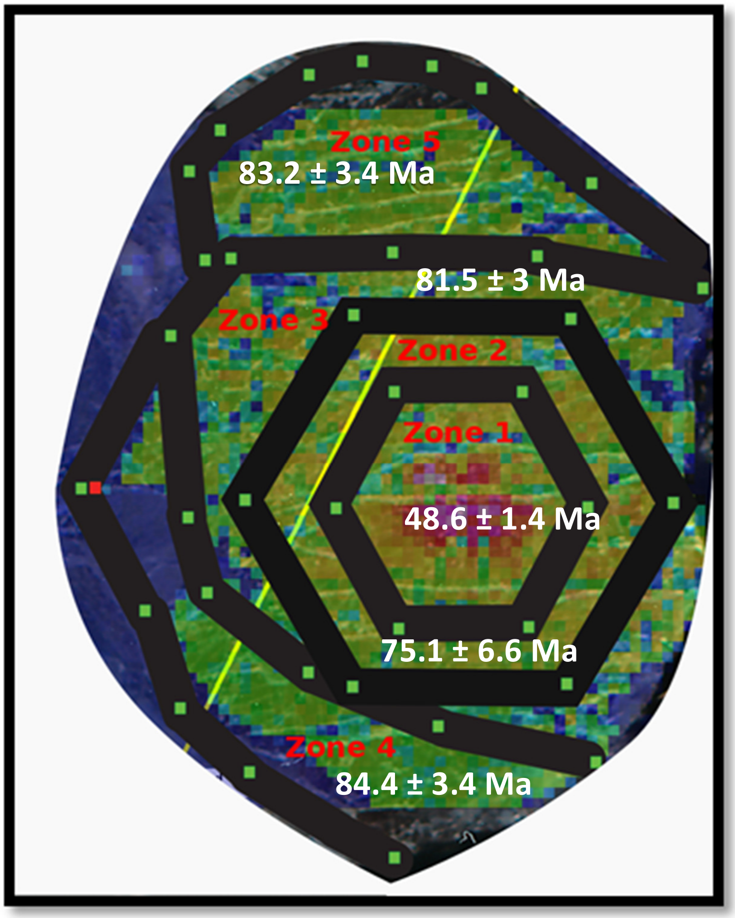

Figure 5-5: EPMA Mn elemental map of the single zoned garnet crystal annotated with age information. Crystal diameter ~ 2.5 cm

A)	Age	Error
Zone 1	48.6	1.4
Zone 2	75.1	6.6
Zone 3	81.5	3
Zone 4	84.4	3.4
Zone 5	83.2	3.4

B)	Age	Error	MSWD
Z3+Z4+Z5+WR	82.9	2	0.85
Z3+Z4+Z5+WR+BG	83.5	1.9	2
Z2+Z3+Z4+Z5+ WR+BG	86	12	3

Table 5-5: A: Age information from 2 point isochrons calculated for each individual zone, B: Age information calculated from a series of different multipoint isochrons displayed in Figure 5-6

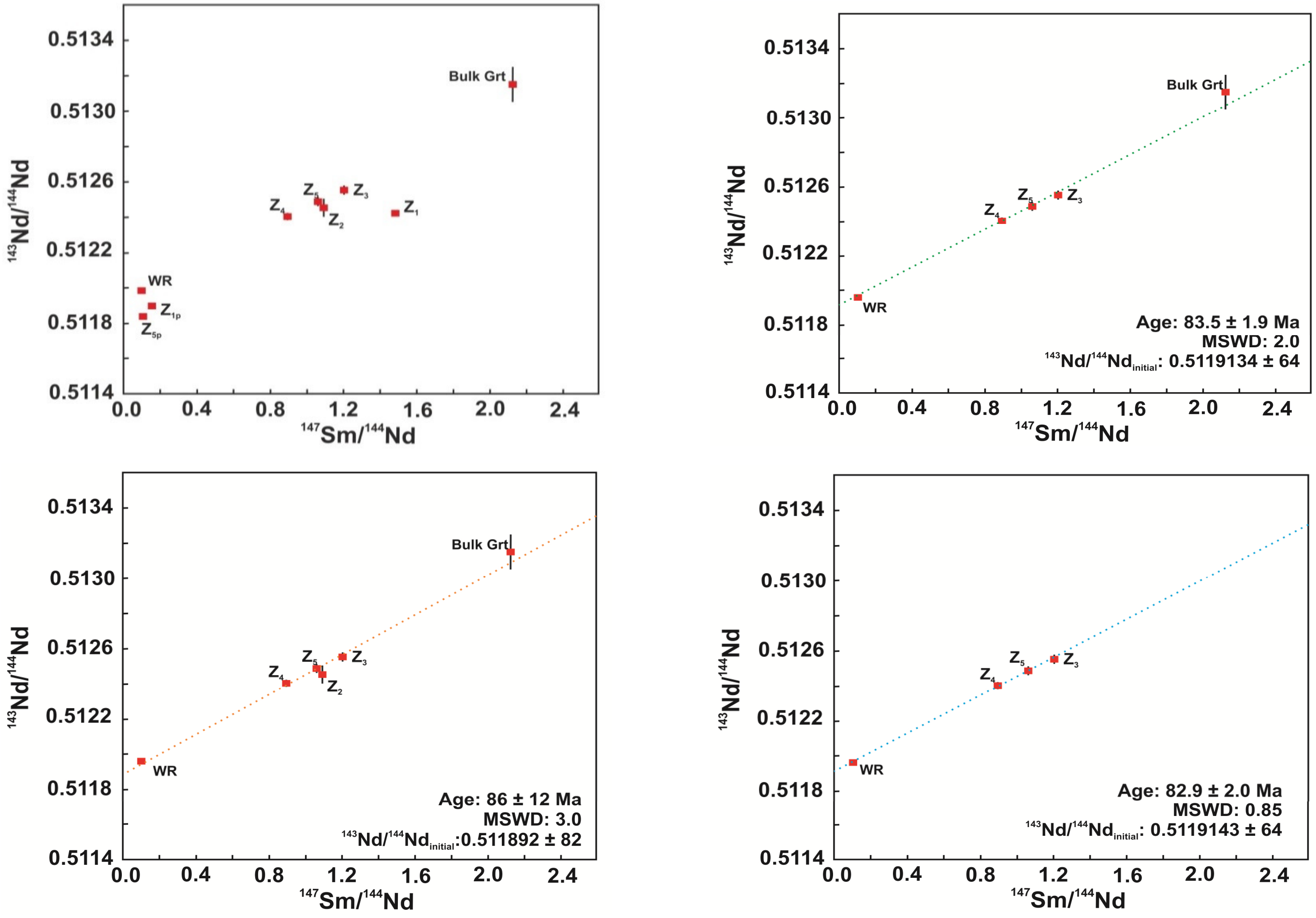

Figure 5-6: TL: Overview of all isotope data collected from the zoned garnet crystal. TR: 5 point isochron calculated using the WR, BG and Z3, Z4 and Z5 values. BL: 6 point isochron calculated using the WR, BG and Z2, Z3, Z4 and Z5 values. BR: 4 point isochron calculated using Z3, Z4, Z5 and WR values.

5.7 Results – Eastern Rhodope Mts.

Results of the Sm-Nd garnet geochronology performed on Eastern Rhodope samples are presented in Table 5-6a, and calculated ages are presented in Table 5-6b. Both samples yielded high ^{147}Sm/^{144}Nd ratios, suggesting successful cleaning of samples and mitigation of the effects of inclusions not in equilibrium the garnet. The large error associated with the analysis of sample 22-1-11 is the result of the very small size of the garnet aggregate post partial dissolution, and subsequent small amount of Nd loaded. The garnet peridotite sample, 22-1-11 yielded ages broadly similar to the metapelites from the Central Rhodope Mts, with an Sm-Nd age of 73.4 ± 4.3 Ma. The kyanite-garnet schist sample, 11-1-11 produced a significantly younger age of 37.6 ± 1.2 Ma.

In addition to the garnet geochronology, U-Pb Zircon dating was performed on a metagabbro sample from the vicinity of the town of Avren. ~ 80 kg of sample were processed, from which zircons were extracted and characterised via cathode luminescence spectroscopy. 8 zircons were then dated in the LA-ICP-MS lab in the Geological Institute at the Bulgarian Academy of Sciences following analytical procedures as outlined in Aysal et al. (2012). A PerkinElmer Elan DRC-eICP-MS connected to a NewWave UP193FC laser ablation system was used for all analyses. CL images of all analysed zircons are presented in Figure 5-8. All collected isotopic data is presented in Table 5-6C, and a Concordia diagram of all results is presented in Figure 5-7. The large spread in ages is inconclusive, but do suggest Proterozoic-Cambrian and Carboniferous age clusters, with Pb loss events around 249, 75 and 34 Ma.

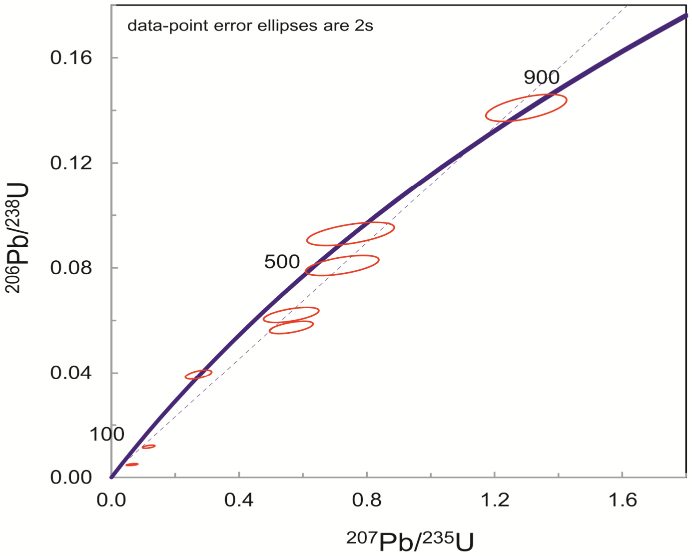

Figure 5-7: Concordia diagram plotted for the 8 zircons analysed from the Avren metagabbro sample (8-1-12) from the Eastern Rhodope Mts., in close proximity to sample 22-1-11, the 73.4 Ma garnet peridotite sample.

	Sample	Sm (ppm)	Nd (ppm)	ng Nd loaded	^{147}Sm/^{144}Nd	± 2 S.E. (ppm)	^{143}Nd/^{144}Nd	± 2 S.E. (ppm)
Kyanite Schist	11-1-11 BG	1.585729	0.336676	5.444055	2.849039	0.000655	0.512900	0.000021
	11-1-11 WR	5.926138	31.087001	54.46773	0.115312	0.000027	0.512228	0.000007
Layered Serpentinite	22-1-11 BG	0.096213	0.032738	0.813208	1.777736	0.000409	0.513553	0.000041
	22-1-11 WR	0.27512094	0.649462879	4.237320	0.256242	0.000126	0.512817	0.000010

	Age	Error
11-1-11 Grt	37.6	1.2
22-1-11 Grt	74	4.3

Zircon	^{207}Pb/^{235}U	1σ error	^{206}Pb/^{238}U	1σ error	^{206}Pb/^{238}U	1σ error
1	1.2994	0.0517	0.1410	0.0021	**850.1**	11.87
3	0.7494	0.0558	0.0929	0.0018	**572.7**	10.63
2c	0.5636	0.0279	0.0574	0.0010	**359.6**	5.83
5	0.7232	0.0469	0.0809	0.0016	**501.6**	9.32
6	0.5633	0.0354	0.0621	0.0012	**388.5**	7.09
8	0.2731	0.0168	0.0394	0.0007	**249**	4.39
9	0.0648	0.0074	0.0049	0.0002	**31.5**	0.93
4	0.1170	0.0079	0.0117	0.0002	**75.2**	1.51

Table 5-6: A: Sm-Nd isotope data collected for Eastern Rhodope samples (BG: Bulk garnet separates, WR: Whole rock sample), B: Age information calculated from Sm-Nd isotope data using 2 point isochrons, C: U/Pb isotope data collected for metagabbro sample 8-1-12, with ages highlighted in red

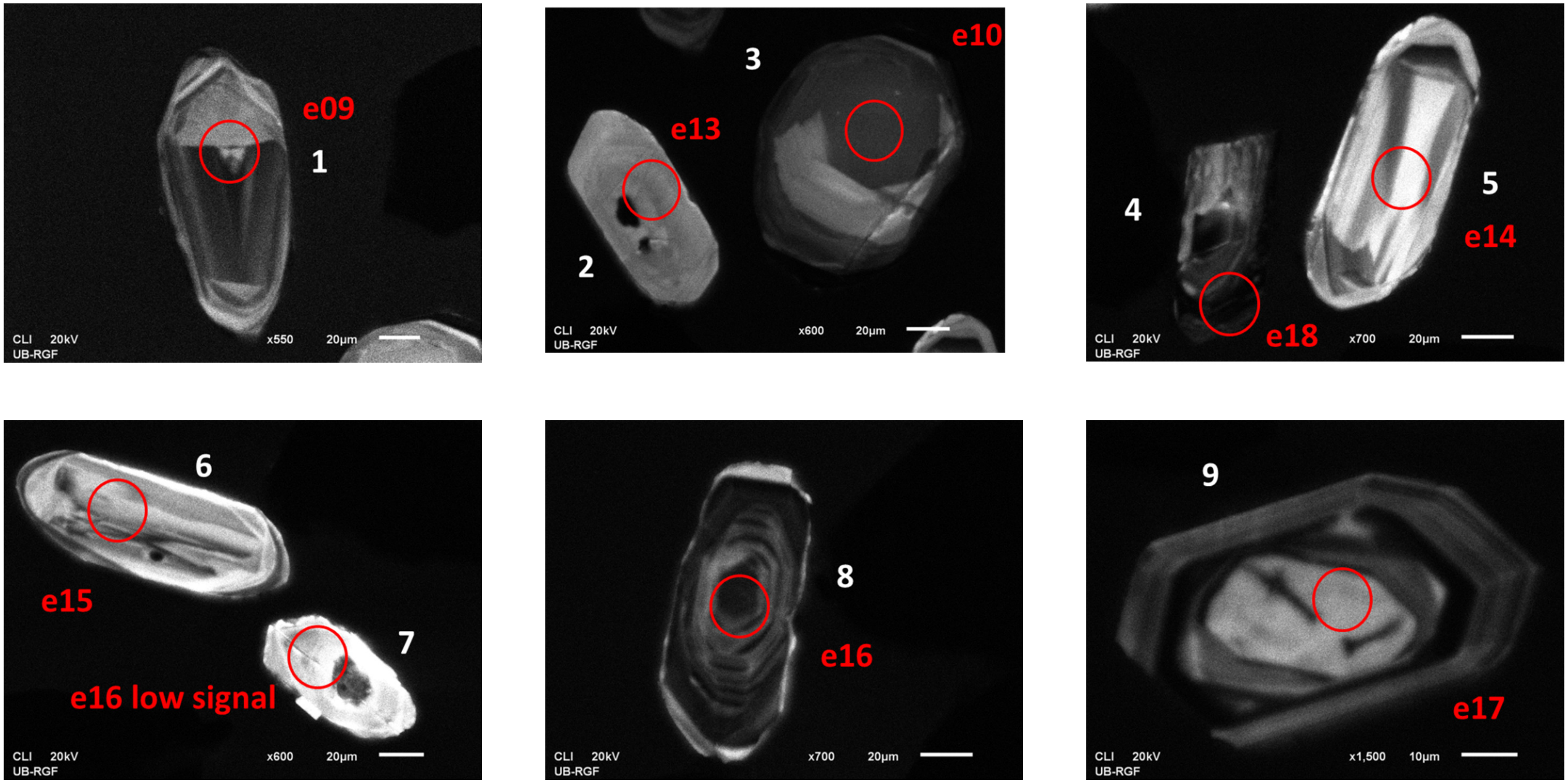

Figure 5-8: Cathode luminescence images of all zircons analysed in this study. Red circles correspond to LA-ICP-MS spots

5.8 Discussion

5.8.1 Metamorphic growth ages or thermal resetting of Sm-Nd age?

As previously shown in chapter 3, metapelites in this study have experienced peak temperature conditions in the range of ~ 750 – 850 ºC and have undergone varying degrees of partial melting, putting the samples at risk of thermal resetting of Sm-Nd profiles (Smit et al., 2013). The preservation of Mn and Ca prograde growth zones by Chepelare metapelites however indicates a limited degree of thermal resetting of garnet ages. Garnet size is another key factor in the extent of thermal resetting of garnet, as discussed in section 5.4.2. It is intuitive that longer timescales are required to fully reset larger garnets (Baxter and Scherer, 2013). No correlation is observed in this study between garnet ages and garnet size. As such the ages determined in this work for Central Rhodope metapelite samples are assumed to represent garnet growth ages, rather than a thermal resetting event.

As described in chapter 3, sample 11-1-11 from the Eastern Rhodope Mts. has a very different appearance to those samples from the Central Rhodope Mts. Quartz, and plagioclase are widespread, and both kyanite and garnet crystals are heavily resorbed and fractured – all of which can be expected by a late stage partial melting event, and therefore the young 37.6 ± 1.2 Ma age determined in this study is unsurprising. Very similar ages have been reported from late stage pegmatite bodies emplaced in the nearby Kimi Complex (Liati and Gebauer, 1999), and for nearby igneous intrusions bodies (Marchev et al., 2013), suggesting a thermal resetting event rather than a distinct metamorphic event. This ca. 40 Ma thermal resetting age recorded in metapelites from the Eastern Rhodopes is related to the Late Eocene – Early Oligocene zone that forms part of the Macedonion-Rhodope-North Aegean belt (Marchev et al., 2013). This is a ~ 250 km belt of post collisional adakitic rocks that formed following the collision of the Rhodope and Pelagonian Massifs (Christofides et al., 1998, Marchev et al., 2013, Rohrmeier et al., 2013). A deep slab break off event has been suggested as the likely trigger for this large scale asthenospheric upwelling, and associated regional core complex formation (Marchev et al., 2013).

5.8.2 Why is there a large spread in ages?

There is a large spread in the calculated ages for the 5 garnet aggregate samples in the vicinity of Chepelare, with over 20Ma between the oldest and youngest samples. Repeat analysis of garnet aggregates from samples 3-1-10 and 47-1-11 yield the same age, suggesting preferential sampling of rim vs. core (or vice versa) during sample preparation is unlikely. There is also no geographical pattern to the ages collected.

Thermal resetting is possible to account for the large spread in ages, owing to the effect of grain size on the cooling rate of crystals – larger crystals would take a longer time to cool below the closure temperature. But as demonstrated in section 5.8.1, thermal setting appears unlikely, and there is no correlation between garnet age and average garnet size. There is however an apparent correlation between the age of sample and its petrological make up. Samples with a biotite rich matrix (3-1-10 & 38-1-11) yield the youngest ages (Ca. 70 Ma and 80.6 Ma). Both samples 2-1-11, and 27-1-10 have a quartz rich matrix, and ages ca. 90 Ma, whereas the two garnet aggregates from sample 47-1-11 yielded ages of 91.5 Ma and 99 Ma. In chapter 3 these distinct petrological end members were linked with varying degrees of partial melting. If partial melting has altered the whole rock ^{143}Nd/^{144}Nd ratio, as suggested by the anomalously young core of the large zoned single crystal from sample 27-1-10, this could account for the observed spread in ages. This is however largely dependent on when in the P-T-t history of samples melting occurred. Although the large zoned garnet indicates melting contemporaneous with garnet growth, repeats of samples 3-1-10 and of 47-1-11 replicating the same age shows the whole rock ^{143}Nd/^{144}Nd in these samples did not change significantly during garnet growth, in keeping with the petrological observations of exhumation related meting tied to phengite/biotite dehydration. Large variations in whole rock ^{143}Nd/^{144}Nd cannot have occurred upon exhumation, owing to the low MSWD values for the 3 point isochrons of samples 3-1-10 and 47-1-11.

The spread in ages could also be related to the partial dissolution technique used to cleanse the garnet of inclusions. The repeat analysis of 47-1-11 yielded a lower Sm/Nd ratio despite a longer time in HF, so some degree of the spread in ages could be related to the inclusion density within crystals and the degree of garnet dissolution during the partial dissolution stages. Alternatively the ages are simply real, reflecting formation of garnet over a ~20 Ma period. This is in keeping with the large spread of ages in the calc-alkaline magmatic rocks found in the Sredno Gora zone to the north, which will be discussed further in section 5.8.4. The cause of age spread cannot be established with the current dataset, but does not detract from the clear evidence for a Late Cretaceous (U)HP metamorphic event in the vicinity of Chepelare.

5.8.3 How significant are these ages relative to published data from both the Central Rhodope Mts. and the entire RM?

Despite being widespread across the RM (Figure 5-1), Late Cretaceous ages have not previously been reported from metamorphic units in the Bulgarian Central Rhodope Mts. The only prior evidence was from zircon rims within Cenozoic pegmatite bodies (Bosse et al., 2009). If just the bulk garnet separates were analysed in this study, the Late Cretaceous ages produced could be interpreted as averaging of the ca. 150 Ma and ca. 40 Ma domains recorded in the monazite record (Bosse et al., 2010, Didier et al., 2012) . The dating of individual zones within a garnet crystal demonstrates that this is not possible, and the garnets in this study do, for the first time record a Late Cretaceous metamorphic event in the Bulgarian Central Rhodope Mts.

There is currently no evidence for HP metamorphism in the Hercynian Gneiss of the Arda dome. All metamorphic zircon populations are Eocene aged, and restricted to discordant leucosomes thought to be related to an amphibolite facies metamorphic event (Cherneva and Georgieva, 2005). Previous studies of metapelites from the Chepelare Shear Zone have also found Eocene aged monazite crystals in the matrix of samples (Bosse et al., 2009). Together, this age information suggests that the juxtaposition of metapelites with the Arda gneiss occurred after the peak metamorphic period, but prior to the Eocene amphibolite facies event, placing key constraints on the exhumation history of the Chepelare metapelites. This will be discussed further in chapter 6.

Late Cretaceous ages rare in the vicinity of Chepelare, but have been widely reported from across the RM. Previously recognised in HP zircon rims from both garnet rich mafic rocks and their surrounding orthogneiss in the Kimi Complex (Liati et al., 2002, Liati et al., 2011), both the layered garnet peridotite and metagabbro samples dated in this study record metamorphic events during this same period. This new age link between the Central and Eastern Rhodopes provides extra credibility to the idea of a Late Cretaceous UHP event, and questions the interpretation of a single long lasting subduction-exhumation cycle spanning the Jurassic to the Eocene as proposed by Turpaud and Reischmann (2010). The Eocene age from the Eastern Rhodope metapelite in this study has been widely reported in previous geochronological studies from across the Rhodope Massif (Liati and Seidel, 1996, Kirchenbaur et al., 2012, Nagel et al., 2012). In these studies it was linked with a distinct metamorphic event rather than thermal resetting as suggested by this work. The implications of these new ages on the geodynamic evolution of the RM will be discussed further in chapter 6.

5.8.4 How do these new ages relate to the surrounding area?

It is widely accepted that the much of the formation history of the RM is closely associated with the northwards subduction of the African plate under the Eurasian Margin and the closure of the Tethys ocean (Burg, 2011). This has been imaged in a number of seismic tomography studies of the Aegean, showing a clear northwards dipping high velocity anomaly, with pooling along the 660 km discontinuity (Bijwaard et al., 1998, Piromallo and Morelli, 2003), and interpreted as evidence for a long protracted subduction event spanning the Jurassic to the Eocene (Krenn et al., 2010, Turpaud and Reischmann, 2010).

There is however increasing evidence in the Eastern Rhodopes for a southern dipping subduction zone during the Late Jurassic – Early Cretaceous associated with the closure of the Meliata–Maliac Ocean (Bonev et al., 2010c, Bonev and Stampfli, 2003). Studies of other continental collision systems (e.g. the Western and Central Alps) have also established that long lasting single subduction exhumation events are unlikely, and instead invoke multiple subduction cycles involving different micro continents and oceanic fragments to explain age peaks (Gebauer, 1999, Froitzheim, 2001, Liati et al., 2011). The pulsed nature of ages preserved in the metamorphic record across the RM, as demonstrated in Figure 5-1 supports this view of multiple subduction exhumation events.

The Late Cretaceous ages reported in this study fit well with the idea of a northwards dipping subduction zone at this time. The Sredna Gora zone to the north of the Rhodope Massif is composed of a series of large largely felsic calc-alklaine magmatic intrusions with subduction related signatures associated with large spread Cu-Au ore deposits. Ages for these intrusions range from 92 – 69 Ma, with a progressive younging from north to south associated with slab retreat (Georgiev et al., 2012, Peytcheva et al., 2008, von Quadt et al., 2005). These ages have been replicated in numerous studies, and similar aged granitic bodies have even been recognised in the Rila Batholith of the Western Rhodopes (Peytcheva et al., 1998). This close geographical proximity between metamorphic and igneous units of the same age allows a number of key constraints to be placed on the evolution of the Massif, which will be discussed in chapter 6.

5.9 Chapter Summary

- 4 different age periods have previously been proposed for UHP metamorphism in the Rhodope Massif – Ca. 150 Ma, 80 Ma, 50 Ma and 40 Ma.
- This study is the first to date metapelitic garnet, the only host of UHP indicators across the RM

- Sm/NdO$^+$ geochronology of both garnet aggregates and zones from within a single crystal suggest a Late Cretaceous metamorphic event.
- The Late Cretaceous age is in keeping with both proposed regional northwards dipping subduction zone, and widespread Late Cretaceous magmatism found with the Sredna Gora zone to the north of the RM.

Chapter 6 : Discussion

6.1 Geodynamic implications of Late-Cretaceous UHP metamorphism on formation of the RM

In Chapter 2, two contrasting geodynamic models for the evolution of the Rhodope Massif were summarised. These were:

1) A long lasting northwards dipping subduction zone spanning the Jurassic to the Late Cretaceous/Paleocene (Burg, 2011, Krenn et al., 2010, Turpaud and Reischmann, 2010),
2) Multiple distinct subduction-exhumation events spanning the Jurassic – Eocene, with UHP samples forming in the southwards dipping Jurassic subduction zone (Jahn-Awe et al., 2010, Jahn-Awe et al., 2012, Kirchenbaur et al., 2012, Nagel et al., 2011)

The two models are based predominantly on observations from the Nestos Shear Zone in the Greek Rhodope Mts., where two microdiamond localities have been reported (Perraki et al., 2006, Schmidt et al., 2010). A common link between the Nestos Shear Zone and Chepelare Shear Zone has previously been proposed on the basis of outcropping style, with melange units being restricted to a thin zone up to 2km wide sandwiched between Orthogneiss units (Jahn-Awe et al., 2010, Kirchenbaur et al., 2012, Nagel et al., 2011, Turpaud and Reischmann, 2010). The establishment of UHP conditions (chapter 3) reinforces this link, and as a result studies of Chepelare samples provide an ideal opportunity to test the feasibility of the two models on other parts of the RM.

6.1.1 Long Lasting Northwards dipping subduction event

Evidence for a long lasting northward dipping subducting slab is seen though seismic imaging of the Aegean (Bijwaard et al., 1998), and confirmed by a uniform SSW sense of shear in the upper high grade basement units (Burg, 2011). In these models, the UHP units form as a result of northwards subduction of the Paleotethys/Neotethys ocean under the Eurasian margin. A single subduction event is envisaged, accounting for both the proposed Jurassic ages UHP metamorphism (Bauer et al., 2007) and the large amount of Jurassic granite with an arc signature found within the Rhodope Terrane of the middle allochthon, in the hanging wall of the Nestos Shear Zone (Turpaud and Reischmann, 2010). This is overviewed in Figure 6-1. The large range of U-Pb zircon ages recorded in UHP metamorphic units across the massif are explained via a complex exhumation history, rather than a series of distinct subduction-exhumation events.

This model effectively accounts for the contrasting protoliths and metamorphic histories of metamafic units from the VF and Arda 2 units, (as described in chapter 4), with the Neoproterozoic/Early Paleozoic units being metamorphosed and emplaced in the Moesian Platform prior to the Jurassic granitic magmatism. It is however difficult to reconcile with geochronological data from across the RM. No possible mechanism is proposed to explain (U)HP Cretaceous or Eocene metamorphism reported from both the Kimi Complex (Liati, 2005, Liati et al., 2011) and the Central Rhodope Mts. (This study, Kirchenbauer et al. 2012). The upper allochthon is also envisaged as a single sheet, and there is no explanation for the occurrence of UHP units at apparently different structural levels in the Rhodope Massif (Kimi complex vs Nestos Shear Zone/Chepelare Shear Zone).

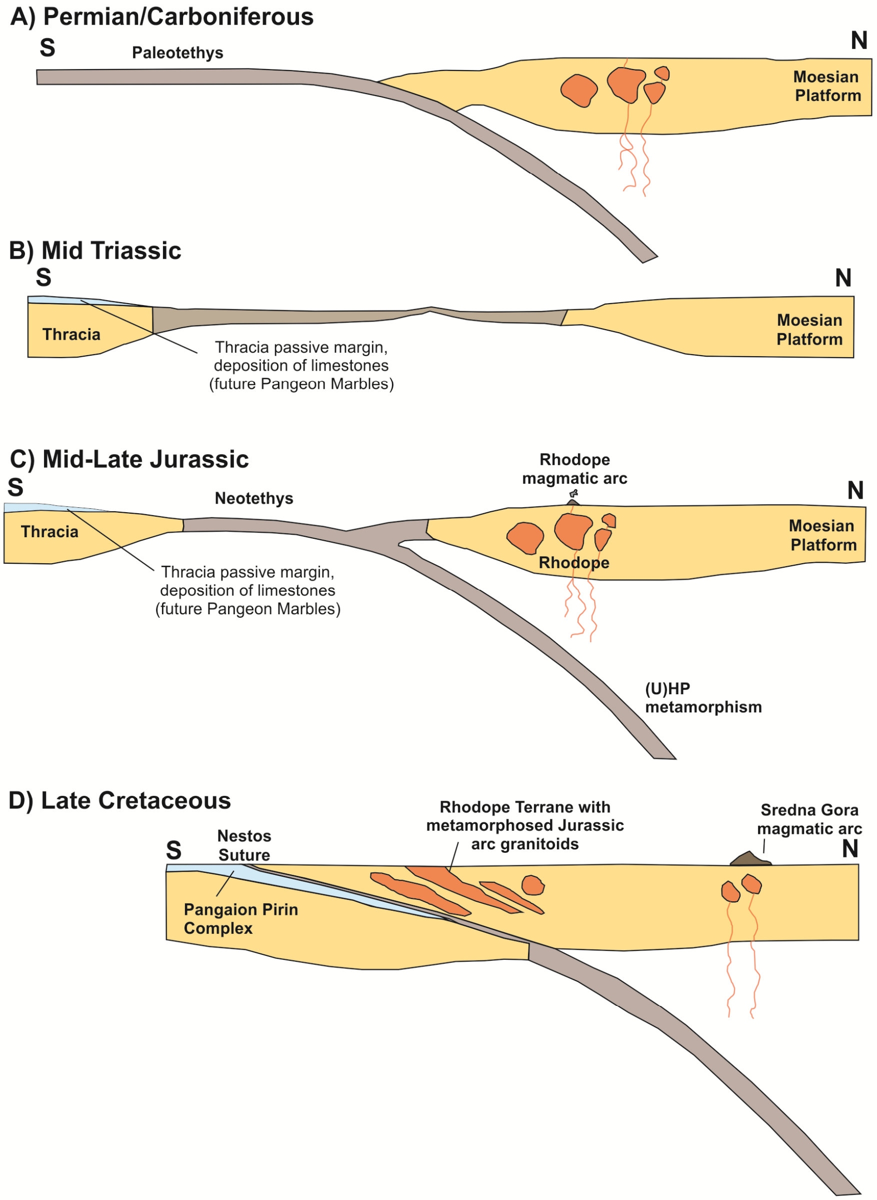

Figure 6-1: Series of schematic cross sections overviewing the single subduction zone model of Turpaud and Reischmann (2010). A: Formation of widespread Variscan arc magmatism following northwards subduction of the Palaeotethys, B: Separation of the two Variscan Terranes through opening of the Neotethys ocean, C: Subduction of the Neotethys ocean resulting in UHP metamorphism and associated Jurassic arc magmatism in the overriding plate, D: Collison and accretion has been continuous since the Late Cretaceous

6.1.2 Multiple Subduction exhumation events

An alternative model proposed by Nagel et al. (2011) allows for multiple subduction-exhumation episodes across the RM. The UHP units are proposed to be the result of southwards subduction of the Meliata and Maliac Oceanic crust during the Jurassic, prior to the opening of the Vardar Ocean and northwards subduction under the Eurasian margin. A northwards directed sense of shear, recognised in low grade Mesozoic units of the Circum Rhodope Belt, is key evidence for this Jurassic southward directed subduction event and associated exhumation (Bonev et al., 2010c, Bonev and Stampfli, 2011). During subduction of the Vardar Ocean, the UHP units of the upper allochthon were already exhumed and emplaced in the overriding plate, as such only units of the middle and lower allochthon are involved in the Cretaceous-Eocene northwards dipping subduction event. Late Cretaceous slab rollback facilitates exhumation along the Nestos Shear Zone, and orogenic wedge collapse results in the present day architecture of the RM. In that sense, the UHP Kimi complex represents the true stratigraphic position for the UHP units in the RM, and the position of the UHP NSZ and CSZ localities are the result of Cenozoic faulting (Figure 6-2). Evidence of Eocene subduction related HP metamorphism, reported from eclogite units in the Arda 2 unit (middle allochthon) is used as key evidence to support this model (Kirchenbaur et al., 2012).

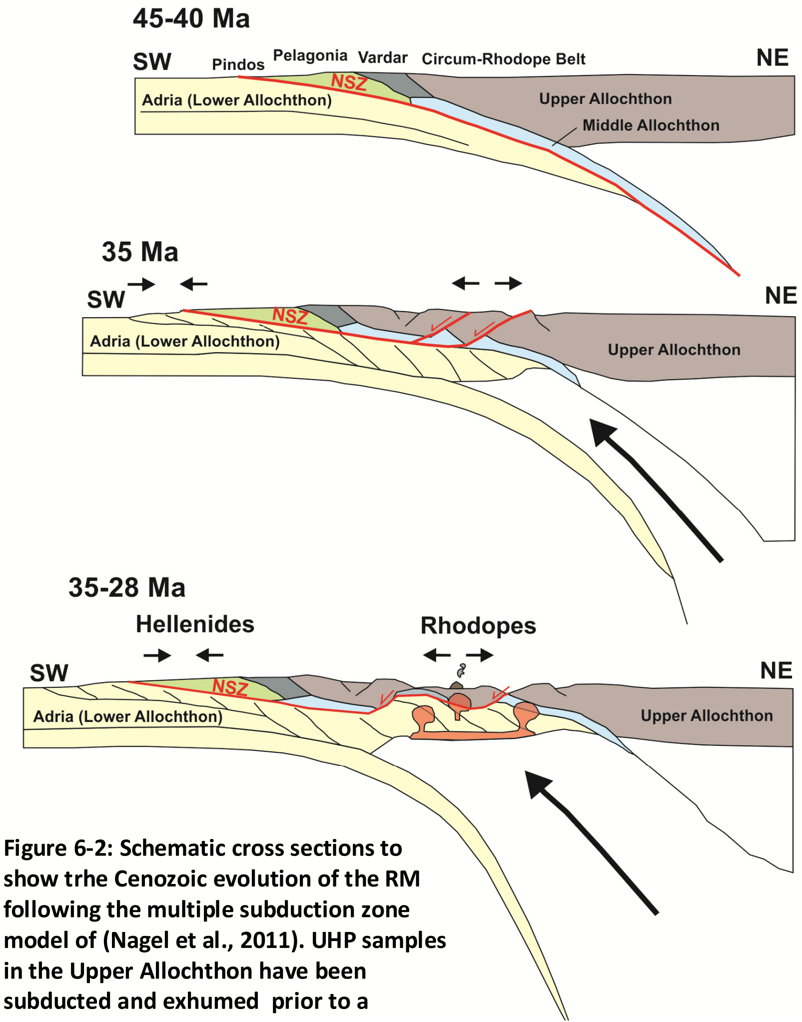

Figure 6-2: Schematic cross sections to show trhe Cenozoic evolution of the RM following the multiple subduction zone model of (Nagel et al., 2011). UHP samples in the Upper Allochthon have been subducted and exhumed prior to a Southwards dipping Jurassic subduction event.

Resutlts of this study raise a number of issues that are not addressed by this geodynamic model. The Sm-Nd garnet geochronology reported in Chapter 5 indicates a Late Cretaceous UHP metamorphic event. Irrespective of whether this age is recording garnet growth or a thermal resetting event (as discussed in chapter 5), this must have occurred as a result of northwards subduction of the Vardar Ocean/Paleotethys. This age is not compatible with the subduction and exhumation of the upper allochthon during the Jurassic prior to a quiescent period in the overriding plate during the Cretaceous subduction event.

The only evidence for a southwards dipping Jurassic subduction zone is seen in the low grade Mesozoic schists of the Cricum Rhodope Belt (Bonev et al., 2010c, Bonev and Stampfli, 2011). Any evidence of a Northwards sense of shear is conspicuously lacking from the UHP units in the Eastern Rhodope Mts. The genetic link between UHP units and the Circum Rhodope Belt is based solely on U-Pb zircon geochronology, which has the added complication of possible inheritance. No Jurassic Sm-Nd or Lu-Hf garnet ages have been recorded in (U)HP units anywhere across the RM.

The Eocene HP metamorphic event is difficult to relate to existing reported Eocene ages. Matrix monazite crystals in metapelites from the Chepelare shear Zone (Bosse et al., 2010, Didier et al., 2012), and pegmatites within the host gneiss (Bosse et al., 2009) all record Eocene ages. Rare Eocene zircon grains have also been reported from within discordant leucosomes in the Arda 2 gneiss (Cherneva et al., 2002, Cherneva and Georgieva, 2005). This recognition of a common Eocene metamorphic event in both the middle and upper allochthon indicates juxtaposition of these units prior to a common Eocene metamorphic (HT?) history. The absence of evidence for Eocene metamorphism in the garnets of the metapelites (chapter 5) indicates that this metamorphic event was restricted to at most amphibolite facies, with temperatures not high enough to reset the Sm-Nd ages.

Previous studies of metamafic units from the Arda 2 gneiss of the Central Rhodope Mts. have also indicated a Neoproterozoic protolith and Variscan metamorphism (Arkadakskiy et al., 2003, Savov et al., 2007). These ages, combined with the uniform geochemistry of Arda metamafic units reported in Chapter 4, are hard to reconcile with an Eocene elcogite facies metamorphic event in the Arda 2 gneiss (Kirchenbaur et al., 2012). A recent study has suggested that the middle allochthon overlying the Eastern extent of the Arda dome should be divided into two distinct units, with Eocene HP eclogites restricted to the base of the middle allochthon (Jahn-Awe et al., 2012). This could explain the Hercynian ages reported from Arda 2 (Cherneva and Georgieva, 2005), and Jurassic ages reported from the Rhodope Terrane, north of the NSZ (Turpaud and Reischmann, 2010). As such, it may be incorrect to assume a common formation history for the units of the middle allochthon, and further studies of the Rhodope Terrane and Arda 2 gneiss are required to resolve this issue.

6.1.3 Implications of this study and requirements of future models

The results of this study indicate that the UHP units formed part of the subducting slab dipping North in the Cretaceous. In this sense, results appear to agree with that of Turpaud and Reischmann (2010) and Burg (2011), however a Late Cretaceous metamorphic event allows sufficient time for a complete subduction-exhumation cycle related to a prior Southwards dipping Cretaceous/Jurassic subduction zone as suggested by (Bonev et al., 2010c). As such, a hybrid of the two existing geodynamic models is envisaged. This is summarised in Figure 6-3 .

This new model incorparates the well documented evidence for a regional southwards dipping subduction zone in the Mid-Jurassic – Early-Cretaceous from the Circum-Rhodope belt (Bonev et al., 2010c, Bonev and Stampfli, 2011). Zircon geochronological studies indicate that this subduction event led to at least HP metamorphism (Liati, 2011). Subsequently, a subduction reversal event occurs. This regional northwards dipping subduction event is widely documented across Bulgaria and led to the formation of the Sredna Gora mountain range (von Quadt et al., 2005). Results of this study are among the first to indicate that the Northward dipping Cretaceous subduction zone is the souce of the regional UHP metamorphism in SE Europe.

Exhumation is likely the result of channel flow or slab rollback, both of which would explain the documented Eocene HP metamorphism (Kirchenbauer et al., 2012, Nagel et al., 2012). Further work is required to address the extent of the Eocene HP metamorphic event, and heterogeneity within the middle allochthon in order to fully understand the Cenozoic evolution of the RM. It remains unclear whether this is a continuartion of the same subduction zone or a distinct separate HP subduction-exhumation event post dating the UHP metamorphism.

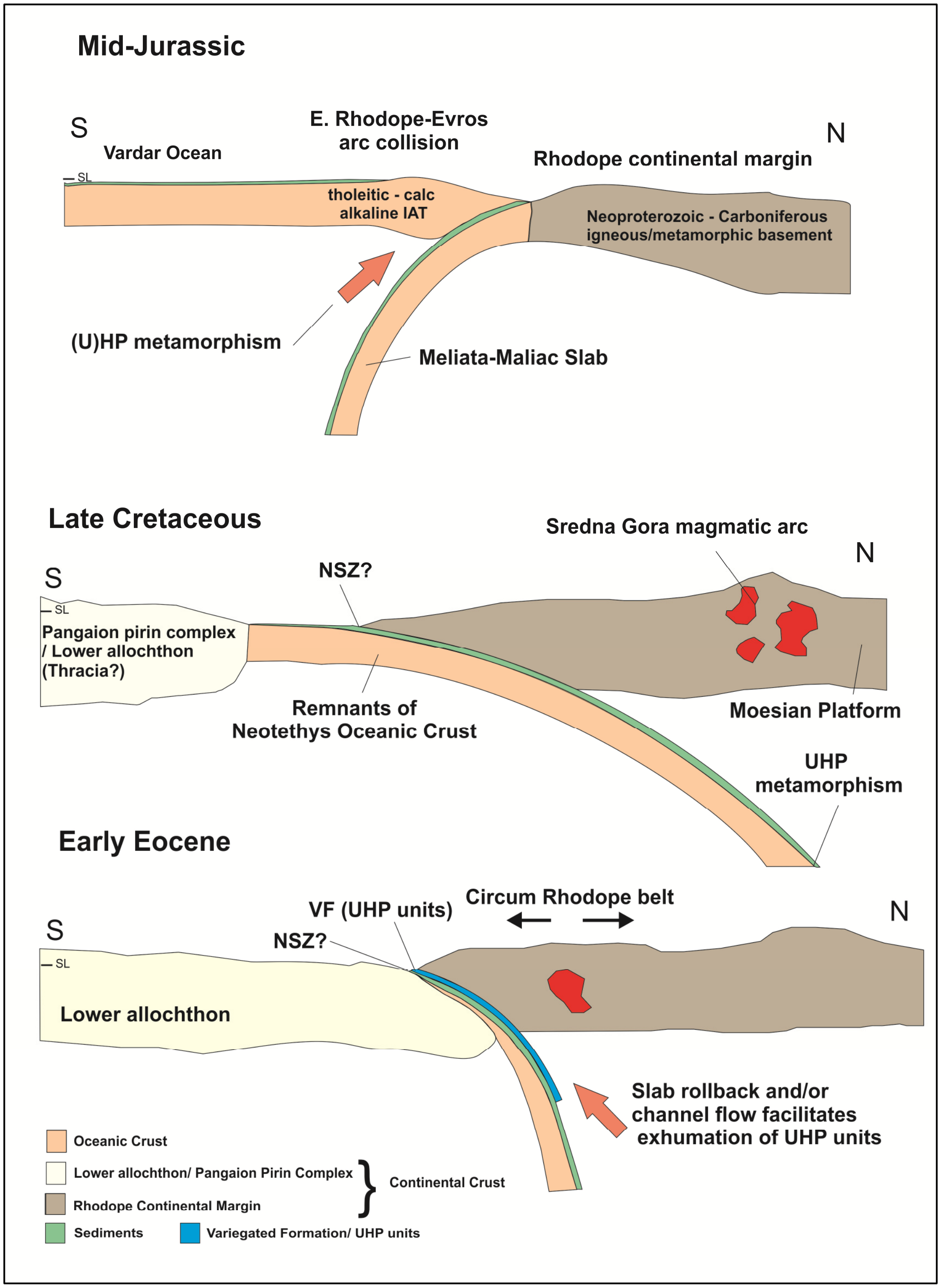

Figure 6-3: New simplified tectonic model for the evolution of the Rhodope Massif incorporating results of this study. This model accomodates a southwards dipping Cretaceous subduction zone (which has been documented in the Circum Rhodope belt (Bonev et al, 2011)) prior to a Late Cretaceous Northwards dipping subduction zone that led to the formation of the Sredna-Gora magmatic arc and the UHP metamorphic units found throughout the Variegated Formation of the Rhodope Massif. Final exhumation of samples occurred in the Early Eocene as a result of slab rolback from the subduction of continental crust or channel flow. It remains unclear whether the Rhodope Massif has experienced multiple periods of UHP metamorphism, or if the Late Cretaceous event suggested by this study is the only UHP metamorphic event.

6.2 Constraints on exhumation mechanism of UHP unit

As Summarised in chapter 1, six different exhumation models have been proposed for UHP samples. These are all based upon numerical modelling, but each is linked to specific field observations including size, structural characteristics, P-T gradient and duration of metamorphism (Hacker and Gerya, 2013, Kylander-Clark et al., 2012, Warren, 2013). Previous work has suggested that a lack of a detailed tectono-chronologic framework for the RM restricts the full understanding of the exhumation mechanism of the UHP units (Kylander-Clark et al., 2012). This is true, but the observations made in this study, combined with recently published results allows a number of important constraints to be placed on the exhumation of the UHP lithologies in the RM.

The relatively small size and inconsistent outcropping of UHP units across the RM suggests that both eduction (reversal of plate motion, and exhumation of buoyant UHP rocks with little strain (Hacker and Gerya, 2013)) and microplate rotation are not viable exhumation mechanisms for the RM. Equally, the lack of UHP units relate to the Sredna Gora arc to the North of the RM indicates that transmantle diapirs did not transport UHP material into the overriding crust. Of the remaining mechanisms, the crustal stacking model of Chemenda et al. (1995) would explain the relative lack of mantle peridotite material seen in the Central Rhodope Mts. The widespread occurrence of perdiotite in the Eastern Rhodopes however, combined with the link in Sm-Nd ages between Central Rhodope metapelites and an Eastern Rhodope garnet peridotite (as reported in chapter 5) indicates a linked formation history for these units, and as such crustal stacking is not viewed as a viable exhumation mechanism.

Whether slab rollback or channel flow exhumed the RM UHP units is dependent on which geodynamic model for the evolution of the RM is correct. The long lasting Jurassic – Paleocene/Eocene model (Burg, 2011, Krenn et al., 2010, Turpaud and Reischmann, 2010) is difficult to reconcile with either model, with no existing model of UHP exhumation currently able to account for such a long, protracted exhumation process (Liati et al., 2011). If UHP metamorphism occurred in the northwards dipping subducting slab during the Late Cretaceous, slab rollback is a viable exhumation mechanism. North to South younging of Late Cretaceous magmatism in the Sredna Gora Volcanic Arc North of the RM (von Quadt et al., 2005) can be explained through the subduction of one of the many buoyant Tethyan microcontinents, and resultant slab steepening due to influx of buoyant crustal material slowing the subduction rate. Subsequent Eocene extension and faulting would then explain the contrasting stratigraphic levels of UHP units with the RM, and restriction of peridotite to the Eastern Rhodope Mts.

If instead a polymetamorphic history is envisaged with a Jurassic UHP metamorphic event, Channel flow (Hacker and Gerya, 2013) or plunger expulsion (Warren, 2013) are more likely mechanisms, accounting for both the restriction of UHP localities to localised areas and the observed mixing of units with contrasting P-T-t histories within the Nestos and Chepelare Shear zones. Ultimately, if this scenario is correct, the complex post peak metamorphic history inhibits further deductions about the exhumation history of these units.

Chapter 7 : Conclusions and Future Work

7.1 Conclusions

This study has established that metapelites in the Bulgarian Central Rhodope Mts. in the vicinity of the town of Chepelare have experienced UHP metamorphism. A microdiamond inclusion within garnet was discovered in a kyanite-garnet schist sample from the Chepelare Shear Zone (CSZ); an approx. 2km wide zone of units of mixed origin sandwiched between orthogneiss units of the Arda dome. Comparisons with existing studies (Jahn-Awe et al., 2010, Mposkos et al., 2010) indicate that the CSZ is analogous to the Nestos Shear Zone of the Greek Central Rhodope Mts. and the Kimi Complex of the Eastern Rhodope Mts. Together these UHP units form the Upper Allochthon, the stratigraphically highest basement units seen across the RM. Petrographical and geochemical investigations indicate widespread partial melting throughout the kyanite garnets schists of the CSZ. The extent of partial melting is varied and likely occurred both during metamorphism, and upon exhumation. The microdiamond inclusion is preserved in a sample that has undergone a limited degree of partial melting. Kyanite-garnet schist is the only lithology to preserve evidence of UHP conditions within this unit, with associated metabasic units recording at most upper amphibolite facies conditions.

Two distinct populations of metabasic samples have been recognised across the RM. This is clearest in the vicinity of the town of Chepelare, where metabasic units with a MORB protolith are restricted to the Chepelare Shear Zone. Metabasic boudins hosted by the Arda 2 gneiss overlying the CSZ have an increased SSZ component, indicating an E-MORB/Island Arc Basalt protolith, and preserve evidence for prior eclogite facies metamorphism. It remains unclear whether the Arda 2 boudins represent remnants of the Variscan orogeny, or instead are the product of a Cenozoic HP metamorphic event. These populations have also been recognised in the Eastern Rhodope Mts., where U-Pb zircon ages clearly delineate Pre-Mesozoic (Ordovician/Neoproterozoic) and Mesozoic metabasic populations (Bauer et al., 2007, Bonev et al., 2013, Carrigan et al., 2003, Liati and Fanning, 2005). Increased variation is observed within these two populations relative to the Central Rhodope Mts., where samples with a MORB protolith were identified in the Ordovician/Neoproterozoic samples. This likely reflects preservation of the original oceanic crust that SSZ units were emplaced onto.

Sm-Nd garnet geochronology indicates a Late Cretaceous age for the UHP metamorphic event across the RM. This is significantly younger than the Jurassic UHP event currently proposed by monazite and zircon geochronology (Bosse et al., 2010, Jahn-Awe et al., 2010, Mposkos et al., 2010, Nagel et al., 2011, Turpaud and Reischmann, 2010, Bauer et al., 2007), but is in keeping with HP metamorphic conditions recorded in zircons across the Eastern Rhodope Mts. (Liati et al., 2011). A Late Cretaceous age for UHP metamorphism indicates that the upper allochthon formed part of the Vardar Ocean which was subducting northwards under the Moesian platform. This is in disagreement with existing geodynamic models of RM formation which suggest UHP metamorphism as a result of southwards subduction of Meliata and Maliac oceanic crust southwards during the Jurassic, and a quiescent Late Cretaceous history for the UHP samples (Jahn-Awe et al., 2010, Jahn-Awe et al., 2012, Kirchenbaur et al., 2012, Nagel et al., 2012).

7.2 Future work

Despite the significant amount of recently collected age data from across the RM (Bauer et al., 2007, Bosse et al., 2010, Didier et al., 2012, Jahn-Awe et al., 2010, Kirchenbaur et al., 2012, Liati et al., 2011), there remains a number of questions that can be answered through further integrated petrological and geochronological investigations of this region:

- Further dating of garnet from other UHP localities is required to better constrain the timing of the peak metamorphic event. Previous studies indicated a smaller degree of partial melt for UHP metapelites samples in the vicinity of Xanthi along the Nestos Shear Zone in the Greek Rhodope Mts. (Cornelius, 2008). These samples are therefore at less risk of thermal resetting, and would provide additional constraints on whether the garnet ages reported in this study represent the age of UHP metamorphism.
- Continued geochronological investigation of the eclogites of the middle allochthon in the Arda 2 gneiss are required to establish the extent of the Eocene age population, and ascertain whether these ages represent a Cenozoic HP metamorphic event as proposed by Kirchenbaur et al. (2012) or are instead the result of a thermal resetting event related to post orogenic extension and core complex formation. A detailed petrological investigation of the Arda 2 gneiss to assess whether this unit also experienced Eocene eclogite facies metamorphism would greatly aid in assessing the validity of the proposed Cenozoic HP metamorphism.
- Further petrological, geochronological and structural studies of the upper high grade basement Bulgarian Eastern Rhodope Mts. are required to assess the degree

of heterogeneity within this unit, the extent of remnants of the Variscan orogeny and ultimately the relationship with the Kimi Complex of the Greek Rhodope Mts.

Other remaining unanswered questions include whether metapelites were the only lithology to experience UHP conditions across the region. A recent study of kyanite bearing eclogite from the Pirin Mts. to the west of the RM indicated UHP conditions through thermobarometry (Janak et al., 2011), suggesting with further investigation more evidence for UHP conditions in different lithologies across the region may be discovered. The link between the metabasic sample studied in this work and ultramafic samples seen across the Eastern Rhodope Mts. is also poorly constrained, and warrants further investigation.

Appendix A: sample location

Kyanite-garnet Schist samples

	Sample	Northing	Easting	Brief description
Central Rhodope Samples	2-1-10	41°43.299	24°42.002	Along path to Quarry
	3-1-10	41°44.137	24°41.457	North of Chepelare behind logging factory
	25-1-10	41°42.14	24°42.278	Along Janchouvska river
	26-1-10	Museum Sample		Near old marble Quarry
	27-1-10	41°42.17	24°42.369	Along Janchouvska river
	2-1-11	41°43.327	24°41.761	Along road to Quarry
	28-1-11	41°41.262	24°39.406	Mechai Chal summit
	33-1-11	41°44.103	24°38.885	Along Sivkoska river
	35-1-11	41°43.846	24°41.587	Behind Ski factory north of Chepelare
	38-1-11	41°44.148	24°41.464	North of Chepelare behind logging factory
	47-1-11	Museum Sample		Near old marble Quarry
	5-1-12	41°42.197	24°42.398	Along Janchouvska river
	13-1-12	41°45.921	24°42.992	North of Boguveto
Eastern Rhodope Samples	11-1-11	41°20.243	25°22.146	1 Km north Kirkovo
	12-1-11	41°17.591	25°19.865	NW of village of Kremen
	13-1-11	41°18.194	25°19.131	1.5 Km NE Chakalarovo

Metabasic Samples - Central Rhodope Mts.

		Sample	Northing	Easting	Brief description
Variegated Formation	**Garnet bearing**	1-1-11	41°41.832	24°42.048	From Janchouvska to summit of St Ilia
		3-1-11	41°42.134	24°42.448	3.5 Km SE of Chepelare, Janchouvska river
		30a-1-11	41°42.492	24°42.297	Heading east from old marble quarry
		1-1-12	41°40.457	24°40.877	Mechai Chal
		6-1-13	41°44.438	24°39.430	Along Sivkoska river
	Garnet Free	30-1-11	41°42.491	24°42.296	Heading east from old marble quarry
		34-1-11	41°44.383	24°38.581	Along Sivoksa river
		37-1-11	41°44.149	24°40.866	Behind Cemetery, North of Chepelare
		39-1-11	41°41.238	24°42.496	Along path from Progled North to St Ilia
		4-1-12	41°44.362	24°41.062	NW of Cemetry, north of Chepelare
		1-1-13	41°41.972	24°41.984	Along path to summit of St Ilia
		2-1-13	41°43.675	24°30.961	North of Breze
		5-1-13	41°44.389	24°38.647	Along Sivkoska river
		7-1-13	41°44.449	24°39.460	Along Sivkoska river
		9-1-13	41°43.834	24°41.944	NE of ski factory in North Chepelare

		Sample	Northing	Easting	Brief description
Arda 2 Gneiss	Garnet bearing	22-1-10	41°42.628	24°27.122	Beden
		23-1-10	41°43.564	24°37.106	West along Sivkoska river
		31-1-11	41°45.119	24°42.343	Along Lapouska river
		36-1-11	41°43.700	24°42.246	Behind Ski factory, at base of Arda 2
		42-1-11	41°45.612	24°40.562	Zornitsa
		44-1-11	41°43.679	24°42.218	Sameish location as 36-1-11
		45-1-11	41°43.564	24°37.106	Along Sivkoska river
		45a-1-11	41°43.565	24°37.107	Along Sivkoska river
		14-1-12	41°43.402	24°36.304	Further west along Sivoska river
		15-1-12	41°43.882	24°35.426	Further west along Sivoska river
		3-1-13	41°43.751	24°31.048	Village of Breze
		11-1-13	41°43.859	24°41.999	NE of Ski factory North of Chepelare
		12-1-13	41°43.904	24°42.139	Summit of hill above 11-1-13
	Garnet free	32-1-11	41°44.868	24°42.410	Lapoushka river north of Chepelare
		36a-1-11	41°43.701	24°42.247	Behind Ski factory, at base of Arda 3
		40-1-11	41°45.117	24°40.686	Along road from Chepelare to Zornitsa
		41-1-11	41°45.390	24°40.640	Along path from Progled towards St Ilia

Metabasic samples – Eastern Rhodope Mts.

Sample	Northing	Easting	Brief description
4-1-10	41°33.457	25°48.551	Along river bed, NW of Bubino
6a-1-10	41°33.459	25°48.553	Along river bed, NW of Bubino
6b-1-10	41°33.460	25°48.554	Along river bed, NW of Bubino
8-1-10	41°20.197	25°42.644	1 km south of Avren, along river bed
9-1-10	41°19.899	25°37.81	Along road into Egrek
4-1-11	41°23.549	25°05.060	Zlatograd
7-1-11	41°24.452	25°12.897	2km NE of Zradvchets
7b-1-11	41°24.453	25°12.898	2km NE of Zradvchets
15-1-11	41°23.721	25°33.997	500 m East of Topolka
18-1-11	41°24.905	25°53.299	Along road, 1.2 km east of Kazak
19-1-11	41°21.548	25°48.542	4 km NE of Chernichevo
26-1-11	41°34.778	26°06.493	Along road to Ivaylovgrad dam, 200m from dam wall
27-1-11	41°32.043	26°03.183	Along road from Ivaylovgrad to Pokrovan
8-1-12	41°19.390	25°40.844	South of Avren
7b-1-02	-	-	Golyama Devesil
1-8-02	-	-	Golyama Devesil
1-14-02	-	-	Egrek
23-1-02	-	-	Ivaylovgrad dam
1-24-02	-	-	Egrek

Appendix B: Details of Sr and Nd Isotope Geochemistry

A total of 23 samples were analysed for bulk rock Sr and Nd isotopes using Thermo Scientific TRITON thermal ionisation mass spectrometer (TIMS) at the University of Leeds.

Chemical separation of Sr and Nd

Approx. 0.1g of powdered samples were dissolved in a mixture of 1.5 ml conc. HF, and 0.5ml conc. HNO_3 in sealed 15ml Teflon jars, heated overnight on a hotplate. Once dissolved, samples were dried down, dissolved in a mix of 1.5ml conc. HNO_3 and 0.5ml conc. HCl, and heated once more overnight. This evaporation-dissolution procedure was repeated with 2ml 6M HCl, before final dissolution in 2ml of 2.5M HCl ready for chemical separation of elements.

1 ml of each sample was centrifuged, and loaded onto Ion exchange columns containing BioRad AG50-X12 resin. Columns were rinsed with a calibrated amount of 2.5M HCl to wash elements away, prior to collection of the Sr fraction, which was dried down ready for loading. Following removal of Rb following a further rinse with 4.25M HCl to remove Ba from samples, the REE fraction was collected. This Nd fraction was dried down and redissolved in 1ml Conc $HNO_{3.}$ Following further drying down, the samples was dissolved in a 75/25 acetic nitric mixture, before loading onto REE ion exchange columns preconditioned with 90/10 acetic nitric mixture. Columns were rinsed with an acetic/nitric mixture prior to elution with 10ml of MeOH cocktail comprising 10% acetic nitric mixture, 5% conc. HNO_3 and 10% UHQ water. The sample was then collected in 30ml of the MeOH cocktail.

Following drying down, samples were dissolved in 1ml 6M HCl. This was then dried down again, redissolved again in 1ml 6M Hcl, before evaporation to a tiny drop. This was dissolved in 250 µl of 0.25M HCl, and loaded onto columns containing LN-Spec resin. Following elution with a calibrated amount of 0.25M HCl, samples were collected in 2.5 ml HCl, and evaporated to just dryness ready for loading.

Sample loading

Sr samples were loaded onto single Tungsten wire filaments with a TaCl activator. A single drop of TaCl solution was loaded onto the filaments in small increments prior to sample loading. The sample was dissolved in a small (approx. 2 µl) drop of 2.5 M HCl, and loaded onto the filament in the smallest possible increments. Nd Isotopes were loaded onto Rhenium wire double filaments, in a small (approx. 2 µl) drop of 10% HNO_3 in the smallest possible increments.

Analytical Precision

For $^{87}Sr/^{86}Sr$ analysis, the TIMS was run between 3 and 5V on ^{87}Sr. 200 ratios were measured per sample, and the 2σ error was 10^{-6}. For $^{143}Nd/^{144}Nd$ analysis the TIMS was run between 0.2 and 0.9 V on ^{144}Nd. 240 ratios were measured pre sample, and the 2σ error was 10^{-6}. The external precision was monitored through analysis of NBS-987 and La Jolla standards for Sr and Nd respectively. Over the duration of analyses (January 2011 – March 2014) NBS 987 $^{87}Sr/^{86}Sr$ averaged 0.710261 ± 0.000028 (2 RSD, n 68), and La Jolla $^{143}Nd/^{144}Nd$ averaged 0.511843 ± 0.000018 (2 RSD, n=43). The literature value for NBS-987 is 0.710248, and the La Jolla value is 0.51185 (Thirlwall, 1991). A correction was applied to all measurements based on deviations of the standard material relative to the literature values within each run.

Results

Results for Sr and Nd isotope from the Central and Eastern Rhodope Mts. are presented in the following tables. The unclear age of these samples complicates calculation of initial $^{87}Sr/^{86}Sr$ and $^{143}Nd/^{144}Nd$ ratios. A number of different corrections have been made on the basis of proposed protolith formation ages in the literature; these are 570Ma, 250Ma and 150 Ma. Half-life values of 1.42 x 10^{-11} for the Rb-Sr system, and 6.54 x 10^{-12} for the Sm-Nd system were used in these calculations.

	Sample	**$^{87}Sr/^{86}Sr$**	**±**	**Initial $^{87}Sr/^{86}Sr$**		
				550 Ma	**250 Ma**	**150 Ma**
Arda	44-1-11	0.706471	4	0.705756	0.706147	0.706277
	1-22-10	0.705717	4	0.703840	0.704866	0.705207
	36-1-11	0.705466	4	0.703260	0.704466	0.704866
	1-23-10	0.707840	4	0.706538	0.707249	0.707486
	45-1-11	0.706631	8	0.704864	0.705830	0.706151
	41-1-11	0.708840	2	0.702409	0.705923	0.707091
	40-1-11	0.709935	6	0.702223	0.706437	0.707838
VF	1-1-11	0.705106	3	0.704583	0.704869	0.704964
	3-1-11	0.711901	5	0.706653	0.709521	0.710474
	30a-1-11	0.706506	6	0.705118	0.705876	0.706128
	34-1-11	0.709136	3	0.704005	0.706809	0.707741

	Sample	**^{143}Nd/^{144}Nd**	**±**	**550 Ma initial**	**ε^t(Nd)**	**250 Ma initial**	**ε^t(Nd)**	**150 Ma initial**	**ε^t(Nd)**
Arda	44-1-11	0.512934	6	0.512006	1.49	0.512512	3.83	0.512681	4.61
	1-22-10	0.512847	6	0.512211	5.50	0.512558	4.72	0.512674	4.46
	36-1-11	0.512788	6	0.512181	4.92	0.512512	3.83	0.512623	3.47
	36a-1-11	0.512785	9	0.512216	5.60	0.512527	4.11	0.512630	3.61
	1-23-10	0.512721	4	0.512123	3.78	0.512449	2.60	0.512558	2.21
	45-1-11	0.512696	3	0.512053	2.43	0.512404	1.72	0.512521	1.48
	41-1-11	0.512488	7	0.511950	0.41	0.512244	-1.41	0.512341	-2.02
	40-1-11	0.512469	4	0.511937	0.14	0.512227	-1.74	0.512324	-2.36
VF	1-1-11	0.512975	6	0.512193	5.16	0.512620	5.93	0.512762	6.19
	3-1-11	0.512692	7	0.511955	0.49	0.512357	0.80	0.512491	0.90
	30a-1-11	0.512876	7	0.512142	4.16	0.512543	4.42	0.512676	4.51
	34-1-11	0.512531	5	0.511720	-4.09	0.512163	-3.00	0.512310	-2.63

				initial ^{87}Sr/^{86}Sr		
		87Sr/86Sr	**±**	**550**	**250**	**150**
Avren Synform	1-14-02	0.70455	6	0.703109	0.703897	0.704158
	1-24-02	0.70866	6	0.706755	0.707796	0.708142
	1-8-02	0.704784	7	0.704118	0.704482	0.704603
	1-8-10	0.706539	5	0.705765	0.706188	0.706328
	1-9-10	0.705153	6	0.704767	0.704978	0.705048
Ivaylovgrad	27-1-11	0.706019	4	0.705612	0.705834	0.705908
Bubino	1-4-10	0.707098	5	0.704688	0.706005	0.706443
	6a-1-10	0.70508	6	0.700654	0.703072	0.703876
	6b-1-10	0.704469	33	0.704079	0.704292	0.704363
Zlatovgrad	4-1-11	0.704521	4	0.703955	0.704264	0.704367

	Sample	**^{143}Nd/^{144}Nd**	**570 Ma initial**	**ε^t(Nd)**	**250 Ma initial**	**ε^t(Nd)**	**150 Ma initial**	**ε^t(Nd)**
Avren Synform	1-14-02	0.512884 **± 7**	0.512053	2.92	0.512520	3.98	0.512666	4.31
	1-24-02	0.512986 **± 18**	0.512171	5.22	0.512629	6.10	0.512772	6.38
	1-8-02	0.512780 **± 16**	0.511910	0.12	0.512399	1.61	0.512551	2.08
	8-1-10	0.512987 **± 5**	0.512172	5.24	0.512630	6.12	0.512773	6.40
	9-1-10	0.512508 **± 4**	0.511990	1.70	0.512281	-0.68	0.512372	-1.42
Ivaylovgrad	23-1-02	0.512608 **± 6**	0.511953	0.97	0.512321	0.09	0.512436	-0.18
	27-1-11	0.512750 **± 7**	0.512049	2.85	0.512443	2.48	0.512566	2.36
Bubino	4-1-10	0.512385 **± 5**	0.511866	-0.72	0.512158	-3.09	0.512249	-3.83
	6a	0.512934 **± 6**	0.512160	5.01	0.512595	5.44	0.512731	5.58
	6b	0.512940 **± 4**	0.512152	4.85	0.512595	5.44	0.512733	5.62
Zlatovgrad	4-1-11	0.512932 **± 7**	0.512221	6.20	0.512620	5.94	0.512745	5.86

Epsilon(t) Nd values were calculated from the three possible initial ^{143}Nd/^{144}Nd ratios using the following equations:

$$\varepsilon^t_{Nd} = \left[\frac{(^{143}Nd/^{144}Nd)_i}{I^t_{CHUR}} - 1\right] \times 10^4$$

$$I^t_{CHUR} = I^0_{CHUR} - \left(\frac{^{147}Sm}{^{144}Nd}\right)^0_{CHUR} (e^{\lambda t} - 1)$$

Where $I^0_{CHUR} = 0.512638$ when normalised to 146Nd/144Nd = 0.7219. and $\left(\frac{^{147}Sm}{^{144}Nd}\right)^0_{CHUR}$ = 0.1967.

Enrichment parameters for both Rb and Sm (*f)* relative to CHUR were calculated for all samples, using the following equations, and are presented in the table below :

$$f_{Sm} = \left(\frac{(^{147}Sm/^{144}Nd)}{(^{147}Sm/^{144}Nd)^0_{CHUR}}\right) - 1$$

$$f_{Rb} = \left(\frac{(^{87}Rb/^{86}Sr)}{(^{87}Rb/^{86}Sr)^0_{CHUR}}\right) - 1$$

	sample	***f*Rb**	***f*Sm**
Arda	44-1-11	0.12	0.31
	1-22-10	1.93	-0.10
	36-1-11	2.45	-0.14
	1-23-10	1.03	-0.16
	45-1-11	1.76	-0.09
	41-1-11	9.05	-0.24
	40-1-11	11.05	-0.25
VF	1-1-11	-0.18	0.10
	3-1-11	7.20	0.04
	30a-1-11	1.17	0.04
	34-1-11	7.02	0.14

		***f*Rb**	***f*Sm**
Avren Synform	1-14-02	1.25	0.13
	1-24-02	1.98	0.11
	1-8-02	0.04	0.18
	8-1-10	0.21	0.11
	9-1-10	-0.40	-0.30
Ivaylovgrad	23-1-02	-	-0.11
	27-1-11	-0.36	-0.05
Bubino	4-1-10	2.77	-0.29
	6a-1-10	5.92	0.05
	6b-1-10	-0.39	0.07
Zlatovgrad	4-1-11	-0.11	-0.03

The widespread variation seen in *f*Rb values indicates varying degrees of enrichment, likely the result of differing interactions with a crustal unit such as the gneiss of the Arda dome in the Central Rhodope Mts. Little variation is seen amongst the *f*Sm values, indicating that any interaction with crustal material has had a neglible effect on the Nd isotope ratios. This is confirmed on the plots of 1/Nd vs ε^t_{Nd} below, where no correlation is seen in samples from the Central Rhodope Mts. A possible correlation is observed is observed in the metabasic samples from the Eastern Rhodope Mts., although this is not clear and requires further investigation.

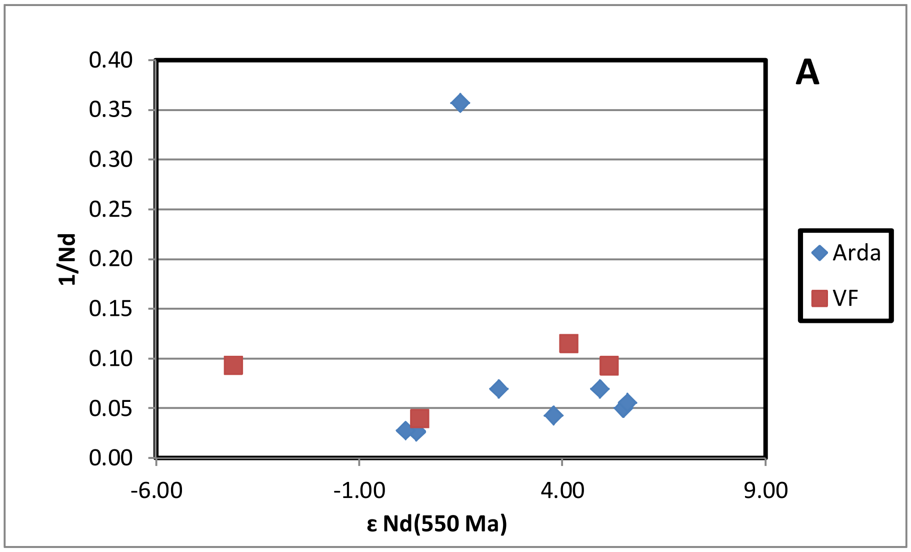

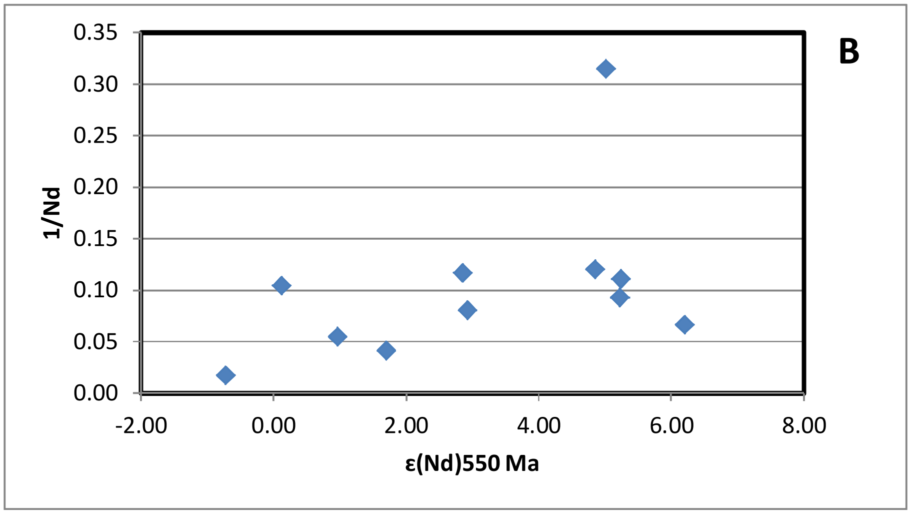

Plots of 1/Nd vs εNd(550)Ma for A) metabasic samples from Central Rhodope Mts., and B) metabasic samples from Eastern Rhodope Mts.

The age of the sample can have a large effect on ε^{t}_{Nd} values, the result of small variations in *f*Sm values, which is likely related to crustal contamination . For the samples from the Central Rhodope Mts, if Neoproterozoic formation ages are used ε^{t}_{Nd} ranges between 0.14 and 5.6, whereas if Jurassic ages are used ε^{t}_{Nd} ranges between -2.3 and 4.6.) A clear correlation between $(La/Sm)_N$ and all ε^{t}_{Nd} values, irrespective of age is seen in this, as shown on the following figure., indicating that $^{143}Nd/^{144}Nd$ still preserved a record of the samples original tectonic setting

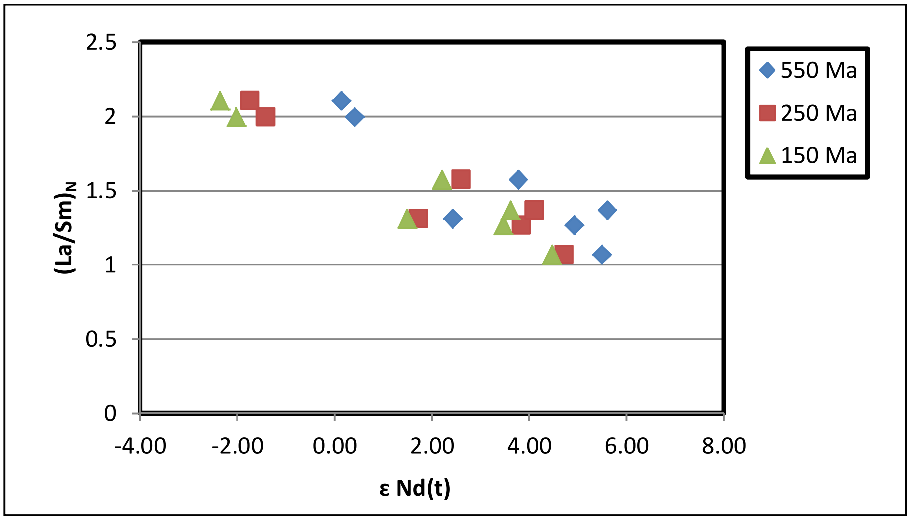

Plot of $(La/Sm)_N$ for metabasite samples from the Central Rhodope Mts.

For the samples from the Eastern Rhodope Mts. a wide range of ε(Nd)t values are reported for across the area, with values spanning from -3.8 to 6.4 for a 150 Ma formation age and -0.72 to 6.2 for a Neoproterozoic formation age. On a plot of $(La/Sm)_N$ vs ε(Nd)t, no correlation is observed for any of the age populations. This is likely the result of an increased degree of crustal contamination although the two samples with the highest $(La/Sm)_N$ values (4-1-10 and 9-1-10) have some of the lowest ε values, as expected if these values represent an increased SSZ component.

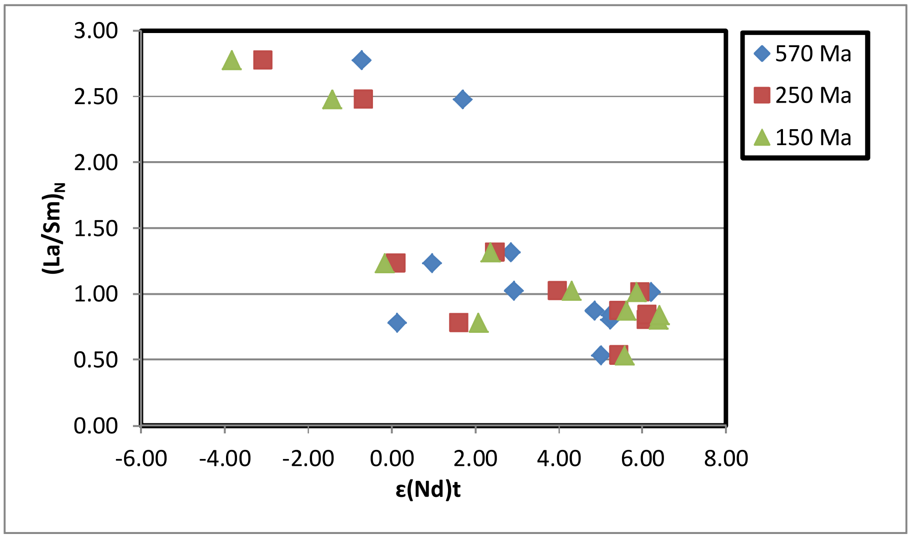

Plot of $(La/Sm)_N$ for metabasite samples from the Easern Rhodope Mts.

References

AMELIN, Y. & ROTENBERG, E. 2004. Sm–Nd systematics of chondrites. *Earth and Planetary Science Letters,* 223**,** 267-282.

ANCZKIEWICZ, R., THIRLWALL, M., ALARD, O., ROGERS, N. W. & CLARK, C. 2012. Diffusional homogenization of light REE in garnet from the Day Nui Con Voi Massif in N-Vietnam: Implications for Sm–Nd geochronology and timing of metamorphism in the Red River shear zone. *Chemical Geology,* 318–319**,** 16-30.

ANCZKIEWICZ, R. & THIRLWALL, M. F. 2003. Improving precision of Sm-Nd garnet dating by H2SO4 leaching: a simple solution to the phosphate inclusion problem. *Geological Society, London, Special Publications,* 220**,** 83-91.

ANDERS, B., REISCHMANN, T., POLLER, U. & KOSTOPOULOS, D. 2005. Age and origin of granitic rocks of the eastern Vardar Zone, Greece: new constraints on the evolution of the Internal Hellenides. *Journal of the Geological Society,* 162**,** 857-870.

ANDERSEN, T. B., JAMTVEIT, B., DEWEY, J. F. & SWENSSON, E. 1991. Subduction and eduction of continental crust: major mechanisms during continent‐continent collision and orogenic extensional collapse, a model based on the south Norwegian Caledonides. *Terra Nova,* 3**,** 303-310.

ARKADAKSKIY, S., BOHM, C., HEAMAN, L., CHERNEVA, Z., STANCHEVA, E. & OVTCHAROVA, M. Remnants of Neoproterozoic oceanic crust in the Central Rhodope metamorphic complex, Bulgaria. Geol. Asoc. Canada, Vancouver Annual Meeting, 2003.

AUZANNEAU, E., SCHMIDT, M. W., VIELZEUF, D. & CONNOLLY, J. A. D. 2010. Titanium in phengite: a geobarometer for high temperature eclogites. *Contributions to Mineralogy and Petrology,* 159**,** 1-24.

AYSAL, N., USTAÖMER, T., ÖNGEN, S., KESKIN, M., KÖKSAL, S., PEYTCHEVA, I. & FANNING, M. 2012. Origin of the Early-Middle Devonian magmatism in the Sakarya Zone, NW Turkey: Geochronology, geochemistry and isotope systematics. *Journal of Asian Earth Sciences,* 45**,** 201-222.

BAUER, C., RUBATTO, D., KRENN, K., PROYER, A. & HOINKES, G. 2007. A zircon study from the Rhodope metamorphic complex, N-Greece: Time record of a multistage evolution. *Lithos,* 99**,** 207-228.

BAXTER, E. F., AGUE, J. J. & DEPAOLO, D. J. 2002. Prograde temperature–time evolution in the Barrovian type–locality constrained by Sm/Nd garnet ages from Glen Clova, Scotland. *Journal of the Geological Society,* 159**,** 71-82.

BAXTER, E. F. & SCHERER, E. E. 2013. Garnet geochronology: Timekeeper of tectonometamorphic processes. *Elements,* 9**,** 433-438.

BAZIOTIS, I. & MPOSKOS, E. Geochemistry and tectonic setting of eclogite protoliths from Kechros Complex in East Rhodope (NE Greece). Proceedings of the 12th international congress, geological society of Greece, 2010. 2522-2531.

BAZIOTIS, I., MPOSKOS, E. & PERDIKATSIS, V. 2008. Geochemistry of amphibolitized eclogites and cross-cutting tonalitic-trondhjemitic dykes in the Metamorphic Kimi Complex in East Rhodope (NE

Greece): implications for partial melting at the base of a thickened crust. *International Journal of Earth Sciences,* 97**,** 459-477.

BEAUMONT, C., JAMIESON, R. A., BUTLER, J. & WARREN, C. 2009. Crustal structure: A key constraint on the mechanism of ultra-high-pressure rock exhumation. *Earth and Planetary Science Letters,* 287**,** 116-129.

BEBIEN, J. 1982. *L'association ignée de Guevgueli (Macédoine grecque): expression d'un magmatisme ophiolitique dans une déchirure continentale.*

BHADRA, S. & BHATTACHARYA, A. 2007. The barometer tremolite+ tschermakite+ 2 albite= 2 pargasite+ 8 quartz: Constraints from experimental data at unit silica activity, with application to garnet-free natural assemblages. *American Mineralogist,* 92**,** 491-502.

BHATTACHARYA, A., MOHANTY, L., MAJI, A., SEN, S. K. & RAITH, M. 1992. Non-ideal mixing in the phlogopite-annite binary: constraints from experimental data on Mg–Fe partitioning and a reformulation of the biotite-garnet geothermometer. *Contributions to Mineralogy and Petrology,* 111**,** 87-93.

BIJWAARD, H., SPAKMAN, W. & ENGDAHL, E. R. 1998. Closing the gap between regional and global travel time tomography. *Journal of Geophysical Research: Solid Earth,* 103**,** 30055-30078.

BLUNDY, J. D. & HOLLAND, T. J. 1990. Calcic amphibole equilibria and a new amphibole-plagioclase geothermometer. *Contributions to Mineralogy and Petrology,* 104**,** 208-224.

BONEV, N. 2006. Cenozoic tectonic evolution of the eastern Rhodope massif (Bulgaria): Basement structure and kinematics of syn- to postcollisional extensional deformation. *Postcollisional Tectonics and Magmatism in the Mediterranean Region and Asia,* 409**,** 211-235.

BONEV, N. & BECCALETTO, L. 2007. From syn-to post-orogenic Tertiary extension in the north Aegean region: constraints on the kinematics in the eastern Rhodope–Thrace, Bulgaria–Greece and the Biga Peninsula, NW Turkey. *Geological Society, London, Special Publications,* 291**,** 113-142.

BONEV, N., MARCHEV, P., OVTCHAROVA, M., MORITZ, R. & ULIANOV, A. U-Pb LA-ICP/MS zircon geochronology of metamorphic basement and Oligocene volcanic rocks from the SE Rhodopes: inferences for the geological history of the Eastern Rhodope crystalline basement. GEOSCIENCES 2010, 2010a Sofia. BULGARIAN GEOLOGICAL SOCIETY.

BONEV, N., MORITZ, R., MARTON, I., CHIARADIA, M. & MARCHEV, P. 2010b. Geochemistry, tectonics, and crustal evolution of basement rocks in the Eastern Rhodope Massif, Bulgaria. *International Geology Review,* 52**,** 269-297.

BONEV, N., OVTCHAROVA-SCHALTEGGER, M., MORITZ, R., MARCHEV, P. & ULIANOV, A. 2013. Peri-Gondwanan Ordovician crustal fragments in the high-grade basement of the Eastern Rhodope Massif, Bulgaria: evidence from U-Pb LA-ICP-MS zircon geochronology and geochemistry. *Geodinamica Acta***,** 1-25.

BONEV, N., PEYCHEV, K. & NIZAMOVA, D. MOR-vs. SSZ-origin of metamafic rocks in the upper high-grade basement unit of the eastern Rhodope: geochemical diversity and tectonic significance. Proceedings of Annual Conference of the Bulgarian Geological Society,"Geosciences, 2006. 181-184.

BONEV, N., SPIKINGS, R., MORITZ, R. & MARCHEV, P. 2010c. The effect of early Alpine thrusting in late-stage extensional tectonics: Evidence from the Kulidzhik nappe and the Pelevun extensional allochthon in the Rhodope Massif, Bulgaria. *Tectonophysics,* 488**,** 256-281.

BONEV, N. & STAMPFLI, G. 2008. Petrology, geochemistry and geodynamic implications of Jurassic island arc magmatism as revealed by mafic volcanic rocks in the Mesozoic low-grade sequence, eastern Rhodope, Bulgaria. *Lithos,* 100**,** 210-233.

BONEV, N. & STAMPFLI, G. 2011. Alpine tectonic evolution of a Jurassic subduction-accretionary complex: Deformation, kinematics and< sup> 40</sup> Ar/< sup> 39</sup> Ar age constraints on the Mesozoic low-grade schists of the Circum-Rhodope Belt in the eastern Rhodope-Thrace region, Bulgaria-Greece. *Journal of Geodynamics,* 52**,** 143-167.

BONEV, N. G. & STAMPFLI, G. M. 2003. New structural and petrologic data on Mesozoic schists in the Rhodope (Bulgaria): geodynamic implications. *Comptes Rendus Geoscience,* 335**,** 691-699.

BOSSE, V., BOULVAIS, P., GAUTIER, P., TIEPOLO, M., RUFFET, G., DEVIDAL, J. L., CHERNEVA, Z., GERDJIKOV, I. & PAQUETTE, J. L. 2009. Fluid-induced disturbance of the monazite Th–Pb chronometer: In situ dating and element mapping in pegmatites from the Rhodope (Greece, Bulgaria). *Chemical Geology,* 261**,** 286-302.

BOSSE, V., CHERNEVA, Z., GAUTIER, P. & GERDJIKOV, I. 2010. Two partial melting events as recorded by the U-Th-Pb chronometer in monazite: LA-ICPMS in situ dating in metapelites from the Bulgarian Central Rhodopes. *Επιστημονική Επετηρίδα του Τμήματος Γεωλογίας (ΑΠΘ),* 39**,** 51-52.

BOYANOV, I. & GORANOV, A. 2001. Late Alpine (Palaeogene) superimposed depressions in parts of South-east Bulgaria. *Geologica Balcanica,* 31**,** 3-36.

BOYANOV, I. & RUSSEVA, M. 1989. Lithostratigraphy and tectonic position of the Mesozoic rocks in the East Rhodopes: Geologica Rhodopica, v. 1. *Postcollisional Tectonics and Magmatism in the Mediterranean Region and Asia***,** 22-33.

BOYNTON, W. Meteoritic evidence concerning conditions in the solar nebula. IN: Protostars and planets II (A86-12626 03-90). Tucson, AZ, University of Arizona Press, 1985, p. 772-787., 1985. 772-787.

BROWN, S. A. M. & ROBERTSON, A. H. F. 2003. Sedimentary geology as a key to understanding the tectonic evolution of the Mesozoic–Early Tertiary Paikon Massif, Vardar suture zone, N Greece. *Sedimentary Geology,* 160**,** 179-212.

BROWN, S. A. M. & ROBERTSON, A. H. F. 2004. Evidence for Neotethys rooted within the Vardar suture zone from the Voras Massif, northernmost Greece. *Tectonophysics,* 381**,** 143-173.

BRUN, J.-P. & FACCENNA, C. 2008. Exhumation of high-pressure rocks driven by slab rollback. *Earth and Planetary Science Letters,* 272**,** 1-7.

BUCHER, K. & GRAPES, R. H. 2011. *Petrogenesis of metamorphic rocks*, Springer.

BUNDY, F., HALL, H., STRONG, H. & WENTORF, R. 1955. Man-made diamonds. *Nature,* 176**,** 51-55.

BURCHFIEL, B. C. 1980. Eastern European Alpine system and the Carpathian orocline as an example of collision tectonics. *Tectonophysics,* 63**,** 31-61.

BURG, J.-P., IVANOV, Z., RICOU, L.-E., DIMOR, D. & KLAIN, L. 1990. Implications of shear-sense criteria for the tectonic evolution of the Central Rhodope massif, southern Bulgaria. *Geology,* 18**,** 451-454.

BURG, J. 2011. Rhodope: from Mesozoic convergence to Cenozoic extension. *Review of petro-structural data in the geochronological frame. Journal of the Virtual Explorer,* 39.

BURG, J. P., RICOU, L. E., IVANOV, Z., GODFRIAUX, I., DIMOV, D. & KLAIN, L. 1996. Syn-metamorphic nappe complex in the Rhodope massif. Structure and kinematics. *Terra Nova,* 8**,** 6-15.

BURTMAN, V. S. & MOLNAR, P. 1993. Geological and Geophysical Evidence for Deep Subduction of Continental Crust Beneath the Pamir. *Geological Society of America Special Papers,* 281**,** 1-76.

BUSIGNY, V., CARTIGNY, P., PHILIPPOT, P., ADER, M. & JAVOY, M. 2003. Massive recycling of nitrogen and other fluid-mobile elements (K, Rb, Cs, H) in a cold slab environment: evidence from HP to UHP oceanic metasediments of the Schistes Lustrés nappe (western Alps, Europe). *Earth and Planetary Science Letters,* 215**,** 27-42.

CANN, J. 1970. Rb, Sr, Y, Zr and Nb in some ocean floor basaltic rocks. *Earth and Planetary Science Letters,* 10**,** 7-11.

CARO, G., BOURDON, B., BIRCK, J.-L. & MOORBATH, S. 2006. High-precision< sup> 142</sup> Nd/< sup> 144</sup> Nd measurements in terrestrial rocks: Constraints on the early differentiation of the Earth's mantle. *Geochimica Et Cosmochimica Acta,* 70**,** 164-191.

CARRIGAN, C. W., MUKASA, S. B., HAYDOUTOV, I. & KOLCHEVA, K. 2003. Ion microprobe U-Pb zircon ages of pre-Alpine rocks in the Balkan, Sredna Gora and Rhodope terranes of Bulagria: constraints on Neoproterozoic and variscan tectonic evolution. *Journal of the Czech geological Society,* 48**,** 32-33.

CARRIGAN, C. W., MUKASA, S. B., HAYDOUTOV, I. & KOLCHEVA, K. 2005. Age of Variscan magmatism from the Balkan sector of the orogen, central Bulgaria. *Lithos,* 82**,** 125-147.

CARSWELL, D. A. 1990. *Eclogite facies rocks*, Springer.

CARSWELL, D. A. & CUTHBERT, S., J 2003. Ultrahigh pressure metamorphism in the Western Gneiss Region of Norway. *Ultrahigh pressure metamorphism, EMU Notes in Mineralogy.*

CHAMBERS, J. A. & KOHN, M. J. 2012. Titanium in muscovite, biotite, and hornblende: Modeling, thermometry, and rutile activities of metapelites and amphibolites. *American Mineralogist,* 97**,** 543-555.

CHEMENDA, A. I., MATTAUER, M. & BOKUN, A. N. 1996. Continental subduction and a mechanism for exhumation of high-pressure metamorphic rocks: new modelling and field data from Oman. *Earth and Planetary Science Letters,* 143**,** 173-182.

CHEMENDA, A. I., MATTAUER, M., MALAVIEILLE, J. & BOKUN, A. N. 1995. A mechanism for syn-collisional rock exhumation and associated normal faulting: Results from physical modelling. *Earth and Planetary Science Letters,* 132**,** 225-232.

CHERNEVA, Z. & GEORGIEVA, M. 2005. Metamorphozed Hercynian granitoids in the Alpine structures of the Central Rhodope, Bulgaria: geotectonic position and geochemistry. *Lithos,* 82**,** 149-168.

CHERNEVA, Z., OVTCHAROVA, M., VON QUADT, A., KOLCHEVA, K., STANCHEVA, E., SAROV, S. & PEYTCHEVA, I. Monazite and zircon U–Pb ages of migmatites from Arda River Valley, Central Rhodopian

Dome, Bulgaria. Proceedings of the annual scientific conference of BGS, Sofia, 2002. 20-22.

CHOPIN, C. 1984. Coesite and Pure Pyrope in High-Grade Blueschists of the Western Alps - a 1st Record and Some Consequences. *Contributions to Mineralogy and Petrology,* 86**,** 107-118.

CHOPIN, C. 1987. Very-High-Pressure Metamorphism in the Western Alps: Implications for Subduction of Continental Crust [and Discussion]. *Philosophical Transactions of the Royal Society of London. Series A, Mathematical and Physical Sciences,* 321**,** 183-197.

CHOPIN, C. & FERRARIS, G. 2003. Mineral chemistry and mineral reactions in UHPM rocks. *In:* CARSWELL, D. A. & COMPAGNONI, R. (eds.) *Ultrahigh Pressure Metamorphism.* Budapest: Eotvos University Press.

CHRISTENSEN, J. N., ROSENFELD, J. L. & DEPAOLO, D. J. 1989. RATES OF TECTONOMETAMORPHIC PROCESSES FROM RUBIDIUM AND STRONTIUM ISOTOPES IN GARNET. *Science,* 244**,** 1465-1469.

CHRISTOFIDES, G., SOLDATOS, T., ELEFTHERIADIS, G. & KORONEOS, A. 1998. Chemical and isotopic evidence for source contamination and crustal assimilation in the Hellenic Rhodope plutonic rocks. *Acta Vulcanologica,* 10**,** 305-318.

CLEMENS, J. D. & VIELZEUF, D. 1987. Constraints on melting and magma production in the crust. *Earth and Planetary Science Letters,* 86**,** 287-306.

COLEMAN, R., LEE, D., BEATTY, L. & BRANNOCK, W. W. 1965. Eclogites and eclogites: their differences and similarities. *Geological Society of America Bulletin,* 76**,** 483-508.

COLEMAN, R. G. & WANG, X. 1995. Overview of the Geology and Tectonics of UHPM. *In:* COLEMAN, R. G. W., X. (ed.) *Ultrahigh Pressure Metamorphism.* Cambridge: CAmbridge University Press.

CORNELIUS, N. K. 2008. *UHP metamorphic rocks of the Eastern Rhodope Massif, NE Greece: new constraints from petrology, geochemistry and zircon ages.* PhD Thesis, Johannes-Gutenberg Universität, Mainz.

DAIEVA, L., HAYDOUTOV, I. & PRISTAVOVA, S. 2007. Geochemical correlation of metabasic rocks from Central and East Rhodopes. *Geochemistry, Mineralogy and Petrology,* 45**,** 109-118.

DASGUPTA, S., SENGUPTA, P., GUHA, D. & FUKUOKA, M. 1991. A refined garnet-biotite Fe– Mg exchange geothermometer and its application in amphibolites and granulites. *Contributions to Mineralogy and Petrology,* 109**,** 130-137.

DE BRESSER, J., TER HEEGE, J. & SPIERS, C. 2001. Grain size reduction by dynamic recrystallization: can it result in major rheological weakening? *International Journal of Earth Sciences,* 90**,** 28-45.

DEPAOLO, D. J. & WASSERBURG, G. J. 1976. Nd isotopic variations and petrogenetic models. *Geophysical Research Letters,* 3**,** 249-252.

DEWOLF, C. P., ZEISSLER, C. J., HALLIDAY, A. N., MEZGER, K. & ESSENE, E. J. 1996. The role of inclusions in U-Pb and Sm-Nd garnet geochronology: Stepwise dissolution experiments and trace uranium mapping by fission track analysis. *Geochimica Et Cosmochimica Acta,* 60**,** 121-134.

DICKINSON JR, J. E. & HESS, P. C. 1985. Rutile solubility and titanium coordination in silicate melts. *Geochimica Et Cosmochimica Acta,* 49**,** 2289-2296.

DIDIER, A., BOSSE, V., CHERNEVA, Z., GEORGIEVA, M., PIERRE G., PAQUETTE, J.-L. & GERDJIKOV, I. 2012. The Role of Fluids in the Monazite Record during Successive Partial Melting Events: A Textural, Chemical and in situ Dating Study in Grt-Ky Gneisses of the Central Rhodope (Bulgaria, Greece). *Goldschmidt, .* Montreal Mineralogical Magazine.

DINTER, D. A. 1998. Late Cenozoic extension of the Alpine collisional orogen, northeastern Greece: Origin of the north Aegean basin. *Geological Society of America Bulletin,* 110**,** 1208-1230.

DINTER, D. A., MACFARLANE, A., HAMES, W., ISACHSEN, C., BOWRING, S. & ROYDEN, L. 1995. U-Pb and 40Ar/39Ar geochronology of the Symvolon granodiorite: Implications for the thermal and structural evolution of the Rhodope metamorphic core complex, northeastern Greece. *Tectonics,* 14**,** 886-908.

DINTER, D. A. & ROYDEN, L. 1993. Late Cenozoic extension in northeastern Greece: Strymon Valley detachment system and Rhodope metamorphic core complex. *Geology,* 21**,** 45-48.

DOBRETSOV, N. L., SOBOLEV, N. V., SHATSKY, V. S., COLEMAN, R. G. & ERNST, W. G. 1995. Geotectonic evolution of diamondiferous paragneisses, Kokchetav Complex, northern Kazakhstan: The geologic enigma of ultrahigh-pressure crustal rocks within a Paleozoic foldbelt. *Island Arc,* 4**,** 267-279.

DOBRZHINETSKAYA, L. F. 2012. Microdiamonds—Frontier of ultrahigh-pressure metamorphism: A review. *Gondwana Research,* 21**,** 207-223.

DOBRZHINETSKAYA, L. F. & FARYAD, S. W. 2011. Frontiers of ultrahigh-pressure metamorphism: view from field and laboratory. *Ultrahigh-Pressure Metamorphism,* 25**,** 1-39.

DOBRZHINETSKAYA, L. F., WIRTH, R. & GREEN, H. W. Mineral microstructures for understanding deep subduction and exhumation. 10 th International Eclogite Conference, 2013. 25.

DRAGOVIC, B., SAMANTA, L. M., BAXTER, E. F. & SELVERSTONE, J. 2012. Using garnet to constrain the duration and rate of water-releasing metamorphic reactions during subduction: An example from Sifnos, Greece. *Chemical Geology,* 314**,** 9-22.

DURETZ, T. & GERYA, T. 2013. Slab detachment during continental collision: Influence of crustal rheology and interaction with lithospheric delamination. *Tectonophysics,* 602**,** 124-140.

DÜRR, S., ALTHERR, R., KELLER, J., OKRUSCH, M. & SEIDEL, E. 1978. The median Aegean crystalline belt: stratigraphy, structure, metamorphism, magmatism. *Alps, Apennines, Hellenides,* 38**,** 455-476.

EBERHART-PHILLIPS, D., CHRISTENSEN, D. H., BROCHER, T. M., HANSEN, R., RUPPERT, N. A., HAEUSSLER, P. J. & ABERS, G. A. 2006. Imaging the transition from Aleutian subduction to Yakutat collision in central Alaska, with local earthquakes and active source data. *Journal of Geophysical Research: Solid Earth,* 111**,** B11303.

FERRY, J. T. & SPEAR, F. 1978. Experimental calibration of the partitioning of Fe and Mg between biotite and garnet. *Contributions to Mineralogy and Petrology,* 66**,** 113-117.

FLOYD, P. & WINCHESTER, J. 1978. Identification and discrimination of altered and metamorphosed volcanic rocks using immobile elements. *Chemical Geology,* 21**,** 291-306.

FRIEDL, G., COOKE, R., FINGER, F., MCNAUGHTON, N. & FLETCHER, I. 2011. Timing of Variscan HP-HT metamorphism in the Moldanubian Zone of the Bohemian Massif: U-Pb SHRIMP dating on multiply zoned zircons from a granulite from the Dunkelsteiner Wald Massif, Lower Austria. *Mineralogy and Petrology,* 102**,** 63-75.

FROITZHEIM, N. 2001. Origin of the Monte Rosa nappe in the Pennine Alps—A new working hypothesis. *Geological Society of America Bulletin,* 113**,** 604-614.

GAUDETTE, H., EADES, J. & GRIM, R. 1966. The nature of illite. *Clays and clay minerals,* 13**,** 35-48.

GEBAUER, D. 1999. Alpine geochronology of the Central and Western Alps: new constraints for a complex geodynamic evolution. *Schweizerische Mineralogische und Petrographische Mitteilungen,* 79**,** 191-208.

GEBAUER, D. & LIATI, A. 1997. Geochronological evidence for Mesozoic rifting and oceanization followed by Eocene subduction in the Rhodope Complex (Northern Greece). *Terra Nova,* 9.

GEORGIEV, S., VON QUADT, A., HEINRICH, C., PEYTCHEVA, I. & MARCHEV, P. 2012. Time evolution of a rifted continental arc: Integrated ID-TIMS and LA-ICPMS study of magmatic zircons from the Eastern Srednogorie, Bulgaria. *Lithos,* 154**,** 53-67.

GEORGIEVA, M., CHERNEVA, Z., GERDJIKOV, I. & STANCHEVA, E. 2010. Metabasic rocks from the Chepelare variegated complex, central Rhodope massif, Bulgaria-preliminary studies. *Επιστημονική Επετηρίδα του Τμήματος Γεωλογίας (ΑΠΘ),* 39**,** 131-132.

GEORGIEVA, M., CHERNEVA, Z., MOGESSIE, A. & STANCHEVA, E. Garnet-kyanite schists from the Chepelare area, Central Rhodopes Mts., Bulgaria: mineral chemistry, thermobarometry and indications for high-pressure melting. Proc. National Conf. GEOSCIENCES 2007, 2007. 97-98.

GERYA, T. V., PERCHUK, L. L. & BURG, J. P. 2008. Transient hot channels: Perpetrating and regurgitating ultrahigh-pressure, high-temperature crust–mantle associations in collision belts. *Lithos,* 103**,** 236-256.

GILOTTI, J. A. & MCCLELLAND, W. C. 2007. Characteristics of, and a Tectonic Model for, Ultrahigh-Pressure Metamorphism in the Overriding Plate of the Caledonian Orogen. *International Geology Review,* 49**,** 777-797.

GRAF, J., VON QUADT, A., BERNOULLI, D. & BURG, J. Geochemistry and geochronology of igneous rocks of the central Serbo-Macedonian Massif (Western Bulgaria). Abstracts, Carpathian–Balkan Geological Association XVI Congress, 1998.

GUIDOTTI, C. V. 1984. Micas in metamorphic rocks. *Reviews in Mineralogy and Geochemistry,* 13**,** 357-467.

GUIDOTTI, C. V. & SASSI, F. P. 2002. Constraints on studies of metamorphic K-Na white micas. *Reviews in Mineralogy and Geochemistry,* 46**,** 413-448.

GUILLOT, S., HATTORI, K. H., DE SIGOYER, J., NÄGLER, T. & AUZENDE, A.-L. 2001. Evidence of hydration of the mantle wedge and its role in the exhumation of eclogites. *Earth and Planetary Science Letters,* 193**,** 115-127.

HACKER, B., LUFFFI, P., LUTKOV, V., MINAEV, V., RATSCHBACHER, L., PLANK, T., DUCEA, M., PATIÑO-DOUCE, A., MCWILLIAMS, M. & METCALF, J. 2005. Near-ultrahigh pressure processing of continental crust: Miocene crustal xenoliths from the Pamir. *Journal of Petrology,* 46**,** 1661-1687.

HACKER, B. R. & GERYA, T. V. 2013. Paradigms, new and old, for ultrahigh-pressure tectonism. *Tectonophysics,* 603**,** 79-88.

HACKER, B. R., RATSCHBACHER, L., WEBB, L., MCWILLIAMS, M. O., IRELAND, T., CALVERT, A., DONG, S., WENK, H. R. & CHATEIGNER, D. 2000. Exhumation of ultrahigh‐pressure continental crust in east central China: Late Triassic‐Early Jurassic tectonic unroofing. *Journal of Geophysical Research: Solid Earth (1978‐2012),* 105**,** 13339-13364.

HARKOVSKA, A., YANEV, Y. & MARCHEV, P. 1989. General features of the Paleogene orogenic magmatism in Bulgaria. *Geologica Balcanica,* 19**,** 37-72.

HARRIS, R. 2003. Geodynamic patterns of ophiolites and marginal basins in the Indonesian and New Guinea regions. *Geological Society, London, Special Publications,* 218**,** 481-505.

HARVEY, J. & BAXTER, E. F. 2009. An improved method for TIMS high precision neodymium isotope analysis of very small aliquots (1–10 ng). *Chemical Geology,* 258**,** 251-257.

HAYDEN, L. A. & WATSON, E. B. 2007. Rutile saturation in hydrous siliceous melts and its bearing on Ti-thermometry of quartz and zircon. *Earth and Planetary Science Letters,* 258**,** 561-568.

HAYDOUTOV, I., KOLCHEVA, K., DAIEVA, L. A., SAVOV, I. & CARRIGAN, C. 2004. Island Arc origin of the Variegated Formations from the East Rhodope, Bulgaria - Implications for the evolution of the Rhodope Massif. *Ofioliti,* 29**,** 145-157.

HERMANN, J. 2003. Experimental evidence for diamond-facies metamorphism in the Dora-Maira massif. *Lithos,* 70**,** 163-182.

HERMANN, J. & RUBATTO, D. 2009. Accessory phase control on the trace element signature of sediment melts in subduction zones. *Chemical Geology,* 265**,** 512-526.

HERMANN, J. & SPANDLER, C. J. 2008. Sediment Melts at Sub-arc Depths: an Experimental Study. *Journal of Petrology,* 49**,** 717-740.

HEURET, A. & LALLEMAND, S. 2005. Plate motions, slab dynamics and back-arc deformation. *Physics of the Earth and Planetary Interiors,* 149**,** 31-51.

HIMMERKUS, F., REISCHMANN, T. & KOSTOPOULOS, D. 2006a. Late Proterozoic and Silurian basement units within the Serbo-Macedonian Massif, northern Greece: the significance of terrane accretion in the Hellenides. *Geological Society, London, Special Publications,* 260**,** 35-50.

HIMMERKUS, F., REISCHMANN, T. & KOSTOPOULOS, D. Permo-Carboniferous and upper Jurassic basement ages in the Kerdillion Unit, eastern Serbo-Macedonian Massif, northern Greece. Geophys Res Abstr, 2006b. 05758.

HIMMERKUS, F., REISCHMANN, T. & KOSTOPOULOS, D. 2009a. Serbo-Macedonian revisited: a Silurian basement terrane from northern Gondwana in the Internal Hellenides, Greece. *Tectonophysics,* 473**,** 20-35.

HIMMERKUS, F., REISCHMANN, T. & KOSTOPOULOS, D. 2009b. Triassic rift-related meta-granites in the Internal Hellenides, Greece. *Geological Magazine,* 146**,** 252-265.

HODGES, K. & SPEAR, F. S. 1982. Geothermometry, geobarometry and the Al 2 SiO 5 triple point at Mt. Moosilauke, New Hampshire. *American Mineralogist,* 67**,** 1118-1134.

HOLDAWAY, M. & LEE, S. M. 1977. Fe-Mg cordierite stability in high-grade pelitic rocks based on experimental, theoretical, and natural observations. *Contributions to Mineralogy and Petrology,* 63**,** 175-198.

HOLLAND, T. & BLUNDY, J. 1994. Non-ideal interactions in calcic amphiboles and their bearing on amphibole-plagioclase thermometry. *Contributions to Mineralogy and Petrology,* 116**,** 433-447.

HUMPHRIES, S.E., 1984. The mobility of the rare earth elements in the crust. In: Henderson,P. (Ed.), Rare Earth Element Geochemistry. Elsevier, Amsterdam, 315–341.

HSU, K. J., NACHEV, I. K. & VUCHEV, V. T. 1977. GEOLOGIC EVOLUTION OF BULGARIA IN LIGHT OF PLATE TECTONICS. *Tectonophysics,* 40**,** 245-256.

IVANOV, Z., MOSKOVSKI, S., DIMOV, D., KOLCHEVA, K. & KLAIN, L. 1985. Geological structure of the Central Rhodopes. II. Structural sequences in the synmetamorphic evolution of the Central-Rhodope metamorphic group. *Geologica Balcanica,* 15**,** 3-32.

JACOBSHAGEN, V., DORNSIEPEN, Ü., GIESE, P. & WALLBRECHER, P. 1986. *Geologie von Griechenland*, Gebr. Borntraeger Berlin.

JAHN-AWE, S., FROITZHEIM, N., NAGEL, T. J., FREI, D., GEORGIEV, N. & PLEUGER, J. 2010. Structural and geochronological evidence for Paleogene thrusting in the western Rhodopes, SW Bulgaria: Elements for a new tectonic model of the Rhodope Metamorphic Province. *Tectonics,* 29**,** TC3008.

JAHN-AWE, S., PLEUGER, J., FREI, D., GEORGIEV, N., FROITZHEIM, N. & NAGEL, T. J. 2012. Time constraints for low-angle shear zones in the Central Rhodopes (Bulgaria) and their significance for the exhumation of high-pressure rocks. *International Journal of Earth Sciences,* 101**,** 1971-2004.

JANAK, M., FROITZHEIM, N., GEORGIEV, N., NAGEL, T. J. & SAROV, S. 2011. P-T evolution of kyanite eclogite from the Pirin Mountains (SW Bulgaria): implications for the Rhodope UHP Metamorphic Complex. *Journal of Metamorphic Geology,* 29**,** 317-332.

JOLIVET, L. & BRUN, J.-P. 2010. Cenozoic geodynamic evolution of the Aegean. *International Journal of Earth Sciences,* 99**,** 109-138.

JONES, C. E., TARNEY, J., BAKER, J. H. & GEROUKI, F. 1992. Tertiary granitoids of Rhodope, northern Greece: Magmatism related to extensional collapse of the Hellenic Orogen? *Tectonophysics,* 210**,** 295-314.

KAUFFMANN, G., KOCKEL, F. & MOLLAT, H. 1976. Notes on the stratigraphic and paleogeographic position of the Svoula formation in the Innermost Zone of the Hellenides (Northern Greece). *Bulletin de la Société géologique de France,* 18**,** 225-230.

KELLY, E. D., CARLSON, W. D. & CONNELLY, J. N. 2011. Implications of garnet resorption for the Lu–Hf garnet geochronometer: an example from the contact aureole of the Makhavinekh Lake Pluton, Labrador. *Journal of Metamorphic Geology,* 29**,** 901-916.

KIRCHENBAUR, M., PLEUGER, J., JAHN-AWE, S., NAGEL, T. J., FROITZHEIM, N., FONSECA, R. O. C. & MÜNKER, C. 2012. Timing of high-pressure metamorphic events in the Bulgarian Rhodopes from Lu–Hf garnet geochronology. *Contributions to Mineralogy and Petrology,* 163**,** 897-921.

KOCKEL, F., MOLLAT, H. & WALTHER, H. 1971. Geologie des Serbo-Mazedonischen Massivs und seines mesozoischen Rahmens (Nordgriechenland). *Geol Jahrb,* 89**,** 529-551.

KOCKEL, F. & WALTHER, H. 1965. Die Strimonlinie als Grenze zwischen Serbo-Mazedonischem und Rila-Rhodope-Massiv in Ost-Mazedonien. *Geol. Jb,* 83**,** 5-602.

KOHN, M. J. 2009. Models of garnet differential geochronology. *Geochimica Et Cosmochimica Acta,* 73**,** 170-182.

KOHN, M. J. & SPEAR, F. S. 1990. Two new geobarometers for garnet amphibolites, with applications to southeastern Vermont. *American Mineralogist,* 75**,** 89-96.

KOLCHEVA, K. & ESKENAZY, G. 1988. Geochemistry of metaeclogites from the central and eastern Rhodope Mts (Bulgaria). *Geol. Balc,* 18**,** 61-78.

KORSAKOV, A. V., PERRAKI, M., ZEDGENIZOV, D. A., BINDI, L., VANDENABEELE, P., SUZUKI, A. & KAGI, H. 2010a. Diamond–graphite relationships in ultrahigh-pressure metamorphic rocks from the Kokchetav Massif, Northern Kazakhstan. *Journal of Petrology,* 51**,** 763-783.

KORSAKOV, A. V., ZHUKOV, V. P. & VANDENABEELE, P. 2010b. Raman-based geobarometry of ultrahigh-pressure metamorphic rocks: applications, problems, and perspectives. *Analytical and Bioanalytical Chemistry,* 397**,** 2739-2752.

KOSTOPOULOS, D., GERDJIKOV, I., GAUTIER, P., REISCHMANN, T. & CHERNEVA, Z. First evidence of UHP metamorphism in the Central Rhodope Massif of southern Bulgaria. Geophys Res Abstr, 2003. 08327.

KOUNOV, A., GRAF, J., VON QUADT, A., BERNOULLI, D., BURG, J.-P., SEWARD, D., IVANOV, Z. & FANNING, M. 2012. Evidence for a “Cadomian” ophiolite and magmatic-arc complex in SW Bulgaria. *Precambrian Research,* 212**,** 275-295.

KRENN, K., BAUER, C., PROYER, A., KLOTZLI, U. & HOINKES, G. 2010. Tectonometamorphic evolution of the Rhodope orogen. *Tectonics,* 29.

KRETZ, R. 1959. Chemical study of garnet, biotite, and hornblende from gneisses of southwestern Quebec, with emphasis on distribution of elements in coexisting minerals. *The Journal of Geology***,** 371-402.

KROHE, A. & MPOSKOS, E. 2002. Multiple generations of extensional detachments in the Rhodope Mountains (northern Greece): evidence of episodic exhumation of high-pressure rocks. *In:* BLUNDELL, D. J., NEUBAUER, F. & VONQUADT, A. (eds.) *Timing and Location of Major Ore Deposits in an Evolving Orogen.* Bath: Geological Soc Publishing House.

KYLANDER-CLARK, A. R. C., HACKER, B. R. & MATTINSON, C. G. 2012. Size and exhumation rate of ultrahigh-pressure terranes linked to orogenic stage. *Earth and Planetary Science Letters,* 321–322**,** 115-120.

LAGOS, M., SCHERER, E. E., TOMASCHEK, F., MÜNKER, C., KEITER, M., BERNDT, J. & BALLHAUS, C. 2007. High precision Lu–Hf geochronology of Eocene eclogite-facies rocks from Syros, Cyclades, Greece. *Chemical Geology,* 243**,** 16-35.

LARDEAUX, J., LEDRU, P., DANIEL, I. & DUCHENE, S. 2001. The Variscan French Massif Central—a new addition to the ultra-high pressure metamorphic 'club': exhumation processes and geodynamic consequences. *Tectonophysics,* 332**,** 143-167.

LEAKE, B. E. 1964. The Chemical Distinction Between Ortho- and Para-amphibolites. *Journal of Petrology,* 5**,** 238-254.

LEAKE, B. E., WOOLLEY, A. R., ARPS, C., BIRCH, W., GILBERT, M., GRICE, J., HAWTHORNE, F., KATO, A., KISCH, H. & KRIVOVICHEV, V. 1997. Nomenclature of amphiboles; report of the Subcommittee on Amphiboles of the International Mineralogical Association Commission on new minerals and mineral names. *Mineralogical Magazine,* 61**,** 295-321.

LEE, J. K., WILLIAMS, I. S. & ELLIS, D. J. 1997. Pb, U and Th diffusion in natural zircon. *Nature,* 390**,** 159-162.

LI, Z., GERYA, T. & BURG, J. P. 2010. Influence of tectonic overpressure on P–T paths of HP–UHP rocks in continental collision zones: thermomechanical modelling. *Journal of Metamorphic Geology,* 28**,** 227-247.

LI, Z. & GERYA, T. V. 2009. Polyphase formation and exhumation of high‐ to ultrahigh‐pressure rocks in continental subduction zone: Numerical modeling and application to the Sulu ultrahigh‐pressure terrane in eastern China. *Journal of Geophysical Research: Solid Earth (1978–2012),* 114.

LIATI, A. 1986. *Regional metamorphism and overprinting contact metamorphism of the Rhodope zone, near Xanthi (N. Greece): petrology, geochemistry, geochronology.* PhD, Technical University Braunschweig.

LIATI, A. 2005. Identification of repeated Alpine (ultra) high-pressure metamorphic events by U-PbSHRIMP geochronology and REE geochemistry of zircon: the Rhodope zone of Northern Greece. *Contributions to Mineralogy and Petrology,* 150**,** 608-630.

LIATI, A. & FANNING, C. 2005. Eclogites and their country rock orthogneisses in East Rhodope representing Upper Permian gabbros and Upper Carboniferous granitoids: geochronological constraints. *Mitt Oesterr Mineral Ges,* 150.

LIATI, A. & GEBAUER, D. 1999. Constraining the prograde and retrograde PTt path of Eocene HP rocks by SHRIMP dating of different zircon domains: inferred rates of heating, burial, cooling and exhumation for central Rhodope, northern Greece. *Contributions to Mineralogy and Petrology,* 135**,** 340-354.

LIATI, A., GEBAUER, D. & FANNING, C. M. 2004. The age of ophiolitic rocks of the Hellenides (Vourinos, Pindos, Crete): first U–Pb ion microprobe (SHRIMP) zircon ages. *Chemical Geology,* 207**,** 171-188.

LIATI, A., GEBAUER, D. & FANNING, C. M. 2011. 10 - Geochronology of the Alpine UHP Rhodope Zone: A Review of Isotopic Ages and Constraints on the Geodynamic Evolution. *In:* LARISSA, D., SHAH WALI, F., SIMON, W. & CUTHBERT, S. (eds.) *Ultrahigh Pressure Metamorphism.* London: Elsevier.

LIATI, A., GEBAUER, D. & WYSOCZANSKI, R. 2002. U-Pb SHRIMP-dating of zircon domains from UHP garnet-rich mafic rocks and late pegmatoids in the Rhodope zone (N Greece); evidence for Early Cretaceous crystallization and Late Cretaceous metamorphism. *Chemical Geology,* 184, 281-299.

LIATI, A. & MPOSKOS, E. 1990. Evolution of the eclogites in the Rhodope Zone of northern Greece. *Lithos,* 25, 89-99.

LIATI, A. & SEIDEL, E. 1996. Metamorphic evolution and geochemistry of kyanite eclogites in central Rhodope, northern Greece. *Contributions to Mineralogy and Petrology,* 123, 293-307.

LIOU, J., ERNST, W., ZHANG, R., TSUJIMORI, T. & JAHN, B. 2009. Ultrahigh-pressure minerals and metamorphic terranes–the view from China. *Journal of Asian Earth Sciences,* 35, 199-231.

LIPS, A. L. W., WHITE, S. H. & WIJBRANS, J. R. 2000. Middle-Late Alpine thermotectonic evolution of the southern Rhodope Massif, Greece. *Geodinamica Acta,* 13, 281-292.

LITTLE, T., HACKER, B., GORDON, S., BALDWIN, S., FITZGERALD, P., ELLIS, S. & KORCHINSKI, M. 2011. Diapiric exhumation of Earth's youngest (UHP) eclogites in the gneiss domes of the D'Entrecasteaux Islands, Papua New Guinea. *Tectonophysics,* 510, 39-68.

LIU, L., ZHANG, J., GREEN II, H. W., JIN, Z. & BOZHILOV, K. N. 2007. Evidence of former stishovite in metamorphosed sediments, implying subduction to> 350 km. *Earth and Planetary Science Letters,* 263, 180-191.

LUDWIG, K. R. 2003. *User's manual for Isoplot 3.00: a geochronological toolkit for Microsoft Excel*, Kenneth R. Ludwig.

LUGMAIR, G., MARTI, K., KURTZ, J. & SCHEININ, N. History and genesis of lunar troctolite 76535 or: How old is old. Lunar and Planetary Science Conference Proceedings, 1976. 2009-2033.

MARCHEV, P., GEORGIEV, S., RAICHEVA, R., PEYTCHEVA, I., VON QUADT, A., OVTCHAROVA, M. & BONEV, N. 2013. Adakitic magmatism in post-collisional setting: An example from the Early–Middle Eocene Magmatic Belt in Southern Bulgaria and Northern Greece. *Lithos,* 180, 159-180.

MASSONNE, H.-J. & SZPURKA, Z. 1997. Thermodynamic properties of white micas on the basis of high-pressure experiments in the systems K2O · MgO · Al2O3 · SiO2 · H2O and K2 · O · FeO · Al3O3 · SiO2 · H3O. *Lithos,* 41, 229-250.

MASSONNE, H.-J., WILLNER, A. P. & GERYA, T. 2007. Densities of metapelitic rocks at high to ultrahigh pressure conditions: What are the geodynamic consequences? *Earth and Planetary Science Letters,* 256, 12-27.

MCDONOUGH, W. F. & SUN, S. S. 1995. The composition of the Earth. *Chemical Geology,* 120, 223-253.

MEINHOLD, G. 2007. Sedimentary rocks of the Internal Hellenides, Greece: age, source, and depositional setting. *Unpublished PhD thesis, Johannes Gutenberg-Universität, Mainz*, 1-303.

MEINHOLD, G., REISCHMANN, T., KOSTOPOULOS, D., LEHNERT, O., MATUKOV, D. & SERGEEV, S. 2008. Provenance of sediments during subduction of Palaeotethys: Detrital zircon ages and olistolith analysis in Palaeozoic sediments from Chios Island, Greece. *Palaeogeography, Palaeoclimatology, Palaeoecology,* 263, 71-91.

MELZER, S. & WUNDER, B. 2000. Island-arc basalt alkali ratios: Constraints from phengite-fluid partitioning experiments. *Geology,* 28**,** 583-586.

MERCIER, J. 1966. *Mouvements orogéniques et magmatisme d'âge jurassique supérieur éocrétacé dans les zones internes des Hellénides (Macédoine, Grèce)*.

MERCIER, J., VERGELY, P. & BEBIEN, J. 1975. Les ophiolites helléniques «obductées» au Jurassique supérieur sont-elles les vestiges d'un Océan téthysien ou d'une mer marginale péri-européenne. *CR Somm Soc Géol France***,** 108-112.

MESCHEDE, M. 1986. A method of discriminating between different types of mid-ocean ridge basalts and continental tholeiites with the Nb---1bZr---1bY diagram. *Chemical Geology,* 56**,** 207-218.

MEZGER, K., ESSENE, E. J. & HALLIDAY, A. 1992. Closure temperatures of the Sm—Nd system in metamorphic garnets. *Earth and Planetary Science Letters,* 113**,** 397-409.

MEZGER, K., HANSON, G. N. & BOHLEN, S. R. 1989. U-Pb systematics of garnet: dating the growth of garnet in the late Archean Pikwitonei granulite domain at Cauchon and Natawahunan Lakes, Manitoba, Canada. *Contributions to Mineralogy and Petrology,* 101**,** 136-148.

MOUNTRAKIS, D. 1986. The Pelagonian zone in Greece: a polyphase-deformed fragment of the Cimmerian continent and its role in the geotectonic evolution of the eastern Mediterranean. *The Journal of Geology***,** 335-347.

MPOSKOS, E., BAZIOTIS, I. & PROYER, A. 2012. Pressure–temperature evolution of eclogites from the Kechros complex in the Eastern Rhodope (NE Greece). *International Journal of Earth Sciences,* 101**,** 973-996.

MPOSKOS, E. & KROHE, A. Petrological and structural evolution of continental high pressure (HP) metamorphic rocks in the Alpine Rhodope Domain (N. Greece). Proceedings of the 3rd International Conference on the Geology of the Eastern Mediterranean, 2000. 221-232.

MPOSKOS, E., KROHE, A. & BAZIOTIS, I. 2010. Alpine polyphase metamorphism in metapelites from Sidironero complex (Rhodope Domian, NE Greece).

MPOSKOS, E. & LIATI, A. 1993. Metamorphic evolution of metapelites in the high-pressure terrane of the Rhodope zone, Northern Greece. *Canadian Mineralogist,* 31**,** 401-401.

MPOSKOS, E. & PERDIKATSIS, V. 1989. Eclogite-amphibolites in the east Rhodope massif. *Geologica Rhodopica,* 1**,** 160-168.

MPOSKOS, E., PERRAKI, M. & PALIKARI, S. 2009. Single and multiphase inclusions in metapelitic garnets of the Rhodope Metamorphic Province, NE Greece. *Spectrochimica Acta Part a-Molecular and Biomolecular Spectroscopy,* 73**,** 477-483.

MPOSKOS, E. & WAWRZENITZ, N. 1995. Metapegmatites and pegmatites bracketing the time of high P-metamorphism in polymetamorphic rocks of the E-Rhodope, N. Greece: petrological and geochronological constraints. *Geol. Soc. Greece Spec. Publ,* 4**,** 602-608.

MPOSKOS, E. D. & KOSTOPOULOS, D. K. 2001. Diamond, former coesite and supersilicic garnet in metasedimentary rocks from the Greek

Rhodope: a new ultrahigh-pressure metamorphic province established. *Earth and Planetary Science Letters,* 192**,** 497-506.

NAGEL, T., FROITZHEIM, N., JAHN-AWE, S., KIRCHENBAUR, M., GEORGIEV, N., FREI, D. & PLEUGER, J. The Eocene Rhodopes. EGU General Assembly Conference Abstracts, 2012 Vienna. 10394.

NAGEL, T. J., SCHMIDT, S., JANÁK, M., FROITZHEIM, N., JAHN‐AWE, S. & GEORGIEV, N. 2011. The exposed base of a collapsing wedge: the nestos shear zone (Rhodope Metamorphic Province, Greece). *Tectonics,* 30.

NAYDENOV, K., VON QUADT, A., PEYTCHEVA, I., SAROV, S. & DIMOV, D. 2009. U-Pb zircon dating of metamorphic rocks in the region of Kostenets-Kozarsko villages: constraints on the tectonic evolution of the Maritsa strike-slip shear zone. *Rev Bulg Geol Soc,* 70**,** 5-21.

OGASAWARA, Y., FUKASAWA, K. & MARUYAMA, S. 2002. Coesite exsolution from supersilicic titanite in UHP marble from the Kokchetav Massif, northern Kazakhstan. *American Mineralogist,* 87**,** 454-461.

OKAY, A. I., BOZKURT, E., SATıR, M., YIĞITBAŞ, E., CROWLEY, Q. G. & SHANG, C. K. 2008. Defining the southern margin of Avalonia in the Pontides: geochronological data from the Late Proterozoic and Ordovician granitoids from NW Turkey. *Tectonophysics,* 461**,** 252-264.

OVTCHAROVA, M., CHERNEVA, Z., QUADT, A. & PEYTCHEVA, I. Migmatitic geochronology and geochemistry-a key to understanding the exhumation of the Madan dome (Bulgaria). Geochimica Et Cosmochimica Acta, 2002. PERGAMON-ELSEVIER SCIENCE LTD THE BOULEVARD, LANGFORD LANE, KIDLINGTON, OXFORD OX5 1GB, ENGLAND, A573-A573.

OVTCHAROVA, M., VON QUADT, A., CHERNEVA, Z., SAROV, S., HEINRICH, C. & PEYTCHEVA, I. 2004. U-Pb dating of zircon and monazite from granitoids and migmatites in the core and eastern periphery of the Central Rhodopean Dome, Bulgaria. *Geochim Cosmochim Acta,* 68**,** A664.

PAPANIKOLAOU, D. The tectonostratigraphic terranes of the Hellenides. Annales geologiques des pays Helleniques, 1997. 495-514.

PAPANIKOLAOU, D. 2013. Tectonostratigraphic models of the Alpine terranes and subduction history of the Hellenides. *Tectonophysics,* 595–596**,** 1-24.

PEARCE, J. A. & CANN, J. 1973. Tectonic setting of basic volcanic rocks determined using trace element analyses. *Earth and Planetary Science Letters,* 19**,** 290-300.

PERCHUK, L. & LAVRENT'EVA, I. 1983. Experimental investigation of exchange equilibria in the system cordierite-garnet-biotite. *Kinetics and equilibrium in mineral reactions.* Springer.

PERRAKI, M., KORSAKOV, A. V., SMITH, D. C. & MPOSKOS, E. 2009. Raman spectroscopic and microscopic criteria for the distinction of microdiamonds in ultrahigh-pressure metamorphic rocks from diamonds in sample preparation materials. *American Mineralogist,* 94**,** 546-556.

PERRAKI, M., PROYER, A., MPOSKOS, E., KAINDL, R. & HOINKES, G. 2006. Raman micro-spectroscopy on diamond, graphite and other carbon polymorphs from the ultrahigh-pressure metamorphic Kimi Complex of the Rhodope Metamorphic Province, NE Greece. *Earth and Planetary Science Letters,* 241**,** 672-685.

PEYTCHEVA, I., KOSTITSIN, Y., SALNIKOVA, E., KAMENOV, B. & KLAIN, L. 1998. Rb–Sr and U–Pb isotope data for the Rila-Rhodopes batholith. *Geochem Mineral Petrol,* 35**,** 93-105.

PEYTCHEVA, I. & VON QUADT, A. 1995. U–Pb zircon dating of metagranites from Byala Reka region in the East Rhodopes, Bulgaria. *Geol Soc Greece Sp Publ,* 4**,** 637-642.

PEYTCHEVA, I., VON QUADT, A., GEORGIEV, N., IVANOV, Z., HEINRICH, C. & FRANK, M. 2008. Combining trace-element compositions, U–Pb geochronology and Hf isotopes in zircons to unravel complex calcalkaline magma chambers in the Upper Cretaceous Srednogorie zone (Bulgaria). *Lithos,* 104**,** 405-427.

PEYTCHEVA, I., VON QUADT, A., OVTCHAROVA, M., HANDLER, R., NEUBAUER, F., SALNIKOVA, E., KOSTITSYN, Y., SAROV, S. & KOLCHEVA, K. 2004. Metagranitoids from the eastern part of the Central Rhodopean dome (Bulgaria): U-Pb, Rb-Sr and (40)At/(39)Ar timing of emplacement and exhumation and isotope-geochemical features. *Mineralogy and Petrology,* 82**,** 1-31.

PIROMALLO, C. & MORELLI, A. 2003. P wave tomography of the mantle under the Alpine-Mediterranean area. *Journal of Geophysical Research: Solid Earth,* 108**,** 2065.

PLANK, T. & LANGMUIR, C. H. 1998. The chemical composition of subducting sediment and its consequences for the crust and mantle. *Chemical Geology,* 145**,** 325-394.

POLLINGTON, A. D. & BAXTER, E. F. 2011. High precision microsampling and preparation of zoned garnet porphyroblasts for Sm–Nd geochronology. *Chemical Geology,* 281**,** 270-282.

RAVNA, E. K. 2000. Distribution of Fe2+ and Mg between coexisting garnet and hornblende in synthetic and natural systems: an empirical calibration of the garnet-hornblende Fe-Mg geothermometer. *Lithos,* 53**,** 265-277.

REISCHMANN, T. & KOSTOPOULOS, D. 2002a. Timing of UHPM in metasediments from the Rhodope Massif, N Greece. *Geochem Cosmochem Acta,* 66**,** A633.

REISCHMANN, T. & KOSTOPOULOS, D. Timing of UHPM in metasediments from the Rhodope Massif, N Greece. Proceedings Goldschmidt Conf., Davos, Switzerland, 2002b. 634.

RICOU, L. E., BURG, J. P., GODFRIAUX, I. & IVANOV, Z. 1998. Rhodope and vardar: the metamorphic and the olistostromic paired belts related to the Cretaceous subduction under Europe. *Geodinamica Acta,* 11**,** 285-309.

ROBERTSON, A. 2004. Development of concepts concerning the genesis and emplacement of Tethyan ophiolites in the Eastern Mediterranean and Oman regions. *Earth-Science Reviews,* 66**,** 331-387.

ROBERTSON, A., DIXON, J., BROWN, S., COLLINS, A., MORRIS, A., PICKETT, E., SHARP, I. & USTAÖMER, T. 1996. Alternative tectonic models for the Late Palaeozoic-Early Tertiary development of Tethys in the Eastern Mediterranean region. *Geological Society, London, Special Publications,* 105**,** 239-263.

ROGER, F. & MATTE, P. 2005. Early Variscan HP metamorphism in the western Iberian Allochthon—A 390 Ma U–Pb age for the Bragança eclogite (NW Portugal). *International Journal of Earth Sciences,* 94**,** 173-179.

ROHRMEIER, M. K., VON QUADT, A., DRIESNER, T., HEINRICH, C., HANDLER, R., OVTCHAROVA, M., IVANOV, Z., PETROV, P. & PEYTCHEVA, I. 2013. Post-orogenic extension and hydrothermal ore formation: High-precision geochronology of the Central Rhodopian metamorphic core complex (Bulgaria-Greece). *Economic Geology,* 108**,** 691-718.

RUBATTO, D. 2002. Zircon trace element geochemistry: partitioning with garnet and the link between U–Pb ages and metamorphism. *Chemical Geology,* 184**,** 123-138.

SAROV, S. 2004. Geological Map of Republic of Bulgaria 1: 50 000 , sheet K 35- 74 B *Bulgarian National Geological Survey,* (Project 425/20/07. 2004).

SAVOV, I., RYAN, J., HAYDOUTOV, I. & SCHIJF, J. 2001. Late Precambrian Balkan-Carpathian ophiolite—A slice of the Pan-African ocean crust?: Geochemical and tectonic insights from the Tcherni Vrah and Deli Jovan massifs, Bulgaria and Serbia. *Journal of Volcanology and Geothermal Research,* 110**,** 299-318.

SAVOV, I. P., BIZIMIS, M., HALAMA, R., SHIREY, S., HAURI, E. & HAYDOUTOV, I. 2007. Li-Sr-Lu-Hf isotope and trace element systematics of eclogites from Bulgaria. *Geochimica Et Cosmochimica Acta,* 71**,** A879-A879.

SCHERER, E. E., CAMERON, K. L. & BLICHERT-TOFT, J. 2000. Lu–hf garnet geochronology: closure temperature relative to the Sm–Nd system and the effects of trace mineral inclusions. *Geochimica Et Cosmochimica Acta,* 64**,** 3413-3432.

SCHMID, R., ROMER, R. L., FRANZ, L., OBERHÄNSLI, R. & MARTINOTTI, G. 2003. Basement-Cover Sequences within the UHP unit of the Dabie Shan. *Journal of Metamorphic Geology,* 21**,** 531-538.

SCHMIDT, S., NAGEL, T. J. & FROITZHEIM, N. 2010. A new occurrence of microdiamond-bearing metamorphic rocks, SW Rhodopes, Greece. *European Journal of Mineralogy,* 22**,** 189-198.

SCHOLL, D. W. & VON HUENE, R. 2007. Crustal recycling at modern subduction zones applied to the past—Issues of growth and preservation of continental basement crust, mantle geochemistry, and supercontinent reconstruction. *Geological Society of America Memoirs,* 200**,** 9-32.

SCHWARTZ, S., ALLEMAND, P. & GUILLOT, S. 2001. Numerical model of the effect of serpentinites on the exhumation of eclogitic rocks: insights from the Monviso ophiolitic massif (Western Alps). *Tectonophysics,* 342**,** 193-206.

SHERVAIS, J. W. 1982. Ti-V plots and the petrogenesis of modern and ophiolitic lavas. *Earth and Planetary Science Letters,* 59**,** 101-118.

SIPPL, C., SCHURR, B., YUAN, X., MECHIE, J., SCHNEIDER, F. M., GADOEV, M., ORUNBAEV, S., OIMAHMADOV, I., HABERLAND, C., ABDYBACHAEV, U., MINAEV, V., NEGMATULLAEV, S. & RADJABOV, N. 2013. Geometry of the Pamir-Hindu Kush intermediate-depth earthquake zone from local seismic data. *Journal of Geophysical Research: Solid Earth,* 118**,** 1438-1457.

SIZOVA, E., GERYA, T. & BROWN, M. 2012. Exhumation mechanisms of melt-bearing ultrahigh pressure crustal rocks during collision of spontaneously moving plates. *Journal of Metamorphic Geology,* 30**,** 927-955.

SKORA, S., LAPEN, T. J., BAUMGARTNER, L. P., JOHNSON, C. M., HELLEBRAND, E. & MAHLEN, N. J. 2009. The duration of prograde garnet crystallization in the UHP eclogites at Lago di Cignana, Italy. *Earth and Planetary Science Letters,* 287**,** 402-411.

SMIT, M., SCHERER, E., BRÖCKER, M. & ROERMUND, H. M. 2010. Timing of eclogite facies metamorphism in the southernmost Scandinavian Caledonides by Lu–Hf and Sm–Nd geochronology. *Contributions to Mineralogy and Petrology,* 159**,** 521-539.

SMIT, M. A., SCHERER, E. E. & MEZGER, K. 2013. Lu–Hf and Sm–Nd garnet geochronology: Chronometric closure and implications for dating petrological processes. *Earth and Planetary Science Letters,* 381**,** 222-233.

SMITH, D. C. 1984. Coesite in clinopyroxene in the Caledonides and its implications for geodynamics.

SOBOLEV, N. & SHATSKY, V. 1990. Diamond inclusions in garnets from metamorphic rocks: a new environment for diamond formation. *Nature,* 343**,** 742-746.

SOUSA, J., KOHN, M. J., SCHMITZ, M. D., NORTHRUP, C. J. & SPEAR, F. S. 2013. Strontium isotope zoning in garnet: implications for metamorphic matrix equilibration, geochronology and phase equilibrium modelling. *Journal of Metamorphic Geology,* 31**,** 437-452.

SPANDLER, C. & PIRARD, C. 2013. Element recycling from subducting slabs to arc crust: A review. *Lithos,* 170–171**,** 208-223.

SPEAR, F. S., KOHN, M. J. & CHENEY, J. T. 1999. P-T paths from anatectic pelites. *Contributions to Mineralogy and Petrology,* 134**,** 17-32.

STAMPFLI, G. M. & KOZUR, H. W. 2006. Europe from the Variscan to the Alpine cycles. *Geological Society, London, Memoirs,* 32**,** 57-82.

STAMPFLI, G. & BOREL, G. 2002. A plate tectonic model for the Paleozoic and Mesozoic constrained by dynamic plate boundaries and restored synthetic oceanic isochrons. *Earth and Planetary Science Letters,* 196**,** 17-33.

STAMPFLI, G. M. & HOCHARD, C. 2009. Plate tectonics of the Alpine realm. *Geological Society, London, Special Publications,* 327**,** 89-111.

STÖCKHERT, B., DUYSTER, J., TREPMANN, C. & MASSONNE, H.-J. 2001. Microdiamond daughter crystals precipitated from supercritical COH+ silicate fluids included in garnet, Erzgebirge, Germany. *Geology,* 29**,** 391-394.

STÖCKHERT, B. & GERYA, T. V. 2005. Pre‐collisional high pressure metamorphism and nappe tectonics at active continental margins: a numerical simulation. *Terra Nova,* 17**,** 102-110.

THIRLWALL, M. F. 1991. Long-term reproducibility of multicollector Sr and Nd isotope ratio analysis. *Chemical Geology: Isotope Geoscience section,* 94**,** 85-104.

THOMPSON, A. B. 1976. Mineral reactions in pelitic rocks; II, Calculation of some PTX (Fe-Mg) phase relations. *American Journal of Science,* 276**,** 425-454.

TIRONE, M., GANGULY, J., DOHMEN, R., LANGENHORST, F., HERVIG, R. & BECKER, H.-W. 2005. Rare earth diffusion kinetics in garnet: Experimental studies and applications. *Geochimica Et Cosmochimica Acta,* 69**,** 2385-2398.

TURPAUD, P. & REISCHMANN, T. 2010. Characterisation of igneous terranes by zircon dating: implications for UHP occurrences and suture identification in the Central Rhodope, northern Greece. *International Journal of Earth Sciences,* 99**,** 567-591.

VAN HUNEN, J. & ALLEN, M. B. 2011. Continental collision and slab break-off: A comparison of 3-D numerical models with observations. *Earth and Planetary Science Letters,* 302**,** 27-37.

VAVASSIS, I., DE BONO, A., STAMPFLI, G., GIORGIS, D., VALLOTON, A. & AMELIN, Y. 2000. U-Pb and Ar-Ar geochronological data from the Pelagonian basement in Evia (Greece): geodynamic implications for the evolution of Paleotethys. *Schweizerische Mineralogische und Petrographische Mitteilungen,* 80**,** 21-43.

VERMEESCH, P. 2006. Tectonic discrimination diagrams revisited. *Geochemistry, Geophysics, Geosystems,* 7**,** Q06017.

VON QUADT, A., MORITZ, R., PEYTCHEVA, I. & HEINRICH, C. A. 2005. 3: Geochronology and geodynamics of Late Cretaceous magmatism and Cu–Au mineralization in the Panagyurishte region of the Apuseni–Banat–Timok–Srednogorie belt, Bulgaria. *Ore Geology Reviews,* 27**,** 95-126.

VON QUADT, A., SAROV, S., PEYTCHEVA, I., VOYNOVA, E., PETROV, N., NEDKOVA, K. & NAYDENOV, K. Metamorphic rocks from northern parts of Central Rhodopes—conventional and in situ U-Pb zircon dating, isotope tracing and correlations. National Conference Geosciences, Bulg. Geol. Soc., Sofia, 2006.

VRIJMOED, J. C., PODLADCHIKOV, Y. Y., ANDERSEN, T. B. & HARTZ, E. H. 2009. An alternative model for ultra-high pressure in the Svartberget Fe-Ti garnet-peridotite, Western Gneiss Region, Norway. *European Journal of Mineralogy,* 21**,** 1119-1133.

WALSH, E. & HACKER, B. 2004. The fate of subducted continental margins: Two‐stage exhumation of the high‐pressure to ultrahigh‐pressure Western Gneiss Region, Norway. *Journal of Metamorphic Geology,* 22**,** 671-687.

WARREN, C. 2013. Exhumation of (ultra-) high-pressure terranes: concepts and mechanisms. *Solid Earth,* 4.

WARREN, C. J., BEAUMONT, C. & JAMIESON, R. A. 2008. Modelling tectonic styles and ultra-high pressure (UHP) rock exhumation during the transition from oceanic subduction to continental collision. *Earth and Planetary Science Letters,* 267**,** 129-145.

WAWRZENITZ, N. & KROHE, A. 1998. Exhumation and doming of the Thasos metamorphic core complex (S Rhodope, Greece): structural and geochronological constraints. *Tectonophysics,* 285**,** 301-332.

WAWRZENITZ, N. & MPOSKOS, E. 1997. First evidence for Lower Cretaceous HP/HT-metamorphism in the eastern Rhodope, North Aegean region, North-east Greece. *European Journal of Mineralogy-Ohne Beihefte,* 9**,** 659-664.

WOOD, D. A. 1980. The application of a Th-Hf-Ta diagram to problems of tectonomagmatic classification and to establishing the nature of crustal contamination of basaltic lavas of the Birtish Tertiary Volcanic Province. . *Earth and Planetary Science Letters,* 50**,** 11-30.

WÜTHRICH, E. D. 2009. *Low temperature thermochronology of the northern Aegean Rhodope Massif.* ETH.

YANG, J.-S., DOBRZHINETSKAYA, L., BAI, W.-J., FANG, Q.-S., ROBINSON, P. T., ZHANG, J. & GREEN, H. W. 2007. Diamond- and coesite-bearing chromitites from the Luobusa ophiolite, Tibet. *Geology,* 35**,** 875-878.

YARDLEY, B. W. D. & BARBER, J. P. 1991. Melting reactions in the Connemara Schists; the role of water infiltration in the formation of amphibolite facies migmatites. *American Mineralogist,* 76**,** 848-856.

YILMAZ ŞAHIN, S., AYSAL, N., GÜNGÖR, Y., PEYTCHEVA, I. & NEUBAUER, F. in press. Geochemistry and U–Pb zircon geochronology of metagranites in Istranca (Strandja) Zone, NW Pontides, Turkey: Implications for the geodynamic evolution of Cadomian orogeny. *Gondwana Research*.

ZACHARIADIS, P. 2007. Ophiolites of the eastern Vardar Zone. *N. Greece. PhD dissertationMainz: Johannes Gutenberg-Universita «t*.

ZACK, T., MORAES, R. & KRONZ, A. 2004. Temperature dependence of Zr in rutile: empirical calibration of a rutile thermometer. *Contributions to Mineralogy and Petrology,* 148**,** 471-488.

ZHENG, Y.-F., XIA, Q.-X., CHEN, R.-X. & GAO, X.-Y. 2011. Partial melting, fluid supercriticality and element mobility in ultrahigh-pressure metamorphic rocks during continental collision. *Earth-Science Reviews,* 107**,** 342-374.